A Multifaceted Approach for Cancer Therapeutics

A Thesis

Submitted in Partial Fulfillment of the Requirements for the Degree of

DOCTOR OF PHILOSOPHY

By

Bidkar Anil Parsram

(Roll no. – 146106024)

Indian Institute of Technology Guwahati

Department of Biosciences & Bioengineering

Indian Institute of Technology Guwahati

Guwahati, Assam

Dedicated to my Family

DECLARATION

I hereby declare that the results and discussions embodied in the thesis titled "**A Multifaceted Approach for Cancer Therapeutics"** are the outcome of research work carried out by me under the supervision of Prof. Siddhartha Sankar Ghosh, Department of Biosciences & Bioengineering, Indian Institute of Technology Guwahati, Guwahati, Assam, India for the award of the degree of Doctor of Philosophy. To the best of my knowledge and belief, the present thesis has not been submitted for any degree, diploma, associateship etc. of any Institute or University elsewhere.

Date:

Place:

Bidkar Anil Parsram

Roll number: 146106024

INDIAN INSTITUTE OF TECHNOLOGY GUWAHATI

DEPARTMENT OF BIOSCIENCES AND BIOENGINEERING

CERTIFICATE

This is to certify that this thesis entitled "**A Multifaceted Approach for Cancer Therapeutics**" has been submitted by **Bidkar Anil Parsram** (Roll No. **146106024**) to **Indian Institute of Technology Guwahati** for the award of the degree of **Doctor of Philosophy.** This thesis is a record of the bonafide research work carried out by him during his degree tenure. The findings presented here are purely derived from his own research work. He has meticulously performed the research and has been ardently adherent of lab protocols. This work in parts or as a whole is novel and is not been produced in any previous diploma or degree.

Date:

Place:

Prof. Siddhartha Sankar Ghosh

(Thesis Supervisor)

ACKNOWLEDGEMENT

First and foremost, I would like to thank my supervisor, Professor Siddhartha Sankar Ghosh for his constant support and encouragement throughout my Ph.D.; your advice and expertise has been invaluable. Additional thanks to Dr. Pallab Sanpui for his suggestions and advices.

I am also enormously grateful to my doctoral committee members- Dr. Biplab Bose, Dr. Ranjan Tamuli and Dr. Bhubaneswar Mandal for their valuable suggestions and critical inputs throughout the course of these five years.

I am heavily indebted to my senior lab members- Archita di, Asif bhaiya, Bandhan, Mahesh bhaiya, Neha di, Sharmila di and Upashi di for painstakingly, yet lovingly, imparting to me all their gathered knowledge. I will always remember the affection bestowed upon me by my beloved seniors.

I sincerely appreciate the help from all my labmates and colleagues- Srirupa, Rajib, Muktashree, Plaboni, Anitha, Vanitha, Gavya, Vimal, Dheerendra and Umed.

I am blessed to have friends like Khandu, Sandip, Srirupa, KK, Satendra, Bapi, Bandhan, Vijay, Amit, and Adarsh.

I must thank my collaborators Gopal, Rupam, Binita, Taufiq and Niranjan, for the interdisciplinary work related discussions.

I am grateful to the Department of Biosciences and Bioengineering, Centre for Nanotechnology, DBT Program Support Facility and Central Instrumentation Facility, IIT Guwahati, for providing me with all the support required for carrying out my thesis work.

Finally, my parents, brothers Ashok, Sunil, Khandu, Kiran and Suraj deserve a special mention here. I would not have reached the position that I am now, if not their love, care, and encouragement.

Anil Bidkar

TABLE OF CONTENTS

ABSTRACT

Cellular, genetic and epigenetic modifications leading to uncontrolled proliferation results in tumor mass formation. At tumor hypoxic core, cells barely proliferate resulting in drug-resistance. Effective monotherapies, as well as combination therapies, are being employed for remission of such tumors. However, chemotherapeutic approaches have limitations mainly due to poor solubility of anticancer drugs, lack of selectivity and multi-drug resistance. Alternative therapeutic strategies including nanomedicine, may improve drug solubility, enhance stability in the circulatory system and reduce drug toxicity. Targeted delivery of anti-cancer drugs is of paramount importance for cancer treatment, as it helps in improving the overall therapeutic efficacy by minimizing killing of normal cells due to non-specific cytotoxicity of chemotherapeutic drugs. In the present study, investigations have persuaded to standardize the procedures for development and use of different nanocarriers (NCs) for drug delivery.

The present thesis aims to exploit the nanocarriers based treatment approaches for cancer therapeutics. In Chapter 1, the review of literature covers fundamentals of nanoparticle-mediated targeted drug delivery to cancer cells. Different types of nanoparticles such as liposomes, dendrimers, micelles, hydrogel, inorganic or polymeric nanoparticles with potential therapeutic applications have been mentioned. Tumor cells specific biomarkers mainly overexpressed in tumor cells such as, folic acid receptor (FAR) and transferrin receptor (TR) are mentioned for targeted delivery. Importantly, development of nanocarriers based on Selenium and RBC membrane have been discussed in this chapter. Finally, key research areas and salient features of the current thesis have been illustrated.

In Chapter 2, development of a novel nanocarrier (NC) based drug delivery system for chemotherapeutic drug paclitaxel (PTX), by employing pluronic F-127 stabilized selenium nanoparticles (SeNPs) has been reported.

Successful delivery of PTX, PTX-loaded SeNPs as well as anti-proliferative activity against lung, breast, cervical and colon cancer cells have been demonstrated. Flow-cytometry based cell cycle analyses of PTX-SeNPs treated cells revealed G_2/M phase arrest in a dose-dependent manner leading to apoptosis. This chapter also describes the cellular mechanism of apoptosis in treated conditions via induction of reactive oxygen species (ROS), disruption of mitochondrial membrane potential (MMP) and activation of caspases.

In Chapter 3, a more selective and targeted therapy have been reported for the tumor cells with high expression of FAR and mutations in the genes of the MAPK pathway. MDAMB231 (breast cancer) cells have G13D and G464V mutations in RAS and BRAF genes, respectively, while A375 (melanoma) cells possess V600E mutations in BRAF. These mutations cause constitutive activation of the MAPK signaling, which leads to uncontrolled proliferation and cancerous growth. The chapter describes use of combination therapy module involving FAR-targeted SeNPs (FA-SeNPs) and MAPK inhibitor PD98059 (PD98).

Chapter 4 demonstrates the use of red blood cell (RBC) membrane for anti-cancer drug delivery. The nanocarriers have been designed for the delivery of chemotherapeutic agent (Curcumin/Cur) and hypoxia activating molecule (Tirapazamine/TPZ). Initially, Cur and TPZ were loaded on biodegradable PLGA NPs, and these drug-loaded PLGA NPs were coated with RBC membrane by extrusion. This chapter describes characterization and the functional assays of the drug-loaded NPs on monolayer as well as hypoxic spheroids. It was found that the RBC membrane provided improved stability and biocompatibility. Functional assays on cells and multicellular spheroids (MCS) suggested facile uptake of these NPs in cancer cells resulting in synergistic activity. Finally, the mechanism of the action of cell death has been elucidated.

In Chapter 5, the therapeutic efficiency of the transferrin bound RBC membrane-coated PLGA NPs to deliver doxorubicin and methylene blue was studied for chemo- and photodynamic therapy. PLGA NPs loaded with doxorubicin and methylene blue were extruded with RBC membranes, forming membrane coated PLGA NPs. To achieve target-specific delivery to tumor cells, transferrin was conjugated onto RBC membranes before extrusion. Transferrin-bound, doxorubicin, and methylene blue loaded RB-NPs (TF-RB-NPs) were characterized and tested on the cells overexpressing transferrin receptors.

The final section on conclusion and future prospects summarizes the findings and major leads of the current thesis work. The experimental evidence demonstrated the importance of targeted delivery of selenium nanoparticles and RBC membrane coated nanocarriers in the modulation of cellular signaling leading to annihilation of cancer monolayer cells as well as spheroids. Inhibition of MAP kinase pathways, treatment of hypoxic spheroids will provide a better strategy for development of successful combination therapy to combat drug-resistant tumor.

List of Abbreviations

β-MCD:	**β**-methylcyclodextrin	**FBS:**	Fetal bovine serum
DNA:	Deoxyribose Nucleic Acid	**FESEM:**	Field emission scanning electron microscopy
CNTs:	Carbon nanotubes	**FTIR:**	Fourier-transform infrared spectroscopy
Cur:	Curcumin	**LPS:**	Lipopolysaccharide
COX-2:	Cyclooxygenase-2	**MDR:**	Multi-drug resistance
CTCF:	Total corrected cell fluorescence	**MRI:**	Magnetic resonance imaging
C_t:	Threshold cycles	**MAPK:**	Mitogen-activated protein kinase
CLSM:	Confocal laser scanning microscopy	**MMP:**	Mitochondrial membrane potential
CI:	Combination index	**MCS:**	Multicellular spheroids
CS:	Chitosan	**MB:**	Methylene blue
DDS:	Drug delivery systems	**NCs:**	Nanocarriers
DOX:	Doxorubicin	**NIR:**	Near-infrared
DMEM:	Dulbecco's modified eagles medium	**PLGA:**	Poly(lactic-co-glycolic acid)
DCFDA:	2',7' – dichlorofluorescin diacetate	**PEG:**	Polyethylene glycol
DLS:	Dynamic light scattering	**PDT:**	Photodynamic therapy
DSC:	Differential scanning calorimetry	**PTX:**	Paclitaxel
DMSO:	Dimethylsulfoxide	**PI:**	Propidium iodide
EPR:	Enhanced permeability and retention	**PD98:**	PD98059
EMT:	Epithelial to mesenchymal transition	**PCR:**	Polymerase chain reaction
FDA:	Food and drug administration	**PBS:**	Phosphate buffer saline
FA:	Folic acid	**PDI:**	Polydispersity index

FAR:	Folic acid receptor
5-FU:	5-Fluorouracil
RES:	Reticuloendothelial system
RBC:	Red Blood Cells
ROS:	Reactive oxygen species
RNA:	Ribonucleic acid
Se:	Selenium
SeNPs:	Selenium nanoparticles
SeO_2:	Selenium dioxide
SDS-PAGE:	sodium dodecyl sulfate polyacrylamide gel electrophoresis
TF:	Transferrin
PVDF:	Polyvinylidene fluoride
PARP:	poly (ADP-ribose) polymerase
TPZ:	Tirapazamine
TEM:	Transmission electron microscopy
TGA:	Thermogravimetric analysis
TM:	Tail moments
TUNEL:	Terminal deoxynucleotidyltransferase dUTP nick end labeling
QD:	Quantum dots
XRD:	X-ray diffraction
XPS:	X-ray photoelectron spectroscopy

List of Schemes

List of Figures

.

List of Tables

CHAPTER 1

Introduction and Review of Literature

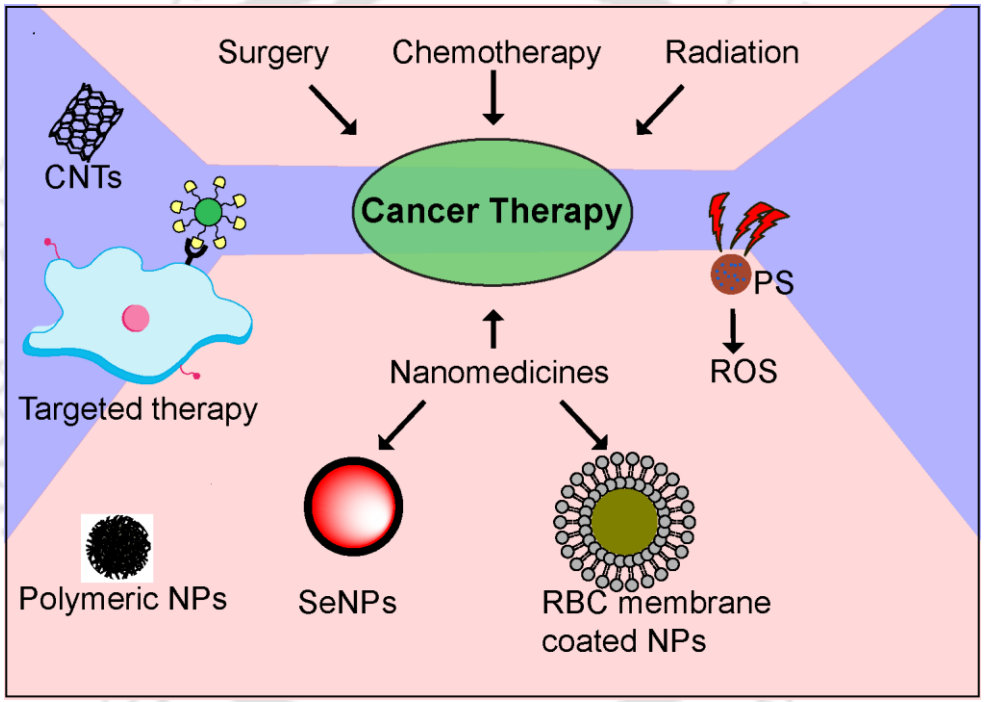

Chapter 1 includes the Introduction and Review of Literature. Starting with the strategies for cancer therapy, this chapter introduces various types of nanocarriers and their applications in drug delivery. The chapter also focuses on the Selenium and the RBC membrane-based drug delivery systems.

भारतीय प्रौद्योगिकी संस्थान गुवाहाटी
Indian Institute of Technology Guwahati

CHAPTER 1

Introduction & Review of Literature

1.1 Cancer at a glance

Cancer is resulted from the abnormal and uncontrolled proliferation of the body cells. Thereafter, the rapidly diving cells spread to other organs or tissues, resulting in metastasis.[1] The human body is made up of trillions of cell, but the course of the new cell to cell death is tightly controlled or regulated. In case of healthy cells, cells divide, grow, and die according to their lifespan. After death, new cells again grow and start functioning. However, in the case of cancer, due to the mutations in DNA, these cells keep multiplying to form abnormal tissue growth (**Figure 1.1**).[2] Among the deaths caused by non-communicable diseases, cancer is at 2nd place accounting for 22% deaths, worldwide.[3] Despite ongoing research and advanced healthcare facilities, the number of death on cancer is increasing annually. Henceforth, researchers, medical professionals, and pharmaceutical companies are working towards developing new strategies to combat cancer.

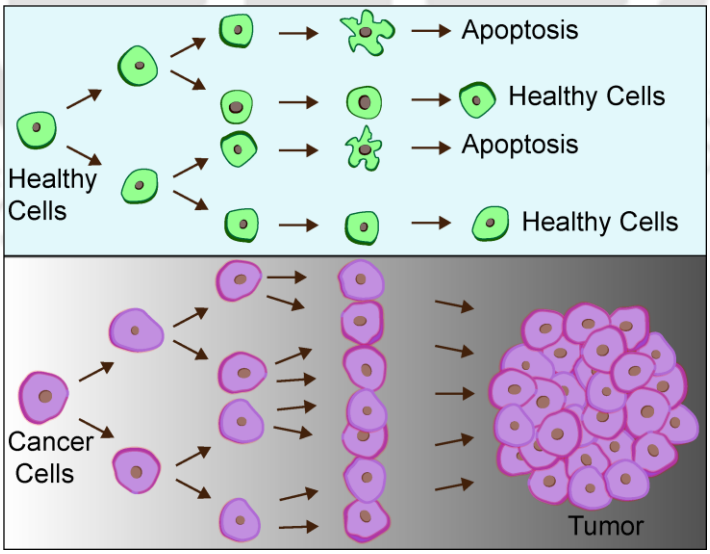

Figure 1.1 Normal vs. cancer cell division and tumor formation.

1.2 Conventional strategies of cancer treatment

For the treatment of cancer, three main conventional therapeutic approaches are available, which are chemotherapy, radiation therapy, and surgery (**Figure 1.2**). The term "Chemotherapy" was initially given by german scientist Paul Ehrlich, which meant 'treatment of the disease with the help of chemicals'.[4] Following this, in 1943, the discovery of the therapeutic action of the nitrogen mustards by Goodman and Gilman translated into treatment of lymphomas.[5] Since then, continuous research in the field of drug discovery has produced a vast number of potential therapeutic molecules, some of which are regularly used for cancer treatment. Since cancer cells divide much faster than non-cancerous cells; the chemotherapeutic approach works by destroying these rapidly dividing cells. Use of cytotoxic drugs on cancer cells causes rewiring of the cell signaling resulting in apoptosis mediated cell death.[6]

Table 1.1 Classification of the anticancer agents, examples and treatment modalities.

Drug Class	**Examples**	**Cancer**
Alkylating agents	Nitrogen mustards, Cyclophosphamide	Lung, Breast cancers, Leukemia, Hodgkin disease, multiple myeloma
Antimetabolites	5-FU, Gemcitabine	Breast, ovary, and the intestinal tract cancers
Antibiotics	Doxorubicin, Bleomycin, Actinomycin D	Lymphoblastic leukaemia, breast, thyroid, ovary, bladder lung cancers, Neuroblastoma.
Plant alkaloids	Vincristine, Paclitaxel, Vinorelbine, Vinblastine	Acute myeloid leukaemia, Hodgkin's disease, Wilms' tumour, Ewing's sarcoma, neuroblastoma carcinoma lung.
Topoisomerase inhibitors	Topotecan, Etoposide,	Ovary, small cell lung cancer, cervical cancer.

Surgery is also an effective strategy to remove the affected tissue or organ areas. Early detection helps in managing removal of tumor.[7] Surgical procedures are comparatively easy for removal of solid tumors, whereas the cancer of vital organs or blood cancers cannot be treated by surgery. Depending on the nature of the tumor and patient's status, single or combinations of the chemotherapy, radiation, and surgery are being used.[8]

Radiation therapy involves use of the high energy beams like X-ray and gamma rays on tumor cells. However, high dose of the radiation causes DNA strand breaks to the extent that cells cannot repair such damage.[9] The laser beam can be directly projected at the affected area. Therefore, radiation can be targeted to the cancer cells avoiding surrounding healthy cells.[10] This results in minimal damage to healthy cells. Along with these three main types of therapies; alternative therapies like targeted, hormonal, and immunotherapies are also essential to eradicate tumor completely.

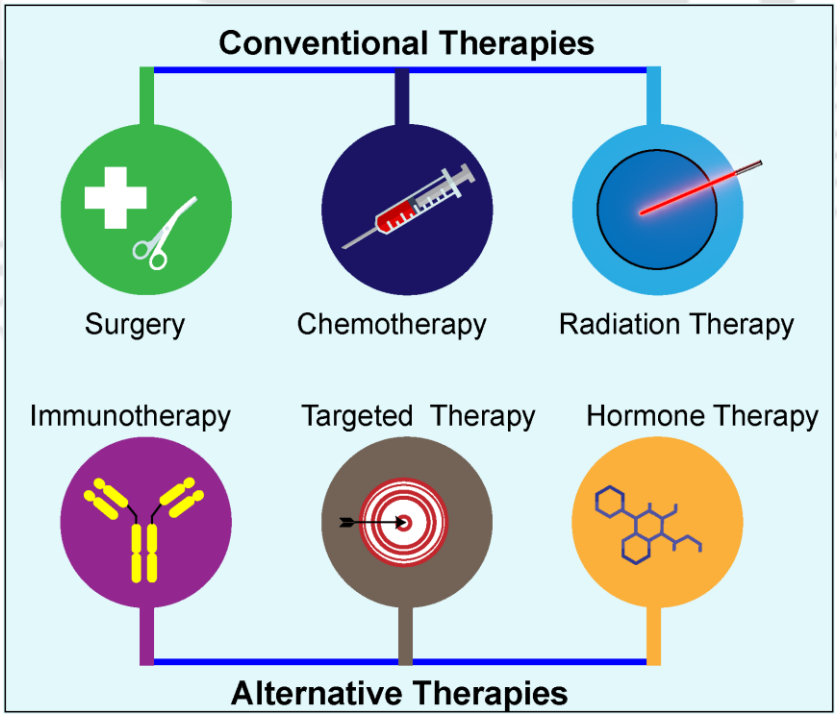

Figure 1.2 Current strategies for cancer treatment (Conceptualized and redrawn).

1.3 Nanocarriers in Cancer Therapy

As mentioned earlier, cancer cells divide and proliferate quickly; thus the chemotherapeutic drug targets these rapidly dividing cells. As a consequence, it also affects the healthy or non-cancerous cells that are growing faster. Henceforth, along with the cancer cells, conventional cancer therapies also kill healthy cells, leaving behind undesired toxic side effect.[11] This non-selective or non-targeted nature of chemotherapy can result in toxicity. Another issue with chemotherapy is the development of the multi-drug resistance (MDR). In MDR, cancer cells show increased expression of the protein molecules involved in drug efflux outside the cells. Due to the MDR, most of the chemotherapeutic drugs are exported out of the cancer cells, making the cells resistant to those drugs. Therefore, to avoid these concerns the newer nano-based drug delivery systems (DDS) are being developed.[12] Different types of NCs with potential therapeutic implications include liposomes, dendrimers, micelles, hydrogel, and inorganic or polymeric nanoparticles (NPs).[13] In this regard, the properties of inorganic NPs that have been exploited for the biomedical purpose include antibacterial, anticancer and optical one for diagnostics.[14]

Nanocarriers possess specific advantages over the bulk materials used for their preparation.[15] As the size of the bulk material reduces to the nanoscale, a significant increase in the surface allows higher cargo loading. Increased drug loading capacity categorically results in increased drug delivery to the site of action, causing a reduction of cancer cell growth. Smartly designed nanocarriers are being used for controlled or sustained release of the payload to maintain enough drug concentration in the blood for a longer time. Similarly, improved physicochemical, as well as optical properties, were observed for metallic or semi-metallic materials based nanomaterials.[16] In addition to the physico-chemical properties, toxicity of specific molecules also reduces after preparation of nanocarriers.[15]

1.4 Targeted drug delivery

Once inside the body, drug-carrying nanocarriers face multiple obstacles, such as penetration through the walls of blood vessels and mucosal barriers. The targeted drug delivery aims to accumulate a higher amount of the drug at the desired site of action. The increased amount of the drugs at the affected area helps to achieve significant therapeutic effect than non-targeted drugs. To achieve the targeting of the nanocarriers, two approaches are utilized, passive targeting and active targeting (**Figure 1.3**).

1.4.1 Passive targeting

Passive targeting takes advantages of the unique nature of tumor biology and the surroundings of the tumor mass. The phenomenon is known as enhanced permeability and retention effect (EPR), EPR plays important role to achieve passive targeting.[17] When the tumor starts developing at a faster rate, it needs all the possible supply of the nutrients and oxygen. In order to achieve these extra nutrients for faster growth, tumor cells secrete angiogenic factors to produce new blood vessels around the tumor mass.[18] The growing tumor solely depends on the newly formed blood vessels for nutrient supply.

Importantly, the new blood vessels formed do not possess complete architecture, which results in leaky vasculature. Along with this, the tumor site also lacks efficient lymphatic drainage system. This EPR effect collectively results in delivery of the macromolecules and nanocarriers at the higher quantity to tumor site. In order to achieve the EPR effect, nanocarriers should be long circulating in blood to avoid the clearance by the reticuloendothelial system. This characteristic of the long circulation in blood can be achieved by coating the nanocarriers with polyethylene glycol (PEG).[19] PEG coating masks the nanocarriers for uptake and clearance from macrophage cells. For example, Doxil PEGylated liposomes of doxorubicin, approved for cancer treatment (Kaposi sarcoma) is delivered to cancer cells through EPR effect.[11,20]

1.4.2 Active targeting

In case of the active targeting, a special features of the diseased cells are being used to distinguish these cells from normal cells. To achieve the drug delivery to a particular tissue or region, drug can be conjugated to a specific targeting moiety. The drug-moiety conjugate interacts with the receptor or proteins on target cells, resulting in specific delivery inside these cells. Here, targeting moiety could be antibody, peptides, aptamers or polysaccharides interacting with target cell surface. For targeted delivery, the simplest approach would be to conjugate drug directly to the targeting moiety, like drug-antibody conjugation. For example, ado-trastuzumab emtansine is a drug antibody conjugate, DM-1 drug is conjugated with trastuzumab antibody.[21] This conjugate is being used for targeting HER2 positive metastatic breast cancer cells. Binding of the trastuzumab to the HER2 receptors results in selective internalization of the drug-conjugate. Once inside the endosome, it releases the DM-1 molecules to show its therapeutic action.[22]

Apart from the direct conjugation of the drug to the targeting moiety, surface modified nanocarriers are also used for targeting. For nanocarrier-mediated targeted drug delivery, nano-formulations are loaded with the active drugs; by conjugating the targeting molecules on the surface of the nanocarriers, target-specific drug delivery can be achieved. Cancer cells possess certain protein or receptors at higher amount than healthy cells. For example, many cancer cells have been shown to have overexpressed transferrin (TF) receptors.[23] Transferrin receptor helps to maintain the iron homeostasis by binding and internalization of iron-bound transferrin molecules. Different type of nanocarriers have been produced by TF-conjugation to achieve targeted drug delivery.[24] For example, TF receptor targeted NPs delivered siRNA in *in-vivo* tumor model to achieve safe and effective strategy for cancer therapy.[25]

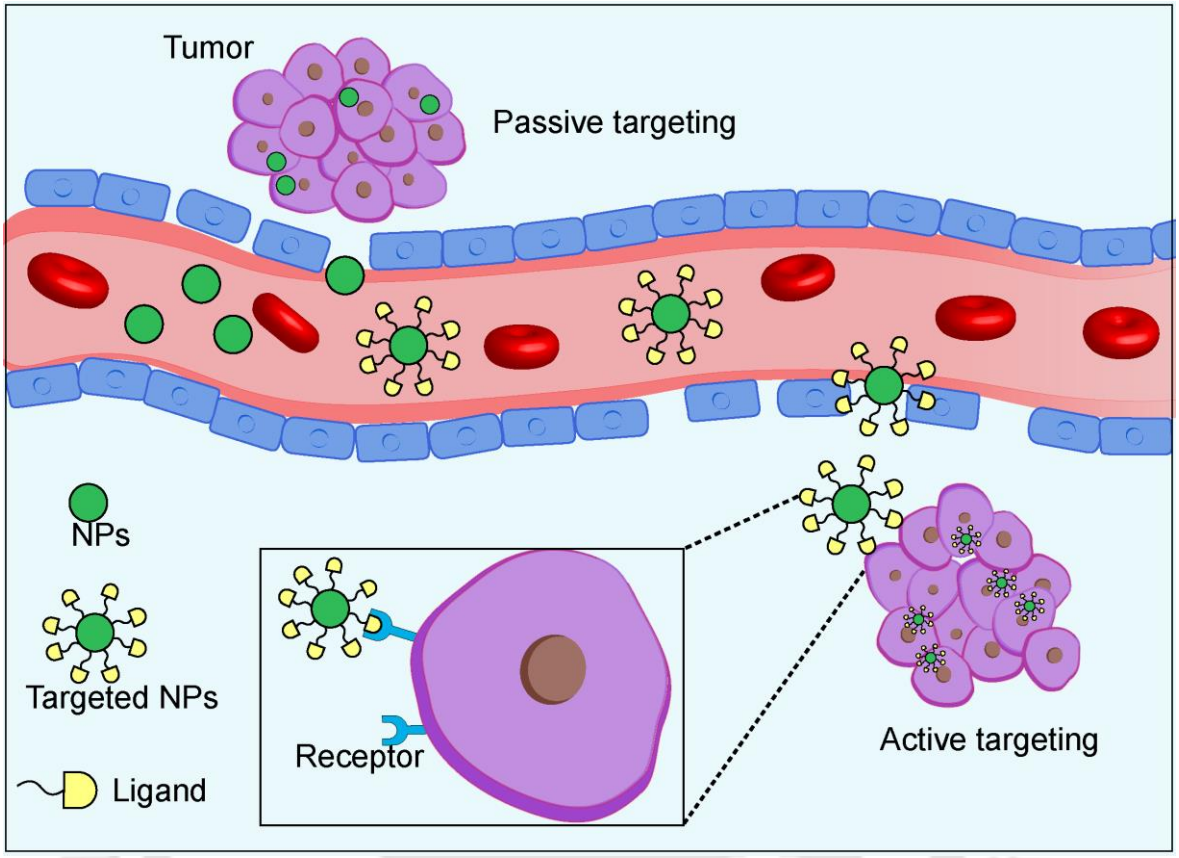

Figure 1.3 Schematic representation of the nanocarriers mediated active and passive targeting of the tumor cells for drug delivery. (Conceptualized and redrawn).

1.5 Types of nanocarriers for cancer therapy

1.5.1 Polymeric nanocarriers

Polymeric nanoparticles are widely used for drug delivery application. Important properties of the polymeric nanocarriers include their stability, high drug loading capacity and sustained drug release ability. Notably, the polymers like poly-caprolactone (PCL), poly (D,L-lactide-*co*-glycolide) (PLGA) and poly(lactic acid) (PLA) are biodegradable in nature, thus are safe for internal use.[26] Along with these polymers, a co-polymers or block polymers are being developed by cross-linking the chitosan, gelatin, and sodium alginate.[27,28] **Table 1.2** shows some of the examples of the polymeric

formulation approved for therapeutic purpose.[29] Along with polymeric nanoparticles, micelles formed from amphiphilic block co-polymers are also gaining importance.[30] These are core-shell type nano-formulations made from self-assembly of the block polymers. Polymeric micelles possess unique characteristics like their nano size, spherical morphology and ability to retain hydrophobic drug molecules, which make them suitable for drug delivery applications.[31] Polymeric nanocarriers like core shell NPs, micelles, dendrimers are shown in **Figure 1.4**.

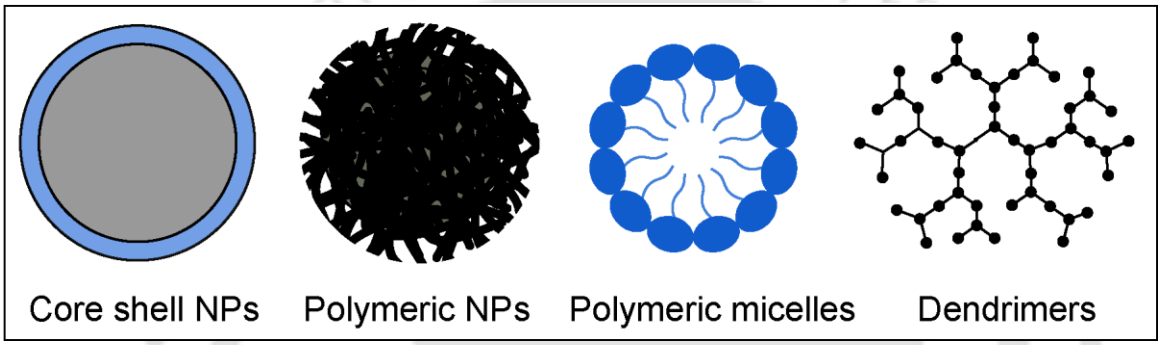

Figure 1.4 Types of polymeric nanocarriers.

1.5.2 Inorganic NPs

Important inorganic nanoparticles include gold, silver, iron, quantum dots (QD) and silica NPs. Size of these NPs ranges from 1-100 nm. Inorganic nanoparticles are well-known for their change in the physico-chemical properties depending on their sizes.[32] Gold NPs, and QDs can be used for drug delivery and due to the fluorescent nature they have wide application in theranostic area. One of the important applications of the inorganic NPs is in biomedical imaging. In this case, imaging probe stains the organ or the tissue for observation by a medical practitioner. Here the magnetic and optical properties of the probes are utilized for diagnosis purpose. Iron oxide NPs have been used for magnet guided drug delivery and magnetic resonance imaging (MRI) due to their unique magnetic properties,.[33]

Table 1.2 Nanomedicines approved by FDA for therapeutic applications. [Adapted from reference 29**,** Copyright: Young Hee Choi (2017)].

Formulations	Product name	Indications
Polymer NP: synthetic polymer particles		
PEGylated adenosine deaminase enzyme	Adagen®/pegademase bovine	Serious immunodeficiency therapy
PEGylated antibody fragment (Certolizumab)	Cimzia®/certolizumabpegol	Chron's disease, rheumatoid arthritis, psoriasis, ankylosing spondylitis
Random copolymer of L-gluta- mate, L-alanine, L-lysine.	Copaxone®/Glatopa	Multiple sclerosis
Leuprolide acetate and polymer [PLGH(poly(DL-lactide-cogly- colide)]	Eligard®	Prostate cancer
PEGylated anti-VEGF aptamer (vascular endothelial growth factor) aptamer	Macugen®/Pegaptanib	Decreased vision
Chemically synthesized ESA (erythropoiesis-stimulating Factor)	Mircera®/Methoxy PEG glycol-epoetin p	Anemia with chronic renal failure
PEGylated GCSF protein	Neulasta®/pegfilgrastim	Leukopenia by chemotherapy
PEGylated IFN alpha-2a protein	Pegasys®	Hepatitis B and C
PEGylated IFN alpha-2b protein	Peglntron®	Hepatitis C
Poly(allylamine hydrochloride)	Renagel®	Chronic renal failure
Polymer-protein conjugate PEGylated L-asparaginase	Oncaspar®/pegaspargase	Acute lymphocytic blood clot
Polymer-protein conjugate (PEGylated porcine-likeuricase)	Krystexxa®/pegloticase	Chronic gout
Polymer-protein conjugate (PEGylated IFNbeta-la)	Plegridy®	Multiple sclerosis
Polymer-protein conjugate (PEGylated factor VIII)	ADYNOVATE	Hemophilia
Liposomes		
Liposomal daunorubicin	DaunoXome®	Karposi sarcoma

Liposomal cytarabine	DepoCyt©	Lymphoma
Liposomal vincristine	Marqibo®	Acute lymphocytic blood clot
Liposomal irinotecan	Onivyde®	Pancreatic cancer
Liposomal amphotericin B	AmBisome®	Fungal infection
Liposomal morphine sulphate	DepoDur®	Loss of pain due to surgery
Liposomal verteporfin	Visudyne®	Decreased vision, Ophthalmic
Liposomal doxorubicin	Doxil®/Caelyx™	Karposi sarcoma, ovarian cancer,
Liposomal amphotericinB lipid complex	Abelcet®	Fungal infection
Micelles		
Micellar estradiol	Estrasorb™	Menopause hormone Therapy
Protein NP		
Albumin-bound paclitaxel NP	Abraxane®/AB1-007	Breast cancer, non-small cell lung Multiple myeloma cancer, pancreatic cancer
Engineered protein combining L-2 and diphtheria toxin	Ontak®	T-Cell lymphoma
Nanocrystals		
Aprepitant	Emend®	Vomiting agent
Fenofibrate	Tricor®	Hyperlipidemia
Sirolimus	Rapamune®	Immunosupressant
Megestrol acetate	MegaceES®	
Morphine sulfate	Avinza®	Mental stimulant
Dexamethyl-phenidate HC1	Focalin XR®	Mental stimulant
Metyhlphenidate HC1	Ritalin LA®	Mental stimulant
Tizanidine HC1	Zanaflex®	Muscle relaxant
Calcium phosphate	Vitoss®	Bone substitute
Hydroxyapatite	Ostim®	Bone substitute
Hydroxyapatite	OsSatura®	Bone substitute
Hydroxyapatite	NanOss®	Bone substitute
Hydroxyapatite	EquivaBone®	Bone substitute
Paliperidone Palmitate	Invega®Sustenna®	Schizoaffective disorder

Dantrolene sodium	Ryanodex®	Malignant benign hypothermia
Inorganic/metallic NPs		
Iron oxide	Nanotherm®	Hybrid species
Ferumoxytol SPION with poly glucose sorbitol carboxy methy-	Feraheme™/ferumoxytol	Chronic renal failure with iron deficiency
Iron sucrose	Venofer®	Chronic renal failure with iron deficiency
Sodium ferric gluconate	Ferrlecit®	Chronic renal failure with iron deficiency
Iron dextran (low MW)	INFeD®	Chronic renal failure with iron deficiency
Iron dextran (high MW)	DexIron®/Dexferrum®	Chronic renal failure with iron deficiency
SPION coated with dextran	Feridex®/Endorem®	Imaging materials
SPION coated with dextran	GastroMARK™/umirem®	Imaging materials

1.5.3 Protein-based nanocarriers

Animal or plants proteins are a great source of the starting material for preparation of nanocarriers. Proteins being natural molecules show unique biological properties. Animal proteins such as gelatin, collagen, albumin, silk and casein are used in the preparation of nanocarriers.[34] Nanoparticles are also being prepared from the proteins isolated from plant sources. Zein and gliadin are the two examples of the highly hydrophobic proteins used to deliver water-insoluble drugs.[34] Advantages of the protein-based nanocarriers include their higher stability, biodegradability and non-immunogenicity. Additionally, the surface modifications on amino acids are possible to achieve targeted therapy.[35] For example, Abraxane is an albumin-bound paclitaxel formulation, which improved the shelf-life of the drug for cancer therapy.

1.5.4 Carbon-based nanomaterials

Carbon-based nanostructures have unique properties like thermal and electrical conductivity. Graphene, fullerene, and carbon-nanotubes (CNTs) have shown their applications in biology, medicine and engineering areas (**Figure 1.5**).[36] In addition, CNTs itself shows photothermal action upon NIR irradiation.[37] Furthermore, graphene quantum dots with excellent luminescent properties are being prepared for detection of the glucose and H_2O_2.[38]

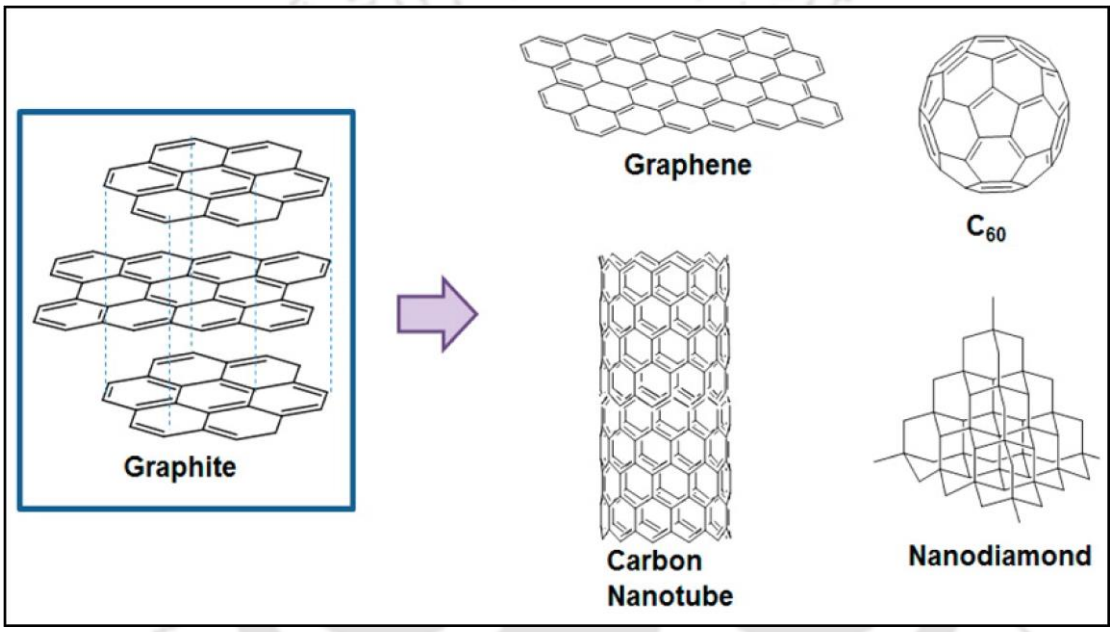

Figure 1.5 Types of carbon-based nanomaterials. [Reprinted with permission from reference 21, Copyright (2019) American Chemical Society].

1.5.5 Liposomes

Liposomes are spherical vesicles prepared from lipid bilayer. Most of the liposomes consist of the phospholipids, cholesterols, and phosphatidylcholine (**Figure 1.6**).[39] As these phospholipids possess polar groups and non-polar side chains, these lipids molecules arrange themselves in such a way that they form hydrophilic core.[40] This characteristic arrangement gives an advantage for loading of hydrophobic as well as hydrophilic drugs. One of the major

disadvantages of the liposome is the rapid clearance through RES; researchers are addressing this issue by coating liposome with inert molecules like PEG.[39]

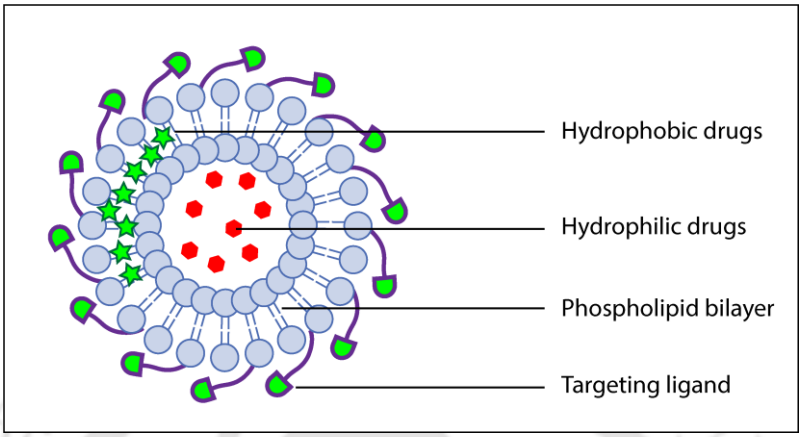

Figure 1.6 Liposome as a drug carrier for hydrophilic and hydrophobic molecules. (Conceptualized and redrawn).

1.5.6 Dendrimers

Dendrimers are synthetic branched molecules prepared with intensions to form core and outer facing branched side chains.[41] Advancements in the field of polymer chemistry helped to form three dimensional branched polymers. Examples of the branched polymeric dendrimers include PAMAM, Poly (propylene imine) (PPI) and Poly-l-lysine (PLL) dendrimer. They are used for targeted delivery of nucleic acids and chemotherapeutic drugs.[42]

1.6 Selenium

Selenium (Se) is an essential trace element in the body, which is a member of non-metallic group of elements. Jon Jacob Berzelius discovered the Se in 1817, and the term "Selenium" was coined after greek 'selene' meaning 'moon'.[43] In human body, Se is a part of the proteins known as seleno-proteins. The incorporation of the Se in seleno-proteins is assisted by the genetic code for seleno-cysteine. Se as a chemical species possess multiple properties.

Naturally, the role of the selenoproteins is to protect the body from oxidative stress. Antioxidant seleno-enzymes like glutathione peroxidase (GSH-P) and thioredoxin reductases reduce oxidative stress inside the cells. Some of the seleno-proteins are mentioned in **Table 1.3**.

Table 1.3 Selenoproteins and their functions.

Selenoprotein	Function
Thioredoxin Reductases	Reduction of oxidized thioredoxin, reduction of nucleotides,
Glutathione Peroxidases	antioxidant defense, reduction of hydrogen peroxide and organic hydroperoxides,
Iodothyronine Deiodinases	Deiodination of T_4 thyroid hormone into active T_3 form.
Selenoprotein P	Antioxidant defense

1.6.1 Involvement of Se in Cancer prevention

Geographical survey has shown that levels of Se in body and the tumor incidence were inversely related.[44] Moreover, the studies carried out on animal models showed the selenium supplementation could inhibit tumor growth.[45] Clark and co-workers carried out Nutritional Prevention of Cancer (NPC) trial, which showed that Se supplementation reduced the prostate cancer-related deaths.[46] As mentioned earlier, Se at the nutritional levels serves as anti-oxidant by boosting the actions of the mentioned seleno-proteins.

Reports have also shown that Se regenerates the other anti-oxidant molecules like Q10, Vitamins C and E.[47] Contrasting to this, Se at above the nutritional levels showed cytotoxic and anti-cell proliferative action.[48] Similar studies performed to compare the effect of different chemical species selenium

confirmed that the therapeutic activity depends on the form of the Se species, redox status of the tissue and the metabolism pathway.[49] Studies have also shown that the malignant cancer cells are more sensitive to Se, as compared to the non-cancerous cells.[50]

1.6.2 Selenium nanoparticles in cancer treatment

Se containing compounds studied for the therapeutic purpose include selenium dioxide, selenodiglutathione, selenomethionine, diselenides, and selnites. All these compounds have shown antiproliferative action against cancer cells. Along with these compounds, Se nanoparticles (SeNPs) have also gained attention of the researchers due to their cytotoxic properties. Multiple studies have shown the potential of the SeNPs for anticancer applications. SeNPs can be prepared by biological, chemical, and physical methods. The biological or chemical method performs reduction of Se containing chemical species to elemental SeNPs. Chemical reduction of the Se involves use of the stabilizing and reducing agents. Similarly, green synthesis of the SeNPs involves the use of microorganisms or plant extract-based biomolecules. The physical method involves top-down approach where bulk materials are fragmented into nanomaterials using microwave, laser ablation and γ-irradiation.[51] As the Se itself has anti-proliferative property, alone SeNPs, SeNPs loaded with drug or combination of the SeNPs and drugs may be used.

Chitosan polymer-stabilized SeNPs showed selective uptake in cancer cells and induced DNA fragmentation and apoptosis.[52] Alone SeNPs treatment have shown induction of apoptosis via various mechanisms. *In-vitro* studies carried out on MDA-MB-231 and HeLa cells have shown dose-dependent (10-40μM) reduction in the cell viability; whereas the S phase arrest of the cell cycle led to the cell death.[53] Another study reported that highly stable SeNPs prepared in

presence of polysaccharide isolated from fungus, induced cell apoptosis via DNA damage and cell cycle arrest at S phase.[54]

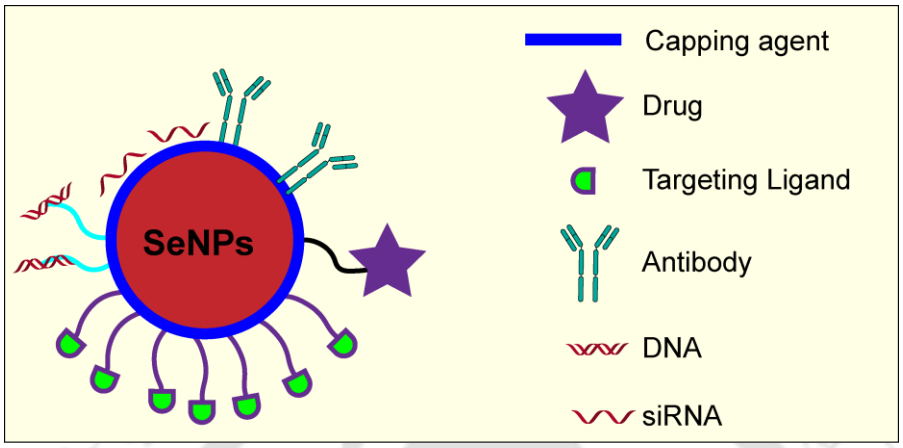

Figure 1.7 Surface modifications of the SeNPs for therapeutic applications (Conceptualized and redrawn).

1.6.3 Selenium NPs as drug carrier

Non-targeted delivery of the drug molecules results in the distribution of the drug molecules to the healthy cells, causing systemic toxicity. Thus, the nanocarriers mediated drug delivery becomes an important tool for targeted therapies. Use of SeNPs for drug delivery, could improve overall therapeutic response due to the contribution from cytotoxic properties of SeNPs.[55] Surface modification can affect the physico-chemical properties of the nanocarriers for a therapeutic approach. Most of the nanoparticle shows destabilization in an aqueous medium; thus, the surface capping agents are helpful to prepare the stable nanoparticles. Similarly, surface capping can also modulate the uptake of the nanomaterials into the desired cells or by body's clearance mechanism. For example, surface capping with neutral polymers like PEG (poly-ethylene glycol) coating of the SeNPs can reduce the uptake and clearance of the SeNPs through reticulo-endothelial cells resulting in prolonged circulation.[56,57] Additionally, the targeted delivery of the SeNPs can be achieved by

conjugating the targeting ligand on the surface by chemical modifications. The possible surface modification of the SeNPs are shown in **Figure 1.7**.

Transferrin conjugated SeNPs were prepared to target the cancer cells overexpressing the transferrin receptor. These TF-conjugated NPs selectively internalized through endocytosis in cancer cells avoiding the healthy cells.[58] Similarly, Folic acid-conjugated SeNPs have also shown enhanced delivery to the folic acid receptor overexpressing cells.[58] In another study, L-arginine capped drug-loaded NPs were used to deliver siRNA for MDR-1 inhibition. The fluorescent labeling of these NPs by ruthenium complexes renders the fluorescent NPs that can be tracked inside the cells.[59] Multiple studies have shown that the synergistic response of the loaded drug and SeNPs making an effective treatment strategy. Recent studies have reported the synthesis of the stimuli-responsive nanocarriers for drug delivery after various stimuli, including temperature and pH.[60]

1.7 Membrane-based drug delivery systems

Advancements in the field of nanotechnology have produced a large number of the nanocarriers for different biomedical application. Conversely, due to body's ability to distinguish self or non-self-materials, these nanocarriers are often cleared from the body via reticuloendothelial system (RES) or macrophage assisted clearance. Apart from this, the immunogenic reaction of the nanocarriers may arise serious issues for *in vivo* applications. In order to achieve the desired therapeutic effect, nano-carrier should remain in the blood for a longer time. As mentioned earlier, this prolonged circulation of the nano-carrier can be achieved by coating the surface of the carrier, thereby avoiding the clearance through RES.[61] Though coating of the nanocarriers with inert molecules like PEG might reduce the clearance, it may show some disadvantages like blood clotting and cell aggregation.[62]

Additionally, PEG coating has also shown to induce the PEG-specific IgM antibodies.[63] Addressing the insufficiency of nano-systems to serve as suitable nanocarriers, various biological membranes derived from red blood cells (RBC), platelet, and cancer cells are currently being explored by researchers to prepare or coat the nanocarriers.[64,65] Merits of these membranes based carrier include their effective interaction with target cell surface, biocompatibility, non-immunogenicity and targeting efficiency without modification of the surface.[66,] Some of the membrane-based drug carriers are illustrated in **Figure 1.8.**

1.7.1 Stem cells as a drug carrier

Stem cells or stem cell membrane coated NPs have been reported for drug delivery applications. Stem cells have shown a migration and accumulation towards tumor mass.[67] Also, stems cells can be genetically engineered for targeted therapeutic approach.[68] A death receptor ligand, tumor necrosis factor apoptosis ligand (TRAIL) overexpressing stem cells induced apoptosis in the metastatic glioma cells.

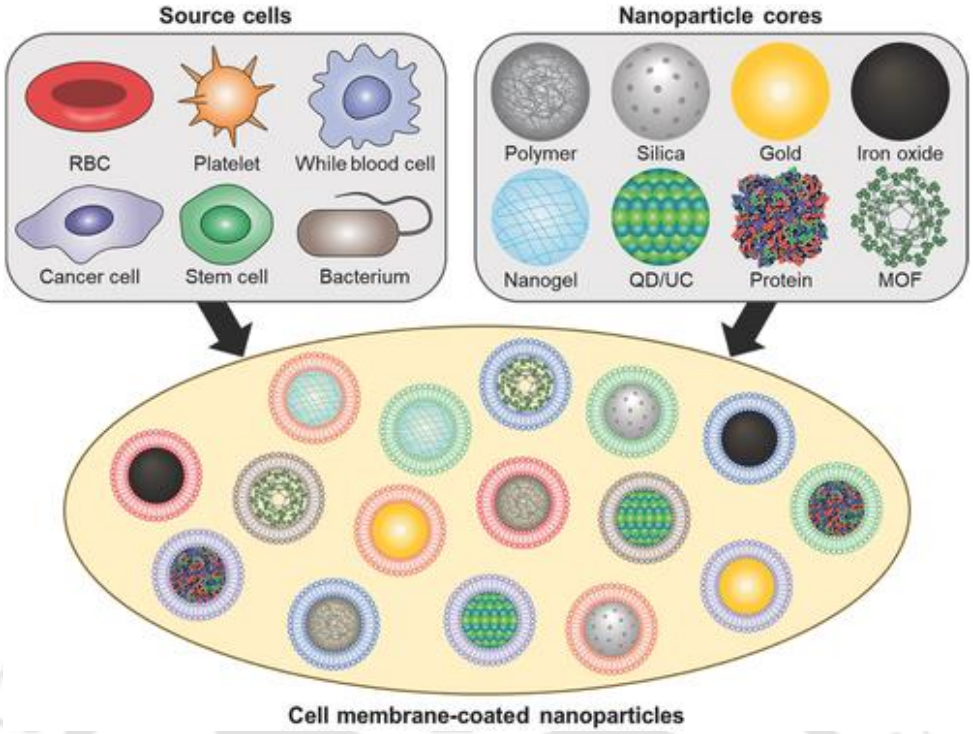

Figure 1.8 Cell membrane-coated nanoparticles. A variety of cell types have been used as sources of membranes to coat nanoparticles. [Reproduced from reference 65 with permission from John Wiley and Sons].

1.7.2 Tumor cell-derived particles

Tumor cell-derived particles are the natural mediators of distant cells. These natural carriers containing drugs can be used to treat cancer cells.[69] Apart from these natural and signaling vesicles, artificial stimuli can induce to shred the cell-derived microparticles. For example, the microparticles were collected after treatment of cells with an anticancer drug (methotrexate) and ultraviolet irradiation. The apoptotic cells generated drug-loaded microparticles can be collected and used for therapeutic applications.[70]

1.7.3 Exosomes

Exosomes are similar to the cell-derived particles regarding the membrane composition. Exosomes are extracellular vesicles generated from cells, which plays an important role in cell-cell communication. Exosome released from cell possess information for target cells in the form of proteins, carbohydrates, lipids or nucleic acids.[71] Due to this ability to carry the cargo, exosomes are being used to delivery therapeutic molecules. Another essential characteristic of the exosome is targeting specificity due to presence of proteins on surface. Doxorubicin loaded exosomes have shown the cancer-specific drug delivery after conjugating ligand on exosome membrane for targeting.[72]

1.7.4 RBC membranes for drug delivery

Apart from the artificial and human-made nano-carriers, the human body has natural carriers like red blood cells (RBCs). A profuse amount of RBCs in body carries oxygen, carbon dioxide, and acts as a buffer system to maintain body pH. RBCs have unique properties like their flexibility, 7-8 μm size and biconcave shape, which allows them to maneuver through the network of capillaries of size less than their own diameter (**Figure 1.9**).[73] Essential properties of the RBCs like non-immunogenicity, biocompatibility, their more prolonged circulation in the blood and larger volume has attracted the scientists to use these natural carriers for therapeutic payload delivery purpose. Researchers are utilizing these unique properties to prepare nanocarriers for different applications.[74] Whole RBCs have shown potential for drug delivery applications. Loading of the cargos or even a bigger biomolecule can be achieved by directly incubating them with intact or lyzed RBCs.[75] Once the cargo is encapsulated, these RBCs can be used for sustained release of the cargo in blood.[76] Apart from using whole RBC as a carrier, researchers have

used RBC membrane to prepare nano-sized vesicles for anticancer drug delivery.

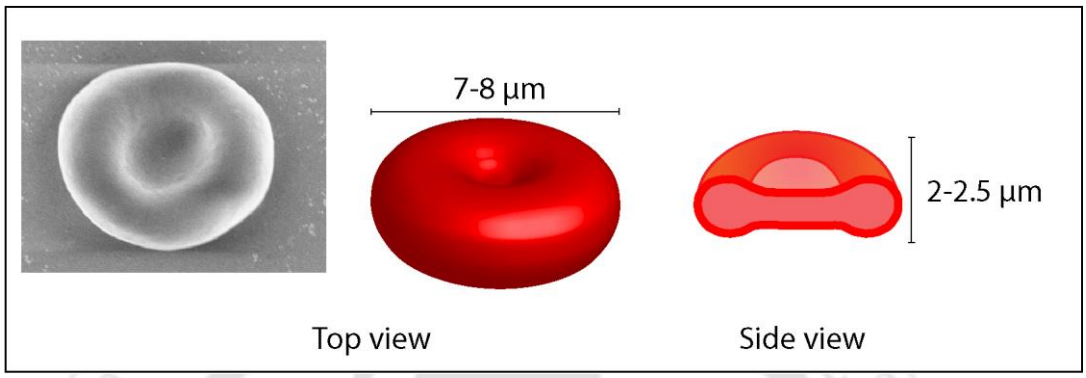

Figure 1.9 Morphology of the Red Blood Cells (RBC).

Isolated RBC membrane can be used to coat nanocarriers to augment the physicochemical properties. RBC membrane coated gold nanocages were prepared to target the 4T1 cancer cells. The membrane coated nanocages precisely delivered paclitaxel to the tumor cells, and the near-infrared irradiation-induced hyperthermia resulted in enhanced cell death.[77] As shown in (**Figure 1.10**), upconversion NPs were coated with RBC membrane to achieve dual targeting of cancer cells and mitochondria.[78] *In-vivo* experimental results showed excellent stability and RES escaping ability after RBC membrane coating. Dual targeting and delivery of the photodynamic agent to these tumors resulted in a reduction in tumor growth and increased the survival rate of tumor-bearing mice.[78]

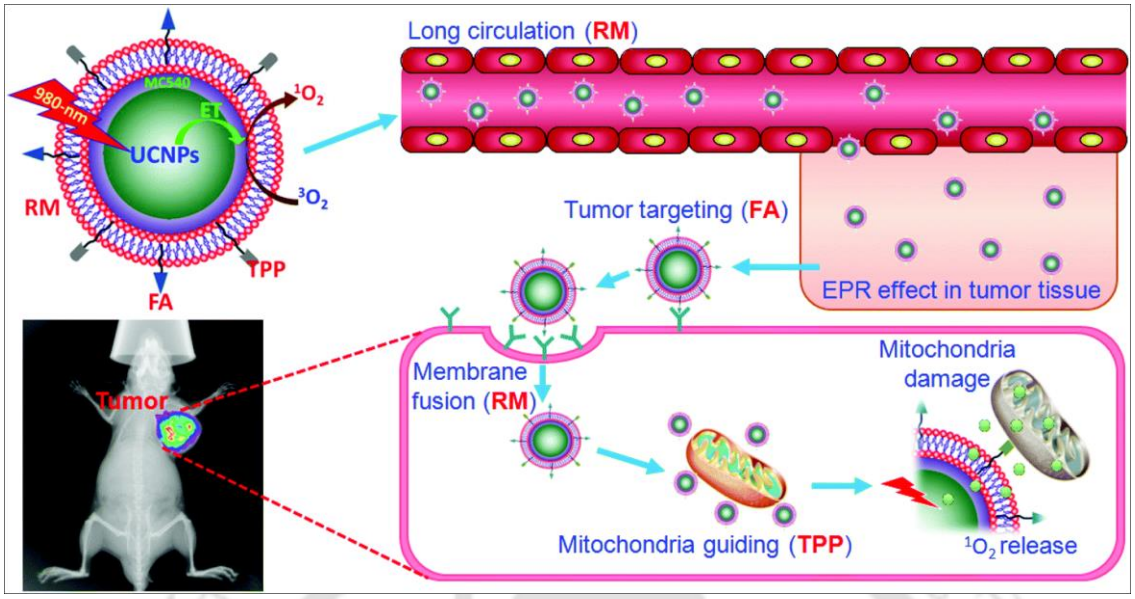

Figure 1.10 UCNP based RBC membrane-coated NPs to target cancer and mitochondria. [Reproduced from reference 77 with permission from the Royal Society of Chemistry].

1.8 Some important anticancer drugs and signaling pathway blockers

1.8.1 Paclitaxel

Paclitaxel (PTX) is a plant alkaloid from *Taxus brevifolia,* initially discovered as the result of screening of plant extracts for anticancer action conducted by National Cancer Institute.[79] Tubulin subunits (α and β subunits) forms microtubules and the spindle fibers required in mitosis. Thus, binding of paclitaxel to tubulin stabilize the microtubule assembly resulting in disruption of the microtubule dynamics and cell division.[80] FDA approved paclitaxel formulations are being used alone, or in combination to treat ovarian cancer, lung cancer, and breast cancer.

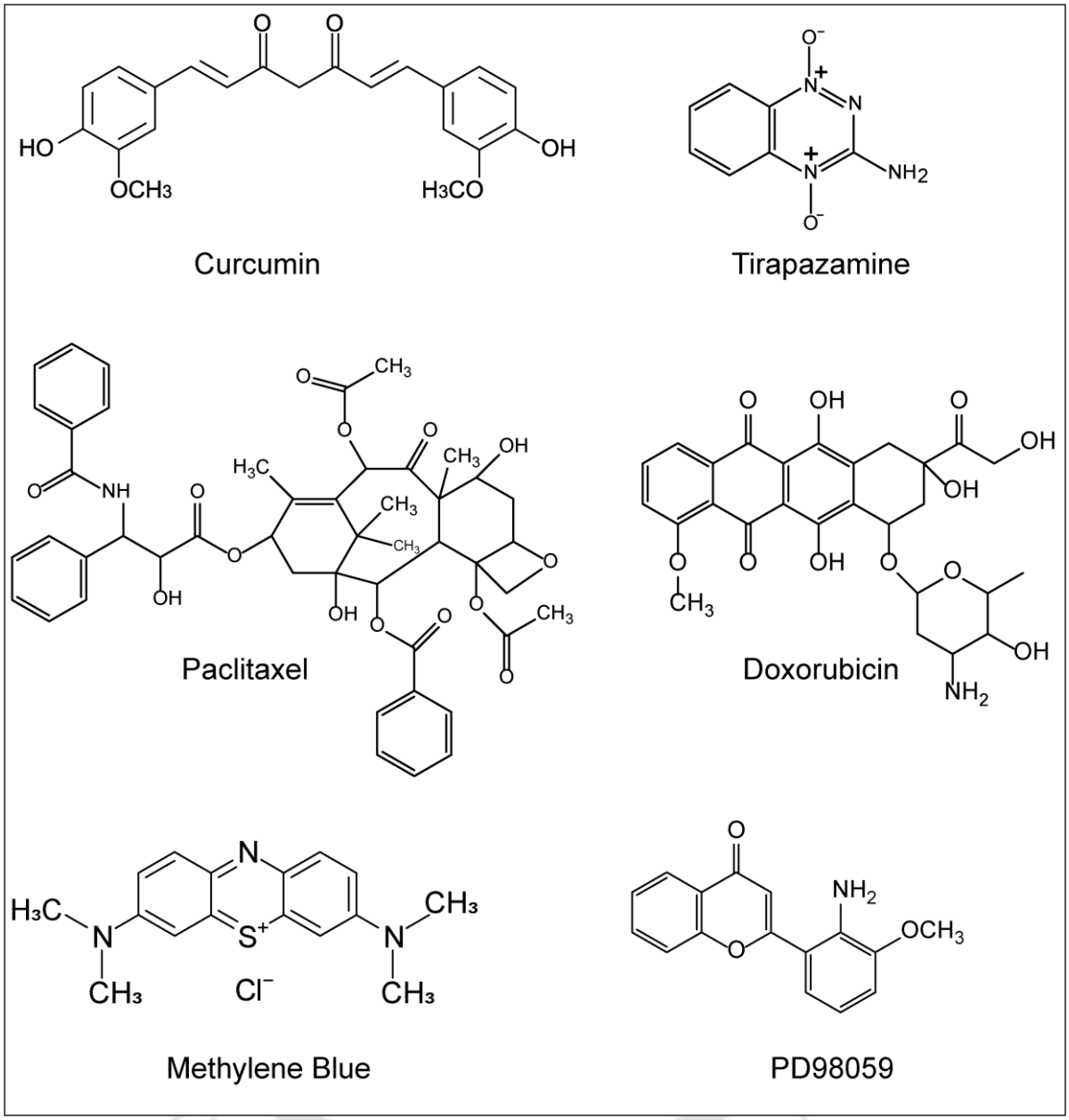

Figure 1.11 Structures of drug and inhibitors.

1.8.2 MAP Kinase pathway inhibitors

Mitogen associated protein kinase cascade is one of the critical signaling pathways in cell proliferation, survival, differentiation, and apoptosis. MAPK pathway is activated upon binding of a ligand, which further initiates the phosphorylation of the proteins involved in the pathway.[81] In ERK MAPK

pathway, binding of ligand leads to activation of the tyrosine kinase domain which triggers RAS GTPase to activate RAF proteins. MEK proteins are phosphorylated by RAF causing phosphorylation of the ERKs, which is a next protein in the cascade. Phosphorylated ERK then translocates to the nucleus, where they act as a transcription factor for many different proteins associated with proliferation and survival. Mutations in the RAF and RAS leads to constitutive activation of the MAPK pathway (**Figure 1.12**)[82] In the case of RAF, the most common mutation is V600E where a mutation causes the constitutive induction of the kinase activity.[83] Similarly, RAS mutation leads to a decrease in GTPase activity which keeps RAS in active form. PD98059 is an inhibitor of the MEK1/2 activation. PD98059 a flavonoid molecule binds to the inactive form of the MEK1/2 and thus makes it unavailable for activation by RAF.[84]

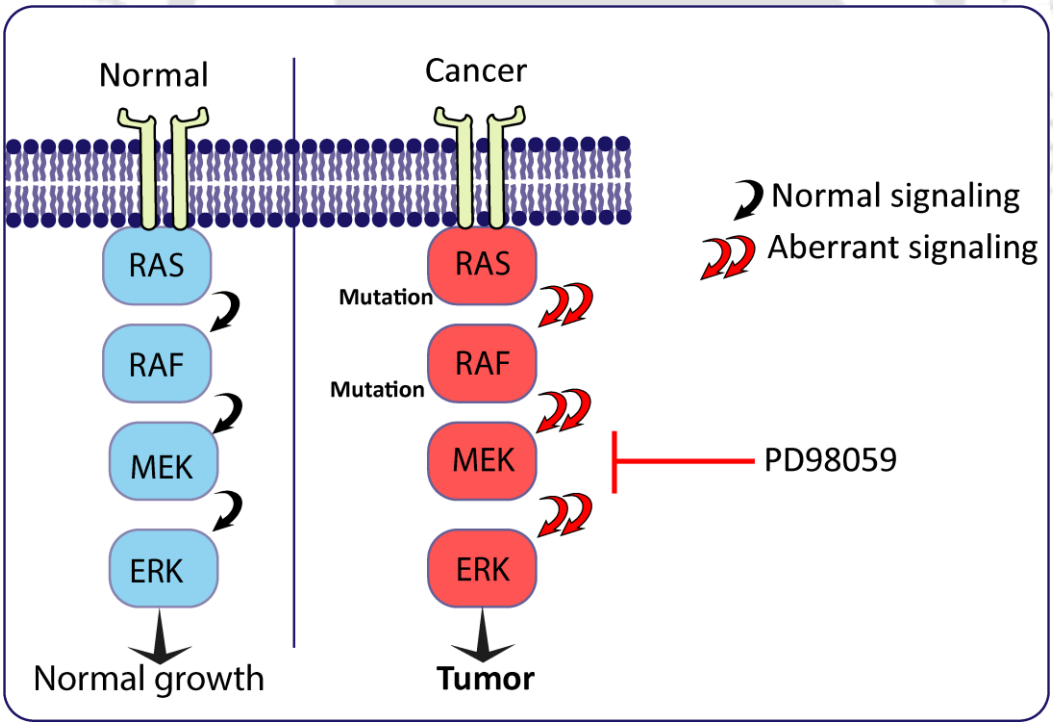

Figure 1.12 Mitogen-activated protein kinase pathway in non-cancerous and RAS and RAF mutated cancer cells (Conceptualized and redrawn).

1.8.3 Curcumin

Curcumin (Cur) is a polyphenolic compound isolated from *Curcuma longa* plant, commonly known as turmeric. Curcumin shows anti-inflammatory activity by inhibiting cyclooxygenase-2 (COX-2), an inflammation-associated enzyme. Studies have also reported that Cur inhibited the expression of COX-2 and PGE2 synthase 1, a mediator of inflammation and tumor development.[85] Similarly, pro-inflammatory response due to nuclear factor-κB (NF-κB) was inhibited with Curcumin treatment.[86] Previous studies have reported that Cur has cell growth inhibition action for multiple cancers, where it affects many cancer-related genes and signaling pathways resulting in cell cycle arrest and apoptosis.[87]

1.8.4 Tirapazamine

The growth of the tumor mass leads to the formation of inner hypoxic core surrounded by oxygenated cells. These solid tumors are associated with hypoxic core renders the anticancer drugs inactive. Thus, it was important to have drug molecules active in hypoxic conditions. The advantage of using tirapazamine (TPZ) is that it is converted to the active form in a hypoxic environment.[88] Along with the hypoxic cells, outer surface cells are also needed to be eliminated; thus, the combination of anticancer drugs and TPZ are suitable to eradicate cancer. At low oxygen levels, the TPZ is converted to its radical form and induces DNA damage. Previous studies have shown that the combinations of TPZ and cisplatin or radiation therapy are very effect for cancer treatment.[89,90]

1.8.5 Doxorubicin

Doxorubicin is an anthracycline based anticancer drug, which was originally isolated from bacteria belonging to the genus *Streptomyces*.[91] Many cancers are being treated with doxorubicin such as leukemia, breast cancer, tumor of the ovaries, lung, testes, prostate, cervix, bladder and Ewing's sarcoma.[92] Doxorubicin works by intercalating with DNA and interfering the function of topoisomerase II. Inhibition of the topoisomerase affects DNA replication and RNA synthesis inducing apoptosis.

A major side effect associated with doxorubicin treatment is cardiotoxicity. It has been reported that the mechanism of the anticancer effect and cardiotoxicity are different; thus, future advanced form of doxorubicin may become useful to reduce cardiotoxic effects.[92] Another approach of reducing the cardiotoxicity would be the targeted delivery to the cancer cells. Therefore, various types of nanocarriers have been prepared for doxorubicin delivery. The FDA-approved Dox (Doxil®, Lipodox®, Myocet®) formulations are being used for systemic administration in cancer treatments.[93]

1.8.6 Methylene blue

Methylene blue is a phenothiazine dye, regularly used in multiple staining procedures including Wright's stain and Jenner's stain. In addition, MB is a photosensitizer used to achieve photodynamic therapy after red light irradiation. The red light (600-700 nm) irradiation on MB generates singlet oxygen species and ROS. Clinically, MB has been used for many applications like methemoglobinemia and cyanide poisoning.[94] MB has shown its effectiveness as a photodynamic agent against bacteria, virus, and cancer cells.[95] Photodynamic therapy (PDT) of the A-549 (lung cancer) cells with MB has shown to induce apoptosis by decreasing the expression of anti-apoptotic

proteins, while generating ROS with alteration in mitochondrial membrane potential (MMP).[96]

1.9 Evaluation of therapeutic potential on spheroids

Majority of the work related to drug delivery or cancer therapeutics has been done on 2D monolayer cells. Unfortunately, the monolayer system fails to achieve the complexity of the tumor in the body. Thus, to simulate the physiological properties of the 3D tumor, spheroids are being used.[97] Multicellular spheroids (MCS) are spherical 3D microstructures formed due to growth of the cells, similar to *in-vivo* tumor. Clustered cells grow in zone to form 3D spheroids giving them the complexity and environment similar to *in-vivo* tumor.[98] As this *in-vitro* tumor grows and cells at surrounding the core starts proliferating, it creates a hypoxic environment with low supply of the nutrient. In addition to hypoxic nature, cells at core become drug-resistant making it more suitable model for drug testing. Use of 3D scaffolds, hydrogels, or microfluidics based systems can help to achieve extracellular matrix deposition, thereby mimicking *in-vivo* tumor. The 3D arrangement of the cells in MCS, makes it possible to develop cell-cell junctions and the communications, which are otherwise difficult in 2D monolayer.[99]

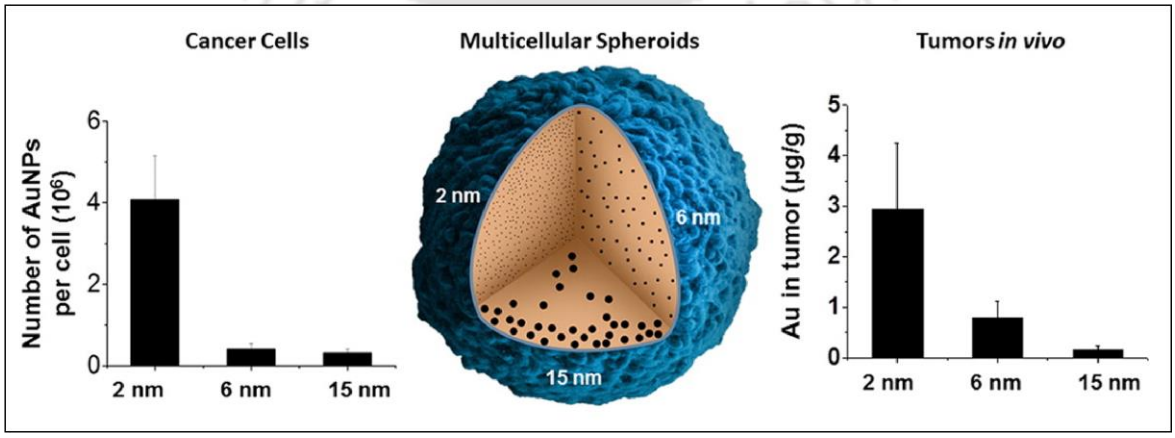

Figure 1.13 Size-dependent localization and penetration of ultrasmall gold nanoparticles in cancer cell multicellular spheroids. [Reprinted with permission from reference 100. Copyright 2017, American Chemical Society].

MCS, due to their complex nature, are being used as a model sytem to study targeting and penetration ability of the nanocarriers. Studies carried out to compare the size dependent penetration of the gold NPs confirmed that the penetrability of the NPs is inversely related to the size (**Figure 1.13**).[100]

1.10 Key areas and scopes

Literature review on cancer therapeutics, nano-based drug delivery system of Se and RBC membranes reveals the following potential areas of research:

- Developing Selenium nanoparticles to deliver hydrophobic drugs to study the antiproliferative properties.
- Designing Selenium nanocarriers to achieve targeted therapy to cancer cells.
- Developing RBC membrane-based nanocarriers to treat hypoxic tumors.
- Targeting drug or photosensitizer loaded RBC membrane-based nanocarriers towards cancer cells to achieve chemo or photodynamic therapy.

1.11 Salient points of this thesis

- Facile synthesis of the F-127 polymer-stabilized SeNPs was achieved for hydrophobic drug delivery to induce apoptosis mediated cell death in HeLa and MCF-7 cells.

- Folic acid receptor-targeted SeNPs were prepared to treat cancer cells overexpressing folic acid receptors. Blockage of the mutated gene signaling in MAPK pathway and targeted SeNPs resulted in synergistic cell death.
- A method for coating of the PLGA NPs with RBC membrane was developed to prepare uniform membrane coated NPs.
- Drug loaded and RBC membrane coated NPs showed prominent antiproliferative action on monolayer as well as on 3D spheroidal cells.
- RBC membrane coating increased the delivery of curcumin and hypoxia-activated drug (tirapazamine) in 3D spheroids of the A375 and MCF-7 cells. This resulted in a significant reduction in cell viability.
- Successful conjugation of the transferrin molecules on RBC membrane coated NPs resulted in high accumulation of NPs and drugs in cancer cells.
- Increased delivery of the doxorubicin and methylene blue in cancer cells resulted in significantly improved chemo- and photodynamic therapy.

1.12 References

(1) Gupta, G. P.; Massagué, J. Cancer Metastasis: Building a Framework. *Cell* **2006**, *127* (4), 679–695. https://doi.org/10.1016/J.CELL.2006.11.001.

(2) Greenman, C.; Stephens, P.; Smith, R.; Dalgliesh, G. L.; Hunter, C.; Bignell, G.; Davies, H.; Teague, J.; Butler, A.; Stevens, C.; et al. Patterns of Somatic Mutation in Human Cancer Genomes. *Nature* **2007**, *446* (7132), 153–158. https://doi.org/10.1038/nature05610.

(3) Pedro, J.; Ortiz, M. *World Health Statistics 2018*; 2018.

(4) Arruebo, M.; Vilaboa, N.; Sáez-Gutierrez, B.; Lambea, J.; Tres, A.; Valladares,

M.; González-Fernández, A. Assessment of the Evolution of Cancer Treatment Therapies. *Cancers (Basel).* **2011**, *3* (3), 3279–3330. https://doi.org/10.3390/cancers3033279.

(5) DeVita, V. T.; Chu, E. A History of Cancer Chemotherapy. *Cancer Res.* **2008**, *68* (21), 8643–8653. https://doi.org/10.1158/0008-5472.CAN-07-6611.

(6) Debatin, K.-M.; Krammer, P. H. Death Receptors in Chemotherapy and Cancer. *Oncogene* **2004**, *23* (16), 2950–2966. https://doi.org/10.1038/sj.onc.1207558.

(7) Sullivan, R.; Alatise, O. I.; Anderson, B. O.; Audisio, R.; Autier, P.; Aggarwal, A.; Balch, C.; Brennan, M. F.; Dare, A.; D'Cruz, A.; et al. Global Cancer Surgery: Delivering Safe, Affordable, and Timely Cancer Surgery. *Lancet Oncol.* **2015**, *16* (11), 1193–1224. https://doi.org/10.1016/S1470-2045(15)00223-5.

(8) Suit, H. D.; Todoroki, T. Rationale for Combining Surgery and Radiation Therapy. *Cancer* **1985**, *55* (9 Suppl), 2246–2249. https://doi.org/10.1002/1097-0142(19850501)55:9+<2246::aid-cncr2820551430>3.0.co;2-n.

(9) Baskar, R.; Lee, K. A.; Yeo, R.; Yeoh, K.-W. Cancer and Radiation Therapy: Current Advances and Future Directions. *Int. J. Med. Sci.* **2012**, *9* (3), 193–199. https://doi.org/10.7150/ijms.3635.

(10) Yildizhan, H.; Barkan, N. P.; Karahisar Turan, S.; Demiralp, Ö.; Özel Demiralp, F. D.; Uslu, B.; Ōzkan, S. A. Treatment Strategies in Cancer from Past to Present. *Drug Target. Stimuli Sensitive Drug Deliv. Syst.* **2018**, 1–37. https://doi.org/10.1016/B978-0-12-813689-8.00001-X.

(11) Hossen, S.; Hossain, M. K.; Basher, M. K.; Mia, M. N. H.; Rahman, M. T.; Uddin, M. J. Smart Nanocarrier-Based Drug Delivery Systems for Cancer Therapy and Toxicity Studies: A Review. *J. Adv. Res.* **2019**, *15*, 1–18. https://doi.org/10.1016/J.JARE.2018.06.005.

(12) Peer, D.; Karp, J. M.; Hong, S.; Farokhzad, O. C.; Margalit, R.; Langer, R. Nanocarriers as an Emerging Platform for Cancer Therapy. *Nat. Nanotechnol.* **2007**, *2* (12), 751–760. https://doi.org/10.1038/nnano.2007.387.

(13) Peer, D.; Karp, J. M.; Hong, S.; Farokhzad, O. C.; Margalit, R.; Langer, R.

Nanocarriers as an Emerging Platform for Cancer Therapy. *Nat. Nanotechnol.* **2007**, *2* (12), 751–760. https://doi.org/10.1038/nnano.2007.387.

(14) Giner-Casares, J. J.; Henriksen-Lacey, M.; Coronado-Puchau, M.; Liz-Marzán, L. M. Inorganic Nanoparticles for Biomedicine: Where Materials Scientists Meet Medical Research. *Materials Today*. **2016**, pp 19–28. https://doi.org/10.1016/j.mattod.2015.07.004.

(15) Khan, I.; Saeed, K.; Khan, I. Nanoparticles: Properties, Applications and Toxicities. *Arab. J. Chem.* **2017**. https://doi.org/10.1016/J.ARABJC.2017.05.011.

(16) Winter, P. M.; Lanza, G. M.; Wickline, S. A.; Madou, M.; Wang, C.; Deotare, P. B.; Loncar, M.; Yap, Y. K.; Rose, J.; Auffan, M.; et al. Physicochemical Properties of Nanoparticles in Relation with Toxicity. In *Encyclopedia of Nanotechnology*; Springer Netherlands: Dordrecht, **2012**; pp 2085–2085. https://doi.org/10.1007/978-90-481-9751-4_334.

(17) Greish, K. Enhanced Permeability and Retention (EPR) Effect for Anticancer Nanomedicine Drug Targeting. In *Methods in molecular biology (Clifton, N.J.)*; 2010; Vol. 624, pp 25–37. https://doi.org/10.1007/978-1-60761-609-2_3.

(18) Fang, J.; Nakamura, H.; Maeda, H. The EPR Effect: Unique Features of Tumor Blood Vessels for Drug Delivery, Factors Involved, and Limitations and Augmentation of the Effect. *Adv. Drug Deliv. Rev.* **2011**, *63* (3), 136–151. https://doi.org/10.1016/J.ADDR.2010.04.009.

(19) Torchilin, V. P. Passive and Active Drug Targeting: Drug Delivery to Tumors as an Example; Springer, Berlin, Heidelberg, **2010**; pp 3–53. https://doi.org/10.1007/978-3-642-00477-3_1.

(20) Dawidczyk, C. M.; Russell, L. M.; Hultz, M.; Searson, P. C. Tumor Accumulation of Liposomal Doxorubicin in Three Murine Models: Optimizing Delivery Efficiency. *Nanomedicine* **2017**, *13* (5), 1637–1644. https://doi.org/10.1016/j.nano.2017.02.008.

(21) Amiri-Kordestani, L.; Blumenthal, G. M.; Xu, Q. C.; Zhang, L.; Tang, S. W.; Ha, L.; Weinberg, W. C.; Chi, B.; Candau-Chacon, R.; Hughes, P.; et al. FDA

Approval: Ado-Trastuzumab Emtansine for the Treatment of Patients with HER2-Positive Metastatic Breast Cancer. *Clin. Cancer Res.* **2014**, *20* (17), 4436–4441. https://doi.org/10.1158/1078-0432.CCR-14-0012.

(22) Lambert, J. M.; Chari, R. V. J. Ado-Trastuzumab Emtansine (T-DM1): An Antibody–Drug Conjugate (ADC) for HER2-Positive Breast Cancer. *J. Med. Chem.* **2014**, *57* (16), 6949–6964. https://doi.org/10.1021/jm500766w.

(23) Wang, J.; Tian, S.; Petros, R. A.; Napier, M. E.; DeSimone, J. M. The Complex Role of Multivalency in Nanoparticles Targeting the Transferrin Receptor for Cancer Therapies. *J. Am. Chem. Soc.* **2010**, *132* (32), 11306–11313. https://doi.org/10.1021/ja1043177.

(24) Daniels, T. R.; Bernabeu, E.; Rodríguez, J. A.; Patel, S.; Kozman, M.; Chiappetta, D. A.; Holler, E.; Ljubimova, J. Y.; Helguera, G.; Penichet, M. L. The Transferrin Receptor and the Targeted Delivery of Therapeutic Agents against Cancer. *Biochim. Biophys. Acta - Gen. Subj.* **2012**, *1820* (3), 291–317. https://doi.org/10.1016/J.BBAGEN.2011.07.016.

(25) Yhee, J. Y.; Lee, S. J.; Lee, S.; Song, S.; Min, H. S.; Kang, S.-W.; Son, S.; Jeong, S. Y.; Kwon, I. C.; Kim, S. H.; et al. Tumor-Targeting Transferrin Nanoparticles for Systemic Polymerized SiRNA Delivery in Tumor-Bearing Mice. *Bioconjug. Chem.* **2013**, *24* (11), 1850–1860. https://doi.org/10.1021/bc400226b.

(26) Panyam, J.; Labhasetwar, V. Biodegradable Nanoparticles for Drug and Gene Delivery to Cells and Tissue. *Adv. Drug Deliv. Rev.* **2003**, *55* (3), 329–347. https://doi.org/10.1016/S0169-409X(02)00228-4.

(27) Soppimath, K. S.; Aminabhavi, T. M.; Kulkarni, A. R.; Rudzinski, W. E. Biodegradable Polymeric Nanoparticles as Drug Delivery Devices. *J. Control. Release* **2001**, *70* (1–2), 1–20. https://doi.org/10.1016/S0168-3659(00)00339-4.

(28) Chan, J. M.; Valencia, P. M.; Zhang, L.; Langer, R.; Farokhzad, O. C. Polymeric Nanoparticles for Drug Delivery; Humana Press, **2010**; pp 163–175. https://doi.org/10.1007/978-1-60761-609-2_11.

(29) Choi, Y. H.; Han, H.-K. Nanomedicines: Current Status and Future

Perspectives in Aspect of Drug Delivery and Pharmacokinetics. *J. Pharm. Investig.* **2018**, *48* (1), 43–60. https://doi.org/10.1007/s40005-017-0370-4.

(30) Croy, S.; Kwon, G. Polymeric Micelles for Drug Delivery. *Curr. Pharm. Des.* **2006**, *12* (36), 4669–4684. https://doi.org/10.2174/138161206779026245.

(31) Kedar, U.; Phutane, P.; Shidhaye, S.; Kadam, V. Advances in Polymeric Micelles for Drug Delivery and Tumor Targeting. *Nanomedicine Nanotechnology, Biol. Med.* **2010**, *6* (6), 714–729. https://doi.org/10.1016/J.NANO.2010.05.005.

(32) Mieszawska, A. J.; Mulder, W. J. M.; Fayad, Z. A.; Cormode, D. P. Multifunctional Gold Nanoparticles for Diagnosis and Therapy of Disease. *Mol. Pharm.* **2013**, *10* (3), 831–847. https://doi.org/10.1021/mp3005885.

(33) Cotin, G.; Piant, S.; Mertz, D.; Felder-Flesch, D.; Begin-Colin, S. Iron Oxide Nanoparticles for Biomedical Applications: Synthesis, Functionalization, and Application. *Iron Oxide Nanoparticles Biomed. Appl.* **2018**, 43–88. https://doi.org/10.1016/B978-0-08-101925-2.00002-4.

(34) Elzoghby, A. O.; Samy, W. M.; Elgindy, N. A. Protein-Based Nanocarriers as Promising Drug and Gene Delivery Systems. *J. Control. Release* **2012**, *161* (1), 38–49. https://doi.org/10.1016/J.JCONREL.2012.04.036.

(35) Verma, D.; Gulati, N.; Kaul, S.; Mukherjee, S.; Nagaich, U. Protein Based Nanostructures for Drug Delivery. *J. Pharm.* **2018**, *2018*, 9285854. https://doi.org/10.1155/2018/9285854.

(36) Cha, C.; Shin, S. R.; Annabi, N.; Dokmeci, M. R.; Khademhosseini, A. Carbon-Based Nanomaterials: Multifunctional Materials for Biomedical Engineering. *ACS Nano* **2013**, *7* (4), 2891–2897. https://doi.org/10.1021/nn401196a.

(37) Maiti, D.; Tong, X.; Mou, X.; Yang, K. Carbon-Based Nanomaterials for Biomedical Applications: A Recent Study. *Front. Pharmacol.* **2019**, *9*, 1401. https://doi.org/10.3389/fphar.2018.01401.

(38) Zhang, M.; Liao, C.; Mak, C. H.; You, P.; Mak, C. L.; Yan, F. Highly Sensitive Glucose Sensors Based on Enzyme-Modified Whole-Graphene Solution-Gated

Transistors. *Sci. Rep.* **2015**, *5* (1), 8311. https://doi.org/10.1038/srep08311.

(39) Torchilin, V. P. Recent Advances with Liposomes as Pharmaceutical Carriers. *Nat. Rev. Drug Discov.* **2005**, *4* (2), 145–160. https://doi.org/10.1038/nrd1632.

(40) Weinstein, J. N.; Leserman, L. D. Liposomes as Drug Carriers in Cancer Chemotherapy. *Pharmacol. Ther.* **1984**, *24* (2), 207–233. https://doi.org/10.1016/0163-7258(84)90035-4.

(41) Madaan, K.; Kumar, S.; Poonia, N.; Lather, V.; Pandita, D. Dendrimers in Drug Delivery and Targeting: Drug-Dendrimer Interactions and Toxicity Issues. *J. Pharm. Bioallied Sci.* **2014**, *6* (3), 139–150. https://doi.org/10.4103/0975-7406.130965.

(42) Palmerston Mendes, L.; Pan, J.; Torchilin, V. P. Dendrimers as Nanocarriers for Nucleic Acid and Drug Delivery in Cancer Therapy. *Molecules* **2017**, *22* (9). https://doi.org/10.3390/molecules22091401.

(43) Weeks, M. E. The Discovery of the Elements. VI. Tellurium and Selenium. *J. Chem. Educ.* **1932**, *9* (3), 474. https://doi.org/10.1021/ed009p474.

(44) Shamberger, R. J.; Frost, D. V. Possible Protective Effect of Selenium against Human Cancer. *Can. Med. Assoc. J.* **1969**, *100* (14), 682.

(45) Medina, D.; Morrison, D. G. Current Ideas on Selenium as a Chemopreventive Agent. *Pathol. Immunopathol. Res.* **1988**, *7* (3), 187–199.

(46) Reid, M.; Duffield-Lillico, A.; Slate, E.; Natarajan, N.; Turnbull, B.; Jacobs, E.; Combs, G.; Alberts, D.; Clark, L.; Marshall, J. The Nutritional Prevention of Cancer: 400 Mcg Per Day Selenium Treatment. *Nutr. Cancer* **2008**, *60* (2), 155–163. https://doi.org/10.1080/01635580701684856.

(47) Hatfield, D. L.; Yoo, M.-H.; Carlson, B. A.; Gladyshev, V. N. Selenoproteins That Function in Cancer Prevention and Promotion. *Biochim. Biophys. Acta - Gen. Subj.* **2009**, *1790* (11), 1541–1545. https://doi.org/10.1016/J.BBAGEN.2009.03.001.

(48) Zeng, H.; Combs, G. F. Selenium as an Anticancer Nutrient: Roles in Cell

Proliferation and Tumor Cell Invasion. *J. Nutr. Biochem.* **2008**, *19* (1), 1–7. https://doi.org/10.1016/J.JNUTBIO.2007.02.005.

(49) Weekley, C. M.; Harris, H. H. Which Form Is That? The Importance of Selenium Speciation and Metabolism in the Prevention and Treatment of Disease. *Chem. Soc. Rev.* **2013**, *42* (23), 8870. https://doi.org/10.1039/c3cs60272a.

(50) Nilsonne, G.; Sun, X.; Nyström, C.; Rundlöf, A.-K.; Potamitou Fernandes, A.; Björnstedt, M.; Dobra, K. Selenite Induces Apoptosis in Sarcomatoid Malignant Mesothelioma Cells through Oxidative Stress. *Free Radic. Biol. Med.* **2006**, *41* (6), 874–885. https://doi.org/10.1016/J.FREERADBIOMED.2006.04.031.

(51) Panahi-Kalamuei, M.; Salavati-Niasari, M.; Hosseinpour-Mashkani, S. M. Facile Microwave Synthesis, Characterization, and Solar Cell Application of Selenium Nanoparticles. *J. Alloys Compd.* **2014**, *617*, 627–632. https://doi.org/10.1016/J.JALLCOM.2014.07.174.

(52) Yu, B.; Zhang, Y.; Zheng, W.; Fan, C.; Chen, T. Positive Surface Charge Enhances Selective Cellular Uptake and Anticancer Efficacy of Selenium Nanoparticles. *Inorg. Chem.* **2012**, *51* (16), 8956–8963. https://doi.org/10.1021/ic301050v.

(53) Luo, H.; Wang, F.; Bai, Y.; Chen, T.; Zheng, W. Selenium Nanoparticles Inhibit the Growth of HeLa and MDA-MB-231 Cells through Induction of S Phase Arrest. *Colloids Surfaces B Biointerfaces* **2012**, *94*, 304–308. https://doi.org/10.1016/j.colsurfb.2012.02.006.

(54) Liao, W.; Yu, Z.; Lin, Z.; Lei, Z.; Ning, Z.; Regenstein, J. M.; Yang, J.; Ren, J. Biofunctionalization of Selenium Nanoparticle with Dictyophora Indusiata Polysaccharide and Its Antiproliferative Activity through Death-Receptor and Mitochondria-Mediated Apoptotic Pathways. *Sci. Rep.* **2016**, *5* (1), 18629. https://doi.org/10.1038/srep18629.

(55) Bidkar, A. P.; Sanpui, P.; Ghosh, S. S. Efficient Induction of Apoptosis in Cancer Cells by Paclitaxel-Loaded Selenium Nanoparticles. *Nanomedicine* **2017**, *12* (21), 2641–2651. https://doi.org/10.2217/nnm-2017-0189.

(56) Mary, T. A.; Shanthi, K.; Vimala, K.; Soundarapandian, K. PEG Functionalized Selenium Nanoparticles as a Carrier of Crocin to Achieve Anticancer Synergism. *RSC Adv.* **2016**, *6* (27), 22936–22949. https://doi.org/10.1039/C5RA25109E.

(57) Li, S.-D.; Huang, L. Nanoparticles Evading the Reticuloendothelial System: Role of the Supported Bilayer. *Biochim. Biophys. Acta* **2009**, *1788* (10), 2259–2266. https://doi.org/10.1016/j.bbamem.2009.06.022.

(58) Huang, Y.; He, L.; Liu, W.; Fan, C.; Zheng, W.; Wong, Y.-S.; Chen, T. Selective Cellular Uptake and Induction of Apoptosis of Cancer-Targeted Selenium Nanoparticles. *Biomaterials* **2013**, *34* (29), 7106–7116. https://doi.org/10.1016/j.biomaterials.2013.04.067.

(59) Chen, Q.; Yu, Q.; Liu, Y.; Bhavsar, D.; Yang, L.; Ren, X.; Sun, D.; Zheng, W.; Liu, J.; Chen, L. Multifunctional Selenium Nanoparticles: Chiral Selectivity of Delivering MDR-SiRNA for Reversal of Multidrug Resistance and Real-Time Biofluorescence Imaging. *Nanomedicine Nanotechnology, Biol. Med.* **2015**, *11* (7), 1773–1784. https://doi.org/10.1016/j.nano.2015.04.011.

(60) Luesakul, U.; Puthong, S.; Neamati, N.; Muangsin, N. PH-Responsive Selenium Nanoparticles Stabilized by Folate-Chitosan Delivering Doxorubicin for Overcoming Drug-Resistant Cancer Cells. *Carbohydr. Polym.* **2018**, *181*, 841–850. https://doi.org/10.1016/j.carbpol.2017.11.068.

(61) Hossen, S.; Hossain, M. K.; Basher, M. K.; Mia, M. N. H.; Rahman, M. T.; Uddin, M. J. Smart Nanocarrier-Based Drug Delivery Systems for Cancer Therapy and Toxicity Studies: A Review. *J. Adv. Res.* **2019**, *15*, 1–18. https://doi.org/10.1016/J.JARE.2018.06.005.

(62) Knop, K.; Hoogenboom, R.; Fischer, D.; Schubert, U. S. Poly(Ethylene Glycol) in Drug Delivery: Pros and Cons as Well as Potential Alternatives. *Angew. Chemie Int. Ed.* **2010**, *49* (36), 6288–6308. https://doi.org/10.1002/anie.200902672.

(63) Ishida, T.; Ichihara, M.; Wang, X.; Yamamoto, K.; Kimura, J.; Majima, E.; Kiwada, H. Injection of PEGylated Liposomes in Rats Elicits PEG-Specific IgM, Which Is Responsible for Rapid Elimination of a Second Dose of PEGylated

Liposomes. *J. Control. Release* **2006**, *112* (1), 15–25. https://doi.org/10.1016/j.jconrel.2006.01.005.

(64) Tan, S.; Wu, T.; Zhang, D.; Zhang, Z. Cell or Cell Membrane-Based Drug Delivery Systems. *Theranostics* **2015**, *5* (8), 863–881. https://doi.org/10.7150/thno.11852.

(65) Fang, R. H.; Kroll, A. V.; Gao, W.; Zhang, L. Cell Membrane Coating Nanotechnology. *Adv. Mater.* **2018**, *30* (23), 1706759. https://doi.org/10.1002/adma.201706759.

(66) Li, R.; He, Y.; Zhang, S.; Qin, J.; Wang, J. Cell Membrane-Based Nanoparticles: A New Biomimetic Platform for Tumor Diagnosis and Treatment. *Acta Pharm. Sin. B* **2018**, *8* (1), 14–22. https://doi.org/10.1016/J.APSB.2017.11.009.

(67) Stuckey, D. W.; Shah, K. Stem Cell-Based Therapies for Cancer Treatment: Separating Hope from Hype. *Nat. Rev. Cancer* **2014**, *14* (10), 683–691. https://doi.org/10.1038/nrc3798.

(68) Sasportas, L. S.; Kasmieh, R.; Wakimoto, H.; Hingtgen, S.; van de Water, J. A. J. M.; Mohapatra, G.; Figueiredo, J. L.; Martuza, R. L.; Weissleder, R.; Shah, K. Assessment of Therapeutic Efficacy and Fate of Engineered Human Mesenchymal Stem Cells for Cancer Therapy. *Proc. Natl. Acad. Sci.* **2009**, *106* (12), 4822–4827. https://doi.org/10.1073/pnas.0806647106.

(69) Guo, M.; Wu, F.; Hu, G.; Chen, L.; Xu, J.; Xu, P.; Wang, X.; Li, Y.; Liu, S.; Zhang, S.; et al. Autologous Tumor Cell-Derived Microparticle-Based Targeted Chemotherapy in Lung Cancer Patients with Malignant Pleural Effusion. *Sci. Transl. Med.* **2019**, *11* (474), eaat5690. https://doi.org/10.1126/scitranslmed.aat5690.

(70) Tang, K.; Zhang, Y.; Zhang, H.; Xu, P.; Liu, J.; Ma, J.; Lv, M.; Li, D.; Katirai, F.; Shen, G.-X.; et al. Delivery of Chemotherapeutic Drugs in Tumour Cell-Derived Microparticles. *Nat. Commun.* **2012**, *3* (1), 1282. https://doi.org/10.1038/ncomms2282.

(71) Bunggulawa, E. J.; Wang, W.; Yin, T.; Wang, N.; Durkan, C.; Wang, Y.; Wang,

G. Recent Advancements in the Use of Exosomes as Drug Delivery Systems. *J. Nanobiotechnology* **2018**, *16* (1), 81. https://doi.org/10.1186/s12951-018-0403-9.

(72) Tian, Y.; Li, S.; Song, J.; Ji, T.; Zhu, M.; Anderson, G. J.; Wei, J.; Nie, G. A Doxorubicin Delivery Platform Using Engineered Natural Membrane Vesicle Exosomes for Targeted Tumor Therapy. *Biomaterials* **2014**, *35* (7), 2383–2390. https://doi.org/10.1016/J.BIOMATERIALS.2013.11.083.

(73) Diez-Silva, M.; Dao, M.; Han, J.; Lim, C.-T.; Suresh, S. Shape and Biomechanical Characteristics of Human Red Blood Cells in Health and Disease. *MRS Bull.* **2010**, *35* (5), 382–388.

(74) Huisjes, R.; Bogdanova, A.; van Solinge, W. W.; Schiffelers, R. M.; Kaestner, L.; van Wijk, R. Squeezing for Life – Properties of Red Blood Cell Deformability. *Front. Physiol.* **2018**, *9*, 656. https://doi.org/10.3389/fphys.2018.00656.

(75) Gutiérrez Millán, C.; Castañeda, A. Z.; Sayalero Marinero, M. L.; Lanao, J. M. Factors Associated with the Performance of Carrier Erythrocytes Obtained by Hypotonic Dialysis. *Blood Cells, Mol. Dis.* **2004**, *33* (2), 132–140. https://doi.org/10.1016/J.BCMD.2004.06.004.

(76) Eichler, H. G.; Rameis, H.; Bauer, K.; Korn, A.; Bacher, S.; Gasic, S. Survival of Gentamicin-Loaded Carrier Erythrocytes in Healthy Human Volunteers. *Eur. J. Clin. Invest.* **1986**, *16* (1), 39–42. https://doi.org/10.1111/j.1365-2362.1986.tb01305.x.

(77) Zhu, D.-M.; Xie, W.; Xiao, Y.-S.; Suo, M.; Zan, M.-H.; Liao, Q.-Q.; Hu, X.-J.; Chen, L.-B.; Chen, B.; Wu, W.-T.; et al. Erythrocyte Membrane-Coated Gold Nanocages for Targeted Photothermal and Chemical Cancer Therapy. *Nanotechnology* **2018**, *29* (8), 084002. https://doi.org/10.1088/1361-6528/aa9ca1.

(78) Ding, H.; Lv, Y.; Ni, D.; Wang, J.; Tian, Z.; Wei, W.; Ma, G. Erythrocyte Membrane-Coated NIR-Triggered Biomimetic Nanovectors with Programmed Delivery for Photodynamic Therapy of Cancer. *Nanoscale* **2015**, *7* (21), 9806–9815. https://doi.org/10.1039/C5NR02470F.

(79) Horwitz;, M. W.; Horwitz, S. B. Nature as a Remarkable Chemist: A Personal

Story of the Discovery and Development of Taxol. *Anticancer. Drugs* **2014**, *25* (5), 482–487. https://doi.org/10.1097/cad.0000000000000063.

(80) Barbuti, A. M.; Chen, Z.-S. Paclitaxel Through the Ages of Anticancer Therapy: Exploring Its Role in Chemoresistance and Radiation Therapy. *Cancers (Basel).* **2015**, *7* (4), 2360–2371. https://doi.org/10.3390/cancers7040897.

(81) Santarpia, L.; Lippman, S. M.; El-Naggar, A. K. Targeting the MAPK–RAS–RAF Signaling Pathway in Cancer Therapy. *Expert Opin. Ther. Targets* **2012**, *16* (1), 103–119. https://doi.org/10.1517/14728222.2011.645805.

(82) Wellbrock, C.; Hurlstone, A. BRAF as Therapeutic Target in Melanoma. *Biochemical Pharmacology*. 2010, pp 561–567. https://doi.org/10.1016/j.bcp.2010.03.019.

(83) Brose, M. S.; Volpe, P.; Feldman, M.; Kumar, M.; Rishi, I.; Gerrero, R.; Einhorn, E.; Herlyn, M.; Minna, J.; Nicholson, A.; et al. BRAF and RAS Mutations in Human Lung Cancer and Melanoma. *Cancer Res.* **2002**, *62* (23), 6997–7000. https://doi.org/10.1093/jnci/93.14.1062.

(84) Richards, J. D.; Davé, S. H.; Chou, C. H.; Mamchak, A. A.; DeFranco, A. L. Inhibition of the MEK/ERK Signaling Pathway Blocks a Subset of B Cell Responses to Antigen. J. Immunol. 2001, 166 (6), 3855–3864. https://doi.org/10.4049/jimmunol.166.6.3855.

(85) Perrone, D.; ArditoO, F.; Giannatempo, G.; Dioguardi, M.; Troiano, G.; Lorusso, L.; Delillo, A.; Laino, L.; LO Muzio, L. Biological and Therapeutic Activities, and Anticancer Properties of Curcumin. *Exp. Ther. Med.* **2015**, *10* (5), 1615–1623. https://doi.org/10.3892/etm.2015.2749.

(86) Wilken, R.; Veena, M. S.; Wang, M. B.; Srivatsan, E. S. Curcumin: A Review of Anti-Cancer Properties and Therapeutic Activity in Head and Neck Squamous Cell Carcinoma. *Mol. Cancer* **2011**, *10*, 12. https://doi.org/10.1186/1476-4598-10-12.

(87) Park, W.; Amin, A. R. M. R.; Chen, Z. G.; Shin, D. M. New Perspectives of Curcumin in Cancer Prevention. *Cancer Prev. Res.* **2013**, *6* (5), 387–400.

https://doi.org/10.1158/1940-6207.CAPR-12-0410.

(88) Brown, J. SR 4233 (Tirapazamine): A New Anticancer Drug Exploiting Hypoxia in Solid Tumours. *Br. J. Cancer* **1993**, *67* (6), 1163–1170. https://doi.org/10.1038/bjc.1993.220.

(89) Marcu, L.; Olver, I. Tirapazamine: From Bench to Clinical Trials. *Curr. Clin. Pharmacol.* **2006**, *1* (1), 71–79.

(90) Evans, J. W.; Yudoh, K.; Delahoussaye, Y. M.; Brown, J. M. Tirapazamine Is Metabolized to Its DNA-Damaging Radical by Intranuclear Enzymes. *Cancer Res.* **1998**, *58* (10), 2098–2101.

(91) Patel, A. G.; Kaufmann, S. H. How Does Doxorubicin Work? *Elife* **2012**, *1*, e00387. https://doi.org/10.7554/eLife.00387.

(92) Thorn, C. F.; Oshiro, C.; Marsh, S.; Hernandez-Boussard, T.; McLeod, H.; Klein, T. E.; Altman, R. B. Doxorubicin Pathways: Pharmacodynamics and Adverse Effects. *Pharmacogenet. Genomics* **2011**, *21* (7), 440–446. https://doi.org/10.1097/FPC.0b013e32833ffb56.

(93) Zhao, N.; Woodle, M. C.; Mixson, A. J. Advances in Delivery Systems for Doxorubicin. *J. Nanomed. Nanotechnol.* **2018**, *9* (5). https://doi.org/10.4172/2157-7439.1000519.

(94) Sikka, P.; Bindra, V. K.; Kapoor, S.; Jain, V.; Saxena, K. K. Blue Cures Blue but Be Cautious. *J. Pharm. Bioallied Sci.* **2011**, *3* (4), 543–545. https://doi.org/10.4103/0975-7406.90112.

(95) Aluigi, A.; Sotgiu, G.; Torreggiani, A.; Guerrini, A.; Orlandi, V. T.; Corticelli, F.; Varchi, G. Methylene Blue Doped Films of Wool Keratin with Antimicrobial Photodynamic Activity. *ACS Appl. Mater. Interfaces* **2015**, *7* (31), 17416–17424. https://doi.org/10.1021/acsami.5b04699.

(96) LIM, E. J.; OAK, C.-H.; HEO, J.; KIM, Y.-H. Methylene Blue-Mediated Photodynamic Therapy Enhances Apoptosis in Lung Cancer Cells. *Oncol. Rep.* **2013**, *30* (2), 856–862. https://doi.org/10.3892/or.2013.2494.

(97) Huang, B.-W.; Gao, J.-Q. Application of 3D Cultured Multicellular Spheroid Tumor Models in Tumor-Targeted Drug Delivery System Research. *J. Control. Release* **2018**, *270*, 246–259. https://doi.org/10.1016/J.JCONREL.2017.12.005.

(98) Mehta, G.; Hsiao, A. Y.; Ingram, M.; Luker, G. D.; Takayama, S. Opportunities and Challenges for Use of Tumor Spheroids as Models to Test Drug Delivery and Efficacy. *J. Control. Release* **2012**, *164* (2), 192–204. https://doi.org/10.1016/j.jconrel.2012.04.045.

(99) Oktem, G.; Bilir, A.; Ayla, S.; Yavasoglu, A.; Goksel, G.; Saydam, G.; Uysal, A. Role of Intercellular Communications in Breast Cancer Multicellular Tumor Spheroids After Chemotherapy. *Oncol. Res. Featur. Preclin. Clin. Cancer Ther.* **2006**, *16* (5), 225–233. https://doi.org/10.3727/000000006783981071.

(100) Huang, K.; Ma, H.; Liu, J.; Huo, S.; Kumar, A.; Wei, T.; Zhang, X.; Jin, S.; Gan, Y.; Wang, P. C.; et al. Size-Dependent Localization and Penetration of Ultrasmall Gold Nanoparticles in Cancer Cells, Multicellular Spheroids, and Tumors *in Vivo*. *ACS Nano* **2012**, *6* (5), 4483–4493. https://doi.org/10.1021/nn301282m.

भारतीय प्रौद्योगिकी संस्थान गुवाहाटी
Indian Institute of Technology Guwahati

CHAPTER 2

Development of novel nanocarriers (selenium-based nanoparticles) for delivery of anticancer drugs.

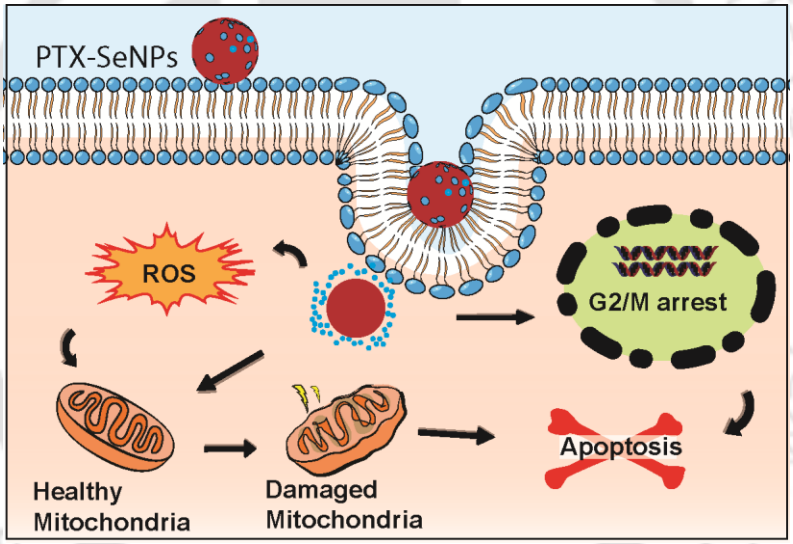

Chapter 2 focuses on preparation and characterization of paclitaxel loaded SeNPs (PTX-SeNPs). Functional ability of the PTX-SeNPs for antiproliferative action was studied. This chapter also explains the mechanism of apoptosis mediated cell death induced by PTX-SeNPs.

Nanomedicine (*Lond*). 2017, 12(21):2641-2651
DOI: 10.2217/nnm-2017-0189

CHAPTER 2

2.1 Introduction

Selenium functions as an essential micronutrient at a lower amount, whereas a higher dose for longer period might lead to selenosis.[1,2] Fortunately, the issue of toxicity can be circumvented by using Se in nanoparticulate form, since SeNPs demonstrate a much broader window of beneficial and toxic doses as compared to other Se-based inorganic and organic compounds.[3] Thus, SeNPs demonstrate the possibility of becoming an effective anticancer platform with reduced toxicity as compared to those associated with conventional metal (silver, copper, etc.) NPs. Surprisingly, researchers have started exploring the potential of SeNPs in anticancer application only recently.[1,4] SeNPs, in this regard, have been shown to sensitize MCF-7 breast cancer cells towards doxorubicin by increasing activation of Akt.[5] Decoration of SeNPs with 5-fluorouracil (5-FU) resulted in their improved uptake by cancer cells leading to synergistic activity with 5-FU.[1] Moreover, Se-carbon nanocomposite has been prepared which showed reduced viability of malignant mesothelioma cells.[6]

Paclitaxel (PTX), a plant-derived alkaloid, has been used in chemotherapy of breast,[7] ovarian,[8] and cervical cancer.[9] However, like most of the chemotherapeutic drugs, it is associated with significant drawbacks, including non-selective cytotoxicity and poor water solubility. In this regard, a promising approach could be the development of a SeNPs-based DDS for PTX, which can enhance the solubility of PTX, leading to its improved bio-availability. Besides, SeNPs – the nanocarriers in this DDS – could also contribute to the overall therapeutic efficacy of such a system.

In this chapter, the impact of the hydrophobic drug (PTX) loaded SeNPs on cancer cells has been delineated. Induction of apoptosis in treated cancer cells and the mechanistic pathway behind the apoptotic cell death caused by PTX-

loaded Se NPs (PTX-Se NPs) was investigated with the evaluation of possible involvement of oxidative stress, altered mitochondrial membrane potential (MMP) and activation of effector caspases in the process. The idea has been schematically conceptualized in **Scheme 2.1**.

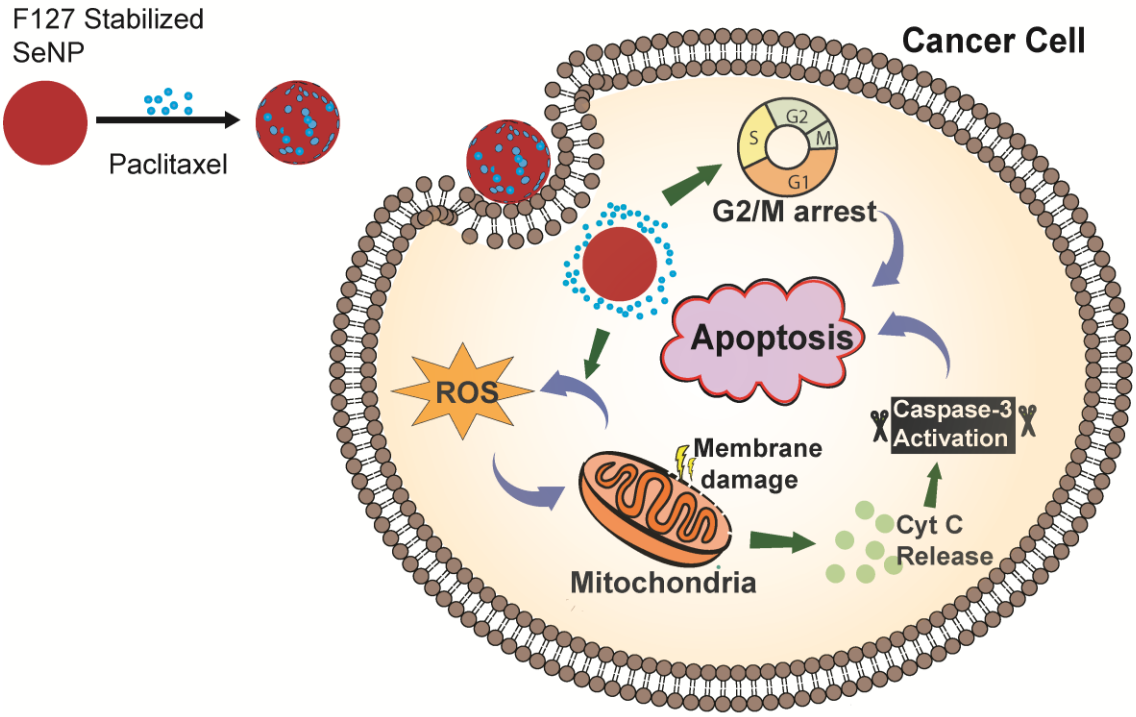

Scheme 2.1: Schematic representation of paclitaxel delivery to a cancer cell by selenium nanoparticles leading to generation of reactive oxygen species, membrane damage and activation of effector caspases for induction of apoptosis.

2.2 Experimental Section

2.2.1 Chemicals

Selenium dioxide (SeO_2), pluronic F-127, paclitaxel (PTX), ascorbic acid, Rhodamine B, 3-(4,5-dimethylthiazol-2-yl)-2,5-diphenyltetrazolium bromide (MTT), 2',7'-dichlorofluorescein diacetate (DCF-DA), propidium iodide (PI) and 5,5',6,6'-tetrachloro-1,1',3,3'-tetraethylbenzimi-dazolylcarbocyanine iodide (JC-1) were purchased from Sigma-Aldrich and used as received. The PE rabbit

anti-active Caspase-3 (Catalog No. 550821) and FITC-Annexin V- PI assay kit were purchased from BD Biosciences.

2.2.2 Cell Culture

Human embryonic kidney cells (HEK-293), lung cells (L-132), cervical cancer cells (HeLa), breast cancer cells (MCF-7), non-small lung carcinoma cells (A549) and colorectal adenocarcinoma cells (HT29) were purchased from National Centre for Cell Science (NCCS), Pune. All the cell lines were maintained in Dulbecco's modified Eagle's medium (DMEM) supplemented with 10% (v/v) fetal bovine serum (FBS) and 1% penicillin & streptomycin at 37 °C in humidified air containing 5% CO_2.

2.2.3 Synthesis and characterization of selenium nanoparticles (SeNPs)

Synthesis of SeNPs was performed according to the method described by Wen Liu et al[1] with slight modification. Stock solutions of Pluronic F-127 (2 mM), selenium dioxide (100 mM) and ascorbic acid (1 M) were prepared freshly just before the experiment. To 8 mL of Milli-Q water, 1 mL of Pluronic F-127, and 0.5 mL of selenium dioxide solution was added. Then, 0.5 mL of ascorbic acid solution was added dropwise with continuous stirring on a magnetic stirrer. As reaction progressed, color of the reaction mixture was changed to orange-red indicating formation of SeNPs. The as-synthesized SeNPs were thoroughly washed with water by repeated centrifugation (20000× g, 20 min). UV-visible absorption spectra of the SeNPs was recorded with Perkin-Elmer Lambda 25 spectrophotometer. Hydrodynamic diameter (d_H) and zeta potential (ζ) measurement were performed in Malvern Zeta Sizer Nano ZS. For TEM analysis, a colloidal suspension of SeNPs was drop cast onto a carbon-coated copper grid and allowed to air dry. TEM images were captured with JEM 2100 (Jeol, Peabody, MA, USA) at 200 kV. Further structural characteristics of SeNPs were evaluated by FESEM and EDX. For this, SeNPs

suspension was drop cast on an aluminum foil coated coverslip and gold coating was done before analysis. Samples were prepared for atomic force microscopy (AFM) by drop-casting SeNPs suspension onto a glass coverslip. FTIR analysis of lyophilized SeNPs was carried out in a Perkin-Elmer Spectrum One spectrophotometer machine.

2.2.4 Cellular uptake of SeNPs

SeNPs were labeled with fluorescent dye Rhodamine B by adding 100 μg of dye during the synthesis of SeNPs as mentioned above. Rhodamine B-loaded SeNPs were washed with water (centrifugation at 20000 rpm, 20 min) repeatedly to remove unbound dye. To observe cellular uptake, cells were incubated with fluorescent (Rhodamine B-labelled) SeNPs for 4 h and subsequently washed with PBS to remove any bound NPs. Cells were then fixed, counterstained with DAPI and observed under a confocal laser scanning microscope (ZEISS LSM 880) using ZEN 2 software.

2.2.5 Loading of paclitaxel (PTX) onto SeNPs and its release

Paclitaxel was loaded by incubating the drug (180 μg) with 50 mL of SeNPs (5 mM) under continuous stirring for 4 h at room temperature. Paclitaxel-loaded SeNPs (PTX-SeNPs) were separated by centrifugation (15,000 rpm), and the unbound drug was quantified by measuring the drug amount in the supernatant. The amount of paclitaxel in the loading or release media was quantified by measuring absorbance at 232 nm.[10] Loading of paclitaxel onto SeNPs was calculated as:

$$\% \text{ of Loading} = \frac{(\text{Amount of drug added to SeNPs} - \text{Amount of free drug})}{\text{Amount of drug added to SeNPs}} \times 100$$

For drug release study, PTX-SeNPs were incubated in phosphate buffer saline (PBS, pH 7.4) and acetate buffer (pH 5) at room temperature. At regular interval, 0.5mL sample was withdrawn and centrifuged at 15, 000 rpm for 20 min to separate the PTX-SeNPs. Absorbance (at 232 nm) of the supernatant was recorded to measure the PTX released in the buffer. Centrifuged PTX-SeNPs were again added into PTX-SeNPs buffer solution.

2.2.6 Cytotoxicity assay

Cytotoxicity of SeNPs and PTX-SeNPs on HEK293, L132, HeLa, MCF-7, A549, and HT29 was studied by MTT assay.[11] Briefly, cells were seeded at a density of 5×10^3 cells/well in 96 well plates. After 48 h of treatment with varying concentration of SeNPs and PTX-SeNPs, 80 µL of MTT (0.5mg/mL in DMEM) was added to each well and incubated for 3 hours. Thereafter, 150µL DMSO was added to each well. Absorbance was measured at 570 nm for dissolved formazon crystals and at 630 nm as reference.

2.2.7 Cell cycle analysis

HeLa and MCF-7 cells were seeded at a density of 10^5 cells/well in 6 well plates and incubated for overnight. Synchronization of the cells was acquired by incubating them with serum-free media for 48 h. Subsequently, HeLa cells were treated with 4.35 µM ($^1/_2$ IC_{50}), 8.7 µM (IC_{50}), and 13 µM ($^3/_2$ IC_{50}) of PTX-SeNPs for 48 h. Similarly, MCF-7 cells were treated with 2.7 µM ($^1/_2\times$ IC_{50}), 5.4 µM (IC_{50}), and 8.2 µM ($^3/_2$ IC_{50}) of PTX-SeNPs for 48 h. On completion of the treatment, cells were harvested by trypsinization, fixed in 70% ethanol and incubated overnight at -20˚C. Next, the cells were treated with RNase A, stained with PI and analyzed in FACS Calibur (BD Biosciences, NJ, USA).

2.2.8 Annexin V-PI apoptosis assay

HeLa and MCF-7 cells were seeded at a density of 10^5 cells/well in 6 well plates and incubated for overnight. After 48 h of treatment with PTX-SeNPs at

$^1/_2$ IC_{50}, IC_{50}, $^3/_2$ IC_{50}, cells were washed with PBS, trypsinized and were stained with Annexin V-FITC PI kit according to the supplier's protocol. Stained cells were incubated for 10 min at room temperature and analyzed by flow cytometer (Cytoflex, Beckman Coulter).

2.2.9 DCF-DA assay

Following treatment with PTX-SeNPs (at $^1/_2$ IC_{50}, IC_{50}, $^3/_2$ IC_{50}) for 12 h, HeLa and MCF-7 cells were washed with PBS, harvested by trypsinization and resuspended into a 0.2 μM DCF-DA in PBS. Thereafter cells were incubated for 30 min at room temperature, pelleted down by centrifugation and resuspended in PBS for further analysis in FACS Calibur (BD Biosciences, NJ, USA). Data analysis was performed using FCS Express 5.

2.2.10 JC-1 staining for mitochondrial membrane potential (MMP)

JC-1 is a cationic dye which enters in mitochondria and forms aggregates that fluoresces orange. However, the fluorescence changes to green (due to monomeric JC1) if the membrane potential decreases. HeLa and MCF-7 cells were treated PTX-SeNPs (at $^1/_2$ IC_{50}, IC_{50}, $^3/_2$ IC_{50}) for 48 h, washed with PBS and stained with JC-1 (10μM) in DMEM for 30 min. JC-1 stained cells were observed immediately under a fluorescence microscope (Nikon Eclipse Ti-U, Tokyo, Japan).

2.2.11 Caspase-3 assay

Phycoerythrin (PE) conjugated anti-active caspase-3 antibody (BD Biosciences, Clontech, Palo Alto, CA, USA) was used to estimate the cell population expressing active caspase 3 due to apoptosis. Cells treated with PTX-SeNPs (at $^1/_2$ IC_{50}, IC_{50}, $^3/_2$ IC_{50}) for 48 h were collected by trypsinization and were fixed by using 4% formaldehyde for 10 min. Cells were permeabilized in 90% ice-cold methanol for 30 min. Thereafter cells were washed twice with incubation buffer (200 mg BSA in 100 mL 1X PBS). Staining was performed

with the required (according to manufacturer's protocol) amount of the PE anti-active caspase-3 antibody for 30 min. After washing the stained cells twice with incubation buffer, they were analyzed in flow-cytometer (FACS Calibur, BD Biosciences, NJ, USA).

2.2.12 Field emission scanning electron microscopy (FESEM)

To observe the morphologies of untreated and treated (with PTX-SeNPs at IC_{50}) cells, cells were harvested, fixed in 70% ethanol, drop cast onto aluminum foil wrapped coverslip and air-dried. Then the cells were observed under FESEM (ZEISS SIGMA).

2.3 Results and Discussions

2.3.1 Synthesis and Characterization of SeNPs

For stabilization of the SeNPs, Pluronic F-127 was used, which is a triblock copolymer consisting of poly (ethylene oxide) -poly (propylene oxide) -poly (ethylene oxide) (PEO-PPO-PEO) units. F-127 is a water-soluble, non-toxic, and FDA approved polymer for clinical applications.[12] Repeating units of PEO (hydrophilic) and PPO (hydrophobic) in Pluronic F-127 provide this polymer with amphiphilic nature allowing it to cap both hydrophobic and hydrophilic surfaces.[13] This intriguing property of Pluronic F-127 can be utilized to deliver hydrophobic as well as hydrophilic drugs inside the cells. The hydrophobic core of the F-127 stabilized SeNPs provides further advantage of loading poorly water-soluble drugs.[14]

For preparation of SeNPs, ascorbic acid was added dropwise to a mixture of selenous acid and pluronic F-127 under constant stirring. As the reaction progressed, the color of the reaction mixture gradually turned red, indicating the formation of SeNPs. The UV-visible absorption spectra (**Figure 2.1A**) of as-prepared SeNPs demonstrated characteristic absorbance peak around 261 nm [15]. Transmission electron microscopic (TEM) image of SeNPs (**Figure 2.1B**) revealed almost spherical particles of 31.3 nm in average size (**Figure**

2.1C). The spherical morphology of the SeNPs was also evident in atomic force microscopy (AFM), as shown in **Figure 2.1D**. Elemental composition of as-prepared SeNPs colloids, determined by EDX analysis (**Figure 2.1E**), confirmed the presence of elemental Se. Average hydrodynamic diameter (d_H) of the SeNPs was found to be 74 nm in dynamic light scattering (DLS) measurements (**Figure 2.1F**). The d_H of the SeNPs was found to be higher than the average particle size found in TEM (31.3 nm) analysis and could be due to the formation of hydration layer at SeNPs surface in aqueous dispersion. Interestingly, the optimum size range of nanomaterials for effective enhanced permeation and retention (EPR) being 20 – 100 nm [16], SeNPs qualified for potential passive targeting of chemotherapeutic payload *in vivo*.

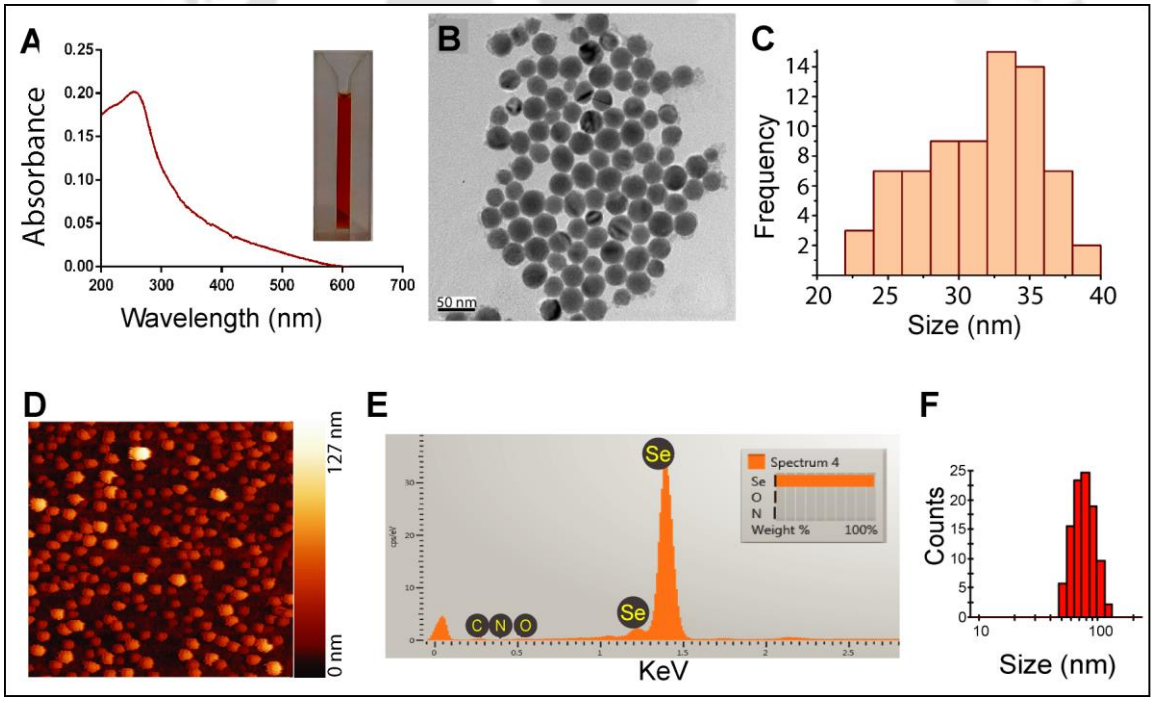

Figure 2.1 (**A**) UV-visible absorbance spectra (inset: digital photograph of SeNPs), (**B**) TEM image (scale: 50 nm) and (**C**) Size distribution of SeNPs calculated from TEM image. (**D**) AFM image of SeNPs. (**E**) EDX spectra of SeNPs confirming the presence of Se. (**F**) DLS measurements showing average hydrodynamic diameter of SeNPs to be 74 nm.

2.3.2 Internalization of the SeNPs by cells

Following this, preliminary experiments were carried out to investigate whether SeNPs could effectively be uptaken by the cancer cells or not. Pertaining to the uptake studies, SeNPs were fluorescently labeled with Rhodamine-B and subsequently incubated with HeLa and MCF-7 cells for 4 h. Fluorescence microscopic images of treated HeLa and MCF-7 cells (**Figure 2.2**) demonstrated successful internalization of SeNPs by cells as evident from the red fluorescence of Rhodamine-B inside the cells. Interestingly, comparison with nuclear staining by DAPI revealed that the SeNPs mostly retained in the cytoplasm of the cancer cells following their internalization.

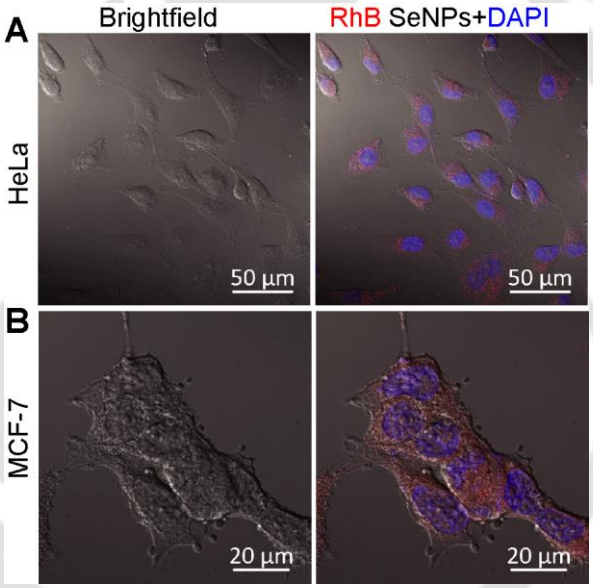

Figure 2.2 Confocal microscopic images of HeLa (**A**) and MCF-7 (**B**) cells treated with Rhodamine B labeled SeNPs demonstrating internalization of SeNPs (red color) by the cells. Cell nuclei were stained with DAPI (blue).

2.3.3 Drug Loading and release

PTX was loaded onto SeNPs by incubating the drug with SeNPs at room temperature for 4 h. PTX loaded SeNPs (PTX-SeNPs) were collected by centrifugation and thoroughly washed for further studies. Fourier transform

infrared spectroscopy (FTIR) spectrum of PTX-SeNPs (**Figure 2.3A**), when compared with that of SeNPs, revealed additional peaks at 1730 cm^{-1} due to carbonyl group confirming successful loading of PTX onto SeNPs.[17] Drug loading efficiency of the SeNPs for PTX was estimated to be ~26%, which corresponded to 1.1 µM of PTX loaded onto SeNPs. Surface charge of the NPs plays an important role in their cellular uptake and distribution.[18] Zeta potential (ζ) of the SeNPs was measured to be -15.4 mV (**Figure 2.3B**). Interestingly, loading of PTX resulted in the increase of the hydrodynamic diameter of SeNPs from 74 nm to 87 nm, possibly due to incorporation of the drug molecules on the surface of SeNPs. On the other hand, zeta potential changed from -15.4 mV in SeNPs to -28 mV in PTX-SeNPs indicating comparatively higher stability of the latter.[1] PTX release from SeNPs was studied at pH 7.4 and pH 5 to mimic blood pH and acidic environment of the tumor respectively. **Figure 2.3C** showed PTX release profile in two different pH conditions, most of the PTX was released from nanoparticles within first 10 h. Rate of drug release at pH 5 was higher as compared to pH 7.4, which is an advantage of this nanocarrier for releasing the drug in a tumor environment.

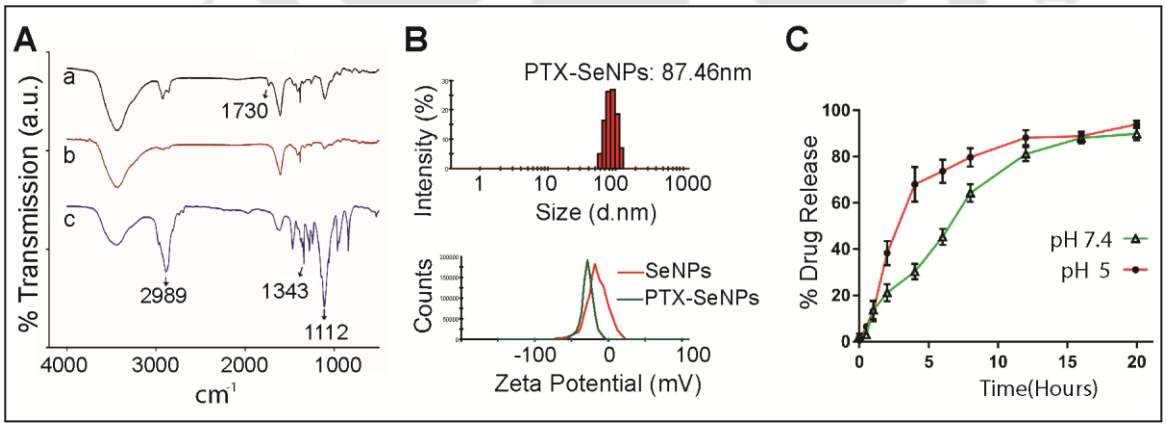

Figure 2.3 (**A**) FTIR spectra of PTX-SeNPs(a), SeNPs(b) and F-127(c). (**B**) hydrodynamic diameter and zeta potential of PTX-SeNPs (as measured by DLS). (**C**) Drug release study at pH 5 and 7.

2.3.4 Cell Viability assays

In order to evaluate the anticancer efficacy of PTX-SeNPs *in vitro*, four different cancer cell lines – lung carcinoma (A549), ovarian carcinoma (HeLa), colon carcinoma (HT29) and breast carcinoma (MCF-7) – were treated with different concentrations of SeNPs, PTX, and PTX-SeNPs for 48 h. The viability assay (**Figure 2.4, 2.5)** indicated that SeNPs were able to inhibit the growth of cancer cells with IC_{50} values of 28.1 μM, 25.3 μM, 10.8 μM, and 12.1 μM in A549, HeLa, HT29 and MCF-7 cells, respectively. However, the anti-proliferative efficiency was greatly enhanced after loading PTX as evident from the decrease in corresponding IC_{50} values (13.8 μM, 8.7 μM, 4.8 μM, and 5.4 μM in A549, HeLa, HT29 and MCF-7 cells, respectively) in all the four cancer cell lines (**Figure 2.4, 2.5**). Most importantly, as evident from **Table 2.1**, the amount of PTX present at the IC_{50} concentrations of PTX-SeNPs were much less than IC_{50} concentrations of free PTX for A549, HT29 and MCF-7 cells; while both being almost comparable in HeLa cells. Overall, the results of MTT assay indicated the improved antiproliferative efficacy of PTX following its loading onto F-127-stabilized SeNPs. From the results shown in **Figure 2.5** and **Table 2.1**, SeNPs and PTX-SeNPs were observed to inhibit the proliferation of normal cells (HEK293 and L132) also in almost similar fashion as that of cancer cells. However, the SeNPs and/or PTX-SeNPs could be targeted to cancer cells specifically by suitable (active or passive) targeting.[19,20]

Table 2.1 IC_{50} concentrations of SeNPs, PTX and PTX-SeNPs.

	SeNPs	PTX-SeNPs		Free PTX
	IC_{50}	Se amount at IC_{50}	PTX amount at IC_{50}	IC_{50}
HeLa	25.3 ±3.2 μM	8.7 ±1.8 μM	2.0±0.5 nM	3.4±0.1 nM
A549	28.1 ±2.6 μM	13.8 ±2.1 μM	3.1 ±0.8 nM	14.5±0.1 nM
HT29	10.9 ±2.1 μM	4.8±1 μM	1.1 ±0.25 nM	13.4±0.2 nM
MCF-7	12.2 ± 1.5 μM	5.4±1.6 μM	1.2 ± 0.2nM	9.2±0.3 nM
HEK	21.9 ±3.7 μM	9.7±1.8 μM	2.2 ±0.4 nM	8.3±0.1 nM
L132	65.0 ±5.4 μM	12.7±2.2 μM	2.8 ±0.24 nM	4.8±0.1 nM

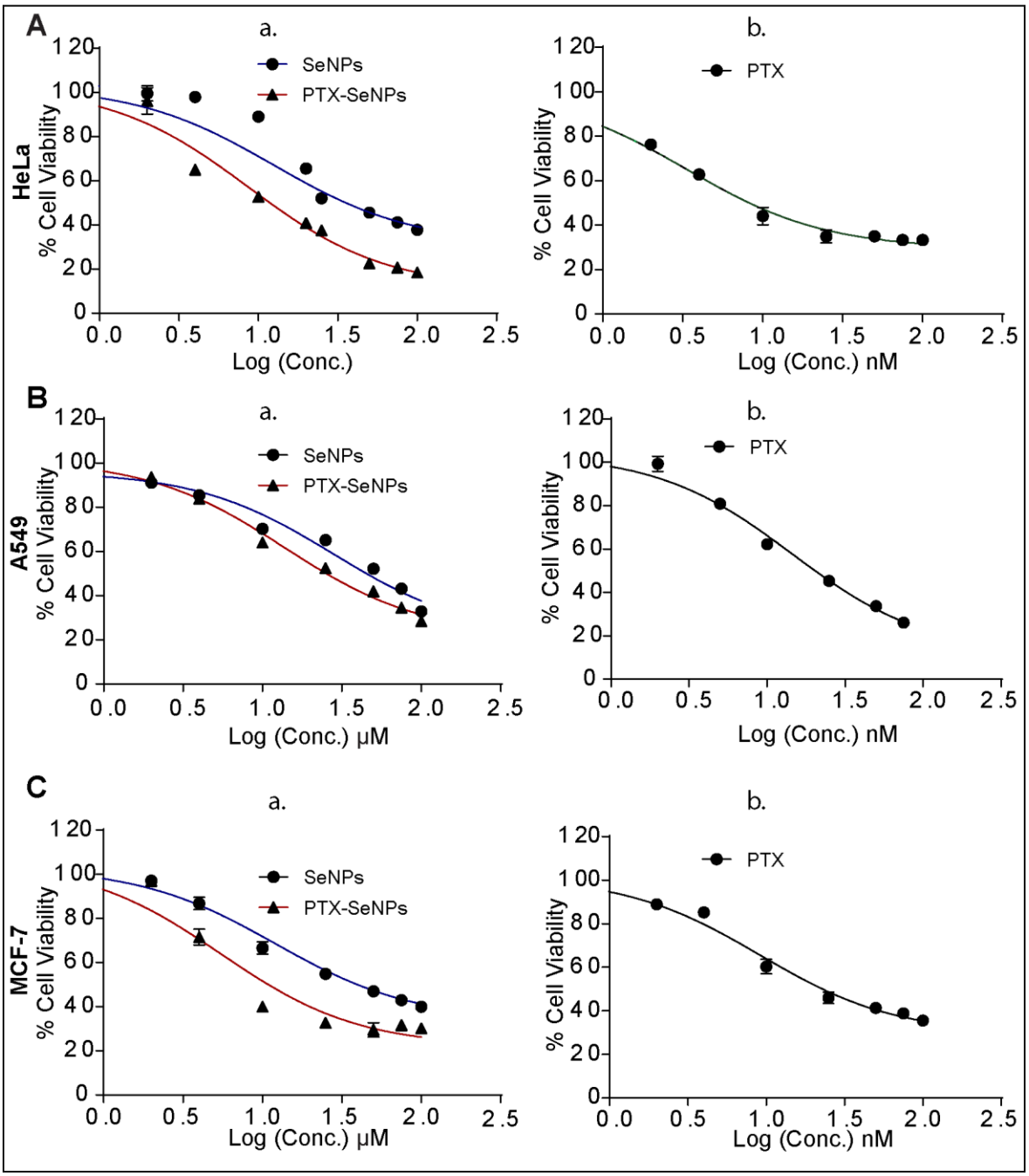

Figure 2.4 Cell viability of (**A**) HeLa, (**B**) A549 and (**C**) MCF-7 cells following treatment with SeNPs, PTX-SeNPs, and PTX for 48 h.

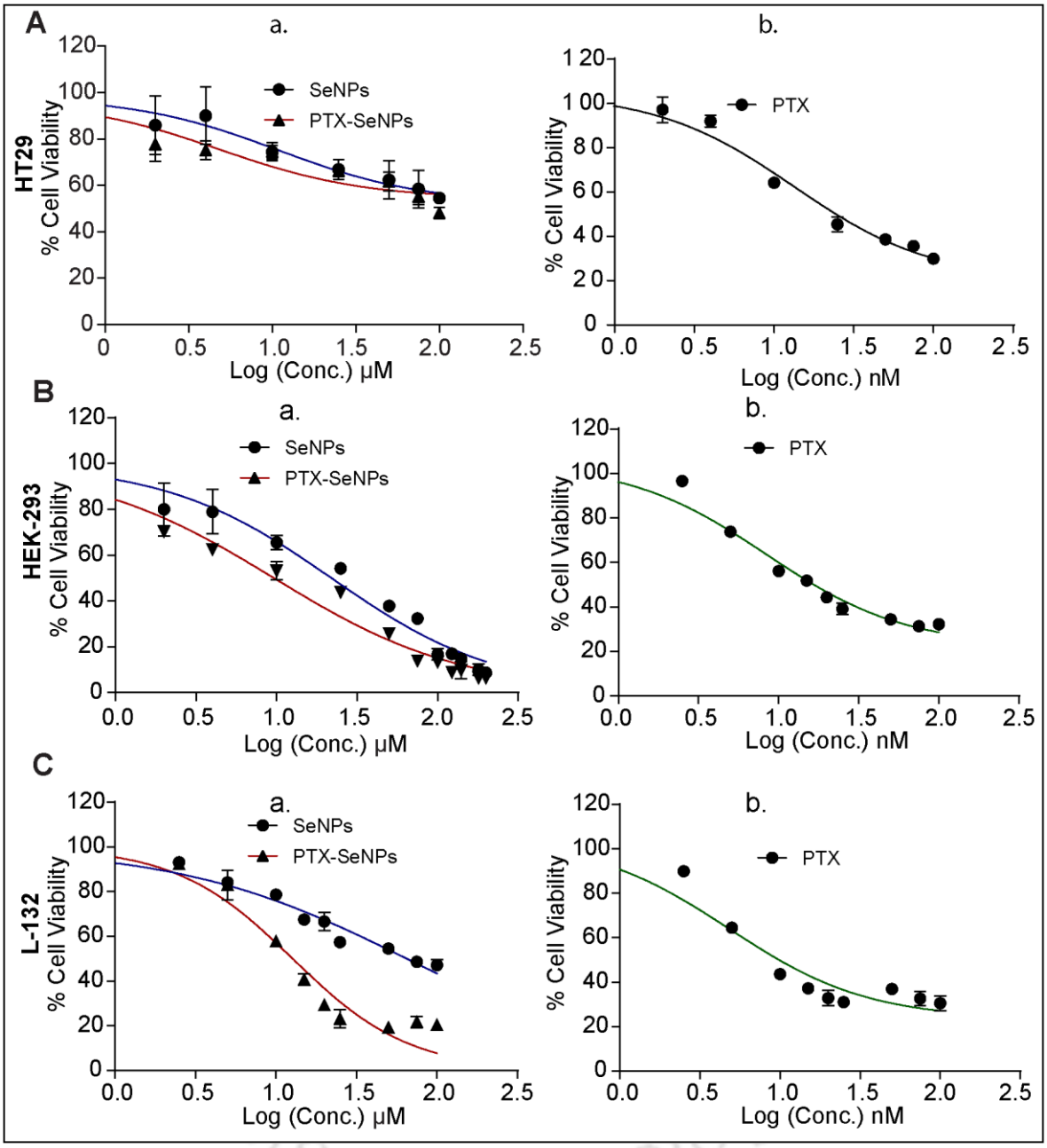

Figure 2.5 Cell viability of (**A**) HT29, (**B**) HEK-293 and (**C**) L-132 cells following treatment with SeNPs, PTX-SeNPs, and PTX for 48 h.

2.3.5 Cell Cycle analysis

The significant anti-proliferative activity shown by PTX-SeNPs against cancer cells was further pursued by checking the cell cycle distribution in HeLa and MCF-7 cells following their treatment with the drug-loaded NPs for 48 h. Summary of the flow cytometric analysis of cell cycle progression,

depicted in **Figure 2.6**, clearly revealed that treatment of HeLa and MCF-7 cells with PTX-SeNPs resulted in cell cycle arrest in G_2/M phase in a dose-dependent manner with a concomitant decrease in G_1 population. For example, G_2/M population increased from 3.8% in non-treated cells to 16.5%, 21.6% and 23.4% in HeLa cells treated with 4.35 µM ($^1/_2$ IC_{50}), 8.7 µM (IC_{50}), and 13 ($^3/_2$ IC_{50}) µM of PTX-SeNPs, respectively. Similarly, PTX-SeNPs-treated MCF-7 cells demonstrated 19%, 20.3%, 29.4% of population in G_2/M as compared to that of 15.7% in control non-treated cells. It may be mentioned here that PTX is known to cause G_2/M cell cycle arrest – by binding to ß subunit of microtubulin – and eventually induce apoptosis in breast and ovarian cancer cells.[21] To this end, the effective G_2/M arrest in treated HeLa and MCF-7 cells in the present study confirmed the successful delivery and subsequent release of PTX inside the cancer cells by SeNPs.

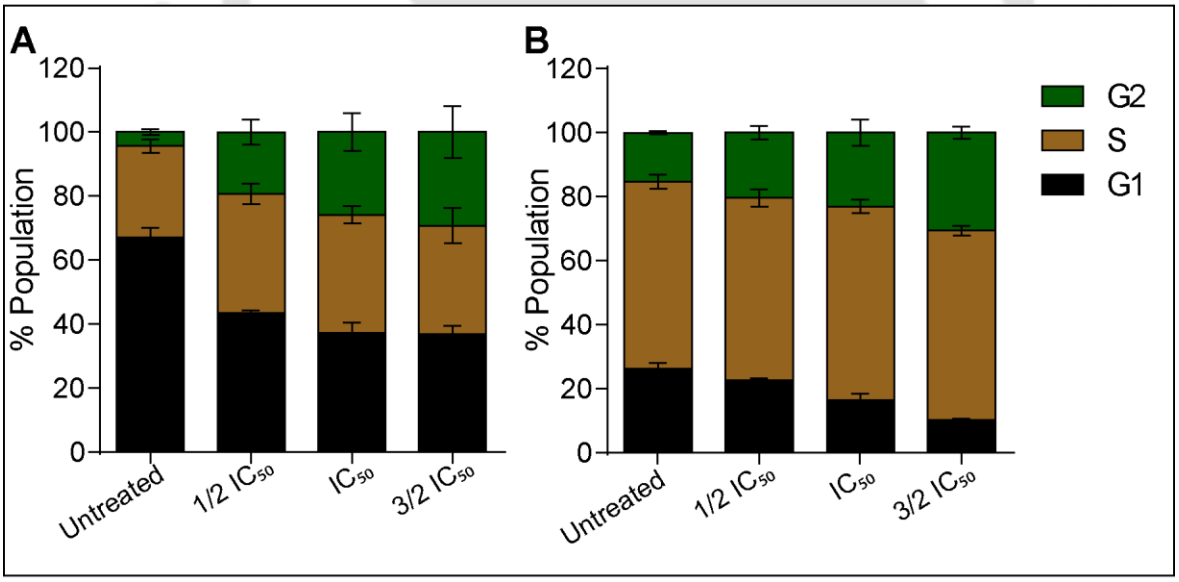

Figure 2.6 PTX-SeNPs induces G_2/M arrest in HeLa (**A**) and MCF-7 (**B**) cells after treatment.

2.3.6 Apoptosis study

The extent of apoptosis in PTX-SeNPs treated HeLa, and MCF-7 cells was quantified by Annexin V-PI assay. Flow-cytometric analysis (**Figure 2.7**) of

the FITC-Annexin V-PI stained cells revealed efficient induction of apoptosis by PTX-SeNPs with apoptotic population of ~61% and ~28.2% in IC_{50} treated HeLa and MCF-7 cells, respectively. It was also evident from **Figure 2.7** that the necrotic population did not increase significantly (<2.5% increase) in both the cell lines as a result of PTX-SeNPs treatment. This essentially indicated the potential of PTX-SeNPs in killing cancer cells without deleterious effects of necrotic cell death, desirable for effective cancer therapy.

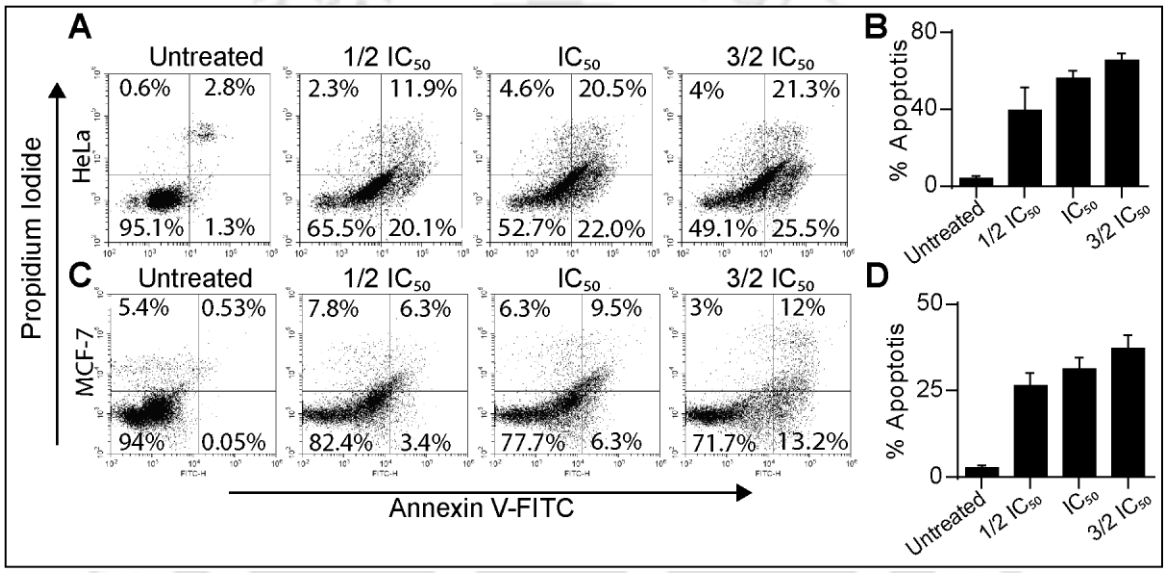

Figure 2.7 FITC-Annexin V – PI based flow-cytometric determination of apoptosis in HeLa (**A, B**) and MCF-7 (**C, D**) cells treated with different concentrations of the PTX-SeNPs.

FESEM analysis of PTX-SeNPs treated cells (**Figure 2.8**) also demonstrated characteristic membrane blebbing indicating apoptosis in treated cells.

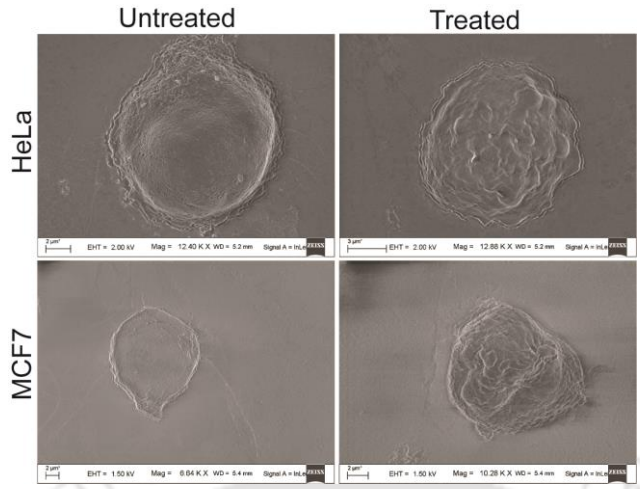

Figure 2.8 FESEM images showing cell morphology after treatment with IC_{50} concentrations of PTX-SeNPs for 48 h.

2.3.7 Mechanism of Apoptosis

Increased level of ROS has been reported to constitute the early events leading toward apoptosis in most of the anticancer drug mechanism of actions including PTX.[22] Furthermore, SeNPs have also been demonstrated to induce oxidative stress in human liver hepatocellular carcinoma (HepG2) and skin malignant melanoma (A375) cells.[4] In this regard, to measure intracellular ROS levels, treated cells were stained with DCF-DA dye and subsequently analyzed by flow cytometry.[23] In the cellular environment, non-fluorescent DCF-DA dye is first cleaved by esterases and oxidized by ROS to produce green fluorescent 2,7-dichlorofluorescein. Flow cytometric analysis of HeLa and MCF-7 cells, following their treatment with PTX-SeNPs (at $^1/_2$ IC_{50}, IC_{50}, and $^3/_2$ IC_{50}), showed increased ROS levels than corresponding untreated cells **(Figure 2.9)**.

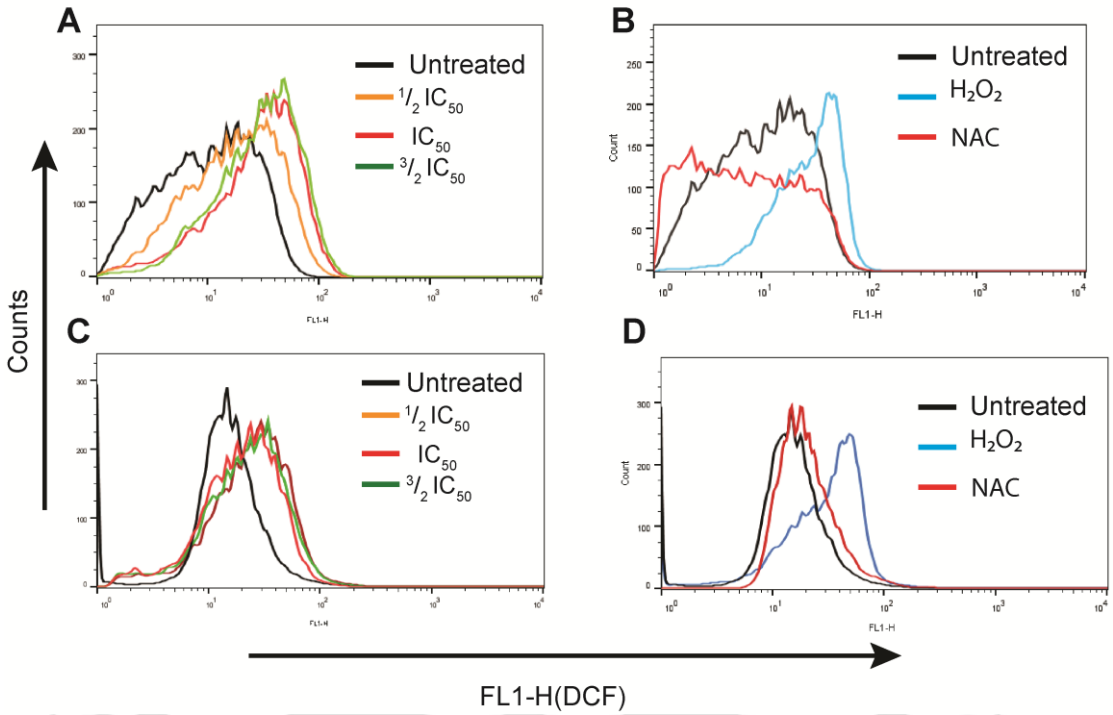

Figure 2.9 Result of DCF-DA based-flow-cytometric assay for detecting ROS in PTX-SeNPs treated (**A, B**) HeLa and (**C, D**) MCF-7 cells.

High levels of the ROS have detrimental effects on several intracellular components including mitochondria. Oxidative stress in cells, due to ROS, damages mitochondrial membrane resulting in alteration of mitochondrial membrane potential (MMP).[24,25]

The changes in MMP in the present study were probed by JC-1 dye, which fluoresces red in healthy mitochondria due to the formation of J-aggregates while emitting green fluorescence in damaged (depolarized) mitochondria.[26] Fluorescence microscopic images of JC-1 stained cancer cells demonstrated healthy mitochondria in non-treated cells as evident from the predominance of red fluorescence in **Figure 2.10A, B**. However, the appearance of green fluorescence in treated HeLa and MCF-7 cells indicated depolarization of mitochondria as a result of PTX-SeNPs treatment. Interestingly, the number of cells with damaged mitochondria (appeared as green dots) increased with increasing dose of PTX-SeNPs especially at IC_{50} or more.

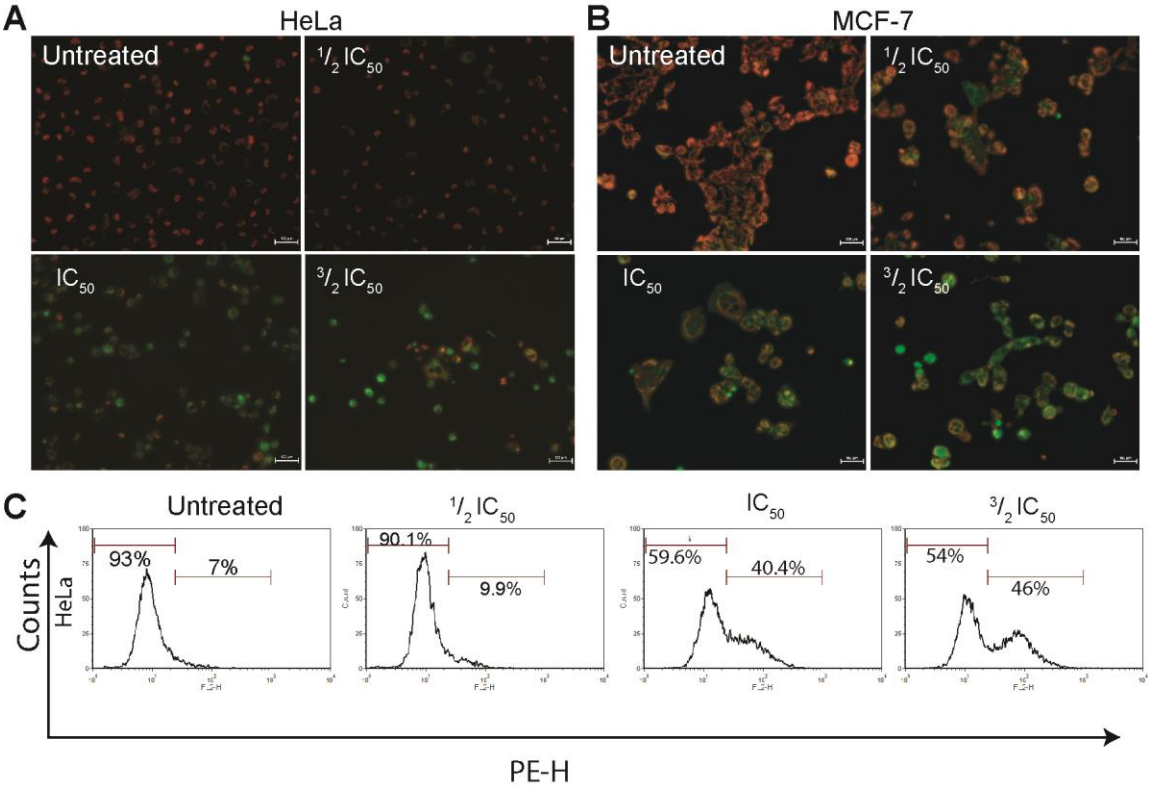

Figure 2.10 JC-1 staining showing the damage in mitochondrial membrane in PTX-SeNPs treated (**A**) HeLa and (**B**) MCF-7 cell lines. (**C**) Flow cytometric detection of the active caspase-3 in untreated and PTX-SeNPs treated HeLa cells.

Changes in the MMP due to damage in mitochondrial membrane results in the secretion of cytochrome c into the cytoplasm. This, in turn, leads to the activation of caspases, a family of proteases playing a significant role in apoptosis [27]. Among several caspases, caspase-3 is one of the frequently activated effector caspases that function downstream in apoptotic pathway. Activation of caspase-3 in HeLa cells after treatment with PTX-SeNPs was studied. As evident in **Figure 2.10C**, a dose-dependent increase in the activation of the caspase-3 was observed in HeLa cells, indicating the involvement of effector caspases in PTX-SeNPs mediated apoptosis. Taken together, the present experimental results demonstrated PTX-Se NPs-mediated oxidative stress and subsequent destabilization in MMP and

activation of effector caspases leading to efficient apoptotic cell death in treated cancer cells.

2.4 Conclusion

In conclusion, Pluronic F-127 stabilized SeNPs were prepared and used for the successful delivery of the chemotherapeutic drug, PTX to various cancer cells. The PTX-loaded SeNPs have demonstrated to mount a significant anti-proliferative response in cancer cells by arresting the treated cells at the G_2/M phase of the cell cycle in a dose-dependent manner. Further analyses in breast (MCF-7) and cervical cancer (HeLa) cells revealed efficient induction of apoptosis. Generation of oxidative stress in the form of ROS due to treatment with PTX-SeNPs and subsequent damage in mitochondrial transmembrane potential leading to activation of effector caspases have been shown to play an important role in apoptotic cell death in treated cancer cells. The efficient apoptosis in various cancer cells induced by the present PTX-SeNPs, with appropriate targeting scheme might lead to development of potential anti-cancer strategies.

2.5 References

(1) Liu, W.; Li, X.; Wong, Y. S.; Zheng, W.; Zhang, Y.; Cao, W.; Chen, T. Selenium Nanoparticles as a Carrier of 5-Fluorouracil to Achieve Anticancer Synergism. *ACS Nano* **2012**, *6* (8), 6578–6591. https://doi.org/10.1021/nn202452c.

(2) Fraga, C. G. Relevance, Essentiality and Toxicity of Trace Elements in Human Health. *Molecular Aspects of Medicine*. 2005, pp 235–244. https://doi.org/10.1016/j.mam.2005.07.013.

(3) Fan, C.; Chen, J.; Wang, Y.; Wong, Y. S.; Zhang, Y.; Zheng, W.; Cao, W.; Chen, T. Selenocystine Potentiates Cancer Cell Apoptosis Induced by 5-Fluorouracil by Triggering Reactive Oxygen Species-Mediated DNA Damage and Inactivation of the ERK Pathway. *Free Radic. Biol. Med.* **2013**, *65*, 305–316. https://doi.org/10.1016/j.freeradbiomed.2013.07.002.

(4) Zhang, Y.; Li, X.; Huang, Z.; Zheng, W.; Fan, C.; Chen, T. Enhancement of Cell

Permeabilization Apoptosis-Inducing Activity of Selenium Nanoparticles by ATP Surface Decoration. *Nanomedicine Nanotechnology, Biol. Med.* **2013**, *9* (1), 74–84. https://doi.org/10.1016/j.nano.2012.04.002.

(5) Li, S.; Zhou, Y.; Wang, R.; Zhang, H.; Dong, Y.; Ip, C. Selenium Sensitizes MCF-7 Breast Cancer Cells to Doxorubicin-Induced Apoptosis through Modulation of Phospho-Akt and Its Downstream Substrates. **2007**, *6* (March), 1031–1039. https://doi.org/10.1158/1535-7163.MCT-06-0643.

(6) Sarin, L.; Sanchez, V. C.; Yan, A.; Kane, A. B.; Hurt, R. H. Selenium-Carbon Bifunctional Nanoparticles for the Treatment of Malignant Mesothelioma. *Adv. Mater.* **2010**, *22* (45), 5207–5211. https://doi.org/10.1002/adma.201002607.

(7) Sparano, J. A.; Wang, M.; Martino, S.; Jones, V.; Perez, E. A.; Saphner, T.; Wolff, A. C.; Sledge, G. W.; Wood, W. C.; Davidson, N. E. Weekly Paclitaxel in the Adjuvant Treatment of Breast Cancer. *N. Engl. J. Med.* **2008**, *358* (16), 1663–1671. https://doi.org/10.1056/NEJMoa0707056.

(8) Kumar, S.; Mahdi, H.; Bryant, C.; Shah, J. P.; Garg, G.; Munkarah, A. Clinical Trials and Progress with Paclitaxel in Ovarian Cancer. *International Journal of Women's Health*. 2010, pp 411–427. https://doi.org/10.2147/IJWH.S7012.

(9) Rose, P. G.; Blessing, J. a; Gershenson, D. M.; McGehee, R. Paclitaxel and Cisplatin as First-Line Therapy in Recurrent or Advanced Squamous Cell Carcinoma of the Cervix: A Gynecologic Oncology Group Study. *J. Clin. Oncol.* **1999**, *17* (9), 2676–2680.

(10) Zhang, C.; Lu, T.; Tao, J.; Wan, G.; Zhao, H. Co-Delivery of Paclitaxel and Indocyanine Green by PEGylated Graphene Oxide: A Potential Integrated Nanoplatform for Tumor Theranostics. *RSC Adv.* **2016**, *6* (19), 15460–15468. https://doi.org/10.1039/c5ra25518j.

(11) Ghoshal, A.; Goswami, U.; Sahoo, A. K.; Chattopadhyay, A.; Ghosh, S. S. Targeting Wnt Canonical Signaling by Recombinant SFRP1 Bound Luminescent Au-Nanocluster Embedded Nanoparticles in Cancer Theranostics. *ACS Biomater. Sci. Eng.* **2015**, acsbiomaterials.5b00305. https://doi.org/10.1021/acsbiomaterials.5b00305.

(12) Yildirim, A.; Demirel, G. B.; Erdem, R.; Senturk, B.; Tekinay, T.; Bayindir, M. Pluronic Polymer Capped Biocompatible Mesoporous Silica Nanocarriers.

Chem. Commun. (Camb). **2013**, *49* (84), 9782–9784. https://doi.org/10.1039/c3cc45967e.

(13) Batrakova, E. V.; Kabanov, A. V. Pluronic Block Copolymers: Evolution of Drug Delivery Concept from Inert Nanocarriers to Biological Response Modifiers. *J. Control. Release* **2008**, *130* (2), 98–106. https://doi.org/10.1016/j.jconrel.2008.04.013.

(14) Torchilin, V. P. Structure and Design of Polymeric Surfactant-Based Drug delivery Systems. *J. Control. Rel.* **2001**, *73*, 137–172.

(15) Pi, J.; Jin, H.; Liu, R.; Song, B.; Wu, Q.; Liu, L.; Jiang, J.; Yang, F.; Cai, H.; Cai, J. Pathway of Cytotoxicity Induced by Folic Acid Modified Selenium Nanoparticles in MCF-7 Cells. *Appl. Microbiol. Biotechnol.* **2013**, *97* (3), 1051–1062. https://doi.org/10.1007/s00253-012-4359-7.

(16) Petros, R. a; DeSimone, J. M. Strategies in the Design of Nanoparticles for Therapeutic Applications. *Nat. Rev. Drug Discov.* **2010**, *9* (8), 615–627. https://doi.org/Doi 10.1038/Nrd2591.

(17) Cao, Z.; Zhu, W.; Wang, W.; Zhang, C.; Xu, M.; Liu, J.; Feng, S. T.; Jiang, Q.; Xie, X. Stable Cerasomes for Simultaneous Drug Delivery and Magnetic Resonance Imaging. *Int. J. Nanomedicine* **2014**, *9* (1), 5103–5116. https://doi.org/10.2147/IJN.S66919.

(18) Fröhlich, E. The Role of Surface Charge in Cellular Uptake and Cytotoxicity of Medical Nanoparticles. *International Journal of Nanomedicine*. 2012, pp 5577–5591. https://doi.org/10.2147/IJN.S36111.

(19) Zhang, J. S.; Gao, X. Y.; Zhang, L. D.; Bao, Y. P. Biological Effects of a Nano Red Elemental Selenium. *Biofactors* **2001**, *15* (1), 27–38. https://doi.org/10.1002/biof.5520150103.

(20) Yin, T.; Yang, L.; Liu, Y.; Zhou, X.; Sun, J.; Liu, J. Sialic Acid (SA)-Modified Selenium Nanoparticles Coated with a High Blood–brain Barrier Permeability Peptide-B6 Peptide for Potential Use in Alzheimer's Disease. *Acta Biomater.* **2015**, *25*, 172–183. https://doi.org/10.1016/J.ACTBIO.2015.06.035.

(21) Das, G. C.; Holiday, D.; Gallardo, R.; Haas, C. Taxol-Induced Cell Cycle Arrest and Apoptosis: Dose-Response Relationship in Lung Cancer Cells of Different Wild-Type P53 Status and under Isogenic Condition. *Cancer Lett.* **2001**, *165* (2),

147–153. https://doi.org/10.1016/S0304-3835(01)00404-9.

(22) Alexandre, J.; Batteux, F.; Nicco, C.; Chéreau, C.; Laurent, A.; Guillevin, L.; Weill, B.; Goldwasser, F. Accumulation of Hydrogen Peroxide Is an Early and Crucial Step for Paclitaxel-Induced Cancer Cell Death Both in Vitro and in Vivo. *Int. J. Cancer* **2006**, *119* (1), 41–48. https://doi.org/10.1002/ijc.21685.

(23) Aranda, A.; Sequedo, L.; Tolosa, L.; Quintas, G.; Burello, E.; Castell, J. V.; Gombau, L. Dichloro-Dihydro-Fluorescein Diacetate (DCFH-DA) Assay: A Quantitative Method for Oxidative Stress Assessment of Nanoparticle-Treated Cells. *Toxicol. Vitr.* **2013**, *27* (2), 954–963. https://doi.org/10.1016/j.tiv.2013.01.016.

(24) Simon, H.; Haj-Yehia, A.; Levi-Schaffer, F. Role of Reactive Oxygen Species (ROS) in Apoptosis Induction. *Apoptosis* **2000**, *5* (5), 415–418. https://doi.org/10.1023/A:1009616228304.

(25) Fleury, C.; Mignotte, B.; Vayssière, J.-L. Mitochondrial Reactive Oxygen Species in Cell Death Signaling. *Biochimie* **2002**, *84* (2), 131–141. https://doi.org/10.1016/S0300-9084(02)01369-X.

(26) Sakamuru, S.; Li, X.; Attene-Ramos, M. S.; Huang, R.; Lu, J.; Shou, L.; Shen, M.; Tice, R. R.; Austin, C. P.; Xia, M. Application of a Homogenous Membrane Potential Assay to Assess Mitochondrial Function. *Physiol Genomics* **2012**, *44* (9), 495–503. https://doi.org/10.1152/physiolgenomics.00161.2011.

(27) Jo, W. S.; Jeong, M. H.; Jin, Y. H.; Jang, J. Y.; Nam, B. H.; Son, S. H.; Choi, S. S.; Yoo, Y. H.; Kang, C. D.; Lee, J. D.; et al. Loss of Mitochondrial Membrane Potential and Caspase Activation Enhance Apoptosis in Irradiated K562 Cells Treated with Herbimycin A. *Int J Radiat Biol* **2005**, *81* (7), 531–543. https://doi.org/P60181383661364Q [pii]\r10.1080/09553000500303773.

CHAPTER 3

Combination therapy with MAPK pathway specific inhibitor and folic acid receptor targeted selenium nanoparticles

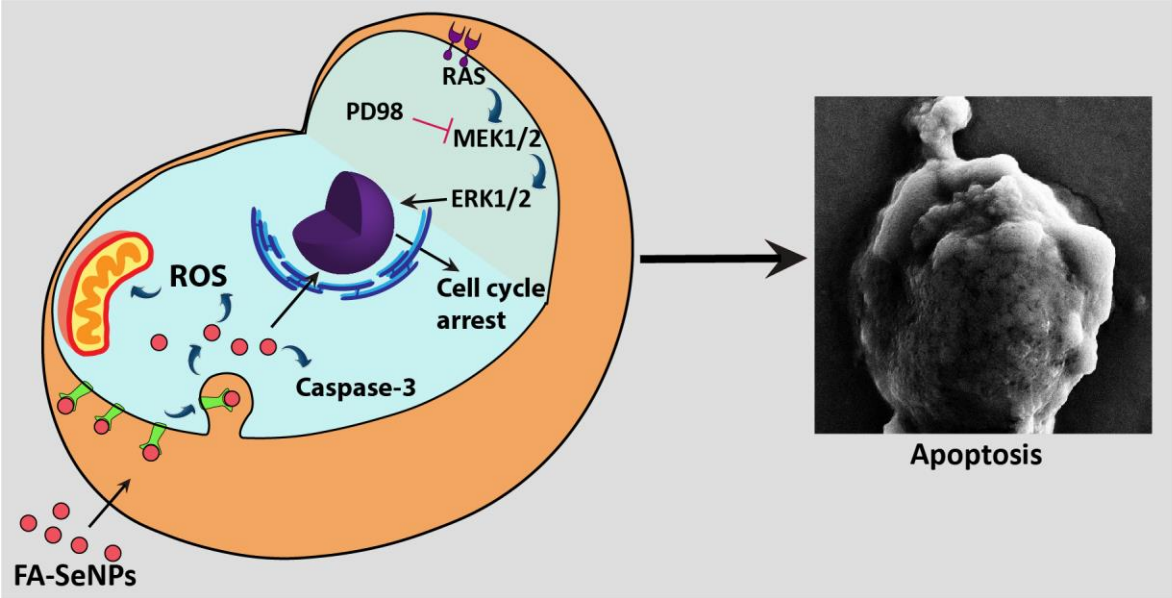

In **Chapter 3,** a selective and targeted therapy has been designed to annihilate MDAMB231 (breast cancer) and A375 (melanoma) cancer cells. These cells have high expression of folic acid receptor (FAR) and mutations in RAS and BRAF genes in MAPK signaling pathway. The combination therapy module involved FAR-targeted SeNPs (FA-SeNPs) and MAPK inhibitor PD98059 (PD98).

ACS Biomaterials Science & Engineering, 2019, 5, 5, 2222- 2234.
DOI: 10.1021/acsbiomaterials.9b00112

CHAPTER 3

3.1 Introduction

Targeted delivery of anti-cancer drugs is of paramount importance for successful cancer treatment as it helps in improving the overall therapeutic efficacy by minimizing the 'bystander' killing of normal cells caused by non-specific cytotoxicity associated with the majority of chemotherapeutic drugs.[1] Current methods of tumor targeting are mostly based on differential protein expression in cancerous cells. Folic acid or Vitamin B9 (FA), being essential in DNA synthesis, plays a crucial role in cell growth and cell division.[2] Cancer cells, not surprisingly, need a higher amount of folic acid than normal cells in order to maintain their characteristic rapid uncontrolled proliferation. Overexpression of folic acid receptor (FAR) is, indeed, one of the prominent features of many cancer types including ovarian, lung, and breast cancer.[3–5] Thus, exploiting FAR-overexpression has become one of the effective approaches for targeted chemotherapy and/or diagnostics. To this end, FA-decorated drug delivery systems have been demonstrated to deliver therapeutic payload selectively to cancer cells.[6–10]

Knowledge of the molecular signaling pathways and the availability of pathway inhibitors could be exploited to combat tumor progression effectively. Mitogen-activated protein kinase (MAPK) pathway is one of the important signaling cascades involved in proliferation, differentiation and developmental processes. RAS and RAF are the most widely mutated genes in the MAPK pathway. RAS (N-RAS, K-RAS, and H-RAS) mutations are associated with the skin, pancreatic, colon and ovarian cancers.[11] Similarly, BRAF is downstream of RAS and mutation in BRAF also causes excessive proliferation of cells seen in breast, colon and skin cancers.[12] The altered signaling, due to a mutation in the genes involved in the pathway, can be blocked by using pathway inhibitors. Consequently, the interest in small molecule kinase inhibitors is progressively increasing due to their inherent tumor-targeting nature.

With respect to cancer treatment, monotherapies involving chemotherapeutic drugs or small molecule kinase inhibitors suffer from the fact that the sensitivity of most of these drugs and kinase inhibitors decrease over the treatment period leading towards drug-resistance by cancer cells. In order to fight against the changing nature of a tumor due to the complex signaling pathways, researchers are always in quest of the newer drug combination which can kill a tumor synergistically.[13] In this regard, the advent of nanotechnology has provided with a plethora of various nanoparticles (NPs) that can be used as a delivery system of conventional anti-cancer drugs leading to better efficacy of the latter. Moreover, in addition to carrying drug payload, some NPs further possess potential therapeutic response of their own. As seen in previous chapter, selenium nanoparticles (SeNPs) showed antiproliferative action against cancer cells. Established synthesis protocols allow the preparation of SeNPs suitable for various purposes while targeting can be achieved by conjugating appropriate targeting ligand on the polymer used for stabilization of the SeNPs.

In this chapter, more selective and targeted therapy for the tumor cells has been investigated (**Scheme 3.1**). MDA-MB-231 (breast cancer) cells have G13D and G464V mutations in RAS and BRAF genes, respectively, while A375 (melanoma) cells possess V600E mutations in BRAF.[14,15] These mutations cause constitutive activation of the MAPK pathway which leads to uncontrolled proliferation and cancerous growth of MDA-MB-231 and A375 cells. To this end, a combination therapy involving FAR-targeted SeNPs (FA-SeNPs) and MAPK inhibitor PD98059 (PD98) was evaluated. Flow-cytometric and confocal microscopic experiments were performed to study the internalization of FA-SeNPs by cancer cells, while viability assays were carried out to evaluate the therapeutic potential of the present combination module. Moreover, the mode of cell death and effects on the cell cycle in treated cells were investigated by flow cytometry, electron microscopy, fluorescence microscopy, and Western blot analyses. Finally, the capability of

the proposed combination module in reducing the size of 3D cancer spheroids was also explored in order to assess its potential in treating a tumor *in vivo*. In addition to the folate receptor-targeted FA-SeNPs, the characteristic RAF-mutation in cancer cells has also been targeted by employing MAPK pathway inhibitors, which block the excessive signaling to bring about enhanced and selective anti-proliferation response in cancer cells.

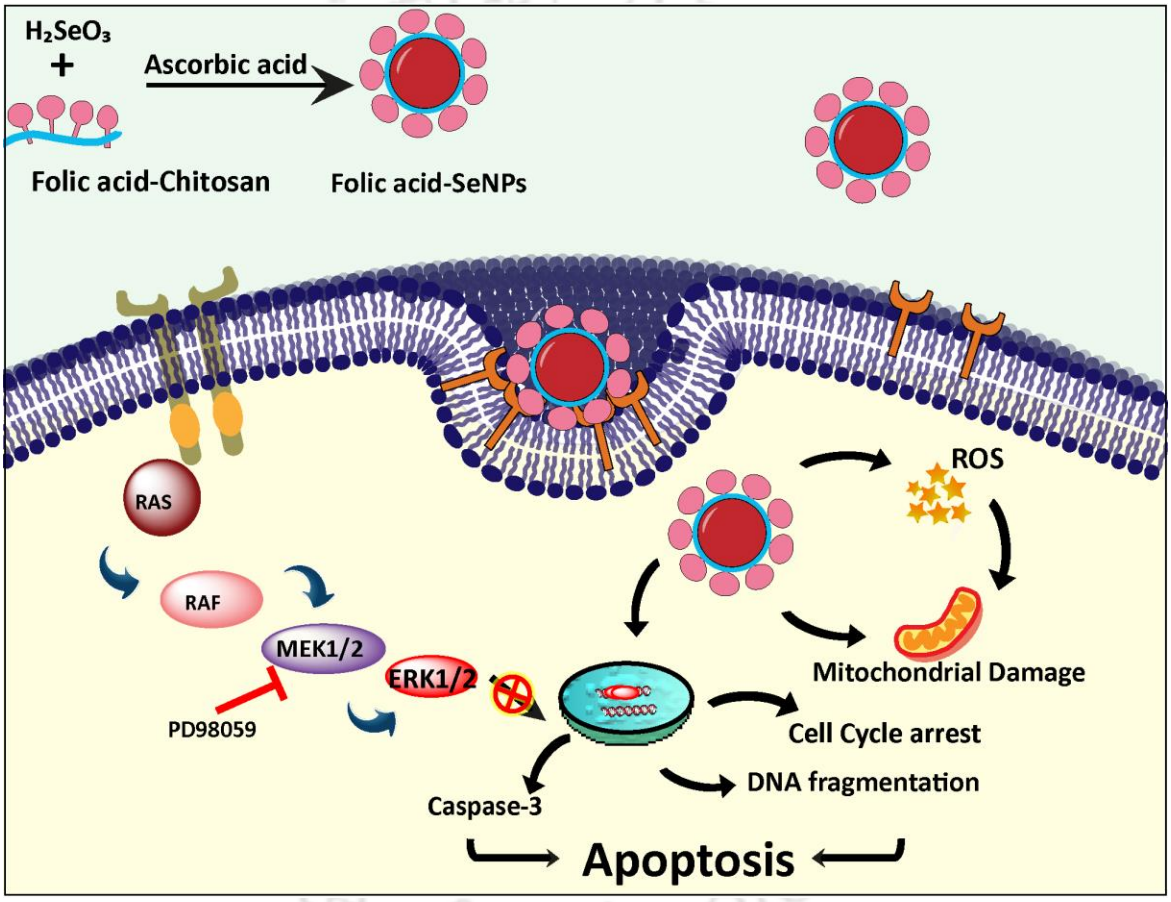

Scheme 3.1: Schematic representation of the combined therapeutic module consisting of folic acid targeted selenium nanoparticles and PD98 for inducing apoptosis in BRAF-mutant cancer cells.

3.2 Experimental Section

3.2.1 Chemicals

Folic acid (FA), chitosan (CS), 1-ethyl-3-(3-dimethylaminopropyl) carbodiimide (EDC), N-hydroxysuccinimide (NHS), dimethyl sulfoxide (DMSO), 2′,7′-Dichlorodihydrofluorescein diacetate (DCFDA), 5,5',6,6'-Tetrachloro-1,1',3,3'-tetraethylbenzimidazolocarbocyanine iodide (JC-1), PD98059, Rhodamine B, and selenium dioxide (SeO_2) were purchased from Sigma-Aldrich. MTT (3-(4,5-dimethylthiazol-2-yl)-2,5-diphenyltetrazolium bromide), p-nitrophenyl phosphate (pNPP) and sodium acetate were purchased from Himedia (India). SYBR green was purchased from Bio-Rad Laboratories. Anti Cox IV (Cat. No. 4850), anti-caspase-3 (Cat. No. 14220), anti-cleaved caspase-3 (Cat. No. 9664), anti-PARP (Cat. No. 9542), and anti-cleaved PARP antibodies (Cat. No. 5625) were purchased from Cell Signaling Technology.

3.2.2 Cell culture

Human malignant melanoma (A375), breast adenocarcinoma (MDA-MB-231) and lung cells (L132) were purchased from National Centre for Cell Science, Pune, India. All cell lines were maintained in Dulbecco's Modified Eagle's Medium (DMEM) supplemented with 10% (v/v) fetal bovine serum and 1% penicillin-streptomycin at 37 °C in humidified air containing 5% CO_2.

3.2.3 Conjugation of folic acid to chitosan

Conjugation of FA to CS was performed according to the protocol described by Yang et al. [16] with slight modification. Briefly, FA, EDC, and NHS were dissolved in DMSO, these mixtures were added dropwise to CS solution (0.5% w/v) and stirred for 24 h in the dark. The resultant product was precipitated by adding sufficient NaOH to adjust pH 8, washed with water, collected by centrifugation and dialyzed against water to remove residual reactant. The yellow precipitate was subjected to lyophilization for further use. As the number of FA molecules on the surface of NPs can affect their cellular uptake,

FA-CS with increasing density of FA were prepared by reacting CS with increasing concentrations of FA as mentioned in **Table 3.1**. Amount of FA conjugated on CS was estimated by UV-visible spectrophotometry from a standard curve for FA. To study the release of FA from FA-CS, FA-CS solution was dialyzed against water for 10 days. Released FA in water was quantified on Day 1, 2, 5 and 10. Conjugation of FA to CS was also confirmed by FTIR analysis with Perkin-Elmer Spectrum One spectrophotometer.

3.2.4 Synthesis and characterization of FA-SeNPs

FA-CS coated SeNPs (FA-SeNPs) were synthesized according to the protocol described by Liu *et al.* with slight modification.[17] To find sufficient amount of the FA-CS required to produce stable and uniform NPs, SeNPs were synthesized in presence of different concentrations of FA-CS. Briefly, 1 ml of H_2SeO_3 (100 mM) and 1 ml of FA-CS (0.03-0.024%w/v) were mixed with 17 ml water for 20 min. The ascorbic acid solution was added dropwise to the above mixture with continuous stirring. The reaction mixture was allowed to stir for 24 h. FA-SeNPs were centrifuged at 20000 g for 20 min at 4 °C.

Hydrodynamic diameter and polydispersity index were monitored in Malvern Zetasizer for each FA-CS concentration used to prepare FA-SeNPs. For transmission electron microscopy (TEM) analysis, FA-SeNPs were drop cast on the carbon-coated copper grid, dried and analyzed in JEM 2100 (Jeol, Peabody, MA, USA) at 200 kV. For field emission scanning electron microscopy (FESEM) analysis, synthesized nanoparticles were allowed to dry on an aluminum foil-coated coverslip and observed under a microscope (Zeiss, Sigma). X-ray diffraction studies were performed to study the crystalline nature of prepared FA-SeNPs. Chemical states of thermogravimetric (TGA) and differential scanning calorimetry (DSC) measurements were performed in thermogravimetric system (Netzsch). About 5 mg of SeNPs and FA-SeNPs were analyzed in a nitrogen environment from 0 °C to 1100 °C.

3.2.5 Gene expression studies

To confirm the mutations in BRAF genes, amplification refractory mutation system based polymerase chain reaction (ARMS-PCR) was carried out using method described by Machnicki *et al.*[18] For ARMS-PCR, genomic DNA from cells (L132 and A375) were amplified with three primers (**Table 3.3)**. One of the primers was mutation specific primer which would give the additional product only in the presence of T1799A mutation (V600E) in BRAF gene. PCR was run with initial melting at 95 °C for 15 min, 40 cycles of 94 °C for 40 sec, 61 °C for 40 sec and 72 °C for 40 sec followed by final extension at 72 °C for 5 min. PCR products were separated on 2% agarose gel. Quantitative analysis of the folic acid receptor was done by real-time PCR. RNA was isolated from healthy L132, MDA-MB-231, and A375 cells, and was employed for cDNA synthesis. SYBR green-based real-time PCR reaction was run using primers for GAPDH and FAR. Expression of the *Bax*, *Bcl-2* and *Bcl-xL* genes in treated cells was studied by semi-quantitative PCR, using gene-specific primers (**Table 3.3**).

3.2.6 Mechanism of the internalization of the FA-SeNPs

Rhodamine B, a fluorescent dye was added during the synthesis of FA-SeNPs. These dye-loaded nanoparticles (RhB-FA-SeNPs) were centrifuged at 20000 g for 20 minutes at 4 °C. Cells were incubated with RhB-FA-SeNPs for 6 h for internalization at 37 °C. Stability of the dye on FA-SeNPs in culture medium was studied by incubating dye loaded- FA-SeNPs at 37 °C. At different time points (upto 28 h), FA-SeNPs were centrifuged and % of the dye amount on the NPs was calculated after taking the fluorescence at 590 nm. For flow cytometry, cells were trypsinized, resuspended in PBS and analyzed in cytometer (Cytoflex, Beckman Coulter). For confocal imaging, following incubation with RhB-FA-SeNPs, cells were washed twice with PBS, stained with DAPI and imaged in LSM 880 microscope (ZEISS). Quantitative analysis of FA-SeNPs uptake was performed on 96 well plates, where cells were

initially treated with endocytosis inhibitors and then FA-SeNPs.[17] To confirm whether uptake of the FA-SeNPs occurs via interaction of FAR, a control sample was kept where cells were treated with a high amount of the FA (1 mM) to saturate FAR and then FA-SeNPs were added. To confirm the active targeting, uptake after sodium azide as well as uptake at 4 °C was recorded. To find out the uptake mechanism of the FA-SeNPs inside the cells, chlorpromazine and hypertonic sucrose were used as an inhibitor of clathrin-mediated pathway while caveolae-mediated pathway was blocked by methyl-ß-cyclodextrin.

3.2.7 Cell proliferation assays

MTT assays were carried out on A375, MDA-MB-231, and L132 cells to study cell viability for different treatment groups. Initially, antiproliferative potential of SeNPs, PD98, and FA-SeNPs was studied on these cells. For combination therapy, groups followed were: (i) PD98 pretreatments for 10 h followed by treatment with FA-SeNPs for 48 h (PD98→FA-SeNPs) and (ii) PD98 in combination with FA-SeNPs for 48 h (PD98+FA-SeNPs). Similar MTT assays were performed to study the effect of DMSO (solvent for PD98) where cells were pre- or co-treated with equal volume of DMSO (0.1% v/v) along with FA-SeNPs instead of PD98.

3.2.8 Annexin V-FITC PI assay

Apoptotic cell population was estimated on flow cytometer by using an apoptosis assay kit (BD Biosciences). Cells were processed according to the supplier's protocol and analyzed in Cytoflex (Beckman Coulter) instrument. MDA-MB-231 and A375 cells were treated with DMSO, PD98 at 10 µM, FA-SeNPs at 20 µM (FA-SeNPs@20) and FA-SeNPs at 100 µM (FA-SeNPs@100) for 48 h. Also for combination studies, treatments were given as- 10 µM PD98 for 10 h followed by FA-SeNPs at 20 µM for 48 h (PD98→FA-SeNPs@20) and

combination of 10 μM PD98 with FA-SeNPs at 20 μM (PD98+FA-SeNPs@20). Data analysis and compensation was performed in Flowjo software.

3.2.9 Cell cycle analysis

Propidium iodide (PI) based cell cycle assay was performed to study the effect of combination treatment of PD98 and FA-SeNPs. Briefly, 10^5 cells were seeded, cells were synchronized with serum-free media for 36 h. Thereafter, cells were treated (PD98→FA-SeNPs@20 and PD98+FA-SeNPs@20), fixed in 70% ethanol, RNase-treated and stained with PI. Stained cells were analyzed in a flow cytometer (Cytoflex, Beckman Coulter).

3.2.10 Western Blots

MDA-MB-231 and A375 cells were treated as mentioned above and cells were lysed in RIPA buffer. Cellular proteins were isolated in a cold environment. An equal amount of the proteins from cell extracts were run on SDS-PAGE and were further transferred to PVDF membrane. Membranes were blocked with blocking buffer (4% BSA in TBST), primary antibodies were added and incubated for 12 h. After washing and incubation with secondary antibody, the chemiluminescent reagent was added and blot images were captured in ChemiDoc (Bio-Rad).

3.2.11 Surface morphology by FESEM

For observing the morphological changes in the cell membrane, cells were treated, trypsinized and fixed with 70% ethanol. A single drop of each sample was placed over an aluminum foil coated coverslip. After drying, cells were observed under a FESEM microscope (Zeiss, Sigma).

3.2.12 Nucleus staining and comet assay

To study the nuclear morphology, treated cells were fixed with 4% formaldehyde, stained with the Hoescht-33423 solution in PBS (0.2 µg/ml). After appropriate washing to remove the residual dye, cells were observed under a fluorescence microscope (Nikon Eclipse Ti-U, Tokyo, Japan). Alkaline lysis and electrophoresis method was utilized to study the single and double-stranded DNA breaks in individual cells.[19] Treated and untreated cells were mixed with the low gelling agarose at 40 °C and were placed onto agarose coated glass slides at the density of 6000 cells/slide. Completely gelled slides were subjected to alkaline lysis overnight at 4 °C in the dark. Electrophoresis was performed for 30 min and slides were stained with PI for 20 min at room temperature. Excess PI was washed off and slides were analyzed under a fluorescence microscope (Nikon Eclipse Ti-U, Tokyo, Japan).

3.2.13 DCFDA and JC-1 staining

Reactive oxygen species in treated cells were detected using DCFDA-based flow cytometric assay.[20] Cells were incubated with 10µM of DCFDA for 30 min, treated for 12 h for all treatments, except PD98→SeNPs@20, where PD98 was added to cells for 10 h before incubating with FA-SeNPs@20 for 12 h. Treated cells were trypsinized and immediately analyzed on a flow cytometer to collect green fluorescence. Mitochondrial staining was performed with JC-1 dye, where cells were treated for 48 h, after completion of treatment, JC-1 dye (10µM) was added in each well for 20 min. Stained cells were trypsinized and analyzed in a flow cytometer, fluorescence was collected in the red and green channel. Data analysis was performed in FlowJo software.

3.2.14 FA-SeNPs uptake, growth and viability of MDA-MB-231 spheroids

For spheroid formation, MDA-MB-231 cells were seeded at a density of $2x10^4$ cells/well in agarose pre-coated 96 well plate. Plates were centrifuged at

1000 x g for 10 min to form cell aggregates and incubated for 3 days for spheroid growth. Following appropriate treatment as mentioned, acid phosphatase assay was carried out to estimate the viability. Briefly, spheroids were treated with PD98, FA-SeNPs@20, and FA-SeNPs@40 (40 μM of FA-SeNPs) for 48 h. For combination module, PD98→FA-SeNPs@20, PD98+FA-SeNPS@20, PD98→FA-SeNPs@40 and PD98+FA-SeNPS@40 treatments were given for 48 h. Subsequently, spheroids were carefully transferred to another 96 well plate, centrifuged and 200 μl assay buffer (0.1M sodium acetate, 0.1% TritonX and 2 mg/ml pNPP) was added in each well. After 4 h incubation, absorbance was measured at 405 nm in the Tecan multiplate reader.[21]

To study the penetrability of NPs, MDA-MB-231 spheroids were treated with Rhodamine-B loaded SeNPs and FA-SeNPs for 6 h, and observed under confocal microscope. Live-dead staining was performed to get an idea about cell death after treatment for 48 h. Spheroids were treated with PD98→FA-SeNPs@40 and PD98+FA-SeNPs@40, after 48 h treatment, spheroids were stained with Calcein-AM (live cell stain) and PI. Z stacking was performed in a confocal microscope to visualize the live and dead cells in spheroids.

3.3 Results and Discussions

3.3.1 Preparation and characterization of FA-conjugated SeNPs

FAR-targeting was achieved by decorating FA on the surface of SeNPs. Initially, FA was conjugated to chitosan (CS) by well-established amine coupling reaction.[22] Presence of FA in FA-CS was confirmed by taking UV-visible absorption spectrum of FA-CS (**Figure 3.1A**), which demonstrated a characteristic peak at 285 from FA.[23] **Table 3.1** showed the amount of FA in FA-CS conjugates as estimated by spectrophotometry. At lowest FA:CS w/w ratio i.e. 0.25 (FA1-CS), FA-conjugation was found to be 36.2%. As amount of FA added to the reactions increased, increase in the % FA-conjugation was observed till 0.88 w/w FA:CS (FA4-CS). Adding more amount of the FA, as mentioned in FA5-CS, did not result in the increased FA-conjugation.

Consequently, FA4-CS was used to prepare FA-SeNPs for further experiments and referred as FA-CS, if not specifically mentioned otherwise. Conjugation of FA to CS was confirmed by FTIR spectroscopy (**Figure 3.1B**). The FTIR spectrum of FA showed characteristic absorption peaks at 1488 cm^{-1} and 1604 cm^{-1} due to stretching vibrations of C=C in the aromatic ring.[23] CS, in FTIR spectrum, demonstrated the typical peak at 1600 cm^{-1} with a shoulder around 1660 cm^{-1} corresponding to N-H bending and C=O stretching, respectively.[24] Along with this, FA-CS was observed to display new peaks at 1640 cm^{-1} and 1609 cm^{-1} due to the amidation between free NH of CS and COOH of FA and the presence of the benzene ring from FA, respectively.[23,25] The release of FA from FA-CS conjugate was measured in order to study the stability of FA-CS conjugation. Over a period of 10 days at room temperature, no release of FA was observed (**Figure 3.1C**).

Table 3.1 Conjugation of CS with different concentrations of FA.

Abbreviation	FA:CS ratio (w/w)	% of FA conjugated
FA1-CS	0.25	36.2
FA2-CS	0.5	31.8
FA3-CS	0.75	23.2
FA4-CS	0.88	22.9
FA5-CS	1.5	13.3

FA-CS was used to prepare FA-SeNPs with an appropriate polydispersity index (PDI) by following previously reported method. FA-SeNPs were prepared at varying concentrations of FA-CS and corresponding hydrodynamic diameter (d_H) as well as PDI were recorded in dynamic light scattering (DLS) instrument. **Figure 3.1E** and **Table 3.2** demonstrated that d_H and PDI of the FA-SeNPs were in the range of 72 nm - 96 nm and 0.06-0.18, respectively. Since PDI of FA-SeNPs prepared at all the FA-CS concentrations were in the

acceptable range (0.1-0.4) considered for monodispersed particles, the ones prepared at 0.015% of FA-CS were chosen for further studies. These FA-SeNPs demonstrated an average d_H of 72 nm and zeta potential (ζ) of −9.9 mV (**Figure 3.1E, 3.2A**). The FTIR spectrum of FA-SeNPs (**Figure 3.1B**) retained the peaks observed in FA-CS at 1600 cm^{-1} for N-H bending in CS as well as aromatic moiety of FA whereas the peak at 1640 cm^{-1} for amide bond was shifted to 1699 cm^{-1}.[23]

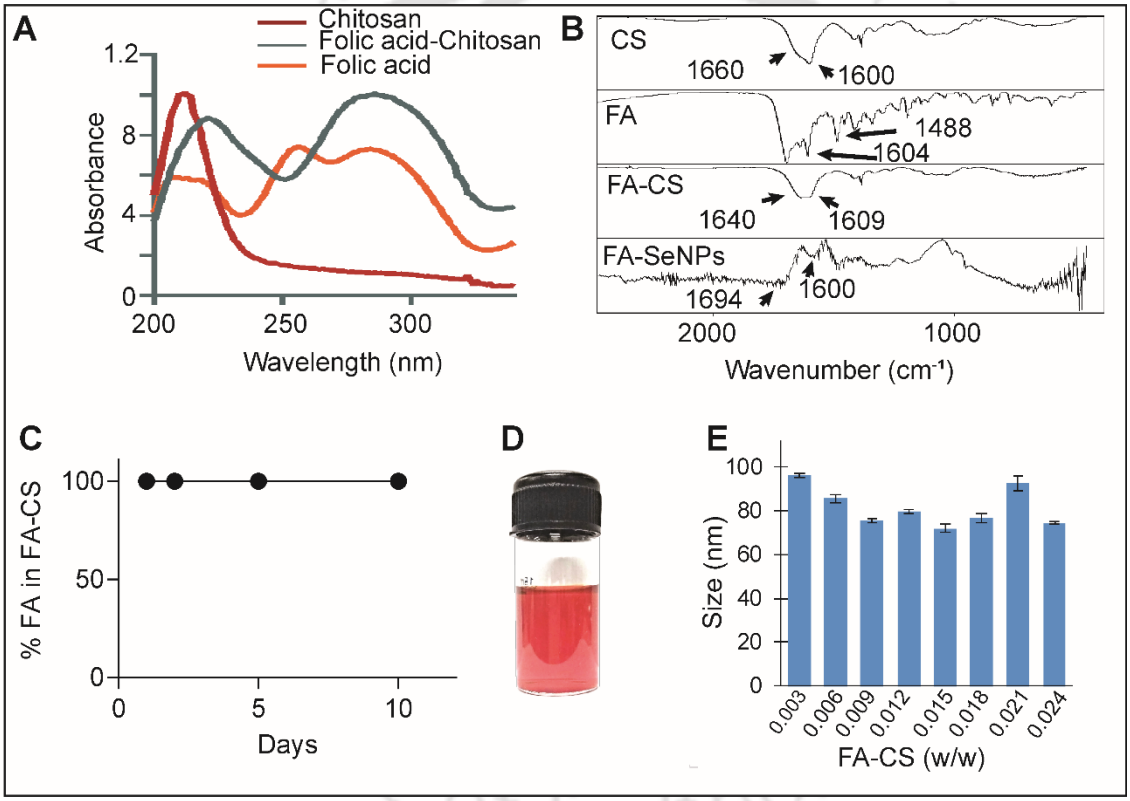

Figure 3.1 **(A)** UV-visible absorption spectra of CS, FA-CS, and FA. **(B)** FTIR spectra for CS, FA, FA-CS and FA-SeNPs, **(C)** % of FA retention in FA-CS conjugate calculated with a UV-visible spectrometer. **(D)** Photograph of FA-SeNPs suspension, **(E)** Hydrodynamic diameter for FA-SeNPs synthesized with different concentrations of FA-CS.

Table 3.2 Mean hydrodynamic diameter and PDI of FA-SeNPs synthesized with different concentrations of FA-CS.

% FA-CS	Mean Diameter	PDI
0.003	96.3 ± 0.8	0.111 ± 0.015
0.006	85.8 ± 1.7	0.063 ± 0.055
0.009	75.6 ± 0.8	0.125 ± 0.043
0.012	79.7 ± 1.0	0.207 ± 0.060
0.015	72.0 ± 1.7	0.142 ± 0.040
0.018	76.6 ± 2.0	0.169 ± 0.062
0.021	92.8 ± 3.3	0.188 ± 0.038
0.024	74.3 ± 0.5	0.068 ± 0.040

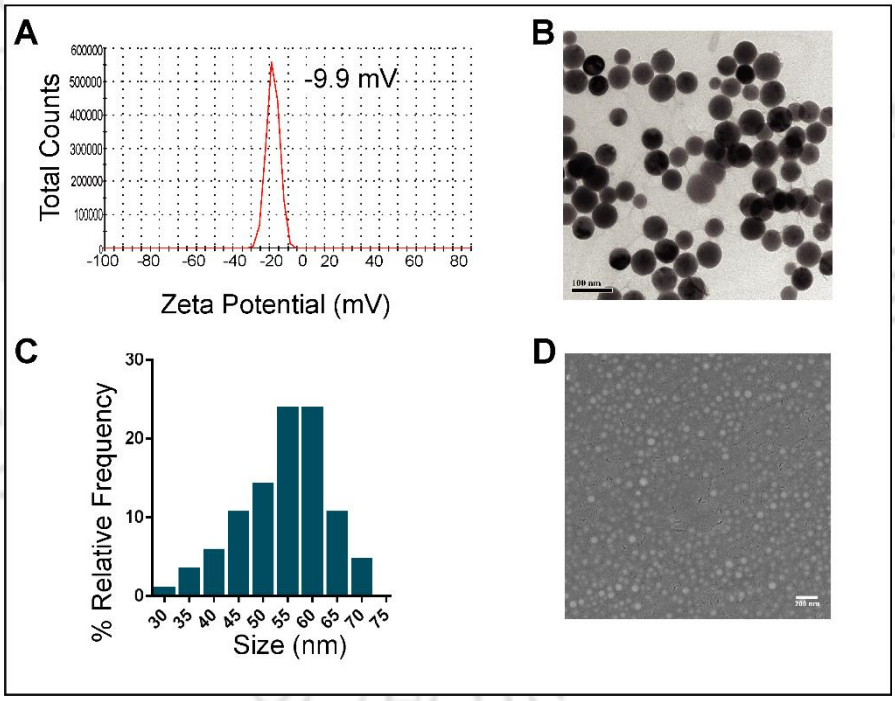

Figure 3.2 (**A**) Zeta potential (ζ) for FA-SeNPs, **(B)** TEM image showing spherical and dispersed FA-SeNPs (scale bar: 100 nm). (**C**) Average size of FA-SeNPs calculated from TEM micrograph. (**D**) FESEM image for FA-SeNPs (Scale bar: 200 nm).

Nanoparticles in the size range of 10-200 nm are considered excellent to attain successful enhanced permeability and retention (EPR) effect implying the potential of the present FA-SeNPs for passive targeting *in vivo*.[26] TEM analyses confirmed that well-dispersed spherical FA-SeNPs were synthesized (**Figure 3.2B**). From the TEM image, the average size of the FA-SeNPs was found to be 54 ±8 nm (estimated based on 100 NPs, **Figure 3.2C**), less than that obtained in DLS. The larger size reordered in DLS was due to the fact that, unlike TEM, DLS probes d_H of the FA-SeNPs in the hydrated state with the hydration layer being taken into consideration. TEM results were also supported by FESEM analysis (**Figure 3.2D**) showing non-aggregated round nanoparticles. Further, EDX analysis **(Figure 3.3A)** confirmed the presence of Se in the sample. Crystalline nature of the lyophilized FA-SeNPs was studied with X-ray diffractometer **(Figure 3.3B)**. XRD peaks 2θ below 30° indicates the FA-SeNPs were in amorphous or nano-crystalline. Phase analysis results revealed that selenium was present in the trigonal phase with lattice constants a= 4.3662 Å and c= 4.9536 Å.[27] The binding-energy profiles of both SeNPs and FA-SeNPs (**Figure 3.3C**), measured by X-ray photoelectron spectroscopy (XPS), showed characteristic peaks at 54.05eV (Se3d) confirming the valence of Se to be zero as well as the binding energy of Se3d to remained unaffected following FA decoration of the SeNPs.

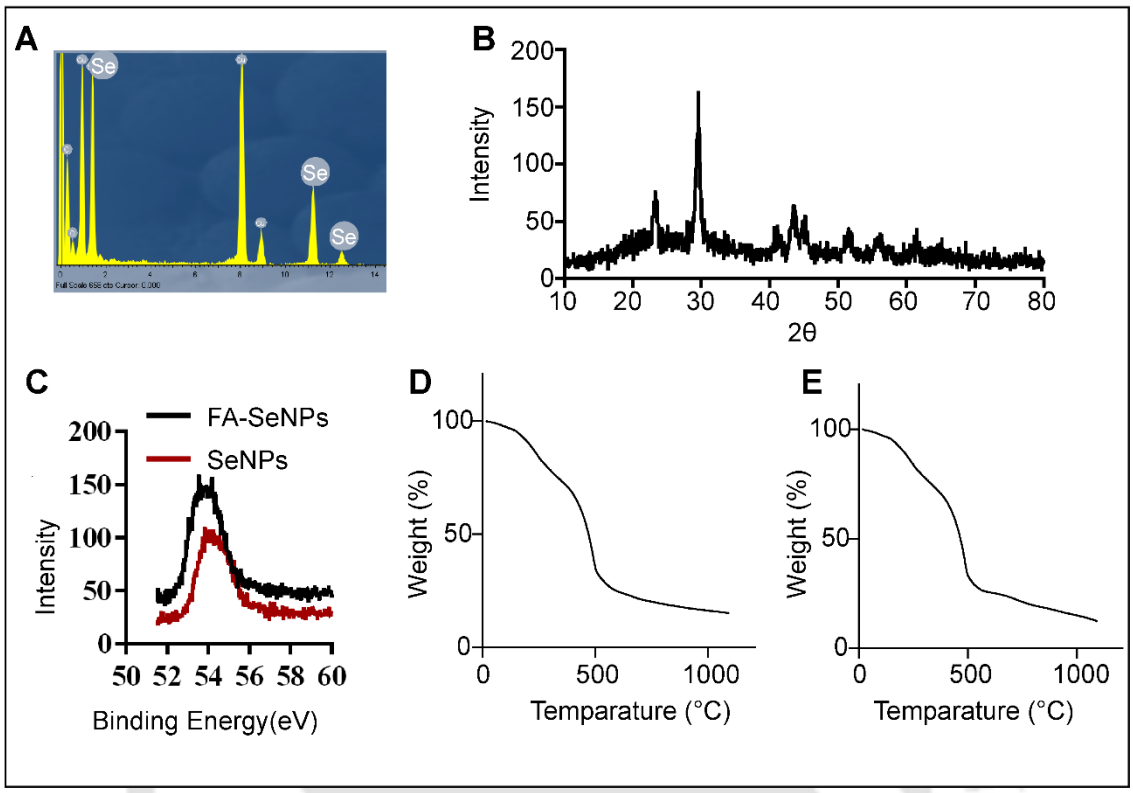

Figure 3.3 **(A)** EDX spectra showing Se peaks. **(B)** XRD analysis of FA-SeNPs. **(C)** XPS measurements for SeNPs and FA-SeNPs. TGA analysis of the FA-SeNPs (**D**) and SeNPs (**E**).

Thermal stability of the prepared SeNPs and FA-SeNPs was studied by thermogravimetric analysis (TGA) (**Figure 3.3 D,E**) which revealed that thermal decomposition occurred in three steps when heated through 1100 °C. In the first step around 100 °C, ca. 4% weight loss was observed possibly due to the removal of moisture from the sample. Further heating (100 °C to 400 °C) resulted in ca. 30% weight loss in the second step due to the decomposition of CS and FA-CS molecules. Thereafter, in the third step, a sharp increase in the percentage (%) weight loss was observed after 400 °C corresponding to the sublimation of the elemental Se leaving the residual mass of ca. 12%.

Table 3.3: Primer sequences used in during gene expression studies.

Gene	Forward	Reverse
GAPDH	GAAATCCCATCACCATCTTCCAGG	GAGCCCCAGCCTTCTCCATG
FOLR	GAGCTGCCTGCCAACCTTTC	GGCTGGGTCGAACCACATCT
Bax	GATGCGTCCACCAAGAAGCT	CGGCCCCAGTTGAAGTTG
Bcl-2	CATGTGTGTGGAGAGCGTCAA	GCCGGTTCAGGTACTCAGTCA
Bcl-xL	GGTCGCATTGTGGCCTTT	TCCGACTCACCAATACCTGCAT
BRAF	GCTTGCTCTGATAGGAAAATGAG	CTGTGGATCACACCTGCCTTA
BRAF-mut	CCCACTCCATCGAGATTTCT	

3.3.2 FA-SeNPs uptake by cancer cells

To aid in studying the internalization of FA-SeNPs by cancer cells, Rhodamine B (RhB) was loaded into FA-SeNPs as well as control SeNPs. In order to check the possible leakage of RhB from FA-SeNPs, the stability of RhB-loaded FA-SeNPs in the cell culture medium was investigated by fluorescence spectroscopy (**Figure 3.4A**). It was evident from **Figure 3.4A** that FA-SeNPs retained around 70% of the loaded dye after 20 h of incubation in the medium. Though RhB started leaching out considerably after 20 h incubation, it would not interfere with the uptake study, as all the uptake studies were performed within 6 h of incubation. Previous reports suggested that cancer cells internalized FA-decorated nanocarriers via FAR.[28] The expression of FAR in L132 (non-cancerous lung cells), A375 (melanoma) and MDA-MB-231 (breast cancer) cells was quantified by real-time PCR (**Figure 3.4B**), which revealed lower Ct (threshold cycles) values for FAR in MDA-MB-231 and A375 than L132 cells indicating higher expression of FAR in these cancer cells compared to L132 cells. Uptake efficiency of FA-SeNPs at different FA densities was studied. FA-SeNPs were prepared using FA1-CS to FA5-CS **(Table 3.1)** and denoted as FA1-SeNPs, FA2-SeNPs, FA3-SeNPs, FA4-SeNPs, and FA5-SeNPs, respectively. Uptake of these FA1- to FA5- FA-SeNPs by MDA-MB-231 and A375 cells after 6 h incubation was studied by flow cytometry. **Figure 3.4C, D** showed the histograms of RhB fluorescence-

emitting cells following incubation with FA1- to FA5-SeNPs, while **Figure 3.4E** depicted the calculated % uptake of these FA-SeNPs relative to SeNPs.

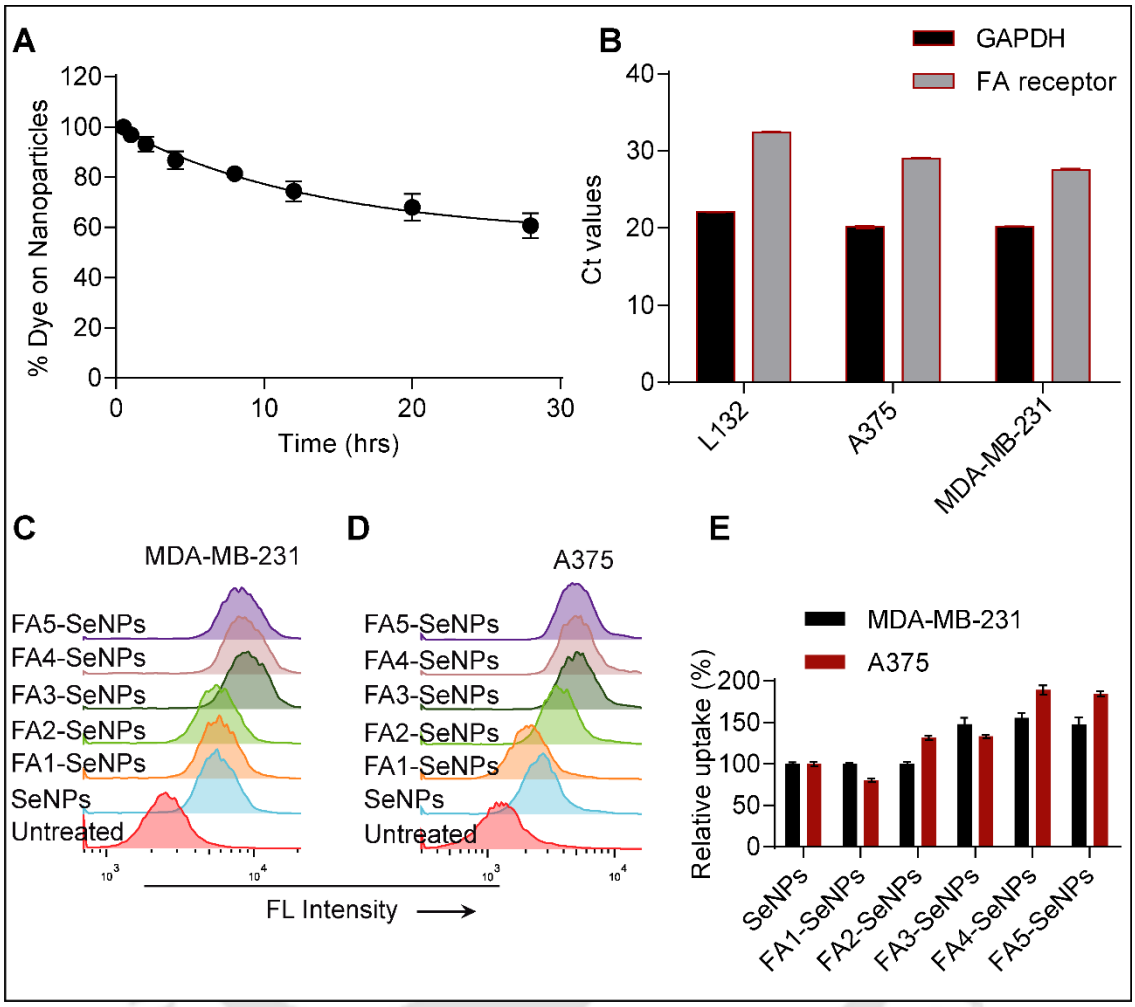

Figure 3.4 (**A**) Stability testing of the Rhodamine B dye loaded on FA-SeNPs, (**B**) Real-time PCR data showing expression of the folic acid receptor in MDA-MB-231, A375 and L132 cells. (**C, D**) Flow cytometric uptake study of the FA-SeNPs with different FA-density in MDA-MB-231 and A375 cells. (**E**) Relative uptake of FA-SeNPs with different FA-densities as compared to SeNPs.

From **Figure 3.4E,** it was observed that uptake of FA-SeNPs gradually increased up to FA4-SeNPs, possibly due to the increasing density of FA on their surfaces. However, FA5-SeNPs did not show any further increase in the uptake due to the similar surface FA density as that of FA4-SeNPs. To gain further insights of the uptake, a competitive FA receptor inhibition experiment

was designed where cells were pre-treated with free FA before the treatment with dye-loaded FA4-SeNPs. The histograms from flow cytometry data demonstrated increased fluorescence intensity of the FA-SeNPs–treated MDA-MB-231 (**Figure 3.5A, B**) and A375 (**Figure 3.5C, D**) cells as compared to L132 cells (**Figure 3.5E, F**), confirming the higher degree of FA-SeNPs internalization by MDA-MB-231 and A375 cancer cells. Pretreatment with FA reduced the FA-SeNPs uptake in cancer cells to a level almost comparable to that with non-targeted control SeNPs. Uptake of SeNPs was remained unaffected in non-cancerous L132 cells irrespective of FA-pretreatment or FA-functionalization indicating FAR-mediated internalization of FA-SeNPs by cancer cells.

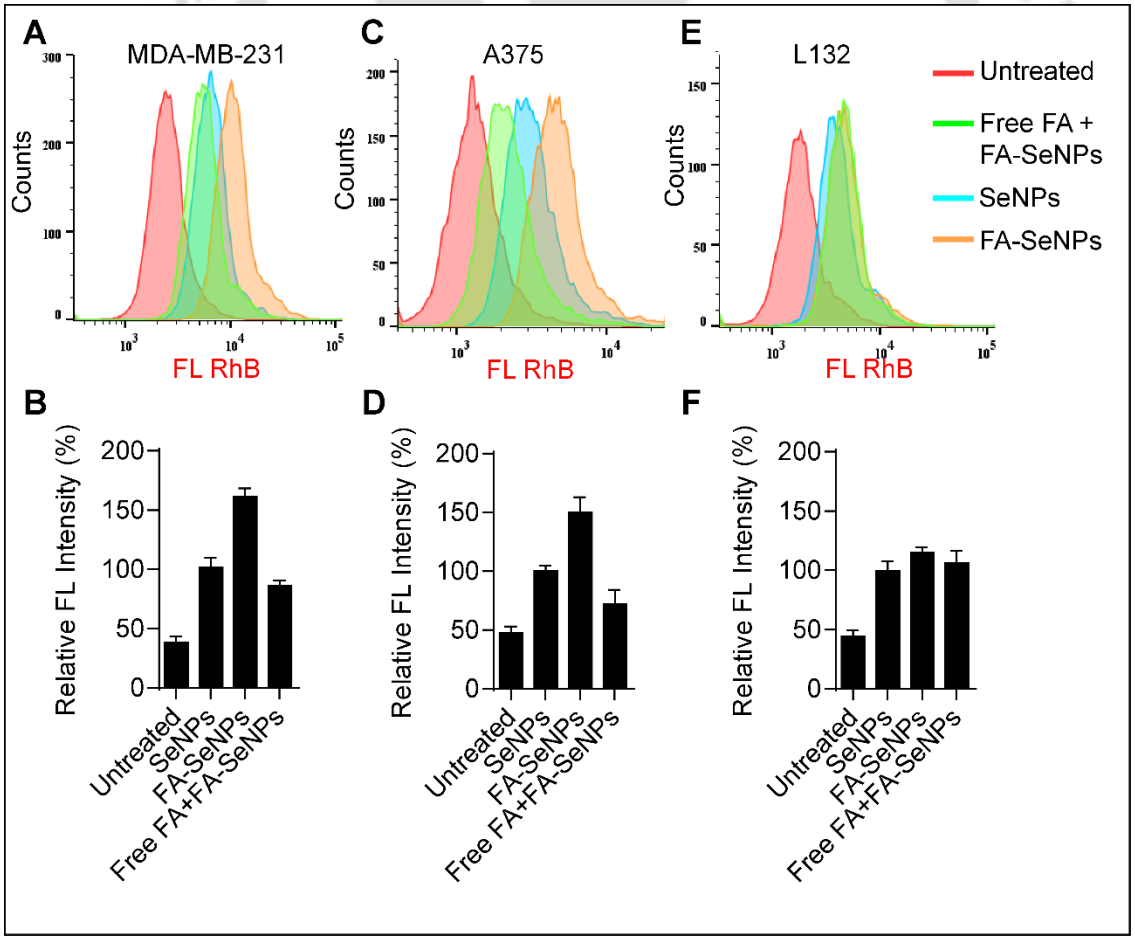

Figure 3.5 Flow-cytometric histograms of **(A)** MDA-MB-231, (**C**) A375 and **(E)** L132 showing fluorescence of untreated, SeNPs, free FA+FA-SeNPs and FA-

SeNPs treated samples. (**B)**, (**D),** and (**F)** show % relative fluorescence intensities with respect to SeNPs-treated cells calculated from histograms of MDA-MB-231, A375 and L132 cells, respectively.

Confocal laser scanning microscopic (CLSM) imaging of treated MDA-MB-231 (**Figure 3.6A**) and A375 cells (**Figure 3.6B**) clearly showed the presence of RhB-loaded FA-SeNPs in the cytoplasm of the cells following the treatment. Furthermore, *Z*-stacked images of the treated cells (**Figure 3.7A, B**) confirmed the successful internalization of RhB-loaded FA-SeNPs. In order to explore the mechanism of FA-SeNPs internalization, uptake studies were performed at varying experimental conditions – incubating the cells with RhB-FA-SeNPs at 4 ºC, and pretreating the cells with sodium azide before incubation with RhB-FA-SeNPs at 37 ºC.

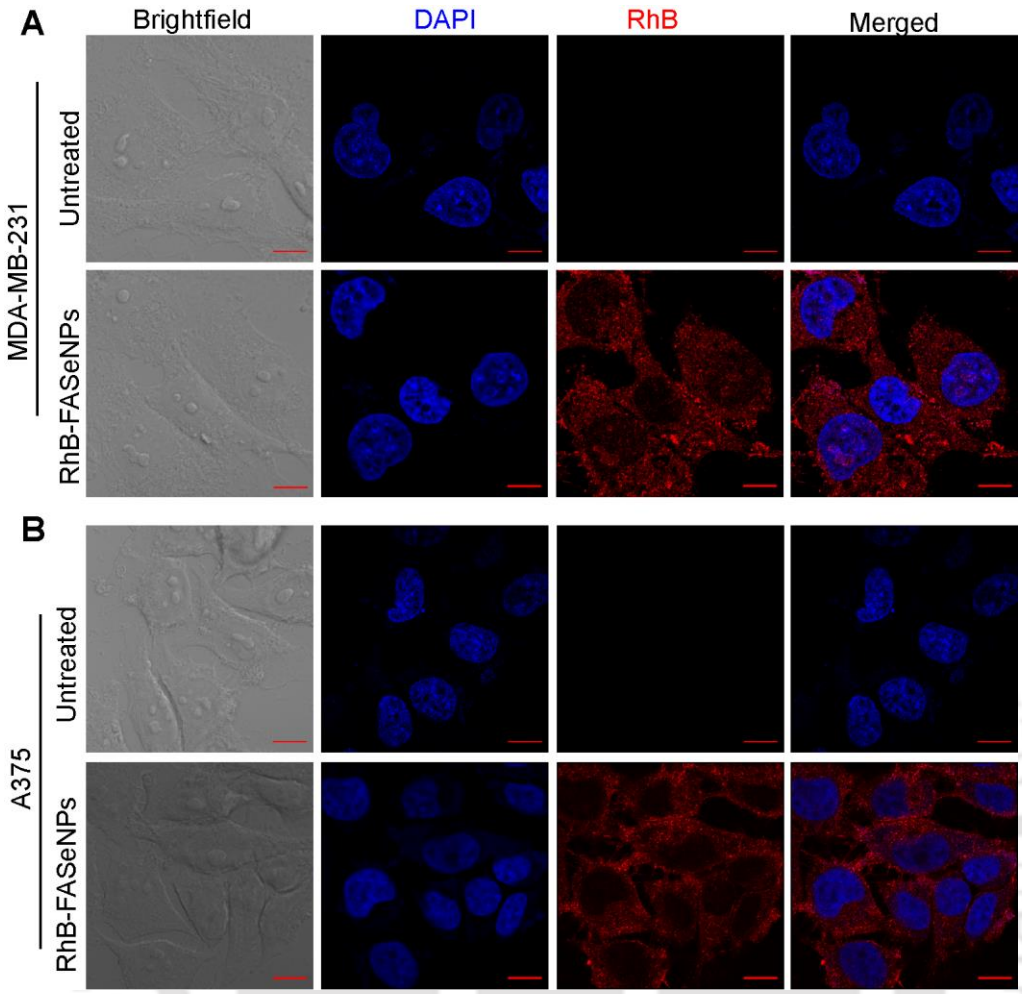

Figure 3.6 Confocal microscopic images of the uptake of RhB loaded FA-SeNPs in **(A)** MDA-MB-231 and **(B)** A375 cells showing the internalization of the nanoparticles inside (Size bar- 10 µm).

The cellular uptake (%) was quantified based on RhB fluorescence considering the uptake in control cells – cells incubated with RhB-FA-SeNPs at 37^{0}C – as 100% **(Figure 3.7C, D)**. In both the cell types, A375 and MDA-MB-231, uptake at 4 ^{o}C or sodium azide pre-treated cells was reduced by more than 60% indicating energy-dependent active uptake of FA-SeNPs involving FAR-mediated endocytosis.

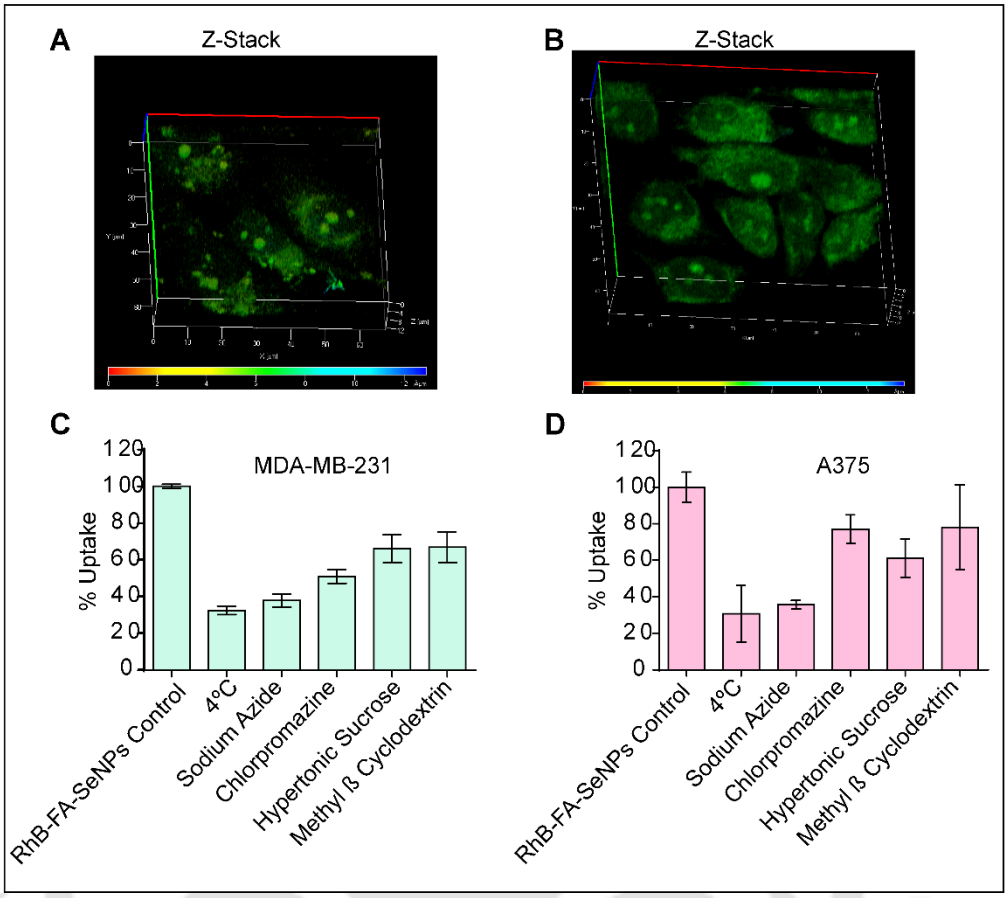

Figure 3.7 (**A**, **B**) *Z*-stacks showing the internalization of the nanoparticles inside **(A)** MDA-MB-231 and **(B)** A375 cells. Uptake (%) of FA-SeNPs in presence of endocytic pathway inhibitors for **(C)** MDA-MB-231 and **(D)** A375 cells.

FAR-mediated endocytosis of FA-SeNPs could occur via two pathways – clathrin-mediated and caveolin-mediated. To further confirm the uptake mechanism, cells were pre-treated with inhibitors of clathrin- or caveolin-mediated endocytic pathway for 4 h and subsequently allowed to internalize RhB-loaded FA-SeNPs for 2 h. Since both A375 and MDA-MB-231 cells were non-phagocytic, no inhibitors were used to study phagocytosis pathway. Inhibitors of the clathrin-mediated pathway, chlorpromazine and sucrose reduced the uptake of the FA-SeNPs as compared to FA-SeNPs control indicating that internalization was occurring via a clathrin-mediated pathway.

3.3.3 Cell viability assay

MTT-based viability assays were carried out to study the anti-proliferative effects of PD98, FA-SeNPs, and their combinations. Before studying the effect of the PD98 on these cells, it was important to confirm whether these cells were positive for BRAF mutations. ARMS-PCR assay was performed on L132 and A375 cells. Forward and reverse primers were designed to amplify 623 bp product containing BRAF DNA. Introducing a third mutation specific primer into the PCR reaction gave a PCR product of 143 bp confirming the BRAF gene mutation. From PCR results in **Figure 3.8**, it was observed that L132 cells (without BRAF mutation) showed the product of 623 bp only while A375 cells demonstrated two products of 623 bp and 143 bp.

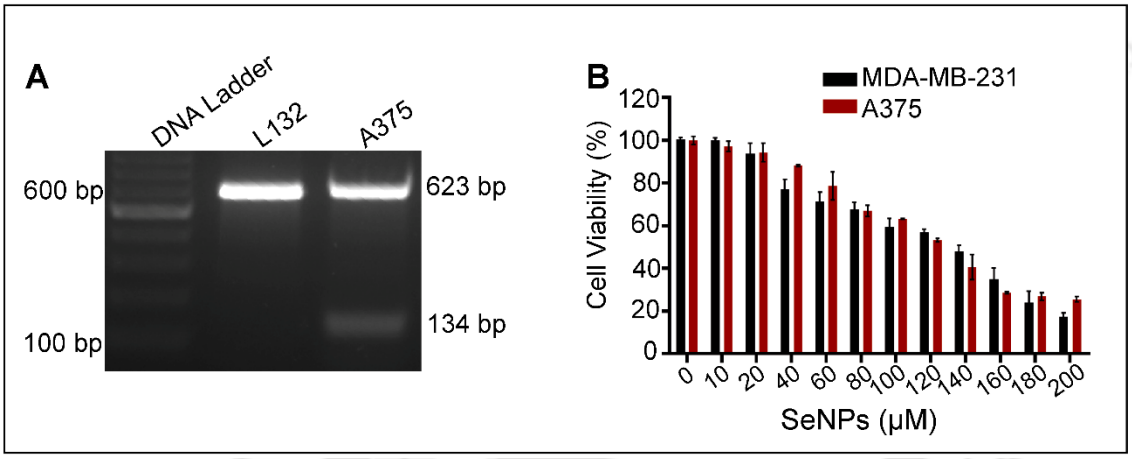

Figure 3.8 (**A**) ARMS-PCR results for detection of BRAF mutations in L132 and A375 cells. (**B**) MTT assay results for SeNPs treated MDA-MB-231 and A375 cells.

These results suggested that A375 cells possessed mutations in the BRAF gene, while L132 cells could serve as a negative control for the mentioned mutation. Similarly, MDA-MB-231 cells also possess G13D, G464V mutation in KRAS and BRAF gene respectively, which are extensively reported in the literature.[15,29]

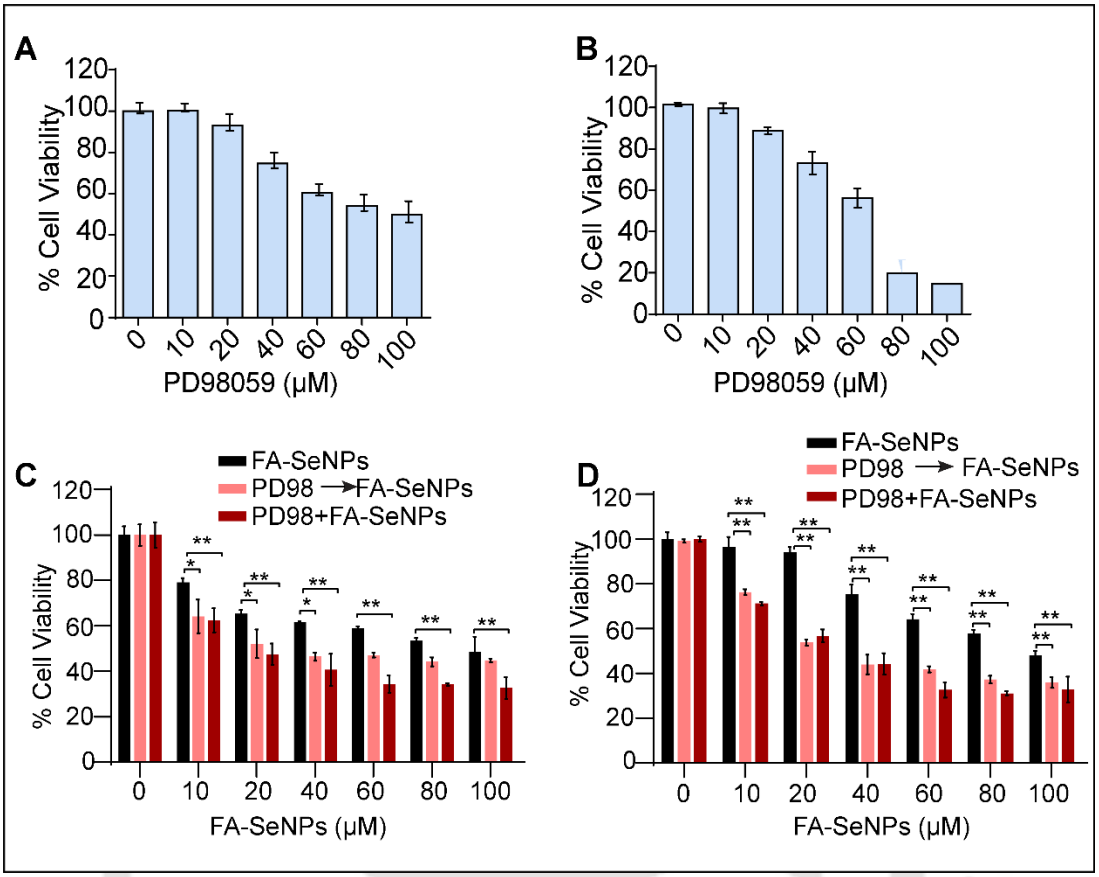

Figure 3.9 Anti-proliferative effect of PD98 on (**A**) MDA-MB-231 and (**B**) A375 cells. Cell viability of (**C**) MDA-MB-231 and (**D**) A375 cells after FA-SeNPs, PD98→FA-SeNPs and PD98+FA-SeNPs treatment. (Data shown as Mean ±SD, n=3. p<0.001, p<0.0001 are denoted as * and ** respectively with reference to FA-SeNPs.)

The proliferation of A375 and MDA-MB-231 cells, following the treatment with varying concentrations of PD98 for 48 h, were observed to decrease in a concentration-dependent manner (**Figure 3.9A & B**). The corresponding IC_{50} values for PD98 treatment were found to be 107 ±7 μM and 60 ±5 μM in MDA-MB-231 and A375 cells, respectively. Similarly, non-targeted control SeNPs **(Figure 3.8B)** were also able to inhibit the proliferation of MDA-MB-231 and A375 cells with IC_{50} values of 118 ±4 μM and 120 ±5 μM. Most importantly, FA-SeNPs treatment reduced the cell viability in both MDA-MB-231 and A375 cells in a dose-dependent fashion with IC_{50} values of 98 ±11 μM and 103 ±5

μM, respectively. The IC_{50} values for SeNPs were higher than those of FA-SeNPs, indicating the targeting ability of the FA-SeNPs towards MDA-MB-231 and A375 cells.

Two treatment strategies were adopted in order to study the combined effect of PD98 and FA-SeNPs on cell proliferation: (1) pretreating the cells with 10 μM PD98 for 10 h followed by treatment with varying concentrations of FA-SeNPs for 48 h (referred as PD98→FA-SeNPs) and (2) treating the cells simultaneously with 10 μM PD98 and varying concentrations of FA-SeNPs for 48 h (referred as PD98+FA-SeNPs). Concentration of 10 μM (as well as 10 h pretreatment) for PD98 was chosen as this was the minimum tested concentration of PD98 that was able to elicit anti-proliferative response as well as a decrease in phospho ERK1/2.[30] From **Figure 3.9C & D**, it was evident that the pretreatment with PD98 enhanced the anti-proliferative efficacy of FA-SeNPs against the cancer cells. Further analyses revealed that PD98-pretreatment resulted in the lowering of IC_{50} values of FA-SeNPs from 98 ±11 μM to 38 ±5 μM in MDA-MB-231 cells and from 103 ±5 μM to 36 ±1 μM in A375 cells. Similarly, co-treatment (PD98+FA-SeNPs) was also found to augment the anti-proliferative response of FA-SeNPs (**Figure 3.9C & D)** with calculated IC_{50} values of 20±4 μM and 31±2 μM in treated MDA-MB-231 and A375 cells, respectively.

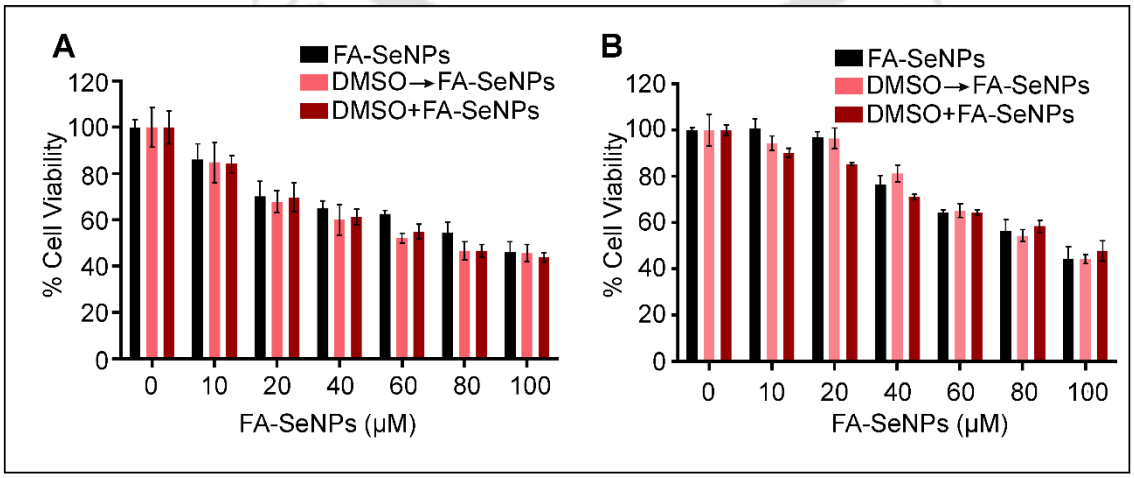

Figure 3.10 Effect of the DMSO pre-treatment on FA-SeNPs treatment was studied by MTT assay. **(A)** MDA-MB-231 and **(B)** A375 cells showing cell viability for FA-SeNPs with pretreatment of DMSO (DMSO→FA-SeNPs) or in a combination of DMSO (DMSO+FA-SeNPs).

The appropriate control experiments with DMSO (**Figure 3.10**), the solvent carrier for PD98, revealed that DMSO (at 0.1% v/v) did not affect cell viability confirming the role of only PD98 in influencing the anti-proliferative effect of FA-SeNPs in combined treatment. The results of combined treatment suggested that PD98 and FA-SeNPs together could inhibit the proliferation of cancer cells more efficiently as compared to that of either PD98 or FA-SeNPs individually. Hence, the Chou-Talalay method was employed to study the isobologram for the potential synergistic behavior of PD98 and FA-SeNPs.[31] The isobologram (**Figure 3.11A-D**) revealed the combination index values for IC_{50} concentrations of PD98→FA-SeNPs and PD98+FA-SeNPs treatment to be less than 1, confirming that FA-SeNPs and PD98 acted synergistically to inhibit the growth of MDA-MB-231 and A375 cells.

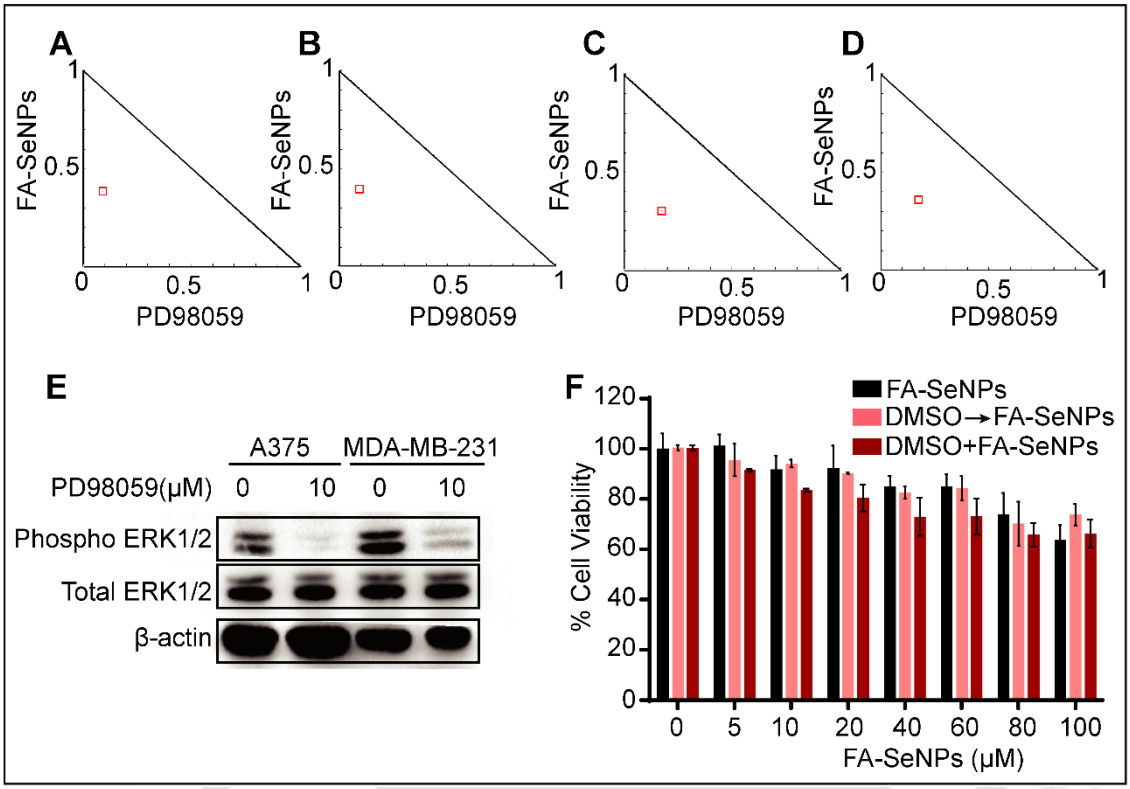

Figure 3.11 Isobologram for **(A)** PD98→FA-SeNPs@20 and **(B)** PD98+ FA-SeNPs@20 treated MDA-MB-231 cells. Isobologram for **(C)** PD98→ FA-SeNPs@20 and **(D)** PD98+ FA-SeNPs@20 treated A375 cells. (**E**) Western blots showing a decrease in phospho ERK1/2 level after treatment with PD98. (**F**) MTT assay results showing cell viability in non-cancerous L132 cells.

The reason behind the synergistic behavior of PD98 and FA-SeNPs was the inhibition of the MAPK pathway in MDA-MB-231 and A375 cells. Both MDA-MB-231 and A375 cells have mutations in BRAF gene, which activate MEK1/2 resulting in the constitutive phosphorylation of ERK1/2. The phosphorylated-ERK1/2 subsequently causes the uncontrolled proliferation and is associated with lung cancer, colon cancer, breast cancer, and melanoma.[11] PD98 is a MEK inhibitor thus signaling of MAPK pathway was blocked at MEK level thereby decreasing the phosphorylation of the ERK1/2. Western blots were performed for phosphorylated ERK1/2 and total ERK1/2 to confirm whether PD98 was able to inhibit the signaling in the present study. From the blots **(Figure 3.11E),** it was observed that treatment with PD98

indeed decreased the phospho-ERK1/2 levels. From MTT data and the decreased phosphorylation of the ERK1/2, it was inferred that PD98 inhibited aberrant MAPK signaling above ERK1/2 while the simultaneous supply of another therapeutic molecule in the form of FA-SeNPs synergistically inhibited the proliferation of MDA-MB-231 and A375 cancer cells. Similar viability assays performed on non-cancerous L132 cells (**Figure 3.11F**), did not demonstrate significant variations in cell viability among FA-SeNPs and combined treatment groups. This could be attributed to the lower expression of the FAR on L132 cells and higher susceptibility of rapidly dividing cancer to therapeutic molecule than normal cells.

3.3.4 PD98 and FA-SeNPs combinedly induce apoptosis

As mentioned in 2nd chapter , the generation of the reactive oxygen species in SeNP-treated HeLa and MCF-7 cells was observed as one of the important driving factors for apoptosis in those cancer cells.[32] In the pursuit of elucidating the mechanism of cell death, flow cytometry-based DCFDA assay was performed to detect ROS generation in treated MDA-MB-231 and A375 cells. From the results of flow-cytometric analyses **(Figure 3.12A, B)**, it was observed that PD98 alone was not able to produce any ROS. However, an increase in the FL intensities in cancer cells (MDA-MB-231 as well as A375) treated with FA-SeNPs@20 alone or in combination with PD98 clearly indicated the potential of ROS generation. As expected, bare SeNPs and FA-SeNPs at 100 μM showed significantly pronounced ROS generation.

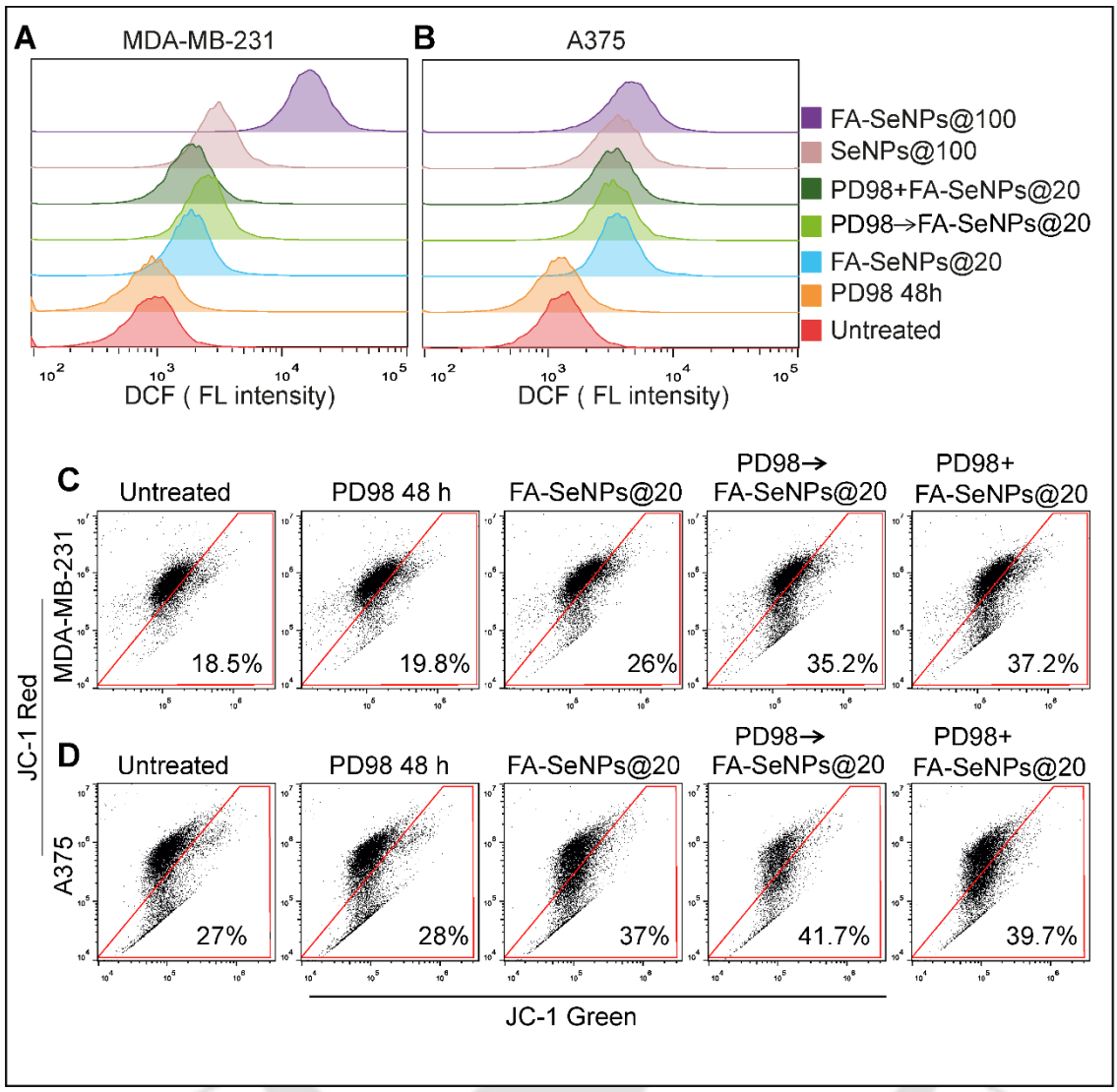

Figure 3.12 (**A**, **B**) DCFDA assay results for the detection of ROS in MDA-MB-231 and A375 cells. JC-1 assay for mitochondrial membrane integrity in treated MDA-MB-231 (**C**) and A375 (**D**) cells.

Increased ROS levels in the cellular environment results in critical damage to intracellular proteins. Additionally, the detrimental effect of elevated level of ROS affects on the integrity of mitochondrial membrane and associated trans-membrane potential, ultimately culminating in the induction of apoptotic cell death.[33] The effect of the ROS on the integrity of mitochondrial membrane in FA-SeNPs treated cancer cells in the present study was assessed by JC-1 based flow cytometric assay. Cationic JC-1 forms red aggregates in

polarised mitochondria, whereas it remains as a monomer in depolarised mitochondria. Flow cytometric analysis **(Figure 3.12C,D)** revealed untreated cells showing predominant red fluorescence from healthy mitochondria but treated samples including FA-SeNPs@20, PD98→FA-SeNPs@20 and PD98+FA-SeNPs@20 showed an increase in green fluorescence suggesting the alteration in the mitochondrial membrane potential.

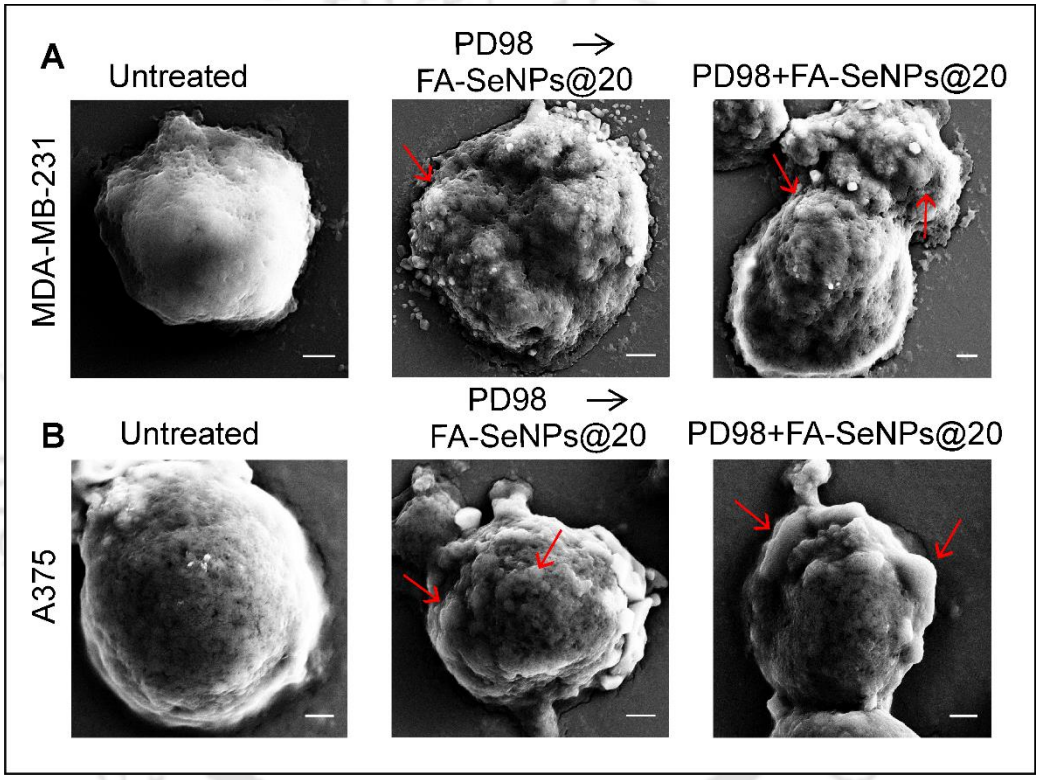

Figure 3.13 FESEM images of **(A)** MDA-MB-231 and (**B**) A375 cells before and after treatment. Membrane blebbing in treated cells is indicated by red arrows.

Nuclear condensation followed by DNA fragmentation and membrane blebbing are considered important characteristics of the apoptotic cells.[34] The morphological changes in the treated cells were first examined by FESEM in order to explore the mode of cell death in cancer cells caused by the combined treatment of 10 μM PD98 and 20 μM FA-SeNPs (FA-SeNPs@20). FESEM images demonstrated membrane blebs in treated MDA-MB-231 and A375 cells

(**Figure 3.13A, B**) suggesting apoptotic cell death. Subsequently, nuclear staining by Hoescht-33423 was performed to study the nuclear changes in the treated cells. As shown in **Figure 3.14,** untreated cells were observed to have a round nucleus with evenly distributed DNA. However, some of PD98→FA-SeNPs@20 and PD98+FA-SeNPs@20 treated cells showed condensed or pycnotic nuclei indicating apoptosis in progression.

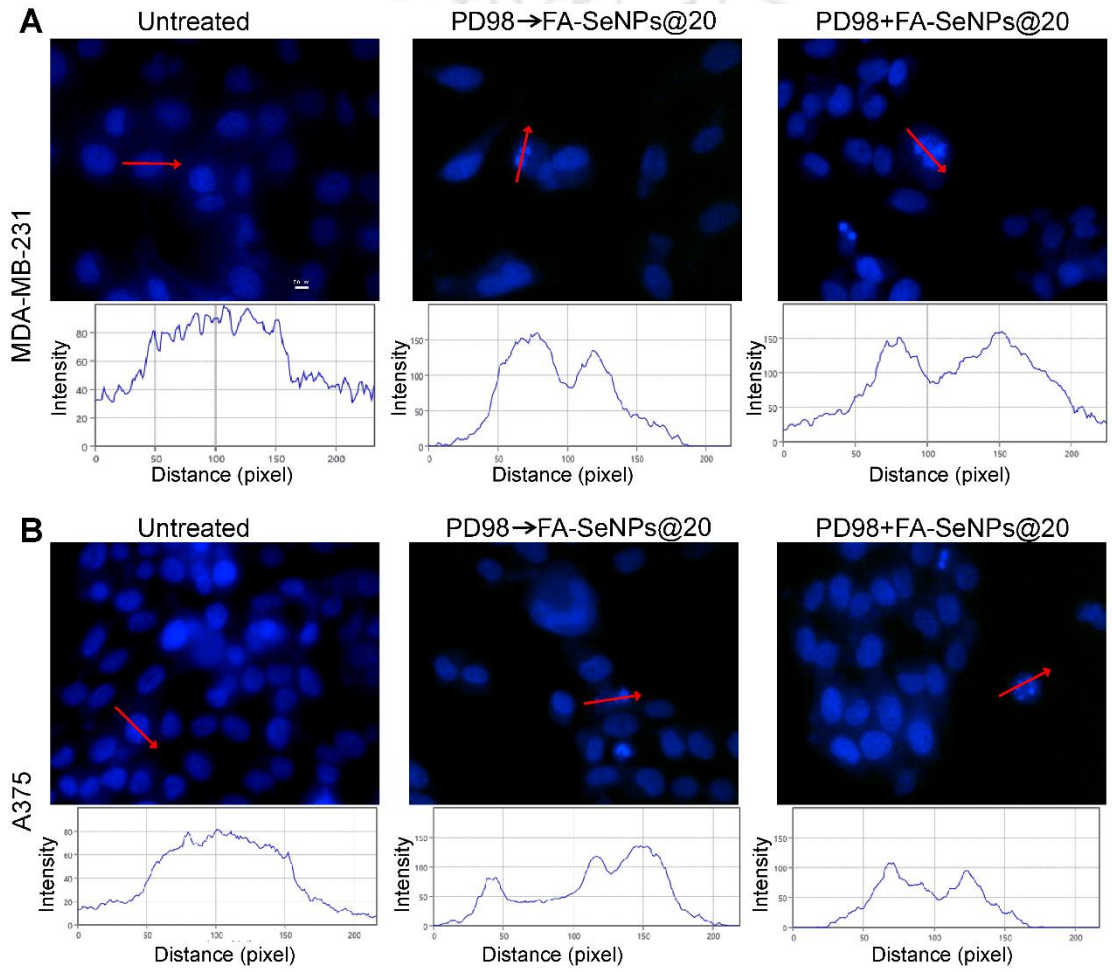

Figure 3.14 (A, B) Nuclear staining by Hoechst 33342 for MDA-MB-231 (**A**) and A375 (**B**) cells. Fluorescent Intensity profiles of the untreated and treated cells are included below the image.

In apoptotic cells, chromatin condensation is generally followed by DNA fragmentation which was studied by comet assay in the present study. As a

representation of DNA damage, comet tail moments (TM) were calculated and presented in **Figure 3.15**. TM for untreated MDA-MB-231 cells was found to be 10. Interestingly, TM increased to 22 and 20 in case of PD98→FA-SeNPs@20 and PD98+FA-SeNPs@20 treatment, respectively, demonstrating DNA fragmentation in MDA-MB-231 cells because of combined treatment.

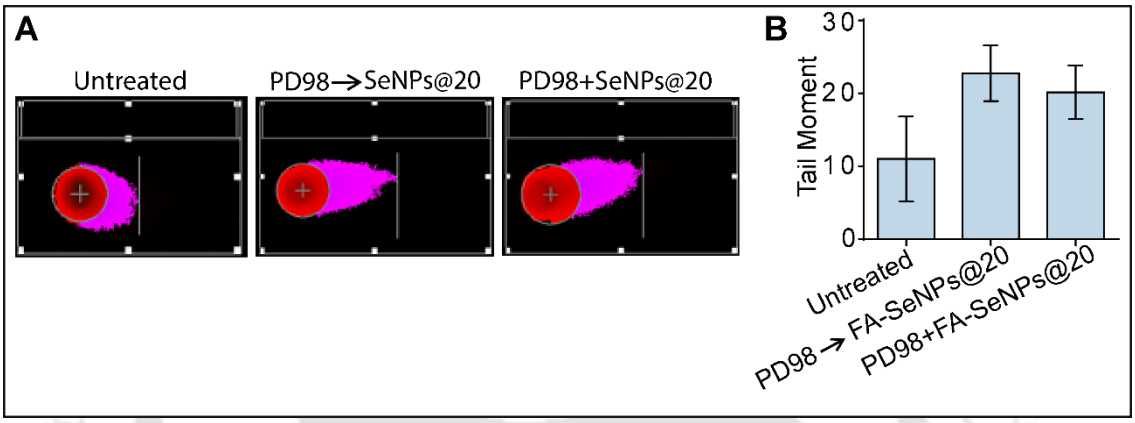

Figure 3.15 Comet assay results (**A**) and Tail Moment values (**B**) from comet assay indicating DNA fragmentation in treated MDA-MB-231 cells.

Apoptosis involves the activation of various initiator and executioner caspases. Executioner caspases including caspase-3 further cause cleavage of cellular proteins leading to cell death. Activation of caspase-3, through its cleavage by initiator caspases, is considered as a marker for apoptosis. Furthermore, the cleaved caspase-3 later cleaves poly (ADP-ribose) polymerase-1 (PARP1) in the final step of the apoptotic signaling pathways. Herein, the presence of cleaved caspase-3 and cleaved PARP1 in treated cancer cells was checked by Western blot. The Western blot (**Figure 3.16A, B)** did not show any band corresponding to cleaved caspase-3 or cleaved PARP1 indicating non-activation of the caspase-3 in untreated as well as PD98-treated cells. However, following PD98→FA-SeNPs@20 and PD98+FA-SeNPs@20 treatment, the presence of cleaved caspase-3 and cleaved PARP1 were detected in both MDA-MB-231 and A375 cells.

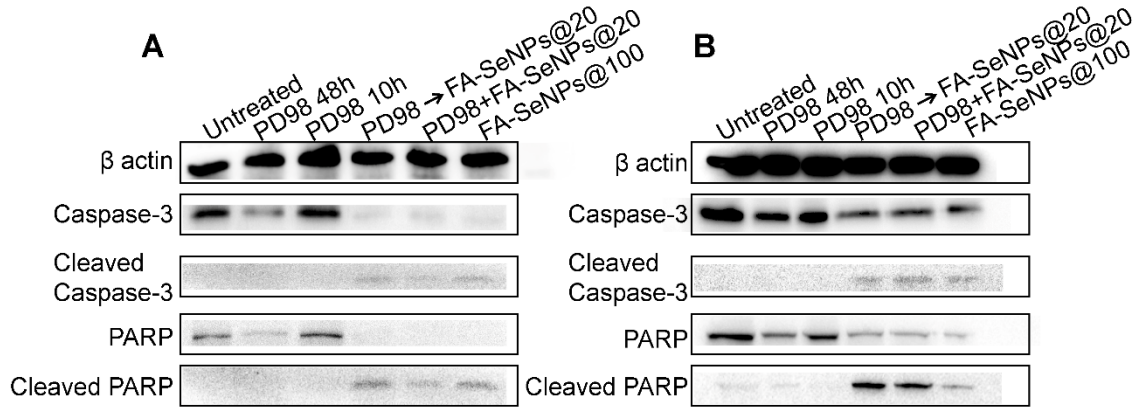

Figure 3.16 Western blots of whole extracts from treated (**A**) MDA-MB-231 and (**B**) A375 showing an intact and cleaved form of caspase-3 and PARP.

The result of Western blot analyses strongly indicated the potential of combined treatment with PD98 and FA-SeNPs@20 for inducing apoptosis in MDA-MB-231 and A375 cells. Bcl-2 family of proteins having pro- and anti-apoptotic roles are the regulators of the apoptosis. Increased expression of pro-apoptotic genes like Bax and Bak leads to decrease in the expression of anti-apoptotic proteins including Bcl-2 and Bcl-xL. The expression of Bcl-2 family genes in treated MDA-MB-231 cells in the present study was examined at the mRNA level via semi-quantitative PCR method. It can be observed from **Figure 3.17A** that, as compared to untreated cells, expression of Bax was increased in PD98→FA-SeNPs@20 and PD98+FA-SeNPs@20 treated MDA-MB-231 cells with a concomitant decrease in Bcl-2 and Bcl-xL expressions. In this regard, it may be noted that increased levels of the Bcl-2 and Bcl-xL expression can lead to inhibition of the apoptosis, as observed in drug-resistant tumors.[35,36] In addition to the expression of pro- and anti-apoptotic proteins, ERK1/2 activity in PD98→FA-SeNPs@20 and PD98+FA-SeNPs@20 treated cells was also studied by Western blot. From Western blot results for both A375 and MDA-MB-231 cells (**Figure 3.17A,B**), it was evident that PD98 was able to reduce the phospho-ERK1/2 levels in PD98→FA-SeNPs@20 and

PD98+FA-SeNPs@20 treated cells. As the excessive ERK1/2 activity is related to the enhanced proliferation, and PD98 was able to inhibit the phospho-ERK1/2, it can be concluded that the inhibition of the MAPK pathway leads to sensitization towards FA-SeNPs, as seen in viability assays.

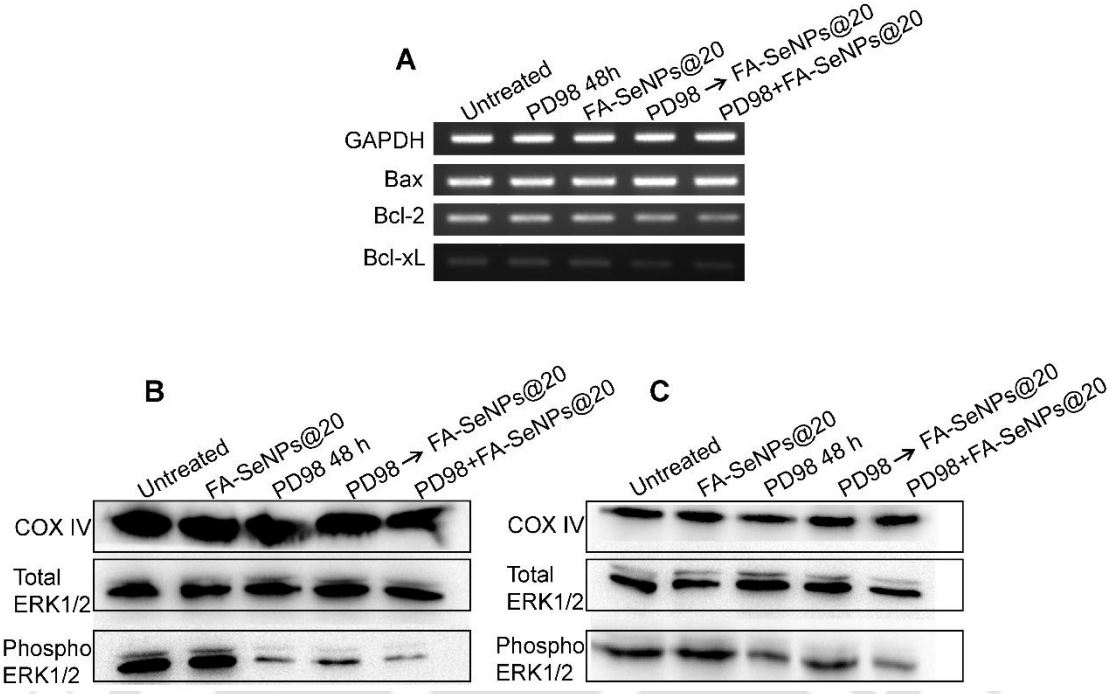

Figure 3.17 (**A**) Polymerase chain reaction results for studying the expression of the genes from Bcl-2 family in treated MDA-MB-231 cells. Western blotting results for treated MDA-MB-231 (**B**) and A375 (**C**) cells.

The contribution of apoptosis in synergistic killing of cancer cells by combined treatment of PD98 and FA-SeNPs was finally confirmed and quantified by flow cytometry. The results of flow cytometric analyses, shown in **Figure 3.18** and **3.19,** revealed that the induction of apoptosis by DMSO (solvent carrier for PD98), PD98 (at 10 μM) and FA-SeNPs at 20 μM (FA-SeNPs@20) were insignificant. However, the combined treatment – both PD98→FA-SeNPs@20 and PD98+FA-SeNPs@20 – showed a significant increase in apoptosis in MDA-MB-231 cells with an apoptotic population of 25.6% and 22.1%, respectively. Similarly, PD98→FA-SeNPs@20 and

PD98+FA-SeNPs treatment in A375 cells resulted in 46% and 56% apoptotic cells. Moreover, it was observed that a much higher concentration of 100 μM (FA-SeNPs@100) was required for FA-SeNPs alone to achieve a similar degree of apoptosis observed in combination treatment in cancer cells, indicating that a heightened apoptosis induction could be achieved at a lower concentration of FA-SeNPs when employed in combination with PD98.

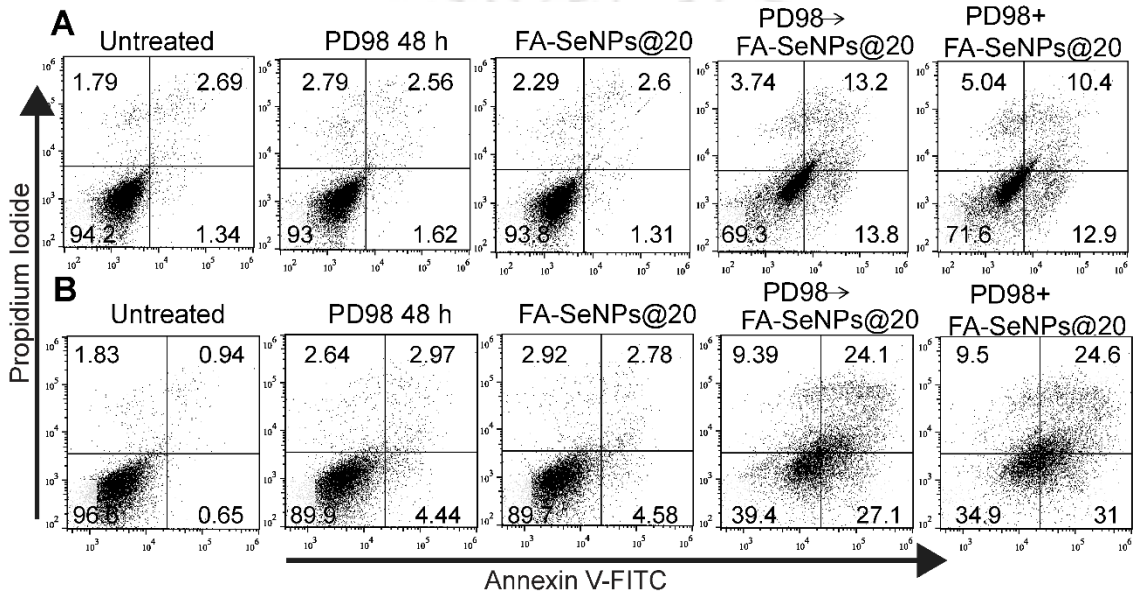

Figure 3.18 Flow cytometric analyses of the apoptotic population in treated (**A**) MDA-MB-231 and (**B**) A375 cells as probed by annexin-V-FITC and PI assay.

The flow cytometric analyses essentially indicated that, though PD98 and FA-SeNPs@20 individually could not induce apoptosis, PD98 might sensitize the cancer cells toward FA-SeNPs-mediated apoptosis resulting in the synergistic killing of the cancer cells in a combination mode of treatment. However, the exact mechanism of the synergistic behavior of PD98 and FA-SeNPs with possible cross-talk of individual pathways in inducing apoptosis in the present study remained unclear and needs to be elucidated in future studies. Nonetheless, as already mentioned, previous reports demonstrated the association of the MAPK pathway with cell survival and prevention of

apoptosis in cancer cells. An additional mechanism of synergistic response could arise from the PD98-mediated inhibition of ERK1/2 activation which might lead to reduced expression of P-glycoproteins and thereby down-regulating the nanoparticle efflux associated with drug resistance in tumor cells. In this regard, previous studies also demonstrated that combined treatment of PD98 and cytotoxic drugs significantly improved the apoptotic potential in spite of minimal apoptosis response with sole treatment with PD98.[37,38]

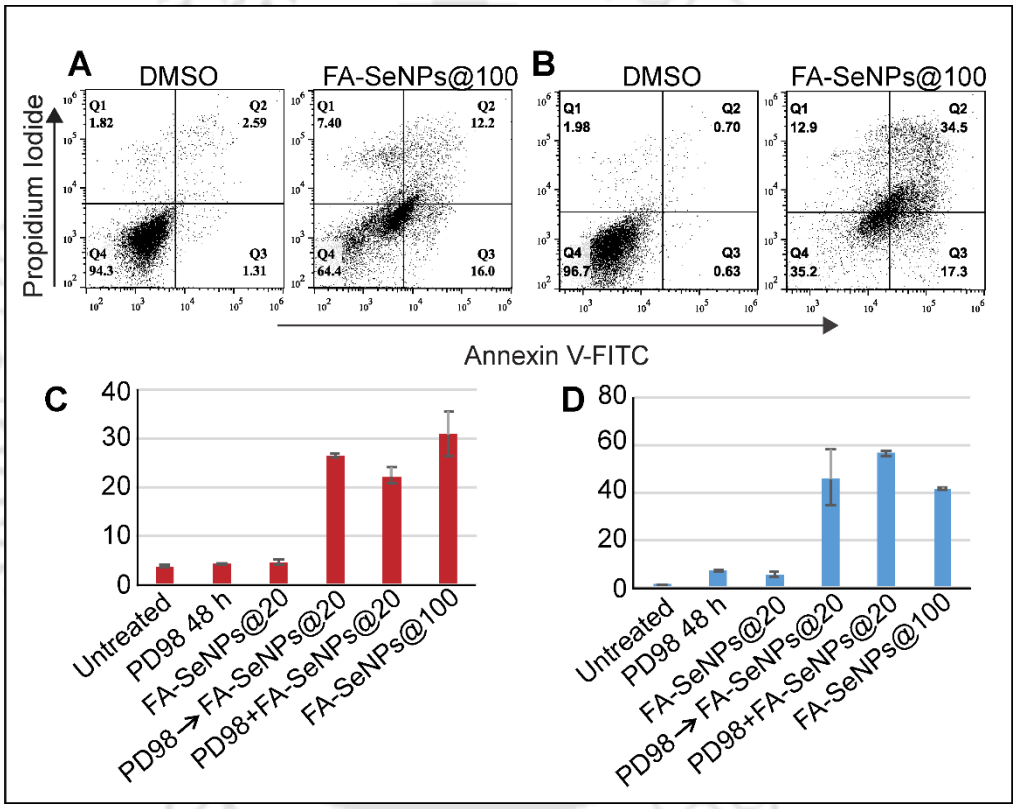

Figure 3.19 Dot plots of the apoptosis assay for DMSO and FA-SeNPs@100 treatments in **(A)** MDA-MB-231 and **(B)** A375 cells. Summary of the % of the apoptotic cells found in all the given treatments in **(C)** MDA-MB-231 and **(D)** A375 cells.

3.3.5 Cell cycle analysis

PD98, as already mentioned, is an inhibitor of MAPK pathway that plays an important role in cell proliferation processes. ERK1/2 activation is vital to the

G1→S transition during mitosis as cyclin D1 activation is influenced by ERK1/2. A constant involvement of ERK1/2 is thus needed for completion of G1/S, as ERK1/2 downregulates the anti-proliferative genes.[39] SeNPs have also been reported to arrest cell cycle at a G2/M phase in A549 cells (lung carcinoma). Since PD98, as well as SeNPs, were previously reported to affect the pattern of cell cycle progression[40,41], cell cycle analyses of treated MDA-MB-231 and A375 cells were carried out by flow cytometry (**Figure 3.20**). In case of MDA-MB-231 cells, although the PD98-treatment for 48 h did not affect much, G2/M population was observed to increase from 22% (untreated) to 57% and 59% in PD98+FA-SeNPs@20 and PD98→FA-SeNPs@20 treatments, respectively, with a concomitant decrease in G1 population. On the other hand, PD98, PD98+FA-SeNPs@20, and PD98→FA-SeNPs@20 caused an increase in the G1 population and subsequent decrease in G2/M population of A375 cells. The increase in G2/M and G1 population in MDA-MB-231 and A375 cells, respectively, suggested possible rewiring of the signaling pathways associated with the cell cycle.

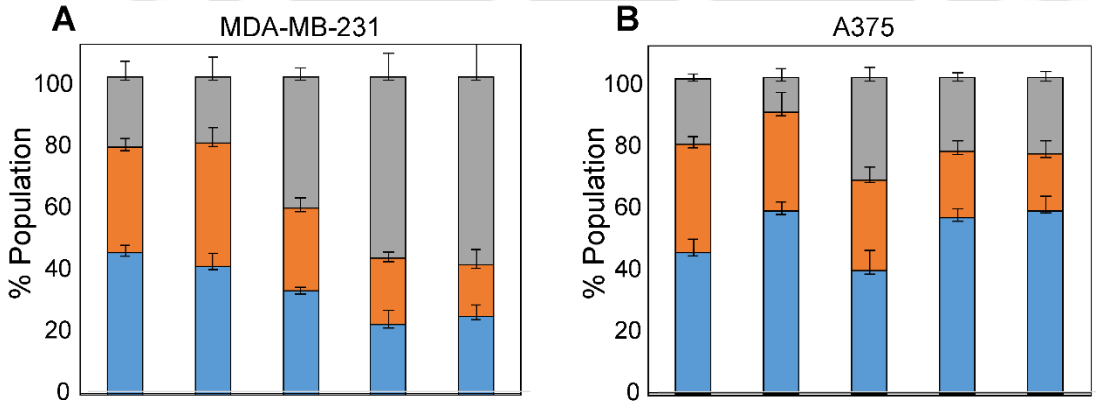

Figure 3.20 Effect of the PD98, FA-SeNPs and their combinations on the cell cycle of the MDA-MB-231(**A**) and A375 (**B**) cells.

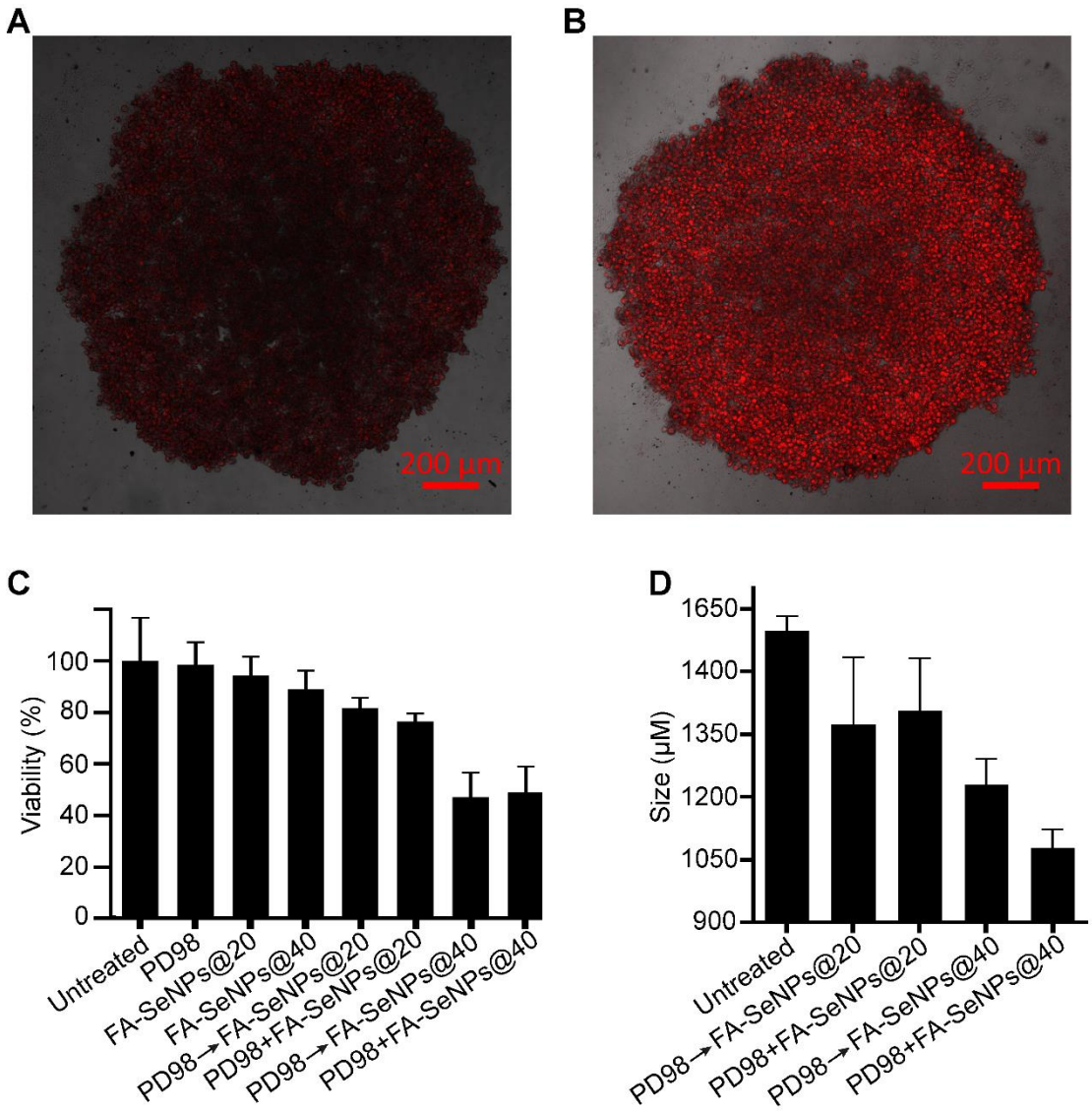

Figure 3.21 (**A,B**) Fluorescence microscopy images FA-SeNPs (**A**) and RhB-loaded SeNPs (**B**) treated MDA-MB-231 spheroids. **(C)** Spheroid viability after 48 h treatment with alone PD98, FA-SeNPs and their combinations at different concentrations. (**D**) Sizes of MDA-MB-231 spheroids after 48 h treatment with PD98→FA-SeNPs and PD98+FA-SeNPs.

3.3.6 Inhibition of spheroid growth by combined treatment of PD98 and FA-SeNPs

Following the demonstration of efficient anti-proliferative efficacy in the 2D culture system of cancer cells, the ability of combined PD98 and FA-SeNPs treatment was further explored in restricting the growth of 3D spheroids of

MDA-MB-231 cells that mimic the 3D tumor environment *in vivo* more closely. First, the penetrability of SeNPs and FA-SeNPs in MDA-MB-231 spheroids was examined using RhB-loaded versions of the corresponding NPs, followed by observation under CLSM.

From the observed RhB red fluorescence from SeNPs **(Figure 3.21A)** and FA-SeNPs **(Figure 3.21B)** in treated spheroids, it can be inferred that FA-SeNPs penetrated the spheroids deeper and accumulated at a higher amount. Following this, the viability of spheroids was estimated by acid phosphatase assay **(Figure 3.21C)** which demonstrated 98%, 94% and 89% viability for PD98, FA-SeNPs@20, and FA-SeNPs@40 treatments, respectively. Viability due to combination treatments PD98→FASeNPs@20 and PD98+FASeNPs@20 was further decreased to 81% and 76%, respectively. It was noticed that the % viability obtained for spheroids treated with PD98→FASeNPs@20 and PD98+FASeNPs@20 showed lesser degree of cell death as compared to that of monolayer (2D) culture possibly due to higher seeding density of cells in case of spheroids. Moreover, PD98→FASeNPs@40 and PD98+FASeNPs@40 treatment decreased the viability of spheroids to 47% and 49%, respectively, indicating the need of increased amount of FA-SeNPs for optimal treatment of spheroids.

Following the treatment with PD98→FASeNPs@20, PD98+FASeNPs@20, PD98→FASeNPs@40 and PD98+FASeNPs@40 for 48 h, the sizes of MDA-MB-231 spheroids were also calculated from corresponding microscopic images using ImageJ **(Figure 3.21D)**. Though much difference was not noticed for PD98→FASeNPs@20 and PD98+FASeNPs@20 treatment, the average size of spheroids was observed to decrease from 1600 ±30 µm in untreated group to 1228 ±54 µm and 1177 ±38 µm in PD98→FASeNPs@40 and PD98+FASeNPs@40 treatment group, respectively. Furthermore, Live/Dead imaging of spheroids was carried out with Calcein-AM/PI staining. As evident from **Figure 3.22**, bright green fluorescence in untreated spheroids indicated

that most of the cells were alive and stained with Calcein-AM. On the other hand, increased PI fluorescence (red) accompanied with decreased green fluorescence of Calcein-AM in PD98→FA-SeNPS@40 and PD98+FA-SeNPs@40 treated samples suggested the presence of dead cell population. Based on the experimental results mentioned above, it was observed that FA decorated SeNPs showed increased distribution in MDA-MB-231 spheroids and, along with PD98, ultimately resulted in increased cell death. Collectively, the results obtained with 3D spheroids indicated the potential of PD98 along with FAR-targeted SeNPs as an effective approach towards tumor therapy.

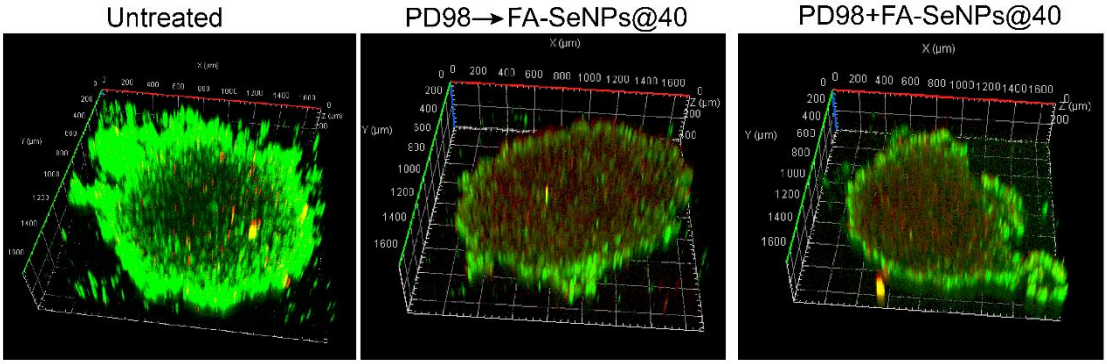

Figure 3.22 Z- stack analyses of Calcein-AM/ PI stained spheroids showing live (green) and dead (red) cells after treatment.

3.4 Conclusion

In summary, folic acid receptor targeted SeNPs (FA-SeNPs) were successfully prepared and thoroughly characterized. FA-SeNPs were demonstrated to accumulate in cancer cells specifically through FAR-binding and, thereby, indicating their potential in avoiding normal cells. Further exploration with endocytic inhibitors revealed the involvement of clathrin as well as caveolin-mediated endocytosis of the FA-SeNPs in MDA-MB-231 and A375 cells. Moreover, in a combination mode of treatment, these tumor-targeted FA-SeNPs along with MEK-inhibitor, PD98 elicited a synergistic anti-proliferative

response in BRAF-mutant MDA-MB-231 and A375 cancer cells. Surprisingly, the synergistic action was observed in the combination treatment at a very low concentration of both FA-SeNPs and PD98. Mechanistic insights revealed that FA-SeNPs operated through ROS production and mitochondrial depolarization, whereas PD98 inhibited the MAPK signaling required for uncontrolled cell division in cancer cells. The present system also demonstrated promising results in a 3D spheroid of MDA-MB-231 with a reduction in spheroid size as well as number of viable cells suggesting the potential of this treatment strategy for *in vivo* tumors.

3.5 References

(1) Brannon-Peppas, L.; Blanchette, J. O. Nanoparticle and Targeted Systems for Cancer Therapy. *Adv. Drug Deliv. Rev.* **2004**, *56* (11), 1649–1659. https://doi.org/10.1016/J.ADDR.2004.02.014.

(2) Chen, C.; Ke, J.; Zhou, X. E.; Yi, W.; Brunzelle, J. S.; Li, J.; Yong, E.-L.; Xu, H. E.; Melcher, K. Structural Basis for Molecular Recognition of Folic Acid by Folate Receptors. *Nature* **2013**, *500* (7463), 486–489. https://doi.org/10.1038/nature12327.

(3) Hartmann, L. C.; Keeney, G. L.; Lingle, W. L.; Christianson, T. J. H.; Varghese, B.; Hillman, D.; Oberg, A. L.; Low, P. S. Folate Receptor Overexpression Is Associated with Poor Outcome in Breast Cancer. *Int. J. Cancer* **2007**, *121* (5), 938–942. https://doi.org/10.1002/ijc.22811.

(4) Toffoli, G.; Cernigoi, C.; Russo, A.; Gallo, A.; Bagnoli, M.; Boiocchi, M. Overexpression of Folate Binding Protein in Ovarian Cancers. *Int. J. Cancer* **1997**, *74* (2), 193–198. https://doi.org/10.1002/(SICI)1097-0215(19970422)74:2<193::AID-IJC10>3.0.CO;2-F.

(5) Wang, Z.; Shi, H.; Guo, J.; Li, C. A Current Review of Folate Receptor Alpha as A Potential Tumor Target in Non-Small-Cell Lung Cancer. *Drug*

Des. Devel. Ther. **2015**, *9*, 4989. https://doi.org/10.2147/DDDT.S90670.

(6) Roger, E.; Kalscheuer, S.; Kirtane, A.; Guru, B. R.; Grill, A. E.; Whittum-Hudson, J.; Panyam, J. Folic Acid Functionalized Nanoparticles for Enhanced Oral Drug Delivery. *Mol. Pharm.* **2012**, *9* (7), 2103–2110. https://doi.org/10.1021/mp2005388.

(7) Rana, S.; Shetake, N. G.; Barick, K. C.; Pandey, B. N.; Salunke, H. G.; Hassan, P. A. Folic Acid Conjugated Fe_3O_4 Magnetic Nanoparticles for Targeted Delivery of Doxorubicin. *Dalt. Trans.* **2016**, *45* (43), 17401–17408. https://doi.org/10.1039/C6DT03323G.

(8) Amjad, M. W.; Amin, M. C. I. M.; Katas, H.; Butt, A. M.; Kesharwani, P.; Iyer, A. K. *In Vivo* Antitumor Activity of Folate-Conjugated Cholic Acid-Polyethylenimine Micelles for the Codelivery of Doxorubicin and SiRNA to Colorectal Adenocarcinomas. *Mol. Pharm.* **2015**, *12* (12), 4247–4258. https://doi.org/10.1021/acs.molpharmaceut.5b00827.

(9) Wang, D.; Ren, Y.; Shao, Y.; Yu, D.; Meng, L. Facile Preparation of Doxorubicin-Loaded and Folic Acid-Conjugated Carbon Nanotubes@Poly(*N* -Vinyl Pyrrole) for Targeted Synergistic Chemo–Photothermal Cancer Treatment. *Bioconjug. Chem.* **2017**, *28* (11), 2815–2822. https://doi.org/10.1021/acs.bioconjchem.7b00515.

(10) Zhang, N.; Wang, M.; Li, N. Folate-Targeted Docetaxel-Lipid-Based-Nanosuspensions for Active-Targeted Cancer Therapy. *Int. J. Nanomedicine* **2012**, *7*, 3281. https://doi.org/10.2147/IJN.S32520.

(11) Dhillon, A. S.; Hagan, S.; Rath, O.; Kolch, W. MAP Kinase Signalling Pathways in Cancer. *Oncogene* **2007**, *26* (22), 3279–3290. https://doi.org/10.1038/sj.onc.1210421.

(12) Roberts, P. J.; Der, C. J. Targeting the Raf-MEK-ERK Mitogen-Activated Protein Kinase Cascade for the Treatment of Cancer. *Oncogene* **2007**, *26* (22), 3291–3310. https://doi.org/10.1038/sj.onc.1210422.

(13) Pritchard, J. R.; Lauffenburger, D. A.; Hemann, M. T. Understanding Resistance to Combination Chemotherapy. *Drug Resist. Updat.* **2012**, *15* (5–6), 249–257. https://doi.org/10.1016/j.drup.2012.10.003.

(14) Sumimoto, H.; Imabayashi, F.; Iwata, T.; Kawakami, Y. The BRAF-MAPK Signaling Pathway Is Essential for Cancer-Immune Evasion in Human Melanoma Cells. *J. Exp. Med.* **2006**, *203* (7), 1651–1656. https://doi.org/10.1084/jem.20051848.

(15) Hollestelle, A.; Elstrodt, F.; Nagel, J. H. A.; Kallemeijn, W. W.; Schutte, M. Phosphatidylinositol-3-OH Kinase or RAS Pathway Mutations in Human Breast Cancer Cell Lines. *Mol. Cancer Res.* **2007**, *5* (2), 195–201. https://doi.org/10.1158/1541-7786.MCR-06-0263.

(16) Yang, C.; Gao, S.; Kjems, J. Folic Acid Conjugated Chitosan for Targeted Delivery of SiRNA to Activated Macrophages in Vitro and in Vivo. *J. Mater. Chem. B* **2014**, *2* (48), 8608–8615. https://doi.org/10.1039/C4TB01374C.

(17) Liu, W.; Li, X.; Wong, Y. S.; Zheng, W.; Zhang, Y.; Cao, W.; Chen, T. Selenium Nanoparticles as a Carrier of 5-Fluorouracil to Achieve Anticancer Synergism. *ACS Nano* **2012**, *6* (8), 6578–6591. https://doi.org/10.1021/nn202452c.

(18) Machnicki, M. M.; Glodkowska-Mrowka, E.; Lewandowski, T.; Ploski, R.; Wlodarski, P.; Stoklosa, T. ARMS-PCR for Detection of BRAF V600E Hotspot Mutation in Comparison with Real-Time PCR-Based Techniques. *Acta Biochim. Pol.* **2013**, *60* (1), 57–64.

(19) Olive, P. L.; Banáth, J. P. The Comet Assay: A Method to Measure DNA Damage in Individual Cells. *Nat. Protoc.* **2006**, *1* (1), 23–29. https://doi.org/10.1038/nprot.2006.5.

(20) Eruslanov, E.; Kusmartsev, S. Identification of ROS Using Oxidized DCFDA and Flow-Cytometry; Humana Press, Totowa, NJ, 2010; pp 57–72. https://doi.org/10.1007/978-1-60761-411-1_4.

(21) Friedrich, J.; Eder, W.; Castaneda, J.; Doss, M.; Huber, E.; Ebner, R.; Kunz-

Schughart, L. A. A Reliable Tool to Determine Cell Viability in Complex 3-D Culture: The Acid Phosphatase Assay. *J. Biomol. Screen.* **2007**, *12* (7), 925–937. https://doi.org/10.1177/1087057107306839.

(22) Yang, C.; Gao, S.; Kjems, J. Folic Acid Conjugated Chitosan for Targeted Delivery of SiRNA to Activated Macrophages in Vitro and in Vivo. *J. Mater. Chem. B* **2014**, *2* (48), 8608–8615. https://doi.org/10.1039/C4TB01374C.

(23) Yang, S.-J.; Lin, F.-H.; Tsai, K.-C.; Wei, M.-F.; Tsai, H.-M.; Wong, J.-M.; Shieh, M.-J. Folic Acid-Conjugated Chitosan Nanoparticles Enhanced Protoporphyrin IX Accumulation in Colorectal Cancer Cells. *Bioconjug. Chem.* **2010**, *21* (4), 679–689. https://doi.org/10.1021/bc9004798.

(24) Huang, S.; Wan, Y.; Wang, Z.; Wu, J. Folate-Conjugated Chitosan–polylactide Nanoparticles for Enhanced Intracellular Uptake of Anticancer Drug. *J. Nanoparticle Res.* **2013**, *15* (12), 2096. https://doi.org/10.1007/s11051-013-2096-1.

(25) Wang, W.; Tong, C.; Liu, X.; Li, T.; Liu, B.; Xiong, W. Preparation and Functional Characterization of Tumor-Targeted Folic Acid-Chitosan Conjugated Nanoparticles Loaded with Mitoxantrone. *J. Cent. South Univ.* **2015**, *22* (9), 3311–3317. https://doi.org/10.1007/s11771-015-2871-5.

(26) Petros, R. a; DeSimone, J. M. Strategies in the Design of Nanoparticles for Therapeutic Applications. *Nat. Rev. Drug Discov.* **2010**, *9* (8), 615–627. https://doi.org/Doi 10.1038/Nrd2591.

(27) Shah, C. P.; Singh, K. K.; Kumar, M.; Bajaj, P. N. Vinyl Monomers-Induced Synthesis of Polyvinyl Alcohol-Stabilized Selenium Nanoparticles. *Mater. Res. Bull.* **2010**, *45* (1), 56–62. https://doi.org/10.1016/J.MATERRESBULL.2009.09.001.

(28) Chen, Y.; Cao, W.; Zhou, J.; Pidhatika, B.; Xiong, B.; Huang, L.; Tian, Q.; Shu, Y.; Wen, W.; Hsing, I. M.; et al. Poly(l -Lysine)- Graft -Folic Acid-Coupled Poly(2-Methyl-2-Oxazoline) (PLL- g -PMOXA- c -FA): A Bioactive Copolymer for

Specific Targeting to Folate Receptor-Positive Cancer Cells. *ACS Appl. Mater. Interfaces* **2015**, *7* (4), 2919–2930. https://doi.org/10.1021/am508399w.

(29) Eckert, L. B.; Repasky, G. A.; Ülkü, A. S.; McFall, A.; Zhou, H.; Sartor, C. I.; Der, C. J. Involvement of Ras Activation in Human Breast Cancer Cell Signaling, Invasion, and Anoikis. *Cancer Res.* **2004**, *64* (13), 4585–4592. https://doi.org/10.1158/0008-5472.CAN-04-0396.

(30) Weber, J. D.; Raben, D. M.; Phillips, P. J.; Baldassare, J. J. Sustained Activation of Extracellular-Signal-Regulated Kinase 1 (ERK1) Is Required for the Continued Expression of Cyclin D1 in G1 Phase. *Biochem. J.* **1997**, *326* (1), 61–68. https://doi.org/10.1042/bj3260061.

(31) Chou, T.-C.; Talalay, P. Quantitative Analysis of Dose-Effect Relationships: The Combined Effects of Multiple Drugs or Enzyme Inhibitors. *Adv. Enzyme Regul.* **1984**, *22*, 27–55. https://doi.org/10.1016/0065-2571(84)90007-4.

(32) Bidkar, A. P.; Sanpui, P.; Ghosh, S. S. Efficient Induction of Apoptosis in Cancer Cells by Paclitaxel-Loaded Selenium Nanoparticles. *Nanomedicine (Lond).* **2017**, *12* (21), 2641–2651. https://doi.org/10.2217/nnm-2017-0189.

(33) Ly, J. D.; Grubb, D. R.; Lawen, A. The Mitochondrial Membrane Potential (Δψm) in Apoptosis; an Update. *APOPTOSIS* **2003**, *8* (2), 115–128. https://doi.org/10.1023/A:1022945107762.

(34) Oberhammer, F. A.; Hochegger, K.; Fröschl, G.; Tiefenbacher, R.; Pavelka, M. Chromatin Condensation during Apoptosis Is Accompanied by Degradation of Lamin A+B, without Enhanced Activation of Cdc2 Kinase. *J. Cell Biol.* **1994**, *126* (4), 827–837. https://doi.org/10.1083/JCB.126.4.827.

(35) Liu, R.; Page, C.; Beidler, D. R.; Wicha, M. S.; Núñez, G. Overexpression of Bcl-x(L) Promotes Chemotherapy Resistance of Mammary Tumors in a Syngeneic Mouse Model. *Am. J. Pathol.* **1999**, *155* (6), 1861–1867. https://doi.org/10.1016/S0002-9440(10)65505-8.

(36) Sartorius, U. A.; Krammer, P. H. Upregulation of Bcl-2 Is Involved in the

Mediation of Chemotherapy Resistance in Human Small Cell Lung Cancer Cell Lines. *Int. J. Cancer* **2002**, *97* (5), 584–592. https://doi.org/10.1002/ijc.10096.

(37) Xu, R.; Sato, N.; Yanai, K.; Akiyoshi, T.; Nagai, S.; Wada, J.; Koga, K.; Mibu, R.; Nakamura, M.; Katano, M. Enhancement of Paclitaxel-Induced Apoptosis by Inhibition of Mitogen-Activated Protein Kinase Pathway in Colon Cancer Cells. *Anticancer Res.* **2009**, *29* (1), 261–270.

(38) Zelivianski, S.; Spellman, M.; Kellerman, M.; Kakitelashvilli, V.; Zhou, X.-W.; Lugo, E.; Lee, M.-S.; Taylor, R.; Davis, T. L.; Hauke, R.; et al. ERK Inhibitor PD98059 Enhances Docetaxel-Induced Apoptosis of Androgen-Independent Human Prostate Cancer Cells. *Int. J. Cancer* **2003**, *107* (3), 478–485. https://doi.org/10.1002/ijc.11413.

(39) Chambard, J.-C.; Lefloch, R.; Pouysségur, J.; Lenormand, P. ERK Implication in Cell Cycle Regulation. *Biochim. Biophys. Acta - Mol. Cell Res.* **2007**, *1773* (8), 1299–1310. https://doi.org/10.1016/J.BBAMCR.2006.11.010.

(40) Pumiglia, K. M.; Decker, S. J. Cell Cycle Arrest Mediated by the MEK/Mitogen-Activated Protein Kinase Pathway. *Proc. Natl. Acad. Sci. U. S. A.* **1997**, *94* (2), 448–452. https://doi.org/10.1073/PNAS.94.2.448.

(41) Wu, H.; Zhu, H.; Li, X.; Liu, Z.; Zheng, W.; Chen, T.; Yu, B.; Wong, K. H. Induction of Apoptosis and Cell Cycle Arrest in A549 Human Lung Adenocarcinoma Cells by Surface-Capping Selenium Nanoparticles: An Effect Enhanced by Polysaccharide-Protein Complexes from Polyporus Rhinocerus. *J. Agric. Food Chem.* **2013**, *61* (41), 9859–9866. https://doi.org/10.1021/jf403564s.

CHAPTER 4

Establishment of membrane coated nanocarriers for anti-cancer drug delivery

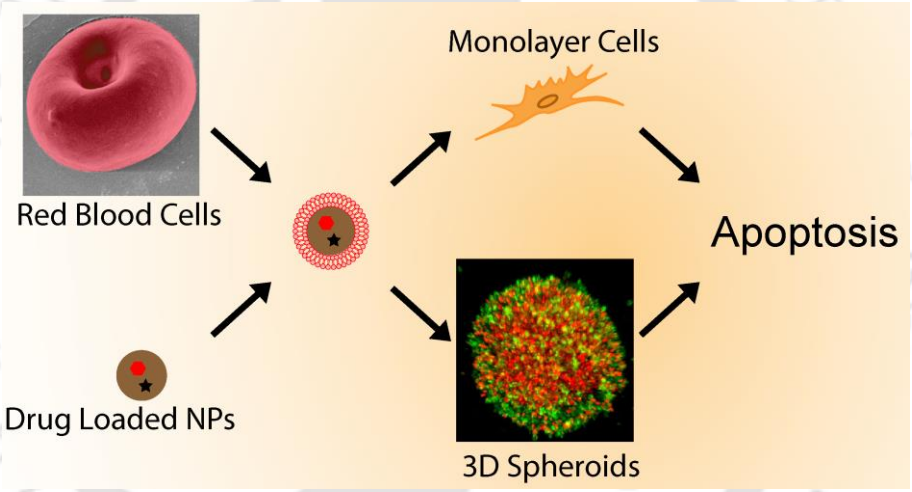

Chapter 4 demonstrates red blood cell (RBC) membrane coated nanocarriers for delivery of chemotherapeutic agent (Curcumin/Cur) and hypoxia activating molecule (Tirapazamine/TPZ). The RBC membrane coating provided improved stability, biocompatibility and facile uptake into cancer cells resulting in synergistic activity of the drugs.

ACS Applied Bio Materials, 2019

DOI: 10.1021/acsabm.9b00584

CHAPTER 4

4.1 Introduction

Clinical studies on patients with hypoxic tumors have shown an increased risk of metastasis, and resistance to chemotherapy and radiotherapy.[1,2] During tumor development, the supply of oxygen and nutrient decreases toward the tumor core causing hypoxic environment, which leads to the release of angiogenic activators to trigger the growth of new blood vessels around the tumor site.[3] Another noteworthy point is that, in most of the cases, it is not the primary tumor which causes mortality; but the metastasis to a secondary site becomes the key deciding factor. During metastasis, cells from the primary tumor lose cell to cell adhesion and become more invasive adding to the increased migration.[4]

With continuous advancements in the field of drug discovery, novel molecular entities are being constantly investigated to treat these resistant and metastatic cancers. However, distribution of the drug molecules in normal body tissues leads to systemic toxicity causing severe side effects and the possibility of chemo-resistance by several cancer cells for multiple anticancer agents. To this end, several different drug delivery systems such as polymeric, metallic, and semi-metallic nanoparticles (NPs) are being developed for drug delivery and theranostic purposes.[5–7]

In this Chapter, RBC membrane-coated PLGA NPs (RBC-NPs) were studied for drug delivery application. RBC-NPs were prepared and thoroughly characterized in terms of morphology, stability, biocompatibility, and hemo-compatibility. Subsequently, Cur and TPZ drug molecules were co-loaded into these NPs (Cur+TPZ@RB) to study the therapeutic effect of these drug combinations on cancer cells (**Scheme 4.1**). The influence of RBC membrane coating on the internalization of the drug-loaded nanoparticles was assessed in

MCF-7 (breast cancer) A375 (malignant melanoma), and HEK293 (human embryonic kidney) cells. The dose-dependent antiproliferation capability of drug loaded RBC-NPs (Cur+TPZ@RB) was tested in A375 and MCF-7 cells in monolayer as well as 3D multicellular spheroids (MCS). Probable involvement of apoptosis-mediated cell death with molecular mechanism behind Cur+TPZ@RB induced antiproliferative response in the treated cells was pursued. Further, the change in elevated levels of EMT markers in MCS following Cur+TPZ@RB treatment was also examined.

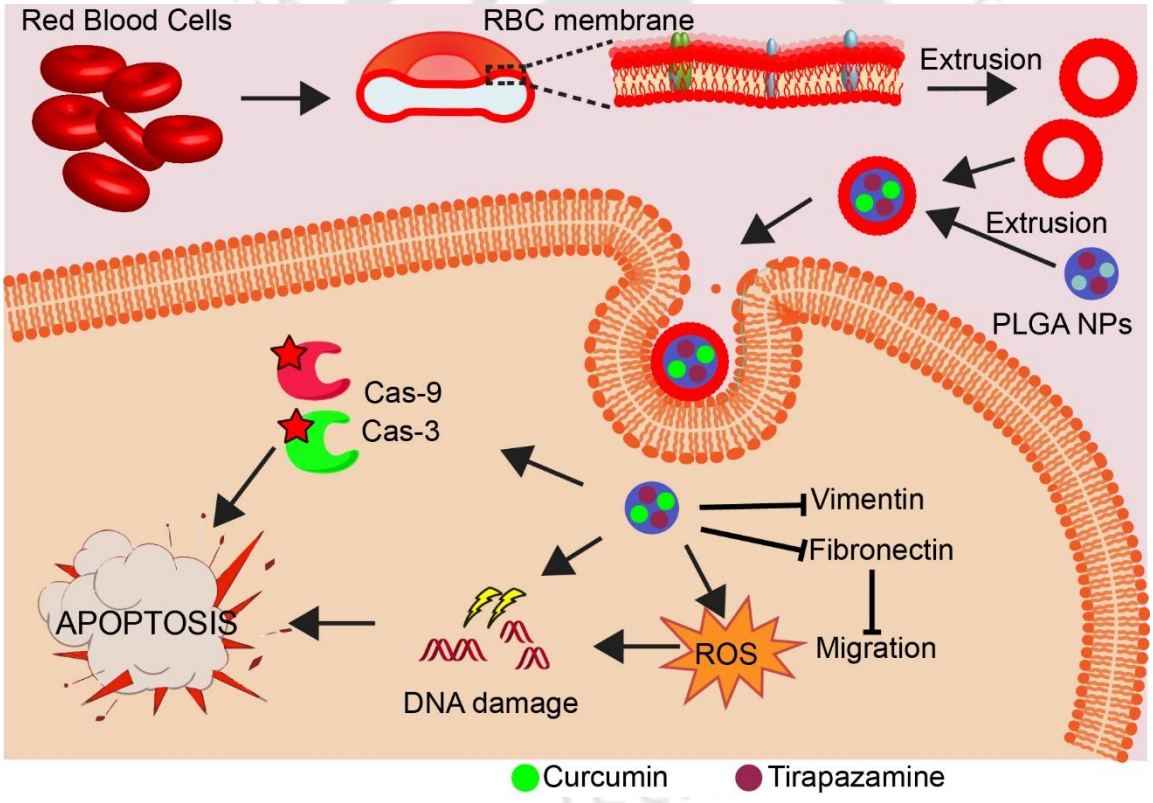

Scheme 4.1: Schematic representation of the preparation of the RBC membrane-coated PLGA NPs for hypoxia-targeted therapy of cancer cells.

4.2 Experimental Section

4.2.1 Materials

Poly(lactic-co-glycolic acid) (PLGA), Ethylenediaminetetraacetic acid (EDTA) salt, Dulbecco's Modified Eagle's medium (DMEM), Lipopolysaccharide (LPS), phorbol 12-myristate 13-acetate (PMA), Resazurin, Curcumin, Tirapazamine, MTT (3-(4,5-Dimethylthiazol-2-yl)-2,5-diphenyltetrazolium bromide), Propidium iodide (PI) were purchased from Sigma Aldrich. Caspase-9 (Cat. No. 9508), cleaved caspase-9 (Cat. No. 52873), anti-poly ADP ribose polymerase (PARP) (Cat. No. 9542), anti-cleaved PARP antibodies (Cat. No. 5625) were purchased from cell signaling technology. The anti-active caspase-3 antibody was purchased from BD Biosciences.

4.2.2 Cell Culture

MCF-7 (breast cancer) A375 (malignant melanoma), HEK293 (human embryonic kidney) and L132 (lung) cells were obtained from National Centre for Cell Science, Pune, India. All the cells lines were maintained in DMEM containing 10% fetal bovine serum, supplemented with the antibiotic solution (1% streptomycin and penicillin) in a CO_2 incubator.

4.2.3 Formation of RBC membrane-coated PLGA NPs

PLGA NPs were prepared using the nanoprecipitation method.[8] PLGA in acetone (1mg/mL) was dropwise added to Millipore grade water with continuous stirring. After 2 h of stirring, NPs were centrifuged and lyophilized. Isolation of the RBC membranes was performed using hypotonic lysis method.[8] Fresh human blood from healthy volunteers was obtained under the approval of the institutional human ethics committee. At first, blood from healthy donors was collected in EDTA coated tubes, centrifuged to remove the plasma

and buffy coat. After washing with 1X PBS, RBCs were lyzed in 0.25X PBS on ice for 45 min. The lyzed RBC membranes were centrifuged at 20000 g for 20 min at 4 °C. Pink colored RBC membrane pellet was further washed with PBS and stored at -20 °C for further use. RBC membranes were serially extruded through 0.8 μm, 0.4 μm, and 0.2 μm pore size membrane in the extruder (Avanti Polar Lipids). To prepare RBC membrane-coated PLGA NPs (RBC-NPs), PLGA NPs and RBC vesicles were combinedly extruded through 0.1 μm pore size membrane. Initially, the amount of RBC membranes required to coat PLGA NPs was determined. The PLGA NPs and RBC membranes were extruded at different weight ratios of PLGA: RBC membrane proteins (from 1:0.5 to 1:4). These coated NPs were stored for eight days and their stability was studied by hydrodynamic diameter measurements. The PLGA: RBC membrane proteins ratio at which the NPs were stable for eight days, was selected for further studies.

4.2.4 Characterization of the Nanoparticles

Hydrodynamic diameter and zeta potential measurements were done using dynamic light scattering (DLS, Malvern Zeta Sizer Nano ZS). For transmission electron microscopy (TEM), NPs were drop cast on a copper grid and counterstained with uranyl acetate and observed under TEM (Jeol, MA). Surface morphology of the RBC-NPs was studied from field emission scanning electron microscope (FESEM) images. For this, samples were dried on aluminum foil coated coverslip, and images were taken in FESEM instrument (SIGMA, ZEISS). DLS measurements were taken to study the stability of the PLGA and RBC-NPs at different conditions. Initially, serum stability of the NPs was studied, where NPs were incubated with 10% serum for 48 h. Long term stability of the RBC NPs was studied at 4 °C and -80 °C.

4.2.5 Sodium dodecyl sulfate-polyacrylamide gel electrophoresis (SDS-PAGE)

The PLGA NPs were coated with RBC membranes, thus, to check the presence of RBC membrane over PLGA NPs. SDS-PAGE was performed. Proteins from RBC, RBC membrane and RBC NPs were isolated and electrophoresed in 12% SDS polyacrylamide gel. To visualize and compare the proteins from the different samples, silver staining was performed.

4.2.6 Biocompatibility and Hemocompatibility analysis

Expression of the interleukins by macrophage cells after exposure to foreign materials causes an immunogenic reaction. We have studied the expression of the interleukin 1ß, interleukin 6, and interleukin 8 by realtime-PCR. For this, macrophage cells (THP-1) were differentiated using PMA (100 ng/mL) for 24 h, followed by treatment with RBC-NPs or lipopolysaccharides (LPS, 500 ng/mL) as a positive control. Later, cells were lysed, and total RNA isolation was performed. SYBR green-based PCR was performed using primers for interleukins and GAPDH as an internal control (Rotor Gene Q, Qiagen). For hemocompatibility testing, intact RBCs were mixed with PBS (negative control), 0.1% Triton-X (positive control) or RBC NPs. Release of the hemoglobin was measured by taking absorbance at 550 nm, and % hemolysis was compared by considering 100% lysis with Triton-X.[9]

4.2.7 Drug Loading, release and nanoparticle uptake studies

For loading of the drugs in the NPs, Cur and TPZ molecules were added in PLGA solution before the synthesis of the PLGA NPs. To remove the unbound or free drug, PLGA NPs suspension was centrifuged at 20000 g for 20 min. The supernatant was collected to measure the amount of the drugs loaded on NPs.

The drug-loaded NPs were further washed with PBS three times by centrifugation. Fluorescence measurements of Cur (at 550 nm) were used for calculations of % loading and release. Similarly, TPZ quantitation was performed using UV-visible spectrometer (λ_{abs}- 266 nm). For release study, 5 ml of the drug-loaded NPs (Cur+TPZ@RB) kept in dialysis bag were consciously stirred in presence of PBS (100 ml). At different time points, 500 µl of the drug solution was aliquoted for quantitation of the drug release. The unknown concentrations of the drugs were studied from a calibration curve of the standard drugs (Cur and TPZ).

Uptake of the drug-loaded NPs in MCF-7 and A375 cells was studied by flow cytometry and confocal microscopy. For microscopy studies, NPs treated cells were fixed with 4% formaldehyde and counterstained with DAPI. Cells were analyzed in a confocal microscope (ZEISS, LSM 880) using 355 nm and 488 nm laser as an excitation source. For flow cytometry studies, cells were treated with free Cur, Cur and TPZ loaded PLGA NPs (Cur+TPZ@PL), and RBC membrane-coated Cur+TPZ@PL (Cur+TPZ@RB). After 4 h incubation with nanoparticles, cells were trypsinized and analyzed in a flow cytometer (Cytoflex, Beckman Coulter). To confirm the route of the internalization of the NPs, cells were stained with Lysotracker red. Cells treated with Cur+TPZ@RB were stained with Lysotracker (75 nM) and fluorescence of Cur, as well as lysotracker, was detected in the confocal microscope. To study the endocytosis mechanism, cells were pretreated with endocytosis inhibitors like; Sodium azide, chlorpromazine, ß-methylcyclodextrin (ß-MCD) for 4 h followed by Cur+TPZ@RB treatment. Macrophage uptake of Cur+TPZ@PL and Cur+TPZ@RB was studied to get an idea about the clearance by macrophage cells. For this, PMA activated THP-1 cells were treated with Cur+TPZ@PL and Cur+TPZ@RB for 4 h and analyzed in a flow cytometer.

4.2.8 Cell viability assays

MTT assays were carried out to study the antiproliferative properties of Cur, TPZ, and their combinations (Cur+TPZ). Similarly, the effect of Cur+TPZ@PL and Cur+TPZ@RB NPs was also studied after treatment with increasing concentrations. After 48 h treatment, cells were incubated with MTT reagent for 2 h. The absorbance of the MTT was taken with DMSO at 570 nm in the multiplate reader (Infinite 200 PRO, TECAN). Compusyn software was used for combination index analysis.

4.2.9 Apoptosis & Cell death analysis

In order to study the cell death and apoptosis, MCF-7 and A375 cells were treated with the drugs or Cur+TPZ@PL and Cur+TPZ@RB at concentrations equal to the IC_{50} concentration of Cur+TPZ@RB for each cell type. For cell death assay in MCF-7 cells, the cells were treated with Cur+TPZ@PL or Cur+TPZ@RB containing Cur at 6 μM and TPZ at 5.4 μM for 48 h. These treated cells were stained with PI (2 μg/mL) for 20 min and analyzed in a flow cytometer. Apoptotic cells were measured by staining with the phycoerythrin-conjugated anti-active caspase-3 antibody. For cell death and apoptosis study in A375 cells, cells were treated with 11 μM Cur and 9.4 μM TPZ containing NPs for 48 h. For apoptosis testing, treated A375 cells were fixed (4% formaldehyde), permeabilized (90% methanol) and stained with the PE-anti active caspase-3 antibody. Subsequently, stained cells were analyzed in a flow cytometer. Data analysis was performed using FlowJo software.

4.2.10 Western blotting

Western blots were performed to study the proteins involved in apoptosis. For this, treatment was given as mentioned in apoptosis study, then the

treated cells were lysed in RIPA buffer, and total protein was isolated. Initially, proteins were run on SDS-PAGE for separation based on molecular weight. Secondly, the proteins were transferred on PVDF membrane. These membranes were blocked (4% BSA) and incubated with the primary followed by horseradish peroxidase bound secondary antibody. Blots were developed by adding peroxidase substrate in ChemiDoc system (BioRad).

4.2.11 Spheroid formation and Viability assays

Spheroids were prepared by seeding cells in 96 well plates precoated with agarose. Briefly, the surface of the 96 well plates was made non-adherent by adding melted agarose in serum-free media. After solidification of the agarose, 20,000 cells were seeded in each well and plates were centrifuged at 700 x g for 10 min. Further, 96 well plates were incubated for 3 days in a CO_2 incubator for spheroid formation. For viability assay on spheroids, resazurin assays were performed after treatment with increasing concentrations of the drug-loaded NPs.[10] After completion of the treatment for 48 h, spheroids were incubated with resazurin solution (60 μM) for 4 h. Fluorescence readings were taken at 590 nm after excitation at 530 nm.

4.2.12 Microscopy of the Multi-Cellular Spheroids

Uptake of the Cur+TPZ@PL and Cur+TPZ@RB in MCF-7, as well as A375 MCSs, was studied by microscopy. Spheroids treated with Cur+TPZ@PL and Cur+TPZ@RB were analyzed in confocal microscopy for Cur fluorescence. For observation of the live/dead cells in spheroids, calcein-AM and PI staining were performed. Untreated, Cur+TPZ@PL, and Cur+TPZ@RB treated spheroids were stained and analyzed in microscopy by keeping controls (Cur+TPZ@PL, Cur+TPZ@RB) for Cur fluorescence.

4.2.13 Flow Cytometry of the MCSs

Cell death analysis and ROS measurements in treated MCSs were performed by flow cytometry. For cell death analysis, MCF-7 MCSs were treated with Cur+TPZ@RB and Cur+TPZ@PL at the IC_{50} concentrations of Cur+TPZ@RB (Cur at 28.2 μM and TPZ at 25.3 μM). Later MCSs were collected in a centrifuge tube and cells were detached using accutase solution. Separated cells were stained with PI and analyzed in a flow cytometer to determine the number of dead cells. For ROS assay, MCSs were incubated with DFCDA (10 μM) for 1 h followed by treatment with Cur@RB (28.2 μM), TPZ@RB (25.3 μM) and Cur+TPZ@RB (Cur-28.2 μM, TPZ- 25.3 μM) for 10 h. Treated spheroids were subjected to accutase treatment and cells were analyzed in a flow cytometer using FlowJo software

4.2.14 Comet assay

DNA damage in the Cur+TPZ@RB treated spheroidal cells was studied by comet assay.[11] For comet assay, cells suspended in 1% low gelling agarose were spread over slides coated with the same agarose. Alkaline lysis of the cells was achieved in lysis buffer (1.2M NaCl, 100 mM Na_2 EDTA, 0.1% SDS and 0.26 M NaOH) at 4 °C for 12 h. Slides containing cells were subjected to electrophoresis and staining with PI. For visualization of the comets, cells were observed under a microscope and tail moments were analyzed in CaspLab program.

4.2.15 Realtime PCR for gene expression

Expression of the vimentin and fibronectin in monolayer MCF-7, and MCF-7 MCS was studied by realtime PCR. For this, RNA from MCF-7 cells, MCSs was isolated with Trizol reagent, and cDNA was prepared using cDNA

synthesis kit (iScript cDNA Synthesis Kit, BioRad). Synthesized cDNA was used as a template for realtime PCR. In order to amplify the genes of interest, the primers specific for vimentin and fibronectin were designed. In the PCR reaction, SYBR green (BioRad) was used as a reporter dye, while GAPDH (glyceraldehyde-3-phosphate dehydrogenase) was used as an internal control (**Table 4.1**). The PCR results provided the C_t (threshold cycles) for all the genes studied; these values were further used to study the fold change in the expression of vimentin and fibronectin using the $\Delta\Delta C_t$ method.

Table 4.1 Nucleotide sequences of the primers used to study gene expression.

Gene	Forward Primer (5' to 3')	Reverse Primer (5' to 3')
GAPDH	GAAATCCCATCACCATCTTCCAGG	GAGCCCCAGCCTTCTCCATG
Vimentin	AGTCCACTGAGTACCGGAGAC	CATTTCACGCATCTGGCGTTC
Fibronectin	GGTGACACTTATGAGCGTCCTAAA	AACATGTAACCACCAGTCTCATGTG
IL1ß	CAGAAGTACCTGAGCTCGCC	AGATTCGTAGCTGGATGCCG
IL6	GGCACTGGCAGAAAACAACC	GCAAGTCTCCTCATTGAATCC
IL8	CAAGAGCCAGGAAGAAACCA	GTCCACTCTCAATCACTCTCAG

4.2.16 Wound healing assay

Migratory properties of the MC7 cells were studied by scratch or wound healing assay. MCF-7 cells were allowed to grow to become confluent. When cells were 90% confluent, a scratch was made by using a sterile pipette tip, and images were taken at 0 h. Cells were treated with Cur+TPZ@RB for 48 h and the images were acquired to confirm the migration. Percentage of wound area was calculated with ImageJ from untreated and treated wells.

4.3 Results & Discussions

4.3.1 Preparation, Characterization and Biological Response of RBC-NPs

In order to prepare RBC membrane-coated PLGA NPs (RBC-NPs), membranes from RBCs were isolated first by hypotonic lysis method.[8] Briefly, blood from healthy individuals was collected, centrifuged and collected RBCs were lysed in 0.25X PBS. Microscopic images (**Figure 4.1**) of the RBCs before and after the hypotonic treatment confirmed the lysis of the RBCs. Following the removal of cellular contents from the RBCs by centrifugation, RBC membrane pellets were collected in PBS. After this, RBC membrane vesicles were prepared by sequential extrusion through 0.8 μm, 0.4 μm, and 0.2 μm pore-sized membranes. On the other hand, PLGA NPs used in this chapter were prepared by nano-precipitation method.[8] The as-prepared PLGA NPs were subsequently characterized for morphology and surface charge (ζ-potential) by dynamic light scattering (DLS) and transmission electron microscopic (TEM) analyses. The hydrodynamic diameter (d_H) and zeta-potential (ζ) of the PLGA NPs (**Figure 4.2A, B)** were found to be 114 ±10 nm and -23mV, respectively.

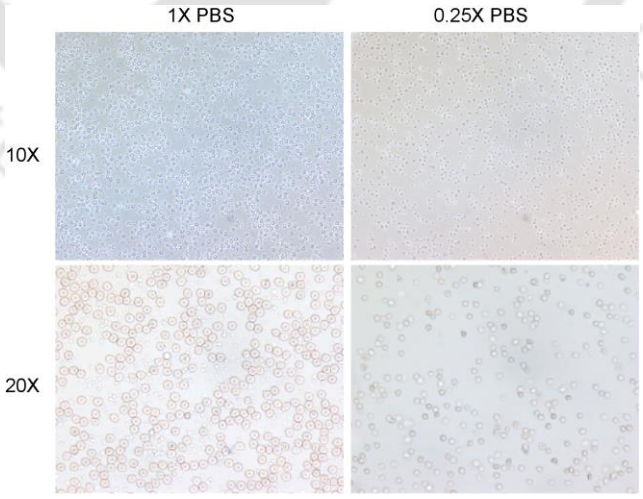

Figure 4.1 Microscopic images of RBCs in 1X PBS and 0.25X PBS, RBCs in 0.25X showed loss in the membrane integrity due to hypotonic treatment.

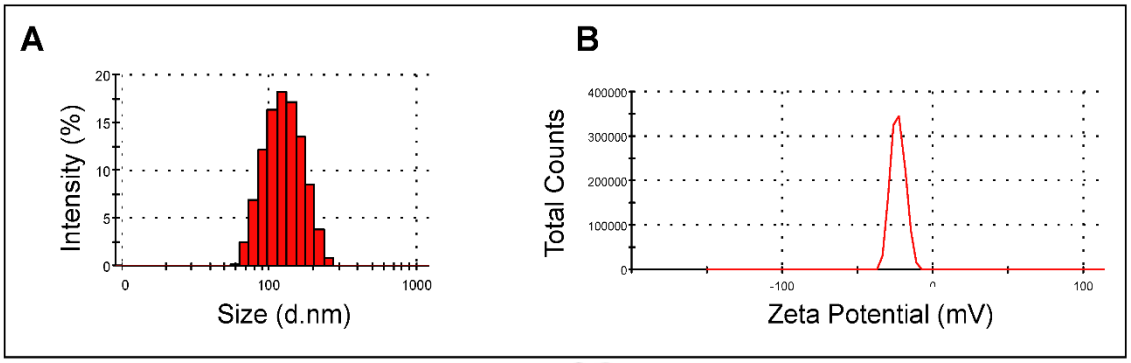

Figure 4.2 (**A, B**) Hydrodynamic diameter (**A**) and zeta potential (**B**) of the PLGA NPs.

The RBC-NPs were finally prepared by extruding the PLGA NPs along with RBC vesicles through 0.1 µm pore size membrane membrane. In order to optimize the amount of the RBC membrane required to coat PLGA NPs, the RBC-NPs were prepared with different PLGA: membrane protein ratios (1:0.5 to 1:4). Resultant RBC-NPS were subjected to DLS analysis to measure the d_H on Day 0 and 8 in PBS.

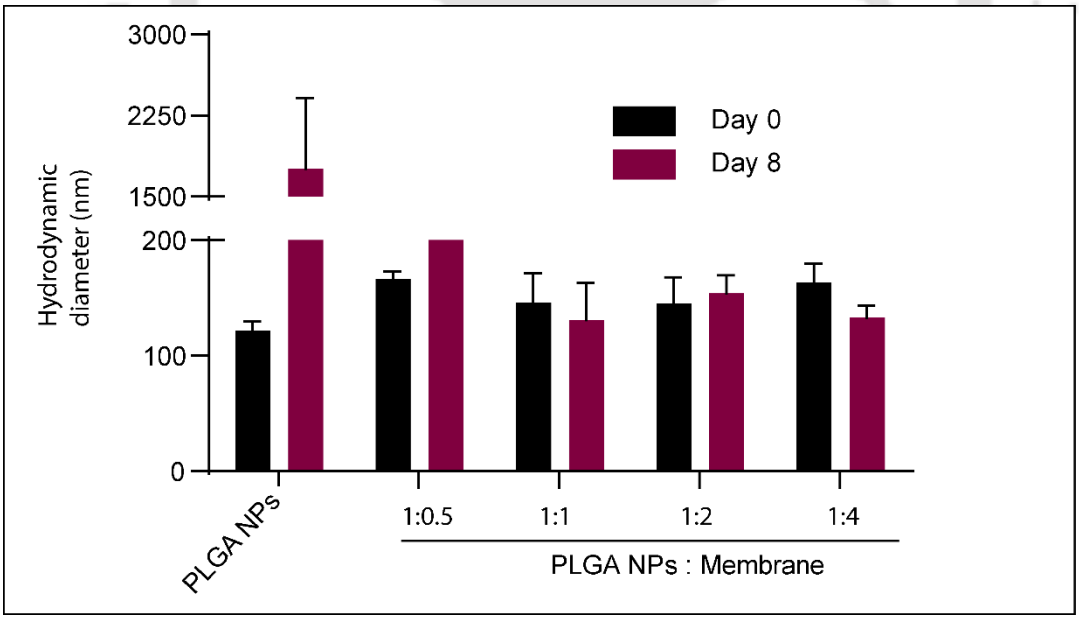

Figure 4.3 Hydrodynamic diameters of RBC-NPs prepared with varying PLGA: RBC membrane ratios after synthesis (Day 0) and storage for 8 days.

Results in **Figure 4.3** suggested that the PLGA NPs and RBC-NPs prepared at 1:0.5 (PLGA: membrane protein) ratio showed an increase in d_H after storage. Nonetheless, RBC-NPs prepared at 1:1 to 1:4 ratio showed greater stability over a period of 8 days, and thus 1:1 ratio was selected for further experiments. Surprisingly, the DLS analyses revealed that the d_H of the PLGA NPs was increased from 114 ±10 nm to 157 ±15 nm after RBC membrane coating **(Figure 4.4)**. However, the average size of RBC-NPs was estimated to be 105 ±23 nm from TEM images (**Figure 4.5A, B)**.

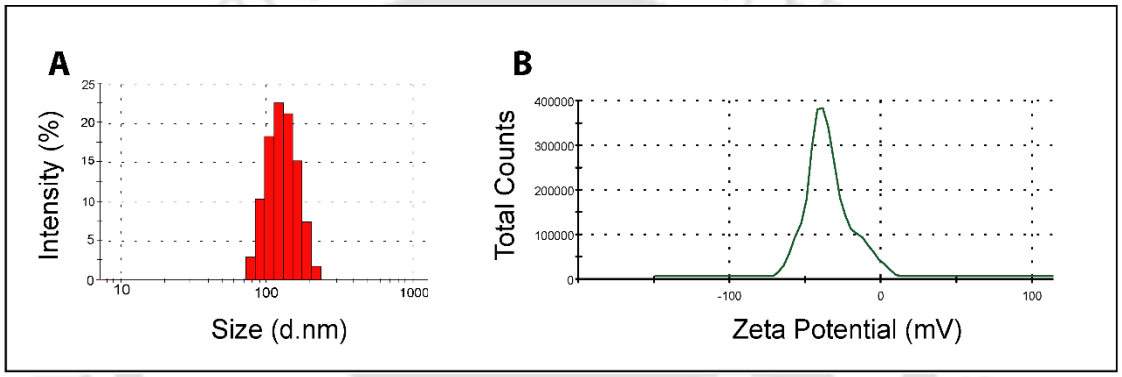

Figure 4.4 (**A,B**) Hydrodynamic diameter (**A**) and zeta potential (**B**) of the RBC-NPs.

Additionally, Field-emission scanning electron microscopic (FESEM) images (**Figure 4.5D**) confirmed the prepared RBC NPs were spherical and possessed almost equal size that was measured in TEM. A possible reason for observation of increased size by DLS measurement, as compared to that of TEM, was due to the hydrodynamic size of the 'solvated' NPs being measured. TEM images of the RBC-NPs, showed a distinct layer on the surface of PLGA NPs confirming the coating with RBC membrane. The surface charge of the NPs plays an important role in their internalization by the cells. In this regard, ζ-potential of RBC-NPs was recorded and shown in **Figure 4.4B**. The ζ-potential of RBC-NPs was found to be −31 mV, lower than that of bare PLGA NPs (−23 mV, **Figure 4.2B**), due to successful coating of PLGA NPs with

negatively-charged RBC membrane. The integrity of the proteins in the RBC membrane following their coating onto the PLGA NPs is crucial for the potential interaction of RBC-NPs with the target cells and thus investigated using sodium dodecyl sulfate-polyacrylamide gel electrophoresis (SDS-PAGE).

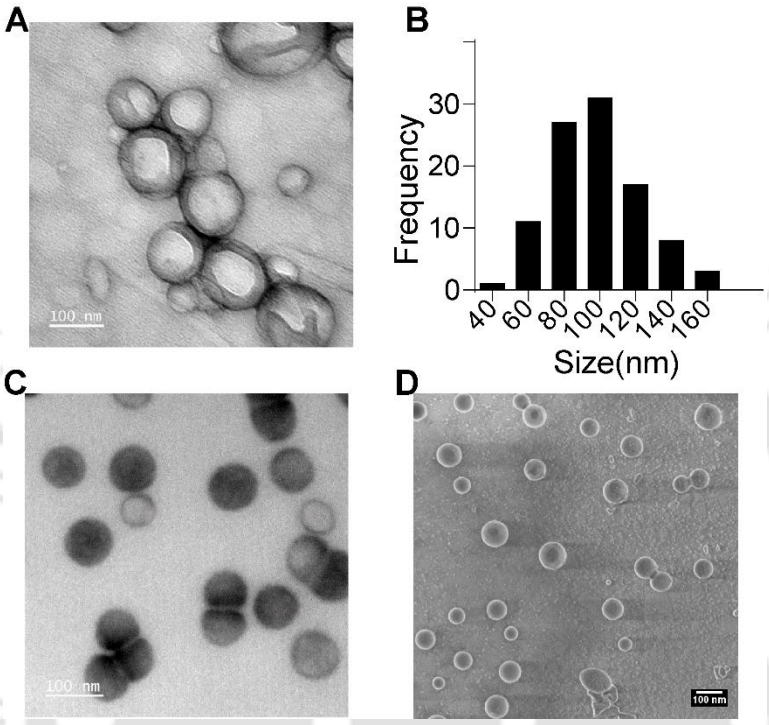

Figure 4.5 (**A, B**) TEM image and Size distribution of the RBC-NPs calculated from TEM images. **C:** TEM micrograph for PLGA NPs. **D**: FESEM image of RBC NPs (Size bar: 100 nm).

The image of SDS-PAGE (**Figure 4.6**) demonstrated that the majority of the proteins from native RBC surface were still present in the RBC-NPs confirming the efficient coating of the PLGA NPs with RBC membrane without loss of the membrane proteins. Taken together, the ability to retain the RBC surface proteins and maintain the size over a period of 8 days confirmed the successful formulation of stable RBC-NPs. Another key point was that the size of the RBC NPs was in accordance with the range required for enhanced permeability and retention (EPR) effect.[12]

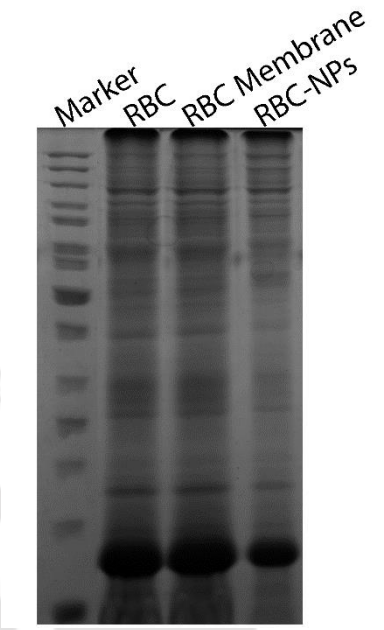

Figure 4.6 SDS-PAGE of the RBC membrane proteins. RBC, isolated RBC membrane and RBC-NPs showed similar protein content confirming the coating of PLGA NPs without loss of the membrane proteins.

Before studying the potential *in-vivo* application of therapeutic nanoparticles, it is important to check their interaction with the biological system *in vitro* to ensure safety.[13] Therefore, the biocompatibility of the RBC NPs was studied on differentiated macrophage-like THP-1 cells. For this, THP-1 cells were treated with RBC-NPs and the expression of pro-inflammatory cytokines including IL6, IL8, and IL1ß was measured with quantitative realtime PCR. Expression of IL6 stimulates acute phase response and thus it is involved in immune response and inflammation.[14] Similarly, production of IL8 attracts the phagocytes to the site of injury or infection, whereas IL1ß is also responsible for inflammation.[15]

Figure 4.7A showed the expression of these cytokines from differentiated macrophage cells after treatment with RBC-NPs and LPS (0.5 µg/mL) as a positive control. From the results, it was observed that the expression of all the cytokines tested was elevated in LPS treatment. However, the expression of

the cytokines was significantly low in RBC NPs treated cells, suggesting the RBC-NPs did not elicit an immune response and thus were biocompatible. Subsequently, hemocompatibility of the present RBC NPs was tested by incubating them with isolated RBCs. Intact RBCs were isolated and incubated with PBS, RBC NPs and Triton-X (1%) for 3 h at room temperature. From **Figure 4.7B**, no release of the hemoglobin was observed in negative control (PBS) and RBC NPs samples; whereas significant lysis of the RBCs occurred in the positive control (Triton-X). Collectively, it was concluded that RBC NPs were efficiently stable and did not show any immunogenic or hemolytic response, thus are safe for therapeutic applications.

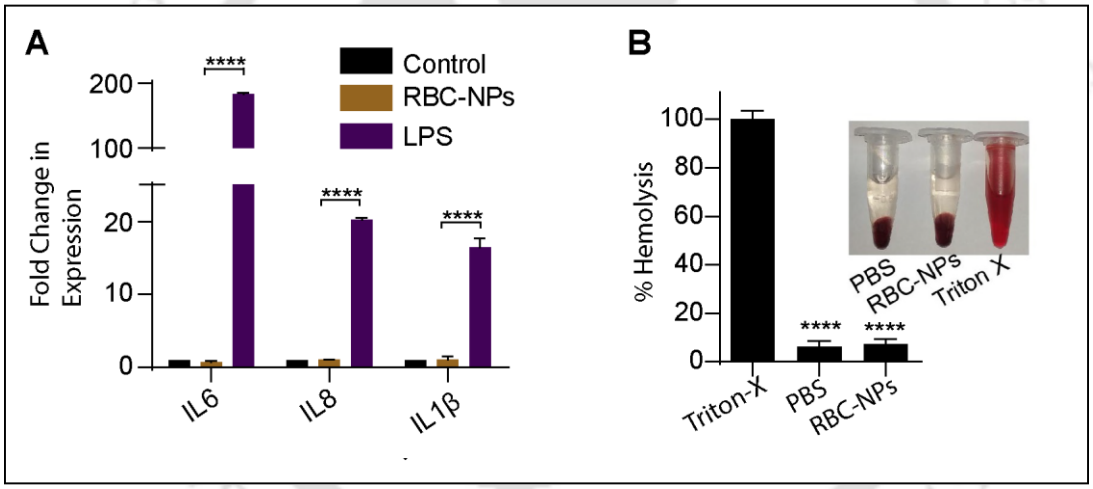

Figure 4.7 (**A**) Expression of IL6, IL8, and IL1ß in THP-1 cells after RBC-NPs or LPS treatment. (**B**) % Hemolysis of RBCs in the presence of RBC-NPs and Triton-X. (Data as Mean ±SD, n=3, $p<0.0001$ denoted as ****).

4.3.2 Preparation of Drug-Loaded RBC-NPs

After confirming the hemo- and biocompatibility of the RBC-NPs, potential anticancer drug curcumin (Cur) and tirapazamine (TPZ) were loaded into these NPs. Loading and encapsulation efficiency Cur and TPZ were estimated by UV visible spectrometry for TPZ and fluorescence spectrometry for Cur. The

results of these studies were included in **Table 4.2**. The maximum loading efficiency of the Cur and TPZ were found to be 34±0.9% and 29±1.2%, when they were added separately in PLGA NPs.

Table 4.2 Loading and encapsulation efficeincy of the curcumin and tirapazamine seperately or in combination with TPZ in PLGA NPs.

	(Drug:PLGA) ratio	*Encapsulation Efficiency (%)*	*Loading Efficiency (%)*
Cur	0.25	80±2.1	20±0.5
	0.5	68±1.8	34±0.9
TPZ	0.25	72±2.3	18±1.1
	0.5	58±3.2	29±1.2
TPZ in Cur+TPZ@PL	0.125	64±2.8	8±0.6
	0.25	25.2±1.6	6.3±0.3
Cur in Cur+TPZ@PL	0.125	56.8±3.2	11±1.2
	0.25	61.2±3.6	15.3±0.9

Similarly, the loading efficiencies of the Cur and TPZ loaded together in PLGA NPs were found to be 15.3±0.9% and 6.3±0.3%, respectively. From serum stability studies, it was observed that the hydrodynamic diameter of the Cur+TPZ loaded RBC-NPs (Cur+TPZ@RB) did not change significantly when incubated with 10% FBS for 48 h, indicating the stability of the drug-loaded nanocarrier in the serum. Long term stability of the Cur+TPZ@RB was studied by incubating them in 10% FBS at 4 °C and recording the hydrodynamic diameter over a period of 15 days. As evident from **Figure 4.8B**, long term storage (2 weeks) at 4 °C did not affect the hydrodynamic diameter of the Cur+TPZ@RB. Similarly, Cur+TPZ@RB demonstrated size stability when stored at -80 °C for 2 weeks, as revealed by DLS measurements (**Figure 4.8C**).

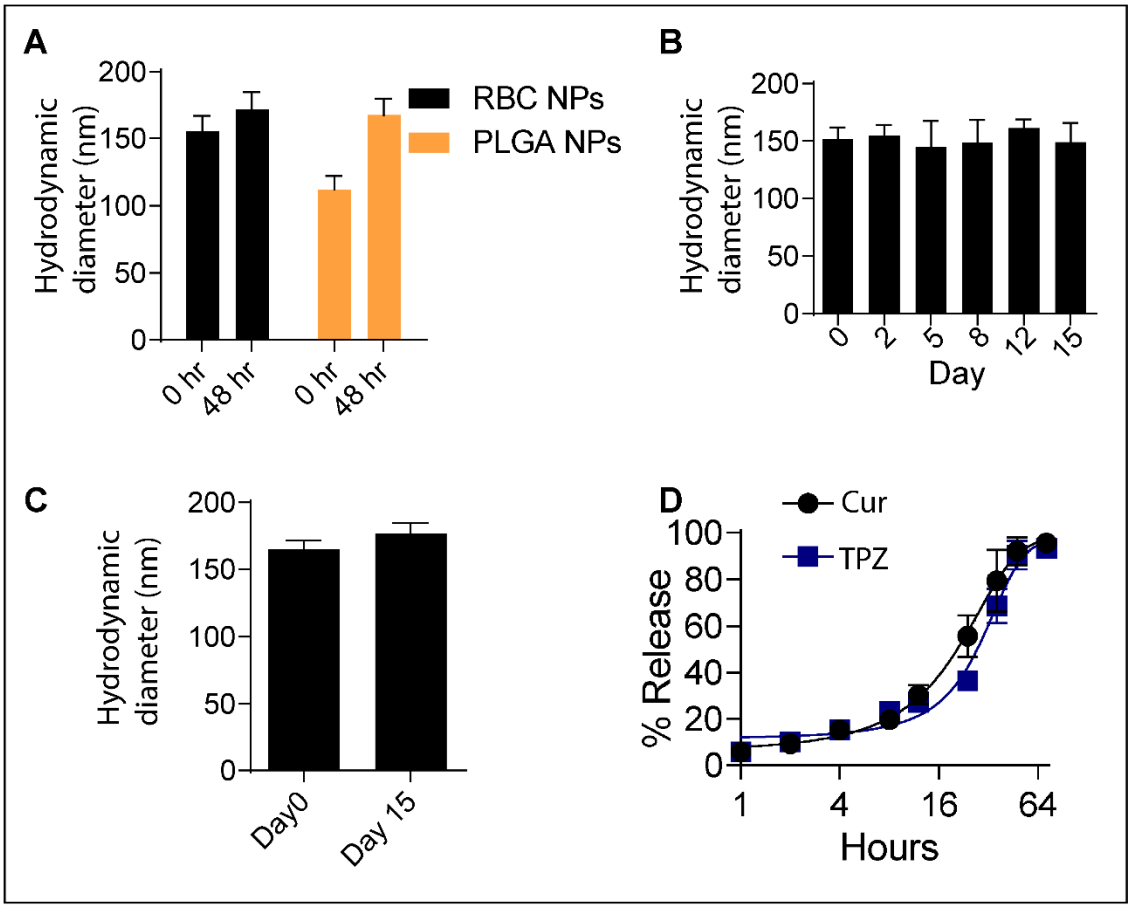

Figure 4.8 (**A**) Size of the PLGA NPs and RBC NPs when stored at 37 °C in FBS for 48 hr. (**B**) Hydrodynamic diameter of the RBC-NPs measured over a period of 15 days. (**C**) Hydrodynamic diameter measured at day 0 and day 15 after storage at -80 °C. (**D**) Release profile of Cur and TPZ from Cur+TPZ@RB NPs.

4.3.3 Drug release study

The release profile of the drugs was studied by incubating the Cur+TPZ@RB at 37 °C and estimating the amount of drug released at regular interval. From the release profile in **Figure 4.8D**, it was observed that both the drugs showed an initial release of the ca. 20-25% within the first 12 h, followed by a sustained release in 4 days. Previous reports demonstrated sustained delivery of paclitaxel from PLGA NPs; whereas a burst release was

documented in case of doxorubicin-loaded NPs.[16,17] Membrane coating of the PLGA NPs may result in the observed sustained delivery of the drugs, Cur and TPZ.

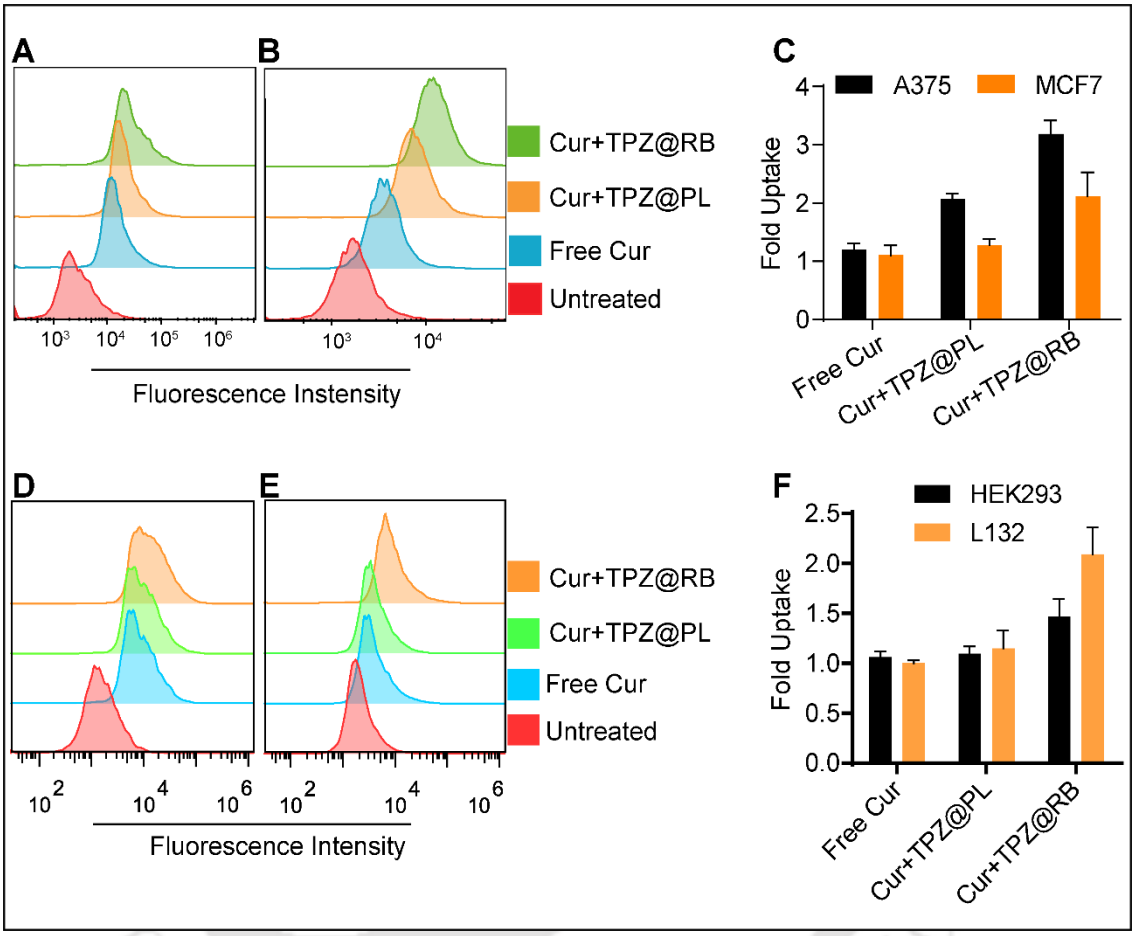

Figure 4.9 (A,B) Flow-cytometric analyses showing Cur fluorescence in MCF-7 (**A**) and A375 (**B**) cells treated with free Cur or nanoparticulate formulations of the drugs. **(C)** Fold uptake calculated from mean fluorescence intensities from MCF-7 and A375 cells. (**D**, **E**) Flow cytometric uptake in HEK293 (**D**) and L132 (**E**) cells and their corresponding fold uptake calculations (**F**).

4.3.4 Improved Internalization of Cur+TPZ@RB

Coating of RBC membrane, as discussed above, provided stability to the RBC-NPs and thereby promising great potential to deliver drug molecules to cancer cells. To assess the effectiveness of RBC NPs for the delivery of Cur and

TPZ, uptake of free Cur, Cur+TPZ loaded PLGA NPs (Cur+TPZ@PL), and Cur+TPZ@RB was studied in A375 (human melanoma cells) and MCF-7 (human breast cancer) cells by probing the Cur fluorescence in flow-cytometer as well as fluorescence microscope.

From flow-cytometric results shown in **Figure 4.9A, B**, it was evident that the Cur+TPZ@RB treated MCF-7 and A375 cells depicted higher Cur fluorescence as compared to free Cur and Cur+TPZ@PL. In **Figure 4.9C**, it was observed that Cur+TPZ@RB treatment resulted in increased Cur uptake by 2 fold in MCF-7 and 3 fold in A375 cells, respectively. Uptake studies in non-cancerous cells namely HEK293 (kidney cells) and L132 (lung cells) also showed 1.4 - 2 fold increased uptake of Cur+TPZ@RB as compared to free Cur (**Figure 4.9D-F**).

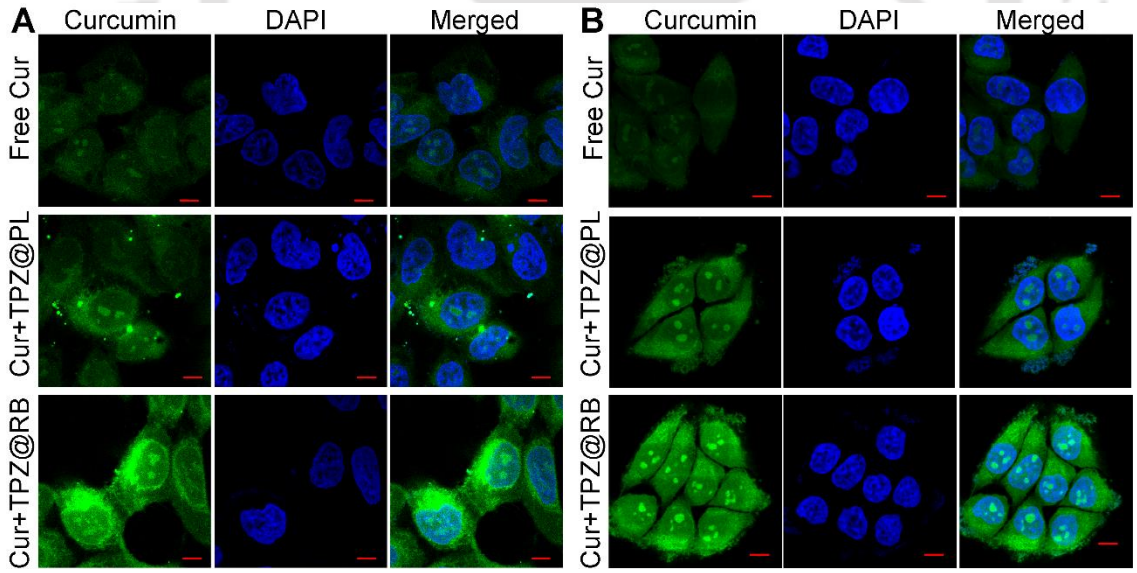

Figure 4.10 (A, B) CLSM images showing Cur uptake in MCF-7 (**A**) and A375 (**B**) cells after incubation with drug-loaded nanoparticles.

Further, fluorescence imaging by confocal laser scanning microscope (CLSM) (**Figure 4.10A, B**) revealed that Cur+TPZ@RB NPs were internalized successfully and localized mostly in the cytoplasm of the MCF-7 and A375 cells. The enhanced uptake of Cur+TPZ@RB than Cur+TPZ@PL, as seen from the increased fluorescence in Cur+TPZ@RB treated cells, could be due to favorable interaction of cells and membrane proteins on Cur+TPZ@RB surface.[18]

4.3.5 Endocytosis pathway study

The endocytosis of the RBC-NPs was confirmed with lysosomal staining (**Figure 4.11**) in CLSM. For this, lysotracker red was used to stain lysosomes in Cur+TPZ@RB treated cells. The results confirmed the presence of the Cur fluorescence within lysosome suggesting Cur+TPZ@RB followed endocytosis route of internalization.

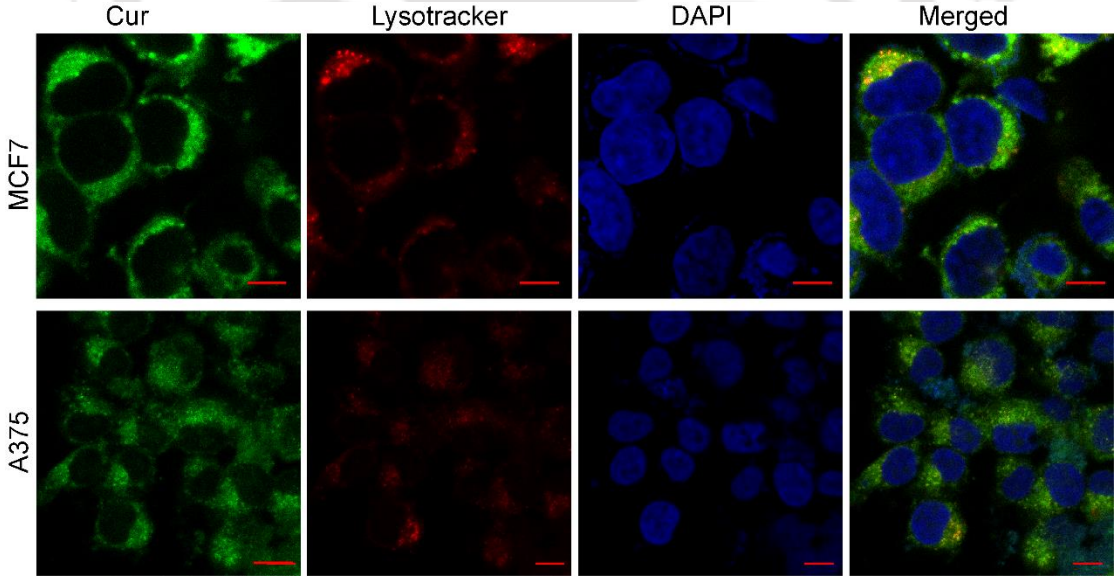

Figure 4.11 Lysosomal staining of MCF and A375 cells treated with drug-loaded nanoparticles showing co-localization of Cur.

Mechanism of the endocytosis was further studied by using endocytosis pathway inhibitors. Clathrin-mediated endocytosis occurs via formation of the clathrin pits after attachment of ligand with the receptor.[19] Additionally, the caveolin/lipid raft-mediated pathway engulfs cholesterol-rich microdomains.[20] In the present study, clathrin and caveolin-mediated endocytosis were inhibited by chlorpromazine and ß-methylcyclodextrin (ß-MCD), respectively. Cur+TPZ@RB uptake at 4°C and in the presence of sodium azide showed a reduction in internalization by 70-90% (**Figure 4.12**), confirming the endocytosis process was energy dependent. Chlorpromazine treatment reduced the Cur+TPZ@RB uptake by 18% and 26% in A375 and MCF-7 cells, respectively; suggesting a possible involvement of the clathrin-mediated pathway. However, ß-MCD reduced the uptake of the Cur+TPZ@RB by 40-50% in A375 and MCF-7 confirming the caveolin mediated pathway played the major role in endocytosis.

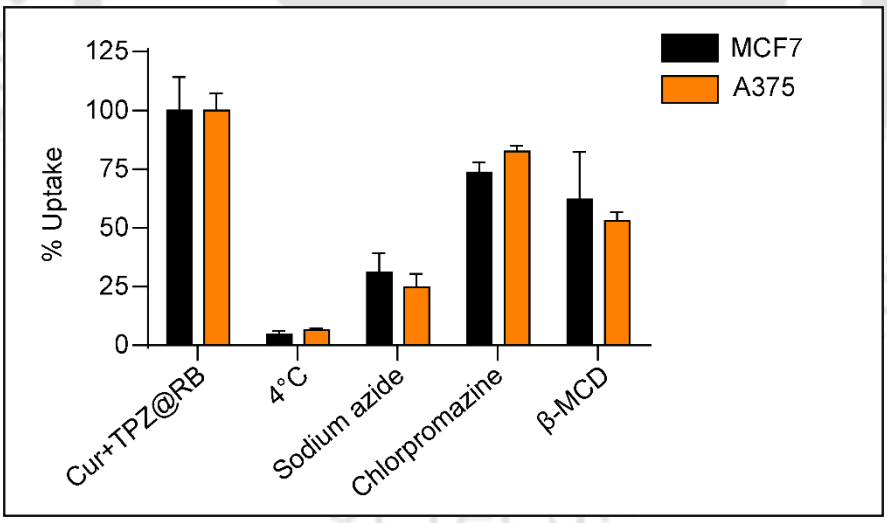

Figure 4.12 Effect of the endocytosis inhibitors on the cellular uptake of Cur+TPZ@RB by MCF-7 and A375 cells.

4.3.6 Macrophage escape of the RBC-NPs

Though the Cur+TPZ@RB NPs showed higher uptake than Cur+TPZ@PL or free Cur, it was important to study the clearance of the NPs by macrophage cells. RBC being a natural carrier in human body essentially skips the uptake and clearance by the macrophage. This escape of the RBCs from macrophage is attributed to the CD47 and other membrane proteins considered as 'self-markers' for macrophages to prevent the uptake.[21] To this end, the uptake of Cur+TPZ@PL and Cur+TPZ@RB NPs was studied in differentiated human macrophage cells (THP-1 cells, **Figure 4.13**). Cur+TPZ@RB treated THP-1 cells demonstrated 60% decrease in uptake as compared to the cells treated with bare Cur+TPZ@PL. Reduced Cur+TPZ@RB uptake by macrophage cells would clearly help to minimize the clearance of these drug-loaded NPs from the body resulting in longer circulation time.

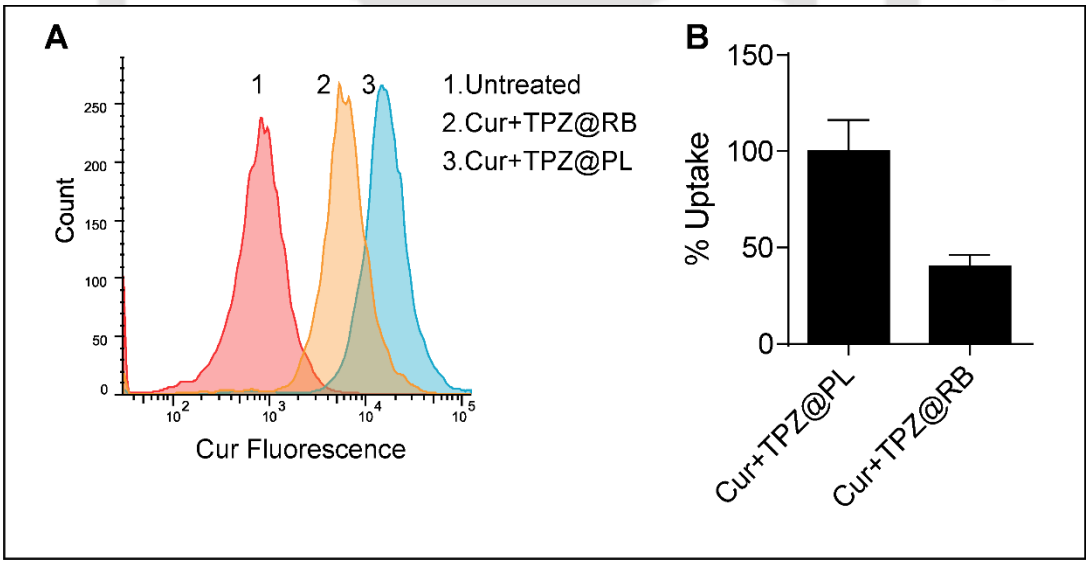

Figure 4.13 Uptake study showing histograms (**A**) of the Cur+TPZ@PL and Cur+TPZ@RB uptake in macrophage cells. (**B**) % Uptake of the Cur+TPZ@RB NPs as compared to Cur+TPZ@PL.

4.3.7 Synergistic Antiproliferative Action of Cur+TPZ@RB in Monolayer Culture:

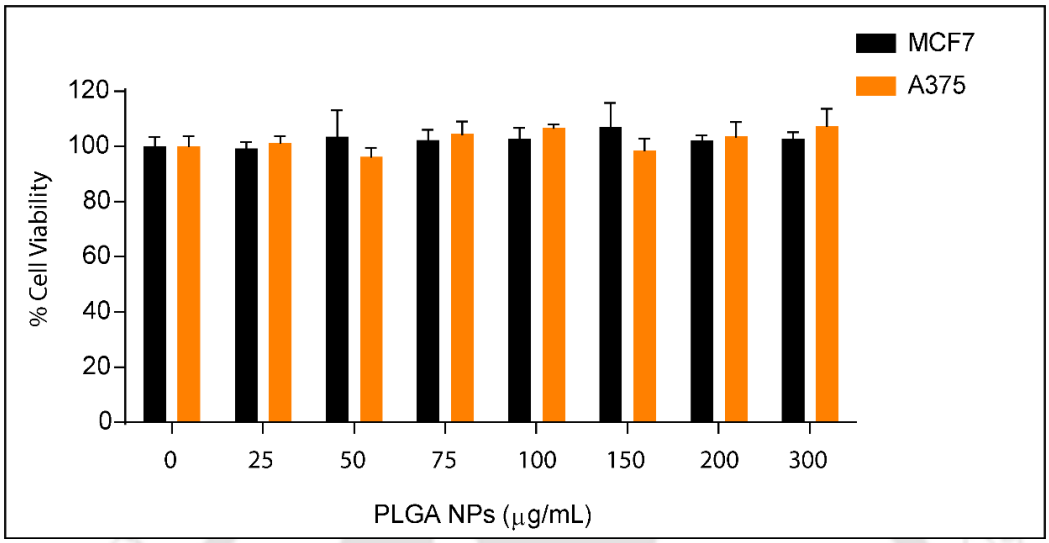

Figure 4.14 Toxicity of the PLGA nanoparticles was studied in MCF-7 and A375 cells for 48 h treatment.

Previous studies reported that PLGA NPs were non-toxic to the cells.[22] The non-toxicity of prepared PLGA NPs (upto the tested concentration of 300 mg/mL) was also observed as depicted in **Figure 4.14** through cell viability assay. In order to evaluate the anticancer potential of the Cur+TPZ@RB, the anti-proliferative efficacies of free drugs (Cur and TPZ), individually and in combination) as well as their nanoparticulate formulations (Cur+TPZ@PL and Cur+TPZ@RB) were examined on MCF-7 and A375 cells by MTT-based viability assay (**Figure 4.15**). As evident from **Figure 4.15** and **Table 4.3**, free Cur and TPZ were able to inhibit the proliferation of MCF-7 (IC_{50}: Cur- 65 μM, TPZ- 142 μM) as well as A375 (IC_{50}: Cur- 98.13 μM, TPZ- 108 μM) cells in a dose-dependent manner when treated individually. Relatively higher IC_{50} values of TPZ corroborated the fact that the drug could only become active in a hypoxic environment while the monolayer cells were mostly normoxic.

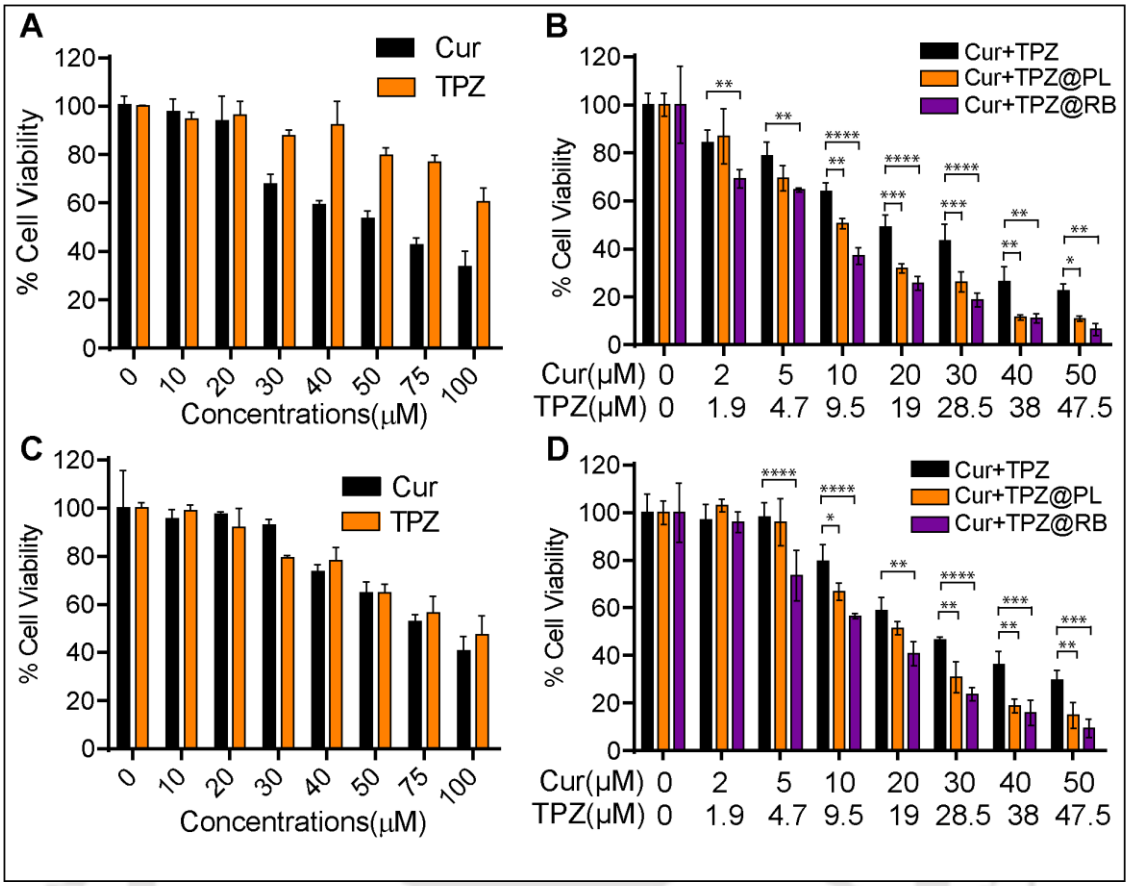

Figure 4.15 (**A**) MTT assay results of Cur and TPZ in MCF-7 cells. (**B**) MTT assay results on MCF-7 cells for Cur+TPZ, Cur+TPZ@PL and Cur+TPZ@RB. (**C**) MTT assay results of Cur and TPZ treatment in A375 cells. (**D**) MTT assay results on A375 cells for Cur+TPZ, Cur+TPZ in PLGA NPs and RBC NPs. (Data shown as mean ± SD, n = 3; $p < 0.05$, $p < 0.01$, $p < 0.001$ and $p < 0.00001$ are denoted as *, **, ***, and **** respectively).

Most importantly, the IC_{50} values calculated from the viability assay (**Table 4.3**) revealed that Cur+TPZ@RB demonstrated higher anti-proliferative response as compared to Cur+TPZ and Cur+TPZ@PL in both MCF-7 and A375 cells. The improved antiproliferative potential of Cur+TPZ@PL or Cur+TPZ@RB could be credited to the increased uptake and probable synergistic action of the drugs employed. To gain insight into the synergism between Cur and TPZ, combination indices (CI) were calculated and summarized in **Table 4.3**. Generally, drug combinations with CI less than 0.3

are considered as strongly synergistic and those with 0.3 to 0.7 are synergistic.[23] Interestingly, for both the cells, CI values calculated using IC_{50} concentrations of Cur+TPZ, Cur+TPZ@PL and Cur+TPZ@RB suggested synergistic behavior of Cur and TPZ with a strong synergistic response in case of Cur+TPZ@RB.

Table 4.3. IC_{50} values of drugs and their nanoparticulate formulations, and combination Indices (CI) calculated from isobolograms for combination treatments.

	Free Drugs					**Nanoparticulate Formulation of Drugs**					
	Individual		***Combination***			***Cur+TPZ@PL***			***Cur+TPZ@RB***		
	IC_{50} (mM)		**IC_{50} (mM)**		**CI**	**IC_{50} (mM)**		**CI**	**IC_{50} (mM)**		**CI**
	Cur	*TPZ*	*Cur*	*TPZ*		*Cur*	*TPZ*		*Cur*	*TPZ*	
	2D Monolayer Culture										
MCF-7	65 ±3	142 ±5	18 ±2	15.5±2	0.6	10 ±3	8.6	0.3	6 ±2	5.1 ±1	0.2
A375	98 ±4	108 ±4	28 ±3	24 ±2	0.5	17 ±4	14.6	0.3	11±1.5	9.4 ±1	0.22
HEK293	33.2±2	128 ±5	25.1 ±2	21.6±2	1	14.3±1	12.3±1	0.5	8 ±1	6.8 ±1	0.3
	3D Multicellular Spheroids										
MCF-7	179 ±9	128 ±6	66.5 ±3	57 ±2	1	60 ±3	52±2	0.8	28.4±2	24±1.2	0.4
A375	194±7	140 ±9	103 ±4	88±3	1	62±5	53±4	0.7	35.9±3	31±2.5	0.4

Similar studies performed on non-cancerous cells (HEK293) confirmed that both Cur+TPZ@PL and Cur+TPZ@RB showed synergistic action in these cells, whereas Cur+TPZ (free drug combinations) were additive in nature (**Table 4.3, Figure 4.16**). One interesting observation from the comparison of the IC_{50} was that TPZ alone showed its effects at very high concentrations. However, when TPZ was used along with Cur, activity increased significantly. Previous studies indicated that delivery of the Cur with nanocarrier caused hypoxia in human neuroblastoma cells.[24] Hence, it was possible that the hypoxic environment generated by Cur possibly triggered activation of the TPZ in monolayer system giving a synergistic antiproliferative response.

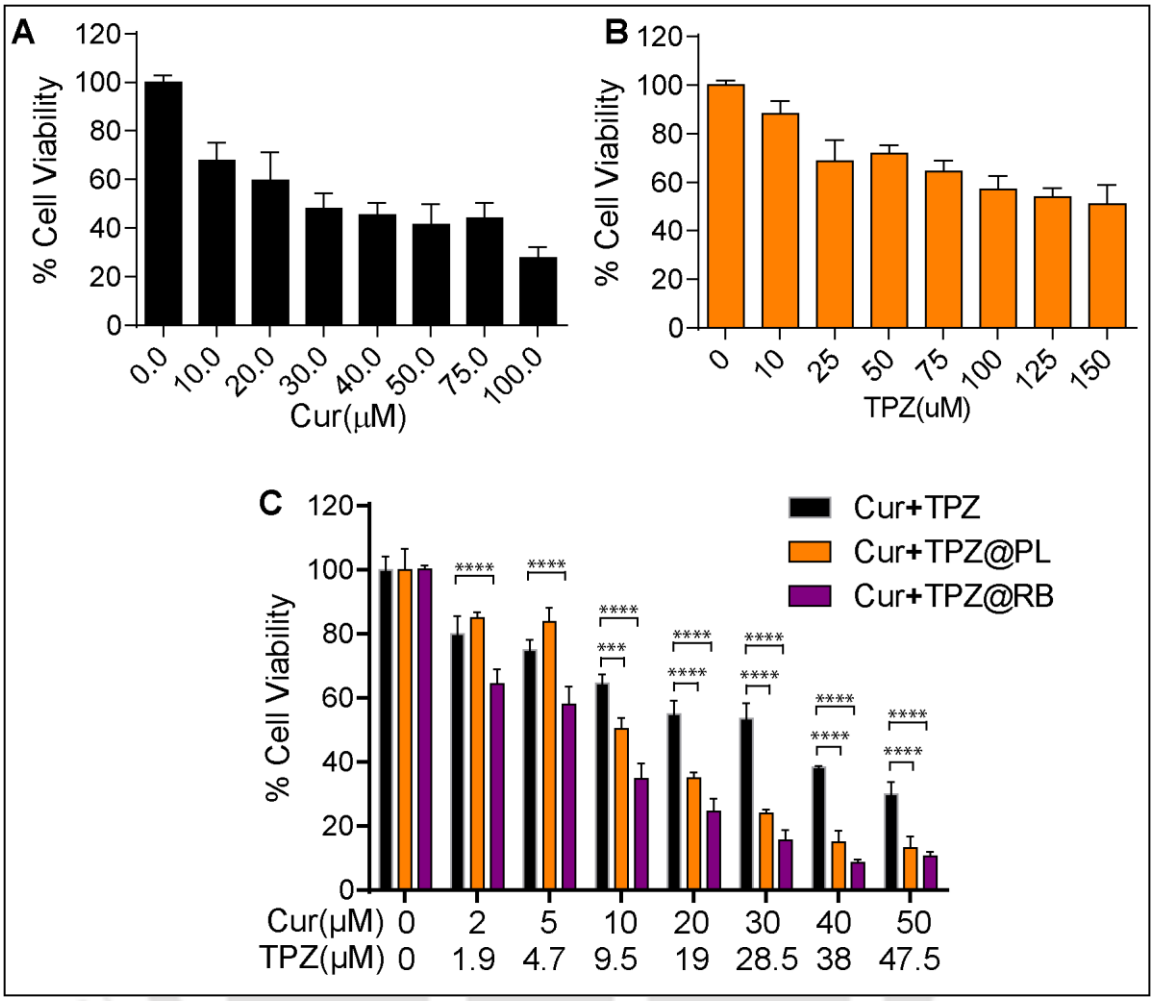

Figure 4.16 (A, B) MTT assay results of Cur and TPZ in HEK293 cells. (**C**) MTT assay results on HEK293 cells for Cur+TPZ, Cur+TPZ@PL and Cur+TPZ@RB. (Data shown as mean ± SD, n = 3; $p < 0.05$, $p < 0.01$, $p < 0.001$ and $p < 0.00001$ are denoted as *, **, ***, and **** respectively).

4.3.8 Apoptosis and cell death analysis study

Quantification of the dead cells after treatment was performed using PI-based flow-cytometric assay (**Figure 4.17A**). The number of dead cells increased in Cur+TPZ@PL (MCF-7- 29%, A375- 25%) treatment when compared to those of free Cur and TPZ. However, maximum killing effect was seen in Cur+TPZ@RB treatment where MCF-7 and A375 cells showed 41% and 39% death,

respectively, due to the enhanced uptake and synergistic behavior of Cur and TPZ as already mentioned.

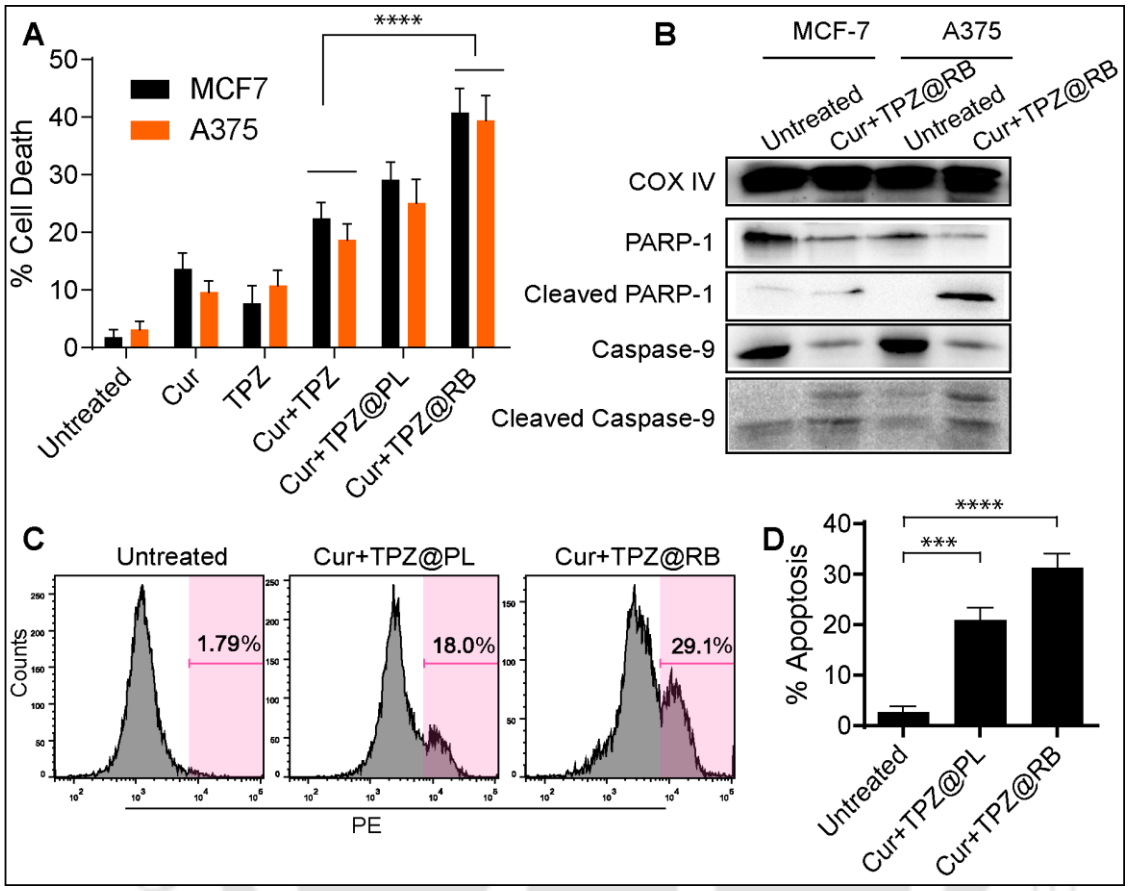

Figure 4.17 (**A**) Measurements of % cell death in treated MCF-7 and A375 cells by flow cytometry. (**B**) Western blots showing cleaved PARP-1 and cleaved caspase-9 after treatment in MCF-7 and A375 cells. (**C**, **D**) Caspase-3 assay results showing number of apoptotic cells positive for active caspase-3.

Cell death via apoptosis – either by extrinsic or intrinsic pathway – involves multiple signaling pathways resulting in activation of caspases. In case of intrinsic pathway, cellular stress or DNA damage results in the release of cytochrome-c, which further cleaves the caspase-9 through the formation of apoptosome. Cleaved caspase 9 finally activates executioner caspases like caspase-3 or 7. The apoptotic potential of the present drug-loaded NPs was studied by measuring caspase-3 activation in A375 cells (**Figure 4.17C, D**).

Cells possessing an active or cleaved form of caspase-3 were quantified. DNA damage in the cells also results in the recruitment of the DNA damage repair proteins like PARP-1, but the presence of active form of the executioner caspases including caspase-3 causes inactivation of the PARP-1 (116 kDa) by cleavage into fragments of 89 kDa and 24 kDa. Flow-cytometric analysis of the cleaved caspase-3 and PI positive cells (**Figure 4.17A, C**) confirmed that Cur+TPZ@RB induces apoptosis more efficiently than Cur+TPZ@PL treated cells. Similarly, it was observed from western blots resulted in **Figure 4.17B** that levels of PARP-1 and caspase-9 decreased in treated MCF-7 and A375 cells followed by a rise in the cleaved counterpart. Collectively, from these results, it was postulated that treatment with Cur+TPZ@RB initiated intrinsic pathway of apoptosis leading to cell death.

4.3.9 Enhanced uptake and cell death in hypoxic 3D multicellular spheroids

Three-dimensional multicellular spheroids (MCS) are considered as a suitable *in-vitro* model, which mimics the *in-vivo* tumor conditions and complexity. To further evaluate the therapeutic potential of Cur+TPZ@RB, we have tested these NPs on MCS of MCF-7 and A375 cells. The presence of hypoxia in monolayer and MCS was assessed by examining the expression of HIF-1α, a well-known marker of hypoxia.[25]

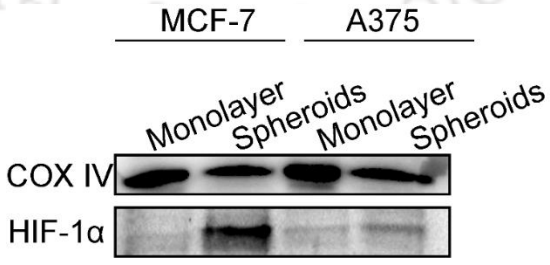

Figure 4.18 Western blot for detection of the HIF-1α protein in MCF-7 and A375 spheroids.

Western blot analysis revealed increased expression of HIF-1α in MCF-7 and A375 spheroids (**Figure 4.18**) as compared to their monolayer counterparts, confirming the MCS as a suitable system to decipher hypoxia-related experiments. Following this, the penetration ability of the nanoparticulate formulations in 3D MCS was studied using CLSM. CLSM images in **Figure 4.19A, B** displayed Cur fluorescence due to the uptake of free Cur, Cur+TPZ@PL, and Cur+TPZ@RB in MCF-7 and A375 MCS, respectively. From the fluorescent intensity representation in 2.5D plots, it was observed that free Cur and Cur+TPZ@PL were able to penetrate the spheroid at the edges, while Cur+TPZ@RB NPs were able to penetrate the spheroid at a deeper level and thus, the fluorescence was seen from the core of the spheroids. As mentioned earlier, RBC coating improved the uptake of the drugs in monolayer and similar results were observed in spheroids. Tumor cores are hypoxic and resistant to therapeutic drugs and thus it becomes important to deliver the therapeutic moiety to the tumor core while retaining the activity.[26]

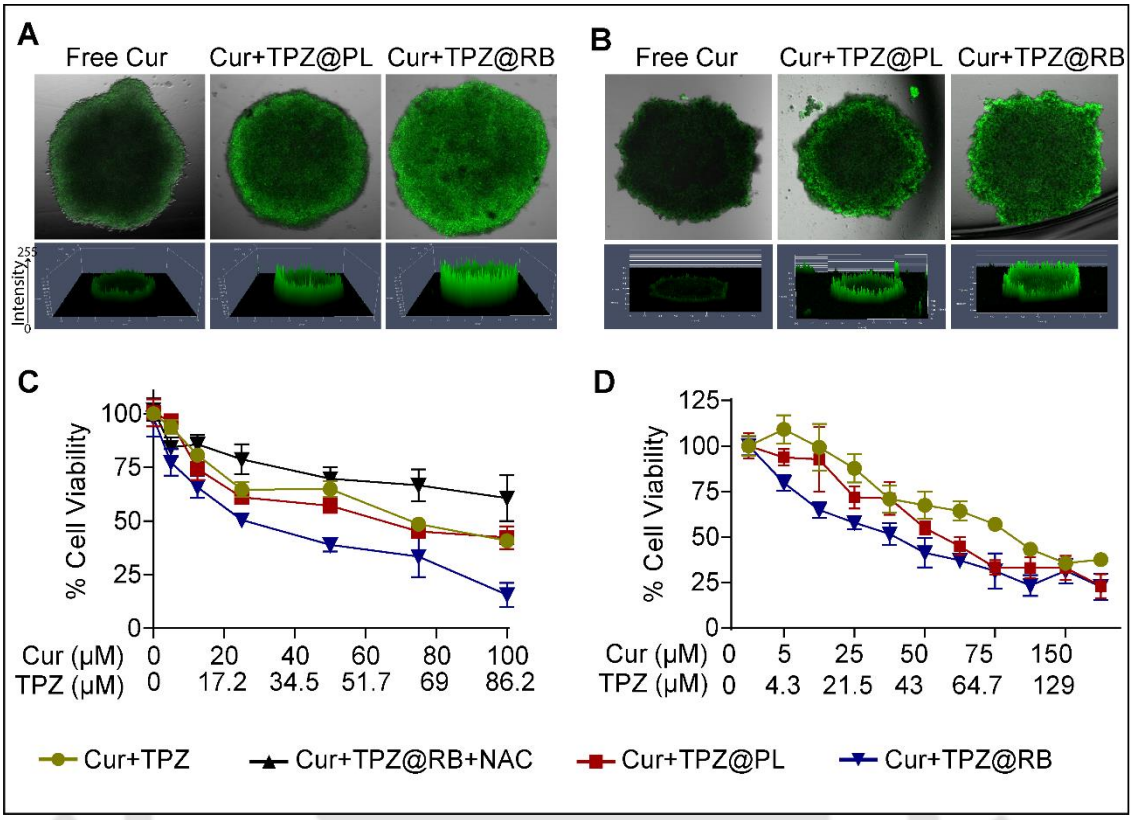

Figure 4.19 (**A**,**B**) Fluorescence microscopic images of (**A**) MCF-7 and (**B**) A375 spheroids showing Cur uptake. (**C**,**D**) Resazurin-based cell viability measurements in MCF-7 (**C**) and A375 (**D**) spheroids after treatment with Cur and TPZ combinations.

In this chapter, anti-proliferative efficiency of Cur and TPZ combinations in the form of Cur+TPZ@PL and Cur+TPZ@RB was also studied. Viability assays were carried out on the MCF-7 and A375 spheroids following 48 h treatment with the free drugs (**Figure 4.20**) as well as their nanoparticulate formulations (**Figure 4.19 C, D**). As expected, the IC_{50} concentrations of free Cur (179±9 μM in MCF-7 and 194 ±7 μM in A375) were much higher in 3D MCS as compared to the 2D monolayer system (6×10^3 cells) (**Table 4.3**), possibly due to the higher cell density in spheroids (2×10^4 cells). Similarly, the IC_{50} values of the TPZ were found to be 128±6 μM and 140±9 μM in MCF-7 and A375 MCS respectively. Even though the cell number was high in MCS,

significant increase in the IC_{50} of the TPZ was not recorded, possibly because of the presence of hypoxia in MCS converting TPZ to its active form and thereby reducing the amount of drug required to reach IC_{50}.

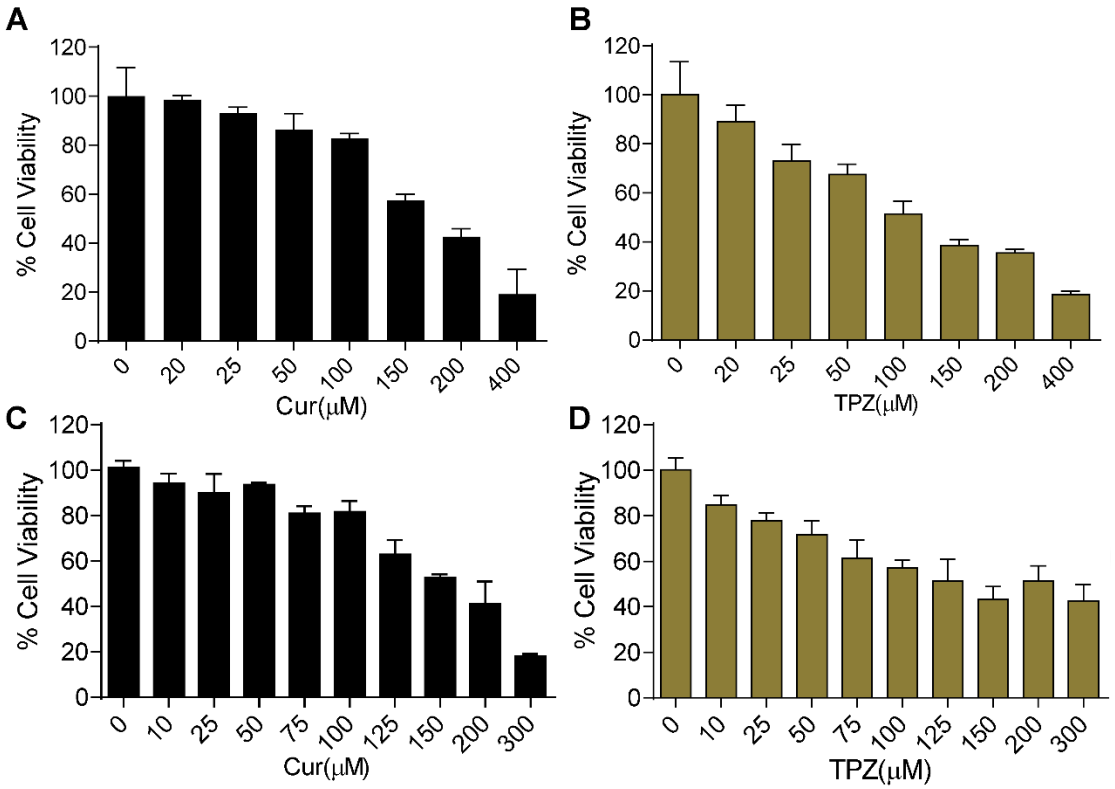

Figure 4.20 Viability assay results after treatment with increasing concentrations of Cur and TPZ on MCF-7 (**A**, **B**) and A375 (**C**, **D**) their respective Spheroids.

In case of drug co-treatment on MCS (**Figure 4.19C-D, Table 4.3**), it was observed that Cur+TPZ@RB was more effective than Cur+TPZ and Cur+TPZ@PL in killing cancer cells as revealed through lower IC_{50} values of the former. As mentioned earlier, spheroids cores are hypoxic in nature and thus provides a suitable environment for the activation of TPZ, whereas Cur can produce reactive oxygen species (ROS).[27] To confirm whether ROS plays any role in cell death, MCF-7 MCS were treated with Cur+TPZ@RB in presence of a ROS-scavenger, N-acetylcysteine (NAC, 1mM). From **Figure**

4.19C, it can be observed that the addition of NAC significantly reduced the cells death suggesting ROS produced by TPZ or Cur played a vital role in cell death in treated MCS. Furthermore, the CI of the Cur+TPZ@PL and Cur+TPZ@RB treatment were found to be less than 1 suggesting the synergistic behavior of the drugs on MCF-7 and A375 MCS (**Table 4.3**).

4.3.10 Cur+TPZ@RB induced cell death observation by Calcein-AM PI staining

The dead cells in MCS following the drug treatment were visualized by fluorescence microscopy. For this, MCF-7 and A375 MCS were treated with Cur+TPZ, Cur+TPZ@PL or Cur+TPZ@RB containing Cur and TPZ equal to the IC_{50} amount of Cur+TPZ@RB. Additionally, by keeping appropriate controls, microscopy was performed to confirm the live and dead cells in spheroid after treatment. Microscopic observation of the Calcein-AM and PI-stained spheroids (**Figure 4.21A, B**) showed green fluorescence from the untreated spheroids confirming the live cells stained with Calcein-AM. On the other hand, the MCS treated Cur+TPZ@PL and Cur+TPZ@RB showed predominantly red fluorescence from PI due to dead cells. The results suggested the penetration ability of the Cur+TPZ@RBs was greatly improved after the RBC membrane coating, thereby increasing the cell-killing ability.

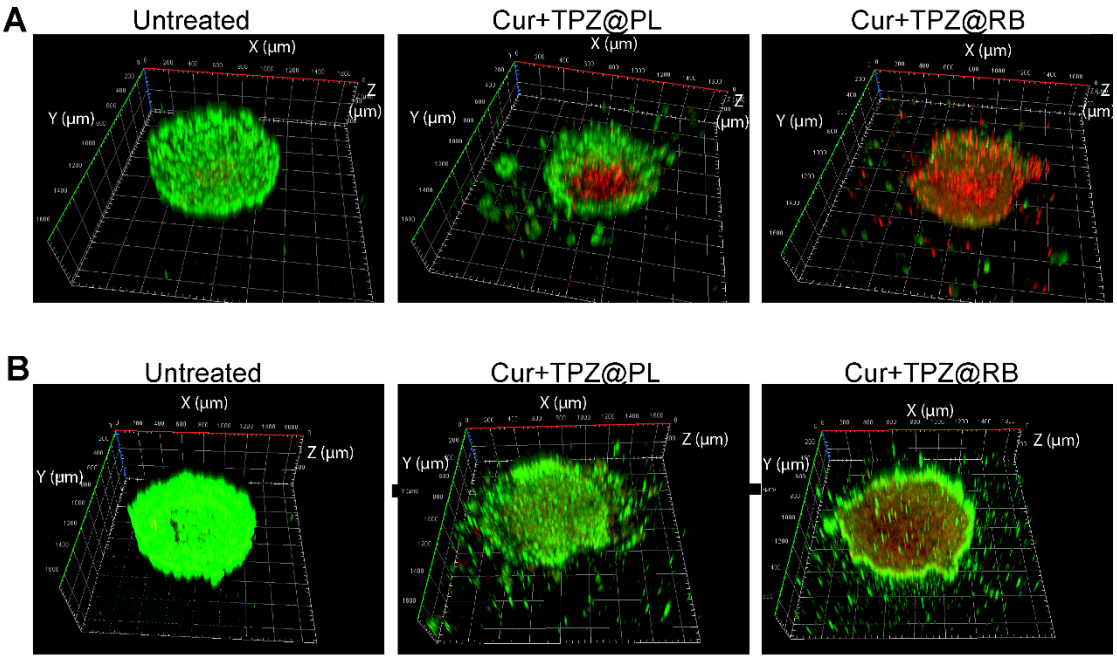

Figure 4.21 (**A**, **B**) Microscopic images of the Calcein-AM/PI stained MCF-7 (**A**) and A375 (**B**) MCS treated with Cur+TPZ@PL or Cur+TPZ@RB.

4.3.11 ROS mediated DNA damage in hypoxic conditions

The investigation into the molecular mechanism of cell death was pursued using ROS and DNA damage analysis. Generation of ROS plays a vital role in cell death and apoptosis.[28] The presence of ROS in treated MCF-7 MCS samples was assessed by DCFDA staining (**Figure 4.22A**). In this regard, RBC-NPs containing only Cur at 28.2 µM (Cur@RB) or TPZ at 24.3 µM (TPZ@RB) were used to study the ROS generation by individual drugs. As expected in Cur@RB treatment, cells showed green fluorescence due to the generation of DCF by ROS. Although this green fluorescence may originate from the Cur itself, when the fluorescence from TPZ@RB and Cur+TPZ@RB treated samples were examined, it was evident that despite the hypoxic environment, Cur+TPZ@RB produced higher ROS than single drug treatments. Cur has been reported to show its antiproliferative activity via producing ROS as well as affecting many signaling pathways.[29] Increased

levels of the ROS affect multiple cellular processes including mitochondrial damage, as a consequence DNA damage events start to follow. Furthermore, the sole mechanism of action of TPZ is the production of single and double-strand breaks in DNA.[30] Herein, DNA damage in treated MCF-7 MCS was investigated by comet assay. Result of the comet assay (**Figure 4.22C**) demonstrated that the Cur+TPZ@RB treatment of MCF-7 spheroids resulted in DNA strand breaks in treated cells. After DNA damage, cells recruit PARP-1 to repair the DNA strand breaks. As already demonstrated **(Figure 4.17B)**, the cleavage of PARP-1 in Cur+TPZ@RB treated cells resulted in apoptosis. It was also found that most of the hypoxia-activated drugs including TPZ show their activity through the production of radical species resulting in DNA damage leading to apoptosis.[31]

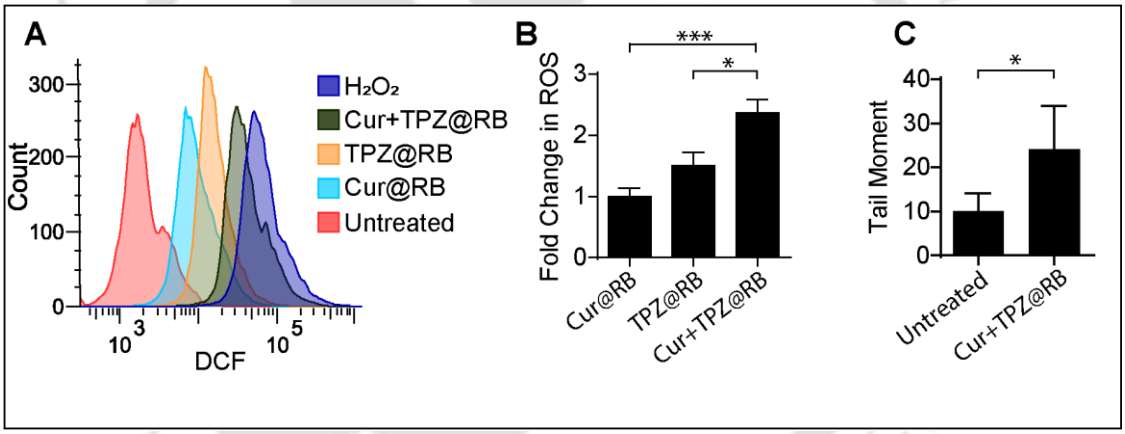

Figure 4.22 (A)Flow cytometric ROS detection assay results in MCF-7 MCS. (**B**) Tail moments calculated from comet assay of treated MCF-7 MCS.

4.3.12 Inhibition of Epithelial to Mesenchymal Transition

Epithelial to mesenchymal transition (EMT) essentially symbolizes the main event of the elaborate metastatic cascade starting from the detachment of the cancer cells from the primary site to migration and growth at secondary organs. In general, epithelial cells at primary tumor site are tightly attached to the basement membrane giving apical-basal polarity to the cells.[32] Under

specific circumstances, multiple biomolecular changes cause cells to become mesenchymal nature gaining invasiveness, migration and altered gene expression.[33] EMT can be characterized by studying the expression of the mesenchymal marker proteins (vimentin, fibronectin, N-cadherin) and epithelial markers (E-cadherin, occludin). It has been observed frequently that the hypoxic cells in the tumor can alter the expression of the hypoxia-related factors resulting in the activation of EMT. In this regard, the expression of vimentin and fibronectin in MCF-7 normoxic monolayer as well as hypoxic MCS was studied. From the realtime PCR results shown in **Figure 4.23,** it was observed that MCF-7 MCS showed higher expression of the vimentin (3.7 fold), and fibronectin (1.9 fold). In earlier studies, increased expression of these two markers in hypoxia was correlated to the mesenchymal state of the metastatic cells. Following this, expression of the vimentin and fibronectin was studied in MCS treated with Cur+TPZ, Cur+TPZ@PL, and Cur+TPZ@RB. The expression of vimentin and fibronectin significantly reduced after treatment at IC_{50} concentration of Cur+TPZ@RB, whereas the Cur+TPZ or Cur+TPZ@PL did not alter the expression significantly (**Figure 4.23).**

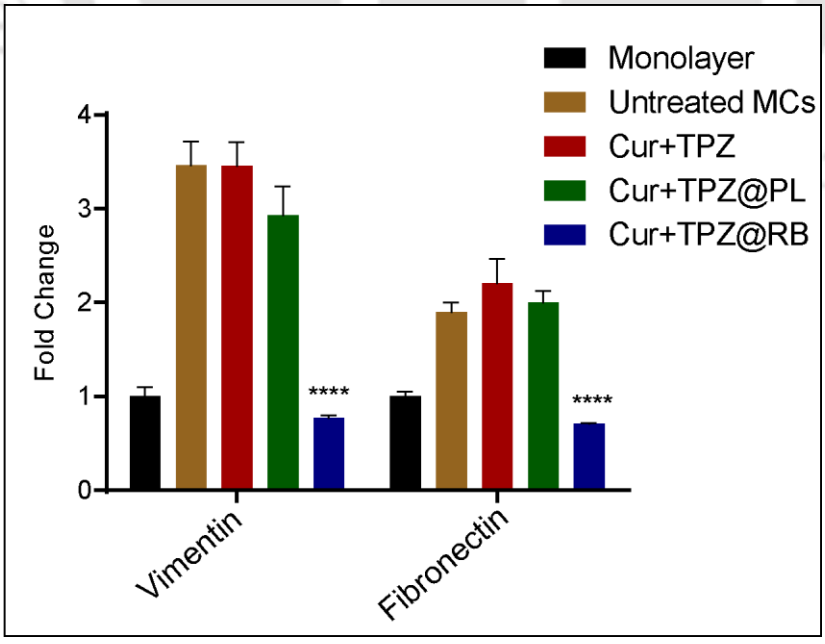

Figure 4.23 Expression of vimentin & fibronectin in untreated and treated MCS by realtime-PCR.

Furthermore, the effect of Cur+TPZ@RB treatment on the migratory behavior of monolayer MCF-7 cells was investigated by wound healing assay. **Figure 4.24A,B** demonstrated 40% wound healing in untreated cells within 48 h, confirming the migration capability of the cells after the scratch was made. Surprisingly, only 22% wound recovery was observed in treated cells because of the reduced migration of the cells due to Cur+TPZ@RB treatment. The reduced migration and down regulations of mesenchymal markers of the treated cells make the Cur+TPZ@RB system an efficient candidate for drug delivery to solid tumors.

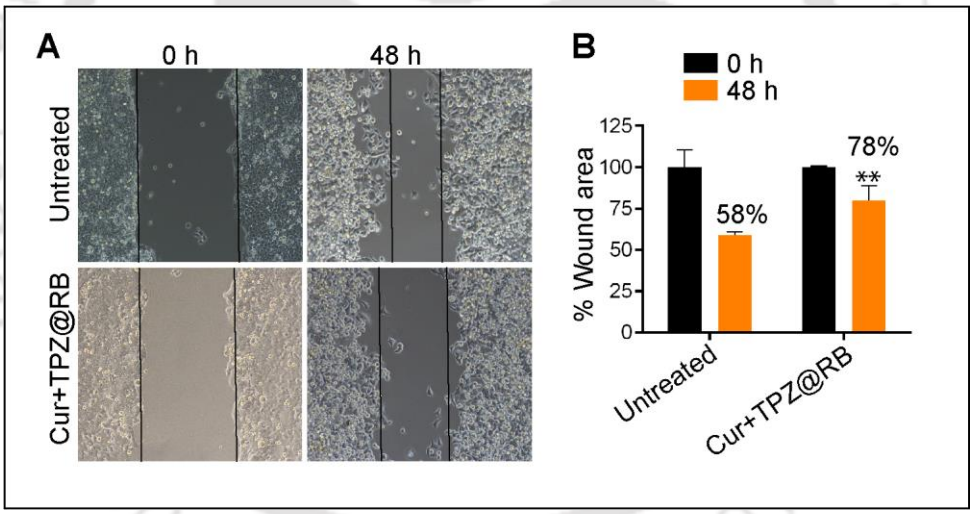

Figure 4.24 (A, B) Wound healing assay results showing percent wound area in untreated and treated samples after 48 h.

4.4 Conclusions

In conclusion, RBC membrane-coated PLGA NPs were prepared and successfully loaded with Cur and TPZ for potential anticancer drug delivery. These drug-loaded nanoparticles (Cur+TPZ@RB) demonstrated excellent

antiproliferative response in MCF-7 and A375 cancer cells, both in 2D monolayer as well as 3D spheroid culture. Uptake studies in A375 and MCF-7 monolayer cells indicated the internalization of the Cur+TPZ@RB occurred via endocytosis with a particular preference toward the caveolin-mediated pathway. Further investigations revealed that Cur+TPZ@RB exhibited synergistic cell death response in A375 and MCF-7 monolayer cells and spheroids. Generation of the reactive oxygen species, DNA damage, and activation of caspases were found to be the major driving factors for apoptotic cell death in Cur+TPZ@RB treated cancer cells. Furthermore, Cur+TPZ@RB were able to reduce the elevated levels of the mesenchymal markers including vimentin and fibronectin in the spheroids of MCF cells suggesting a reduction of EMT with improved therapeutic efficacy of the anticancer drugs.

4.5 References

(1) Hockel, M.; Schlenger, K.; Aral, B.; Mitze, M.; Schaffer, U.; Vaupel, P. Association between Tumor Hypoxia and Malignant Progression in Advanced Cancer of the Uterine Cervix. *Cancer Res.* **1996**, *56* (19), 4509–4515.

(2) Bao, B.; Azmi, A. S.; Ali, S.; Ahmad, A.; Li, Y.; Banerjee, S.; Kong, D.; Sarkar, F. H. The Biological Kinship of Hypoxia with CSC and EMT and Their Relationship with Deregulated Expression of MiRNAs and Tumor Aggressiveness. *Biochim. Biophys. Acta - Rev. Cancer* **2012**, *1826* (2), 272–296. https://doi.org/10.1016/J.BBCAN.2012.04.008.

(3) Schindl, M.; Schoppmann, S. F.; Samonigg, H.; Hausmaninger, H.; Kwasny, W.; Gnant, M.; Jakesz, R.; Kubista, E.; Birner, P.; Oberhuber, G.; et al. Overexpression of Hypoxia-Inducible Factor 1alpha Is Associated with an Unfavorable Prognosis in Lymph Node-Positive Breast Cancer. *Clin. Cancer Res.* **2002**, *8* (6), 1831–1837. https://doi.org/10.1158/1078-0432.ccr-03-0135.

(4) Valastyan, S.; Weinberg, R. A. Tumor Metastasis: Molecular Insights and Evolving Paradigms. *Cell* **2011**, *147* (2), 275–292. https://doi.org/10.1016/j.cell.2011.09.024.

(5) Li, H.; Sun, H.; Qian, Z. M. The Role of the Transferrin-Transferrin-Receptor System in Drug Delivery and Targeting. *Trends Pharmacol. Sci.* **2002**, *23* (5), 206–209.

(6) De Jong, W. H.; Borm, P. J. A. Drug Delivery and Nanoparticles:Applications

and Hazards. *Int. J. Nanomedicine* **2008**, *3* (2), 133–149.

(7) Brigger, I.; Dubernet, C.; Couvreur, P. Nanoparticles in Cancer Therapy and Diagnosis. *Advanced Drug Delivery Reviews*. 2002, pp 631–651. https://doi.org/10.1016/S0169-409X(02)00044-3.

(8) Hu, C.-M. J.; Zhang, L.; Aryal, S.; Cheung, C.; Fang, R. H.; Zhang, L. Erythrocyte Membrane-Camouflaged Polymeric Nanoparticles as a Biomimetic Delivery Platform. *Proc. Natl. Acad. Sci. U. S. A.* **2011**, *108* (27), 10980–10985. https://doi.org/10.1073/pnas.1106634108.

(9) Foo, Y.; Periasamy, V.; Kiew, L.; Kumar, G.; Malek, S.; Foo, Y. Y.; Periasamy, V.; Kiew, L. V.; Kumar, G. G.; Malek, S. N. A. Curcuma Mangga-Mediated Synthesis of Gold Nanoparticles: Characterization, Stability, Cytotoxicity, and Blood Compatibility. *Nanomaterials* **2017**, *7* (6), 123. https://doi.org/10.3390/nano7060123.

(10) Ivanov, D. P.; Parker, T. L.; Walker, D. A.; Alexander, C.; Ashford, M. B.; Gellert, P. R.; Garnett, M. C. Multiplexing Spheroid Volume, Resazurin and Acid Phosphatase Viability Assays for High-Throughput Screening of Tumour Spheroids and Stem Cell Neurospheres. *PLoS One* **2014**, *9* (8), e103817. https://doi.org/10.1371/journal.pone.0103817.

(11) Olive, P. L.; Banáth, J. P. The Comet Assay: A Method to Measure DNA Damage in Individual Cells. *Nat. Protoc.* **2006**, *1* (1), 23–29. https://doi.org/10.1038/nprot.2006.5.

(12) Petros, R. A.; DeSimone, J. M. Strategies in the Design of Nanoparticles for Therapeutic Applications. *Nat. Rev. Drug Discov.* **2010**, *9* (8), 615–627. https://doi.org/10.1038/nrd2591.

(13) Wolfram, J.; Zhu, M.; Yang, Y.; Shen, J.; Gentile, E.; Paolino, D.; Fresta, M.; Nie, G.; Chen, C.; Shen, H.; et al. Safety of Nanoparticles in Medicine. *Curr. Drug Targets* **2015**, *16* (14), 1671–1681.

(14) Tanaka, T.; Narazaki, M.; Kishimoto, T. IL-6 in Inflammation, Immunity, and Disease. *Cold Spring Harb. Perspect. Biol.* **2014**, *6* (10), a016295–a016295. https://doi.org/10.1101/cshperspect.a016295.

(15) Akdis, M.; Burgler, S.; Crameri, R.; Eiwegger, T.; Fujita, H.; Gomez, E.; Klunker, S.; Meyer, N.; O'Mahony, L.; Palomares, O.; et al. Interleukins, from 1 to 37, and Interferon-γ: Receptors, Functions, and Roles in Diseases. *J. Allergy Clin. Immunol.* **2011**, *127* (3), 701–721.e70. https://doi.org/10.1016/J.JACI.2010.11.050.

(16) Fonseca, C.; Simões, S.; Gaspar, R. Paclitaxel-Loaded PLGA Nanoparticles: Preparation, Physicochemical Characterization and in Vitro Anti-Tumoral Activity. *J. Control. Release* **2002**, *83* (2), 273–286. https://doi.org/10.1016/S0168-3659(02)00212-2.

(17) Malinovskaya, Y.; Melnikov, P.; Baklaushev, V.; Gabashvili, A.; Osipova, N.; Mantrov, S.; Ermolenko, Y.; Maksimenko, O.; Gorshkova, M.; Balabanyan, V.; et al. Delivery of Doxorubicin-Loaded PLGA Nanoparticles into U87 Human Glioblastoma Cells. *Int. J. Pharm.* **2017**, *524* (1–2), 77–90. https://doi.org/10.1016/J.IJPHARM.2017.03.049.

(18) Dehaini, D.; Wei, X.; Fang, R. H.; Masson, S.; Angsantikul, P.; Luk, B. T.; Zhang, Y.; Ying, M.; Jiang, Y.; Kroll, A. V.; et al. Erythrocyte-Platelet Hybrid Membrane Coating for Enhanced Nanoparticle Functionalization. *Adv. Mater.* **2017**, *29* (16), 1606209. https://doi.org/10.1002/adma.201606209.

(19) Kaksonen, M.; Roux, A. Mechanisms of Clathrin-Mediated Endocytosis. *Nat. Rev. Mol. Cell Biol.* **2018**, *19* (5), 313–326. https://doi.org/10.1038/nrm.2017.132.

(20) Nabi, I. R.; Le, P. U. Caveolae/Raft-Dependent Endocytosis. *J. Cell Biol.* **2003**, *161* (4), 673–677. https://doi.org/10.1083/jcb.200302028.

(21) Oldenborg, P. A.; Zheleznyak, A.; Fang, Y. F.; Lagenaur, C. F.; Gresham, H. D.; Lindberg, F. P. Role of CD47 as a Marker of Self on Red Blood Cells. *Science* **2000**, *288* (5473), 2051–2054. https://doi.org/10.1126/SCIENCE.288.5473.2051.

(22) Hung, H.-I.; Klein, O. J.; Peterson, S. W.; Rokosh, S. R.; Osseiran, S.; Nowell, N. H.; Evans, C. L. PLGA Nanoparticle Encapsulation Reduces Toxicity While Retaining the Therapeutic Efficacy of EtNBS-PDT in Vitro. *Sci. Rep.* **2016**, *6* (1), 33234. https://doi.org/10.1038/srep33234.

(23) Chou, T.-C.; Talalay, P. Quantitative Analysis of Dose-Effect Relationships: The Combined Effects of Multiple Drugs or Enzyme Inhibitors. *Adv. Enzyme Regul.* **1984**, *22*, 27–55. https://doi.org/10.1016/0065-2571(84)90007-4.

(24) Kalashnikova, I.; Mazar, J.; Neal, C. J.; Rosado, A. L.; Das, S.; Westmoreland, T. J.; Seal, S. Nanoparticle Delivery of Curcumin Induces Cellular Hypoxia and ROS-Mediated Apoptosis via Modulation of Bcl-2/Bax in Human Neuroblastoma. *Nanoscale* **2017**, *9* (29), 10375–10387. https://doi.org/10.1039/C7NR02770B.

(25) Sullivan, R.; Pare, G. C.; Frederiksen, L. J.; Semenza, G. L.; Graham, C. H. Hypoxia-Induced Resistance to Anticancer Drugs Is Associated with Decreased Senescence and Requires Hypoxia-Inducible Factor-1 Activity. *Mol. Cancer Ther.* **2008**, *7* (7), 1961–1973. https://doi.org/10.1158/1535-7163.MCT-08-0198.

(26) Guppy, M. The Hypoxic Core: A Possible Answer to the Cancer Paradox. *Biochem. Biophys. Res. Commun.* **2002**, *299* (4), 676–680. https://doi.org/10.1016/S0006-291X(02)02710-9.

(27) KIM, J. W.; HO, W. J.; WU, B. M. The Role of the 3D Environment in Hypoxia-Induced Drug and Apoptosis Resistance. *Anticancer Res.* **2011**, *31* (10), 3237–3245.

(28) Redza-Dutordoir, M.; Averill-Bates, D. A. Activation of Apoptosis Signalling

Pathways by Reactive Oxygen Species. *Biochim. Biophys. Acta - Mol. Cell Res.* **2016**, *1863* (12), 2977–2992. https://doi.org/10.1016/J.BBAMCR.2016.09.012.

(29) Thayyullathil, F.; Chathoth, S.; Hago, A.; Patel, M.; Galadari, S. Rapid Reactive Oxygen Species (ROS) Generation Induced by Curcumin Leads to Caspase-Dependent and -Independent Apoptosis in L929 Cells. *Free Radic. Biol. Med.* **2008**, *45* (10), 1403–1412. https://doi.org/10.1016/J.FREERADBIOMED.2008.08.014.

(30) Reddy, S. B.; Williamson, S. K. Tirapazamine: A Novel Agent Targeting Hypoxic Tumor Cells. *Expert Opin. Investig. Drugs* **2009**, *18* (1), 77–87. https://doi.org/10.1517/13543780802567250.

(31) Baran, N.; Konopleva, M. Molecular Pathways: Hypoxia-Activated Prodrugs in Cancer Therapy. *Clin. Cancer Res.* **2017**, *23* (10), 2382–2390. https://doi.org/10.1158/1078-0432.CCR-16-0895.

(32) Heerboth, S.; Housman, G.; Leary, M.; Longacre, M.; Byler, S.; Lapinska, K.; Willbanks, A.; Sarkar, S. EMT and Tumor Metastasis. *Clin. Transl. Med.* **2015**, *4*, 6. https://doi.org/10.1186/s40169-015-0048-3.

(33) Mittal, V. Epithelial Mesenchymal Transition in Tumor Metastasis. *Annu. Rev. Pathol. Mech. Dis.* **2018**, *13* (1), 395–412. https://doi.org/10.1146/annurev-pathol-020117-043854.

CHAPTER 5

Targeted drug delivery using membrane coated nanocarriers

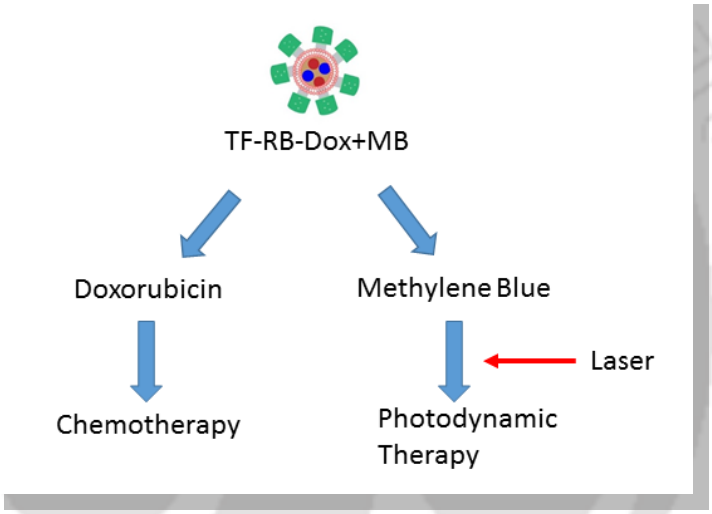

Chapter 5 demonstrates the therapeutic efficiency of the transferrin bound RBC membrane-coated PLGA NPs to deliver doxorubicin and methylene blue for chemo- and photodynamic therapy. PLGA NPs loaded with doxorubicin and methylene blue were extruded with transferrin bound RBC membranes, forming TF-DoxMB NPs. These targeted NPs improved the therapeutic potential of the doxorubicin. Additionally, laser irradiation on methylene blue synergistically improved the activity due to photodynamic therapy.

CHAPTER 5

5.1 Introduction

In recent past, several anticancer agents have been discovered, but their use is mostly limited due to certain disadvantages.[1] Major drawbacks include non-specific delivery, unexpected pharmacodynamics and pharmacokinetic properties, which are subjected to change, if such potent molecules are delivered by suitable carriers at the desired sites. Therefore, development of carriers have been aggressively persuaded to improve drug bioavailability and efficacy with concomitant reduction of undesirable side effects due to non-specific delivery.[2] To this end, research in the field of nano-based drug delivery systems (DDS) for targeted drug delivery applications has been progressed significantly.[3] Designing nanocarriers to deliver the payloads at specific sites is the primary goal for developing newer nano-based vehicles. Another essential characteristic of the nanocarriers is the possibility of surface modification, which allows targeting of the nanocarriers to specific cells or tissue.[4] Surface modification results in the delivery of the cargo, specifically to the target cells, thereby avoiding the off-target delivery and side effects associated with it. Tumor cells specific biomarkers, which are usually overexpressed in only tumor cells, can be utilized for targeting the nanocarriers towards cancer cells.

Additionally, biodegradability, long-circulating, and non-immunogenicity of the nanocarriers are the desirable aspects that are achieved for slow and efficient release of drug molecules.[5] Although multiple nanocarriers have been developed for targeted drug delivery, the rise of the new drug-resistant tumors has made it impossible to cure them completely with the help of monotherapies. Therefore, most of the cancer treatment includes drug combinations as well as the use of radiation therapy.[6,7] In this domain,

photodynamic therapy has gained attention due to development of the newer photodynamic agents. In case of the photodynamic therapy, light irradiated on photosensitizer generates ROS, killing nearby cells.[8] Recent studies reported that the combination of the chemo- and photodynamic therapy could help to eradicate the tumor effectively.[9,10]

In this study, we have developed multifunctional RBC membrane-coated nanoparticles for delivery of doxorubicin (Dox) and methylene blue (MB) for chemo- and photodynamic therapy. PLGA NPs loaded with Dox and MB were coated with RBC membranes by extrusion, forming membrane coated PLGA NPs (RB-DoxMB NPs). Further, to target specific delivery of RB-DoxMB NPs to tumor cells, transferrin was conjugated onto RBC membranes before extrusion (**Scheme 5.1**). Drug (Dox and MB) loaded, transferrin-bound RBC membrane coated PLGA NPs (TF-DoxMB NPs) were characterized and used to achieve targeted chemo and photodynamic therapy. Microscopic and flow cytometric assays were carried out to study the route of internalization of TF-DoxMB. Along with specific action of Dox, red laser irradiation of the treated cells resulted in the production of ROS due to MB inside the cells. Anti-proliferative effects of the laser-irradiated TF-DoxMB (TF-DoxMB+L) were studied on a monolayer (2D) as well as the 3D spheroids.

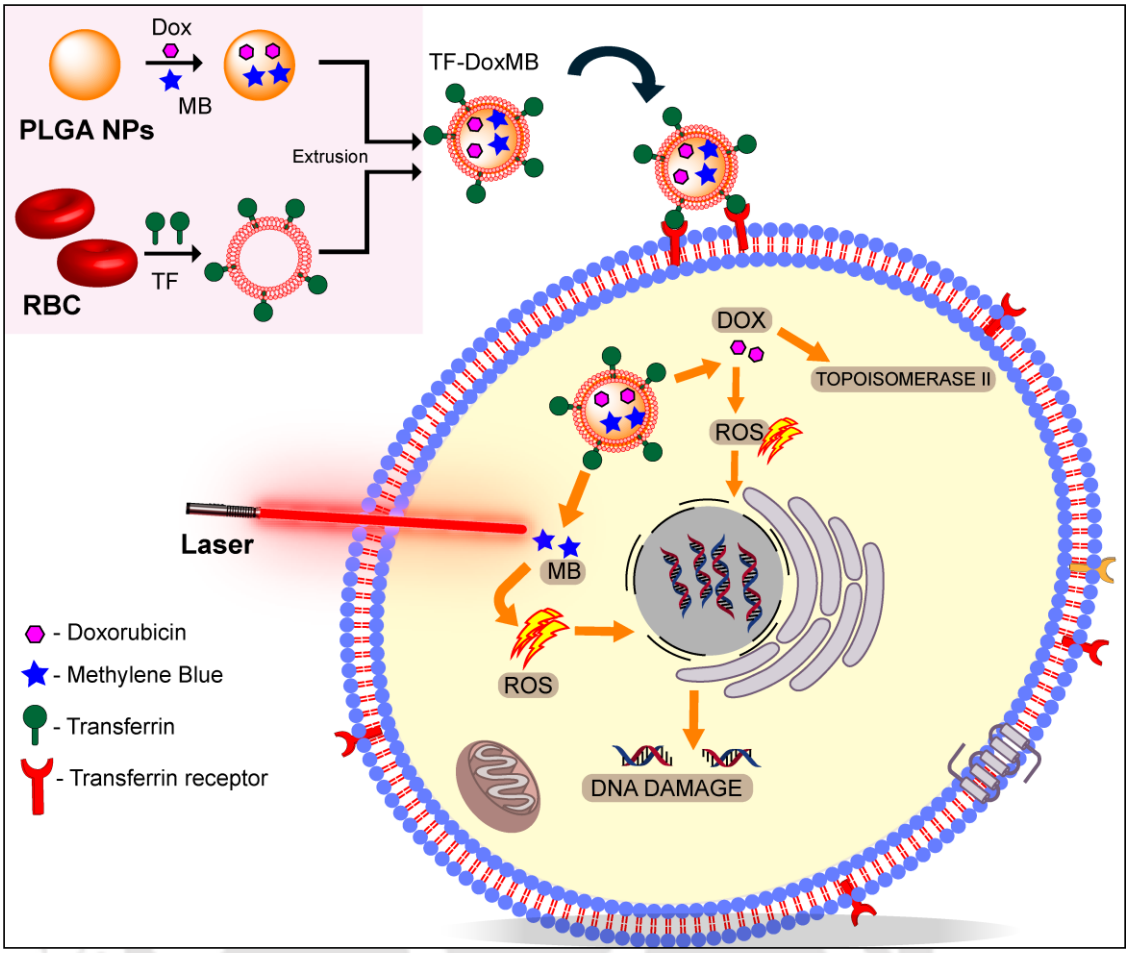

Scheme 5.1 Schematic representation of the therapeutic approach by combining chemo- and photodynamic therapy.

5.2 Experimental Section

5.2.1 Materials

Poly(lactic-co-glycolic acid) (PLGA), Ethylenediaminetetraacetic acid (EDTA) salt, Dulbecco's Modified Eagle's medium (DMEM), MTT (3-(4,5-Dimethylthiazol-2-yl)-2,5-diphenyltetrazolium bromide), Propidium iodide (PI), Doxorubicin, Methylene blue, were purchased from Sigma Aldrich. The anti-active caspase-3 antibody and APO-DIRECT Kit were purchased from BD Biosciences. Anti- AE-1 antibody (Cat. No. 23276) was purchased from cell signalling technology.

5.2.2 Preparation of PLGA NPs and RBC membrane coated PLGA NPs (RB-NPs)

PLGA cores were prepared by nanoprecipitation method with slight modifications.[11] PLGA (1mg/mL) was dissolved in acetone; this PLGA solution was added dropwise to 5 mL water while continuous stirring. Formed PLGA NPs were centrifuged at 20000 g and lyophilized. Hemoglobin free-RBC membrane was isolated according to the method described by Hu *et al.*[11] Whole blood was collected from healthy individuals, according to Institute Human Ethics Committee guidelines. Blood was centrifuged at 900xg (5 min, 4 ^{o}C), buffy coat and plasma were removed without disturbing RBC pellet. RBCs were resuspended and washed with 1X PBS thrice before subjecting to the hypotonic treatment of 0.25X PBS (4 ^{o}C, for 30 min). After complete lysis, cells membranes were centrifuged at 15000xg for 20 min, washed with PBS two times to remove free hemoglobin. These RBC membranes were extruded through 0.8, 0.4, 0.2 μm pore size membranes to form RBC vesicles. PLGA NPs and membrane vesicles were extruded together to form RBC membrane-coated NPs (RB-NPs).

5.2.3 Preparation of the TF-conjugated RBC membrane coated PLGA NPs (TF-RB-NPs)

In order to achieve TF receptor-targeted therapy, TF molecules were conjugated to RBC membranes, and these TF-conjugated RBC membranes were utilized to coat PLGA NPs to form TF-RB-NPs. To conjugate the TF on RBC membranes EDC-NHS coupling mechanism was utilized. In order to prepare RBC membranes with varying density of TF on their surface, different ratios of the TF: membrane proteins (0.02 to 0.4, as mentioned in (**Table 5.1**) were reacted. The concentrations ratios of TF:EDC:NHS were selected on the basis of number of amine side chain containing amino acids of TF protein. The

molar ratios of TF(NH_2):EDC: NHS were kept constant at 1:2:4 for all reactions. Amount of the TF bound on the RBC membrane surface was determined by Bradford assay. The TF-conjugated membranes were collected and used to coat Dox loaded PLGA NPs. The prepared TF-conjugated membrane coated NPs (TF-Dox-NPs) were named as TF-0.02- to TF0.4-Dox-NPs based on the membrane used for coating (**Table 5.1**).

5.2.4 Characterization of the PLGA-NPs, RB-NPs, and TF-RB-NPs

All the prepared NPs were characterized for their hydrodynamic diameter (d_H) and zeta potential (ζ) in Malvern Zetasizer. For TEM analysis, NPs were drop cast on a copper grid, allowed to dry. These NPs were negatively stained with uranyl acetate and observed under a TEM microscope. For FESEM imaging, NPs were drop cast on aluminum foil coated NPs, dried and observed under the microscope (SIGMA, ZEISS). For long-term stability study of the drug loaded TF-RB NPs, NPs were stored at 4 ºC for 14 days, and the d_H were measured at different intervals. Similarly, for serum stability studies, NPs incubated with FBS (10%, at 37 ºC, for 24 h) were studied in DLS to record changes in hydrodynamic diameter.

5.2.5 Western blot analysis

Western blot analysis of the residual proteins from RBC membranes was performed. RBC membrane proteins from intact RBC, RBC membrane pellet and RBC membrane coated NPs were isolated in RIPA buffer. The amount of the proteins were quantified Bradford assay, and 25 µg of the proteins from all the samples were separated on SDS-PAGE (sodium dodecyl sulfate-polyacrylamide gel electrophoresis). These separated proteins were transferred to PVDF membrane, and AE-1 protein was detected after primary and secondary antibody staining.

5.2.6 Drug loading and release study

In order to load Dox and MB molecules in the NPs, these drugs were mixed water and PLGA NPs prepared in the presence of the drugs to form drug-loaded PLGA NPs. These drug-loaded PLGA NPs were coated with RBC membranes by extrusion to form TF-DoxMB NPs. Amount of the drugs loaded onto the NPs were calculated by taking fluorescence measurements for Dox ($\lambda_{excitation}$: 480 nm, $\lambda_{emission}$: 595 nm) and UV-visible spectra for MB (λ_{abs} 667 nm). Release of the Dox and MB from TF-DoxMB was studied in PBS (pH 7.4) at room temperature. Drug loaded NPs were incubated in PBS for different periods, and release of the Dox and MB was monitored for upto 48 h.

5.2.7 Uptake study of the NPs

Internalization of the free drugs, drug-loaded PLGA NPs (PLGA-DoxMB), RBC membrane coated and drug loaded PLGA NPs (RB-DoxMB) and TF conjugated RBC membrane coated and drug loaded PLGA NPs (TF-DoxMB) was studied by flow cytometry and microscopy. For flow cytometry study, HeLa, MCF-7, and HEK293 cells were seeded in 6 well plate at the density of $1x10^5$ cells/well. After incubation of the cells with drug or NPs for 5 h, cells were washed with PBS and trypsinized for detachment. These cells were collected and analyzed on a flow cytometer (Cytoflex, Beckman Coulter). For microscopy studies, HeLa and MCF-7 cells were treated with NPs for 5 h in an incubator, after treatment, cells were washed with PBS and fixed with 4% formaldehyde for 20 min. After fixation, cells were again washed with PBS and visualized in confocal microscope for Dox fluorescence. For endosome staining, HeLa and MCF-7 treated with TF-DoxMB for 5 h, stained with lysotracker, and were washed with PBS. After this, cells were fixed with 4% formaldehyde and counterstained with DAPI. After removal of the unbound dye, cells were observed under a confocal microscope.

For assessment of the pathway of the endocytosis, cells were pretreated with different endocytosis inhibitors followed by the treatment with TF-DoxMB NPs. For confirming the the active pathway of the endocytosis, sodium azide treatment was given 2 h before the TF-DoxMB NPs treatment. Similarly, for clathrin- and caveolin mediated pathway inhibition chlorpromazine and filipin were given to cells before TF-DoxMB treatment. After this, cells were trypsinized and analyzed on a flow cytometer (Cytoflex, Beckman Coulter).

5.2.8 Semi-quantitative Polymerase Chain Reaction

PCR was performed to study the expression of the transferrin receptor and GAPDH in studied cells. HeLa, MCF-7, and HEK293 cells were lysed and total RNA was isolated. cDNAs were synthesized from the RNA isolated from three types of cells. Following this, by using gene-specific primers (**Table S3**) PCR was performed to study the expression transferrin receptor. PCR conditions used were as follows: 95 ºC for 10 min, 30 cycles of 95 ºC for 40 s, 59 ºC for 30 s and 72 ºC for 40 s. The final extension was given at 72 ºC for 5 min. After completion of the reaction, PCR products were run on 1.5% acrylamide gel containing ethidium bromide, and images were taken in ChemiDoc (Bio-Rad).

5.2.9 Antiproliferative assay for viability assessment

To study the activity of the Dox, MB, and their formulations in the form of NPs, phosphatase activity based viability assays were carried out.[12] Initially, the ability of the assay to detect the difference in viable cells was studied. HeLa cells were seeded in 96 well plate at increasing density, from $1.2x10^2$ cells to $4x10^4$ cells/well. After 12 h incubation, cells were washed with PBS, and 200 µl assay buffer (0.1M sodium acetate pH 5, 0.1% Triton X-100, and 5 mM p-nitrophenyl phosphate) was added in each well. After 2 h incubation, absorbance was measured at 405 nm. Similarly, for viability testing of the

drugs, HeLa, MCF-7, and HEK293 ($5x10^3$ cells/well) were treated with increasing concentrations of the Dox, MB, and phosphatase assays were carried out. To study the effect of the free MB and laser treatment (MB+L), HeLa and MCF-7 cells treated with MB for 8 h and irradiated with red laser for 2 min. For viability assays of the NPs and laser treatment, cells were treated with a mixture of the Dox+MB or RB-DoxMB and TF-DoxMB for 8 h, and then red laser (100 mW, 650 nm) was irradiated on treated cells for 2 min. The laser irradiated treatments were referred as DoxMB+L, RB-DoxMB+L, and TF-DoxMB+L. After 40 h incubation, cells were subjected to phosphatase assay.

5.2.10 Measurement of Singlet oxygen generation

In order to identify the singlet oxygen species generated after laser treatment on MB, ABDA [9,10-Anthracenediyl-bis(methylene)dimalonic acid] absorbance was measured at 400 nm. ABDA and MB were mixed at (1:1) molar ratio and red laser was focused on to this mixture in the cuvette. The absorbance of the ABDA was taken after every 30 sec laser irradiations.

5.2.11 DCFDA assay for ROS detection

For measurement of the ROS after TF-DoxMB and laser treatment, DCFDA dye-based ROS detection was performed. Initially, HeLa and MCF-7 cells were incubated with 10 μM DCFDA dye (30 min). Following this, cells were treated with Free Dox, PLGA-DoxMB, RB-DoxMB, and TF-DoxMB for 8 h; and laser was irradiated to the cells treated with MB containing formulations. The concentrations of the Dox and MB were kept constant in all the treatment for HeLa (Dox- 30 nM and MB- 78 nM) and MCF-7 (Dox- 20 nM, MB- 52 nM) cells. After 5 h incubation, cells were trypsinized and analyzed for DCF fluorescence in flow cytometer (Cytoflex, Beckman Coulter).

5.2.12 TUNEL assay

To study the DNA fragmentation in treated cells, TUNEL (terminal deoxynucleotidyltransferase dUTP nick end labeling) assay was carried out using APO-DIRECT Kit. HeLa and MCF-7 cells were treated with with IC_{50} concentrations of TF-DoxMB+L for 48 h. Initially, cells were fixed in 4% formaldehyde on ice for 30 min, followed by ethanol (70%) treatment on ice. After that, cells were washed with wash buffer and incubated with TdT enzyme and FITC-dUTP. Subsequently, cells were incubated for 1 h and washed with rinse buffer before analysis. Cells were analyzed for FITC fluorescence and data analysis was performed in FlowJo software.

5.2.13 Apoptosis assays

Apoptotic cells were measured using annexin-v FITC based antibody staining. HeLa and MCF-7 cells seeded at $1x10^5$ density in each well. Cells were subjected to treatment with drugs or NPs containing similar concentrations for HeLa (Dox 30 nM, MB- 78 nm) and MCF-7 (Dox- 20 nM, MB- 52 nM) cells. After 8 h treatment, a laser was irradiated on treated cells, these cells were further incubated for 40 h in incubator. After completion of the treatment, cells were trypsinized and stained with annexin-v-FITC antibody in staining buffer. Stained cells were immediately analyzed in a flow cytometer.

5.2.14 Spheroid generation

3D spheroids of the HeLa and MCF-7 cells were generated for studying the cell-killing activity of the TF-receptor targeted formulation. For, spheroid generation, HeLa and MCF-7 cells were seeded in 96 well plates, precoated with 1.5% agarose. Bottom of the 96 well plate was made to be non-adherent by adding melted agarose (1.5% in serum-free DMEM media) in each well.

After solidification of the media, HeLa and MCF-7 cells were seeded at the density of the $2x10^4$ cells/well. These 96 well plates were centrifuged at 700 xg for 10 min and kept in a CO_2 incubator for growth of the spheroid. After 4 days of incubation, spheroids were generated and used for viability assays.

5.2.15 Uptake and Viability assays on spheroids

HeLa and MCF-7 spheroids were treated with free Dox, PLGA-DoxMB RB-DoxMB and TF-DoxMB for 6 h. The internalization of the NPs was studied by taking the fluorescent images for Dox fluorescence. In order to compare the fluorescence of the different treatments, total corrected cell fluorescence (CTCF) were calculated form fluorescent images.

CTCF = Integrated Density – (Area of selected cell X Mean fluorescence of background readings).

For viability assays, 4 day old spheroids were treated with free drugs, or DoxMB+L, RB-DoxMB+L, and TF-DoxMB+L; as mentioned in monolayer cells treatment. After completion of the treatment, spheroids were transferred to new 96 well plates, washed with PBS and centrifugation. Spheroids were incubated with 200 µl phosphatase assay buffer for 4 h, and absorbance was measured at 405 nm in multiplate reader (TECAN).

5.2.16 Microscopy of the spheroids

Calcein-AM staining was performed to access live cells present before and after the treatment with TF-DoxMB and laser (TF-DoxMB+L). For this purpose, untreated and TF-DoxMB+L treated spheroids were stained with Calcein-AM (500 nM) for 1 h, and images were taken under a confocal

microscope. For detection of the ROS in DoxMB+L and TF-DoxMB+L treatments, spheroids were incubated with DCFDA for 1 h, followed by DoxMB and TF-DoxMB treatment for 8 h. Following this, the red laser was irradiated on the spheroids for 2 min. After 5 h incubation, spheroids were washed with PBS and analyzed in a confocal microscope for DCF fluorescence.

5.3 Results & Discussions

5.3.1 Preparation and characterization of the Transferrin-conjugated NPs

Initially, PLGA NPs were synthesized and characterized for their hydrodynamic size (*dH*) and zeta potential (ζ). *dH* and ζ of the PLGA NPs were found to be 104 nm and -18 mV, respectively (**Figure 5.1A**). Similarly, TEM analysis revealed that PLGA NPs were of 95±10 nm size (**Figure 5.1B**). Following this, isolated RBC membranes were extruded to form vesicles; these vesicles were then extruded with PLGA NPs at 1:1 ratio of PLGA: membrane protein to form RBC membrane-coated PLGA NPs (RB-NPs). The *dH* and ζ of these RB-NPs were changed to 141 nm and -26 mV, respectively (**Figure 5.1A**). Increase in *dH* and changes in the ζ were mainly due to extra layer of the RBC membrane coating on PLGA NPs. Previous studies have shown that RBC membrane coating improved the circulation of nanoparticles as well as drug delivery efficiency to cancer cells.[13]

Table 5.1 Weight ratio of the TF:RBC membrane protein to prepare TF-conjugated RBC membranes and the denotations of the NPs prepared with these membranes.

TF: RBC	% Conjugation	TF@Mem
0.02	86.5	TF0.02-Dox-NPs
0.05	56	TF0.05-Dox-NPs
0.1	32.4	TF0.1-Dox-NPs
0.2	17.4	TF0.2-Dox-NPs
0.4	11.3	TF0.4-Dox-NPs

Here we have studied the effect of TF conjugation over RBC membrane-coated NPs. To prepare NPs having TF on their surface, TF molecules were conjugated on RBC membrane, and these TF-conjugated membranes were used to coat PLGA NPs forming TF-decorated RB-NPs (TF-RB-NPs). To determine the required amount of the transferrin on the NPs surface to achieve maximum uptake, RBC membranes with varying densities of the TF on their surface were prepared. For this, RBC membranes were reacted with increasing weight ratios of TF: Membrane protein (0.02 to 0.4), and amount of the TF conjugated on the RBC membranes was calculated (**Table 5.1**). With increasing TF concentration in the reaction, an increase in the conjugation of TF on RBC membrane was observed.

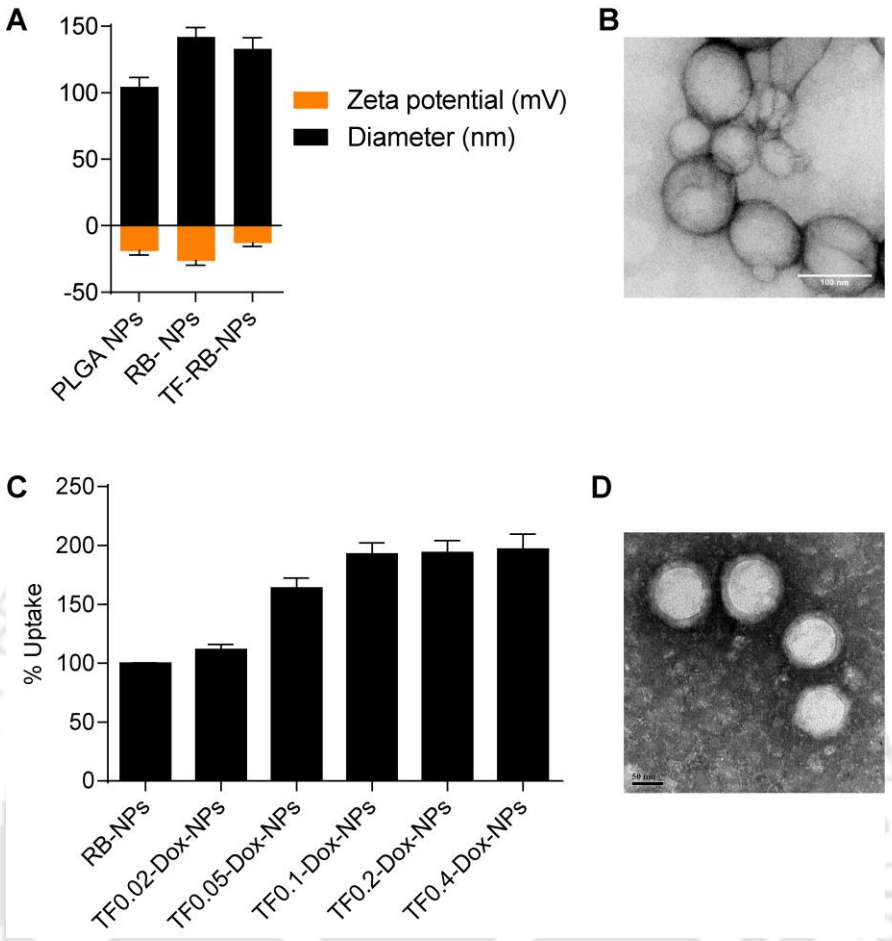

Figure 5.1 (**A**) Hydrodynamic diameter and zeta potential of the PLGA NPs, RB-NPs, TF-RB-NPs. (**B**) TEM micrographs of PLGA NPs. (**C**)Uptake of the TF-Dox-NPs containing an increasing density of the TF on their surface. (**D**) TEM image of the TF-DoxMB.

After this, to confirm the targeting efficiency of these TF conjugated RBC membranes, doxorubicin-loaded TF-Dox-NPs were prepared. Doxorubicin-loaded PLGA NPs were prepared and coated with RBC membranes containing increasing densities of TF molecules. These prepared TF-Dox-NPs were denoted as TF0.02-Dox-NPs to TF0.4-Dox-NPs according to the used ratio of TF: RBC membrane protein (**Table 5.1**). Uptake of these TF-Dox-NPs was studied in HeLa cells. It was found that TF0.1-Dox-NPs showed the highest

uptake as compared to only RBC vesicles, TF0.02-Dox-NPs, and TF0.05-Dox-NPs, whereas although the TF content was higher in TF0.2@Mem and TF0.4@Mem than TF0.1@Mem, no further increase in the uptake was observed for them (**Figure 5.1C**). Thus, for further experiments, reaction with 0.1 ratio of the TF: RBC membrane was selected. The NPs prepared at this ratio containing Dox and MB were denoted as TF-DoxMB NPs. The *dH* and ζ of the TF-DoxMB NPs were recorded to be 132 nm and -12.6 mV, where significant increase in the ζ denoted the presence of the TF over the surface of TF-DoxMB NPs (**Figure 5.1A**). Similarly, from the TEM image of the TF-DoxMB in **Figure 5.1D,** a halo around the PLGA NPs was observed specifying the efficient coating of the RBC membrane. The average size of the TF-DoxMB NPs measured from the TEM images was found to be 106±23 nm (**Figure 5.1D, Figure 5.2A**).

Similarly, FESEM images (**Figure 5.2B**) also confirmed the round morphology of the TF-DoxMB NPs. For stability studies, *dH* of the TF-DoxMB NPs in PBS or fetal bovine serum (FBS) were measured at different time points. **Figure 5.2C** showed the *dH* of the TF-DoxMB NPs for 14 days in PBS at 4 ºC, there was no significant increase in the size over the time period. These stable, NPs were further mixed with FBS (10%) and kept at 37 ºC for 24 h to test serum stability. From DLS study (**Figure 5.2D**), it was confirmed that there was neither a size change nor any protein adsorption on NPs. The long term stability and the serum stability of the NPs makes them a suitable candidate for delivery purpose.

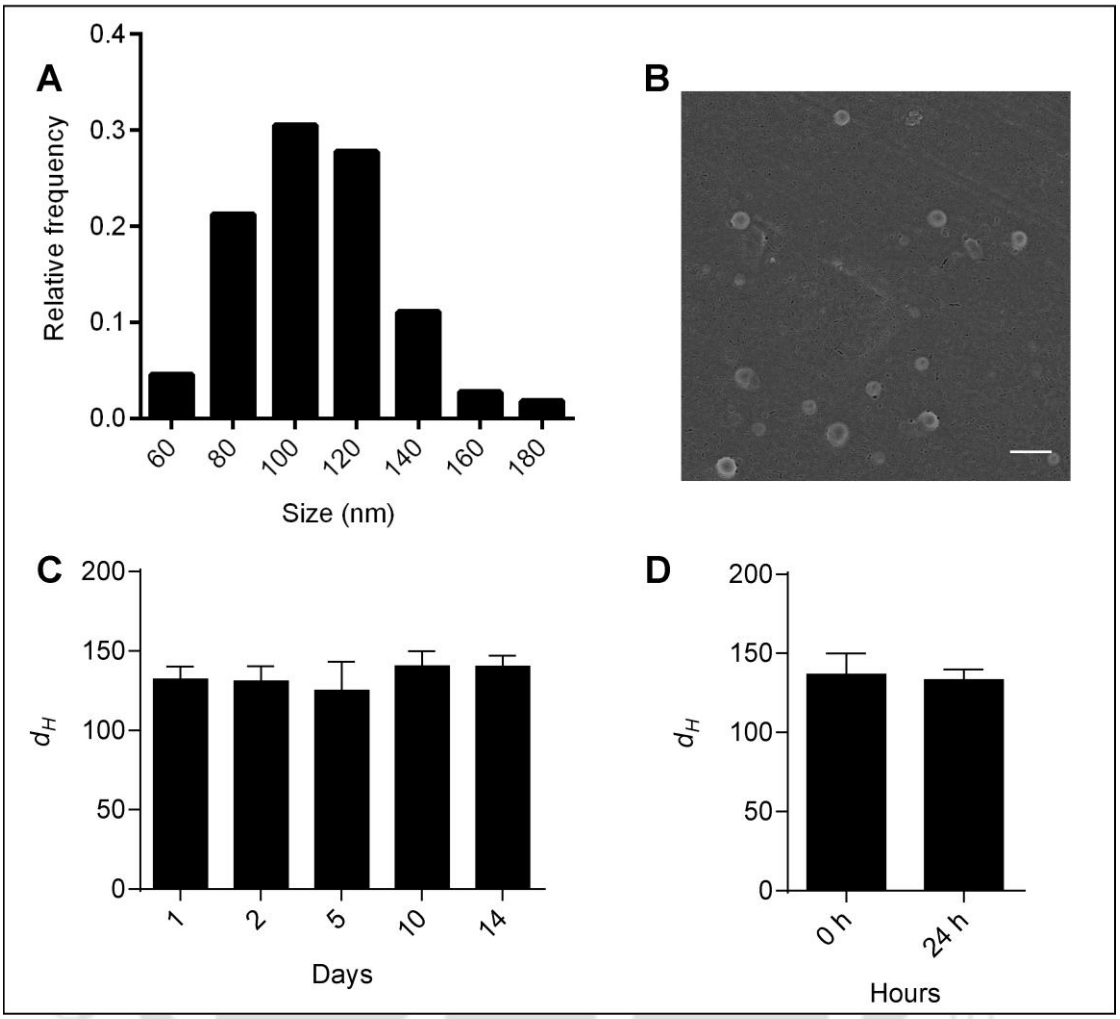

Figure 5.2 (**A**) Average size of the TF-DoxMB NPs calculated from TEM images. (**B**) FESEM images of the TF-RB-NPs (Size bar:100 nm). (**C**) Long-tern stability of the TF-DoxMB at 4 ºC. (**D**) Serum stability of the TF-DoxMB after incubation in FBS for 24 h.

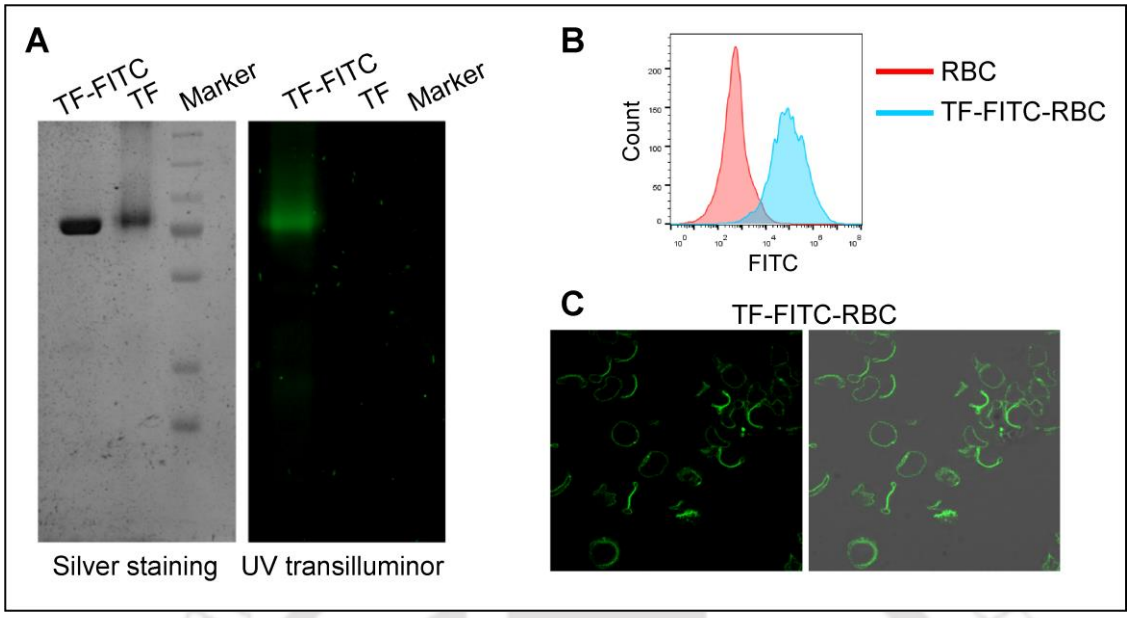

Figure 5.3 (**A**) SDS PAGE showing TF, TF-TFIC in UV transilluminator or after silver staining. (**B**) Flow cytometry of the RBC, and TF-FITC conjugated RBCs. (**C**) Microscopy of the TF-FITC conjugated RBCs.

Further, to confirm the TF conjugation on RBC membrane, TF was fluorescently tagged with FITC, and this FITC-tagged-TF (TF-FITC) was conjugated with isolated RBC membranes. **Figure 5.3A** showed SDS-PAGE of the TF-FITC and TF under UV illuminator and silver staining. A green fluorescent band in TF-FITC lane of equal size of TF confirmed the initial FITC binding. This FITC-TF was further conjugated with RBC membrane, and TF conjugation was studied. The presence of the green fluorescence in flow cytometry and microscopic analysis revealed the presence of the TF-FITC on the surface of the RBC membranes (**Figure 5.3B**), confirming successful conjugation. To establish the coating of PLGA NPs with only RBC membrane or TF-RBC membrane, Western blots were carried out for detection of the anion exchanger AE-1 protein from RBC membrane. The results showed that that AE-1 was present on membrane coated PLGA NPs and TF-DoxMB NPs (**Figure 5.4A**), which supported efficient coating of PLGA NPs as seen in TEM images.

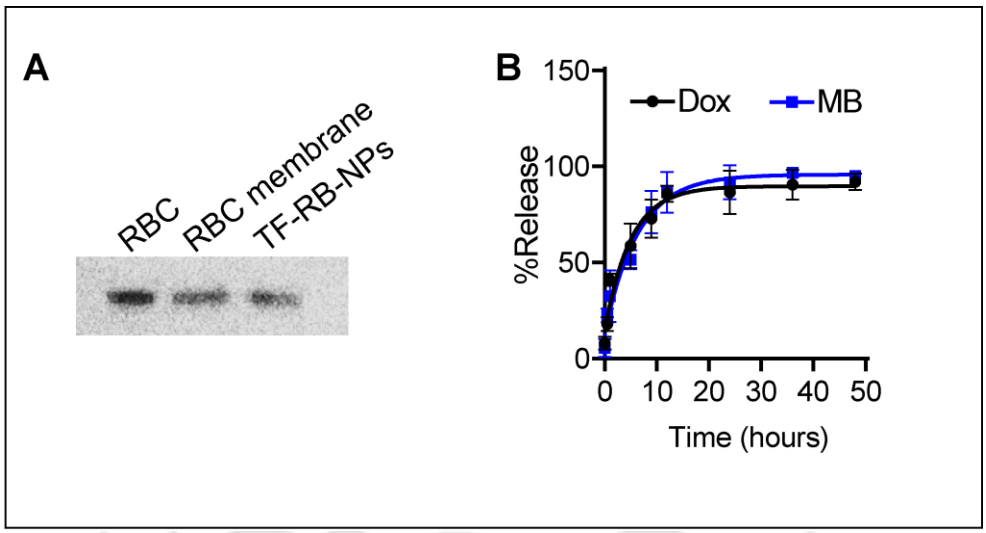

Figure 5.4 (**A**) Western blot analysis to study AE-1 protein in RBC, RB-NPs, and TF-RB-NPs. (**B**) The release profile of the Dox and MB from TF-DoxMB NPs.

5.3.2 Drug loading and Release study

To measure the effectiveness of the NPs to deliver drugs and inhibit the proliferation of the cells, two drug molecules were loaded onto these NPs. To achieve drug loading, PLGA NPs were prepared in the presence of the Dox and MB. In the study, MB was used as photodynamic agents to produce reactive oxygen species (ROS) after laser irradiation. Encapsulation efficiencies of the doxorubicin and methylene blue in NPs were found to be 36% and 52%, respectively. TF conjugated - Dox and MB loaded RB-NPs (TF-DoxMB NPs) were prepared by coating these drug-loaded PLGA NPs with TF-bound RBC membranes by extrusion. Furthermore, the release of the Dox and MB from TF-DoxMB NPs was studied in the phosphate buffer (pH 7.4). Release study results in **Figure 5.4B** confirmed the similar release profile of both Dox and MB, where approximately 75% of the drug release was seen in the first 12 h of incubation.

5.3.3 Selective internalization of TF-DoxMB NPs inside cancer cells

After confirmation of drug loading and release, the uptake of these TF-DoxMB NPs was studied in HeLa (cervical cancer), MCF-7 (breast cancer) and HEK (human embryonic kidney) cells. Flow cytometric uptake study results (fold uptake) for HeLa and MCF-7 cells (**Figure 5.5A**, **B)** showed the 2- and 6-fold higher uptake of the TF-DoxMB NPs as compared to the free Dox, respectively. Similar studies carried out on non-cancerous cells HEK did not show a significant increase (1.3 fold) in the uptake for TF-DoxMB NPs as compared to Dox or RB-DoxMB NPs, probably due to lower expression of the TF receptor on HEK cell surface (**Figure 5.5C**).

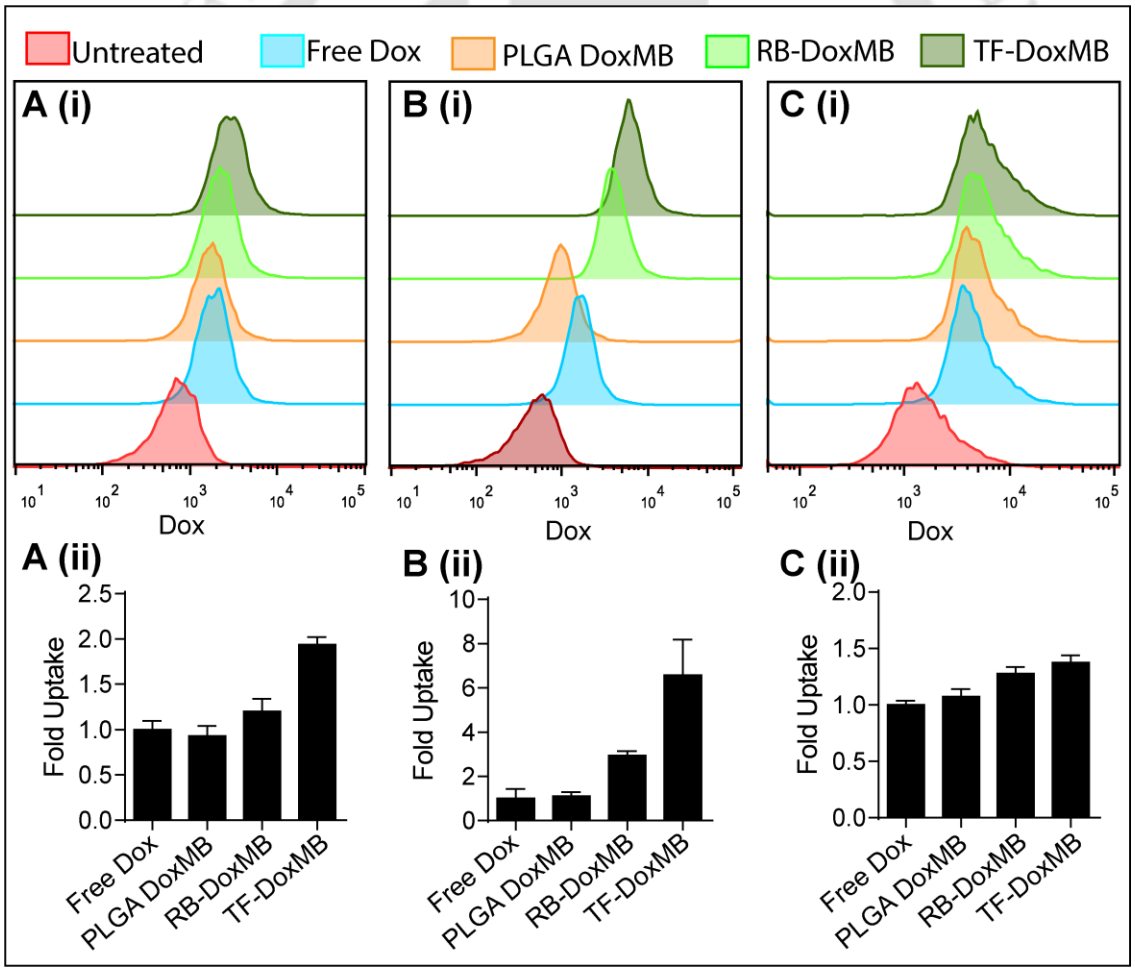

Figure 5.5 A(i), B(i), C(i) are representative histograms of the Flow cytometric uptake study of the free dox, PLGA DoxMB, RB-DoxMB,and TF-

DoxMB in HeLa (**A**), MCF-7 (**B**) and HEK293 (**C**) cells. Similarly, **A(ii), B(ii), C(ii)** showed change in the uptake as compared to free Dox in HeLa, MCF-7 and HEK293 cells, respectively.

Another important observation made from the uptake study was that non-targeted RBC membrane NPs (RB-DoxMB) also showed higher uptake as compared to the free drugs. From uptake analysis, highest FL intensity or fold uptake was seen in case of TF-conjugated NPs, whcih confirmed the targeting efficiency of the TF-DoxMB NPs. To show differential uptake of the TF-DoxMB NPs in cancer and non-cancerous cells, expression of the transferrin receptor was studied. From PCR results in **Figure 5.6**, it was observed that HeLa and MCF-7 cells possessed higher expression of the TF receptor. The higher expression of the TF receptor on HeLa and MCF-7 cells resulted in selective uptake of the TF-bound NPs. As evident by uptake study with microscopy (**Figure 5.7A**, **B**), free dox was mainly localized in the nucleus of the cells, while the drug-loaded NPs showed localization in the cytoplasm of the cells. Increased fluorescence of the Dox was seen in TF-DoxMB NPs treated cells confirming the targeted delivery of the drug molecules to HeLa and MCF-7 cells.

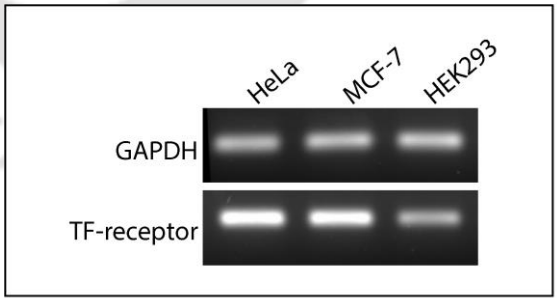

Figure 5.6: Semi-quantitative expression analysis of the TF receptor in HeLa, MCF-7, and HEK293 cells.

5.3.4 TF-DoxMB NPs enters inside the cells by clathrin mediated pathway

Previous studies reported that the internalization of the transferrin-conjugated NPs is an active and energy-dependent process.[14] Thus to study endocytosis of the TF-DoxMB NPs, lysosomal staining of the cells after treatment with NPs was performed. **Figure 5.8A** showed lysotracker green staining of the HeLa and MCF-7 cells. From fluorescence images, it was observed that most of the TF-DoxMB NPs were internalized and localized in the lysosomes, whereas a low fraction of the NPs escaped the lysosome and were present in the cytoplasm. In the same manner, route of the internalization of NPs may differ based on the material or surface coating. Henceforth, the pathway of the internalization of TF-DoxMB NPs in HeLa and MCF-7 cells was studied using endocytosis pathway inhibitors.

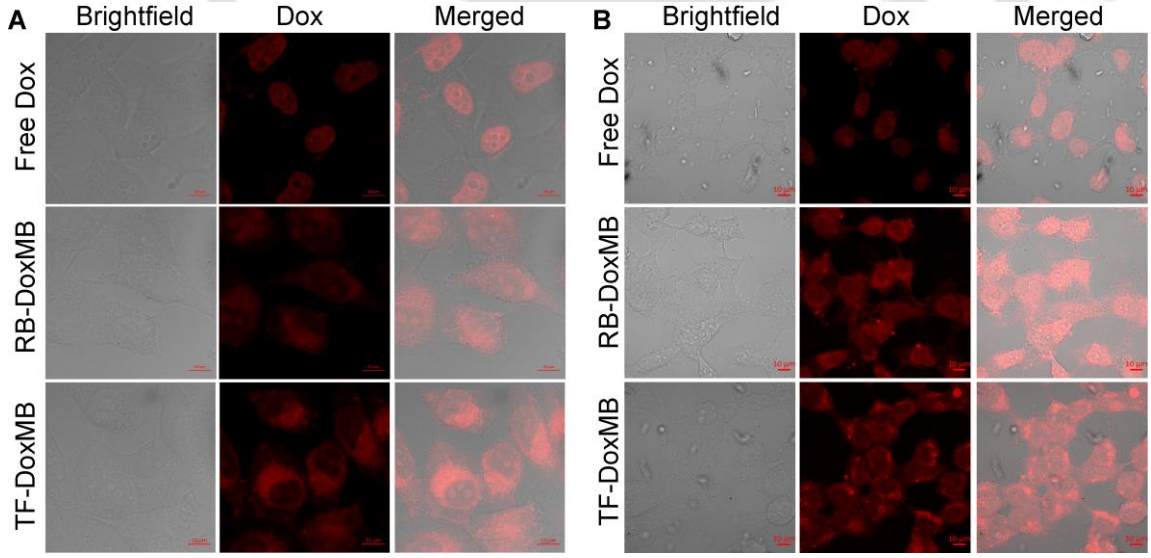

Figure 5.7 (**A**, **B**) Microscopic fluorescence images for the uptake of the Dox, RB-DoxMB, and TF-DoxMB NPs in HeLa (**A**) and MCF-7 (**B**) cells. (scale bar: 10 μm).

Pretreatment of the cells with sodium azide resulted in 40% to 60% decrease in the uptake of TF-DoxMB NPs in HeLa and MCF-7 cells, respectively; confirming the internalization was energy-dependent and active process (**Figure 5.8B**). Use of the filipin, a caveolin mediated pathway inhibitor did not show a significant reduction in the uptake, but the clathrin-mediated endocytosis pathway inhibitor; chlorpromazine reduced the uptake by 40% to 78% in MCF-7 and HeLa cells, respectively (**Figure 5.8B**). From results, it was concluded that TF-DoxMB were getting internalized via TF receptor and clathrin-mediated endocytosis pathway. Our results showed the similar route of the endocytosis mentioned in previous studies carried out with TF conjugated nanocarrier.[15]

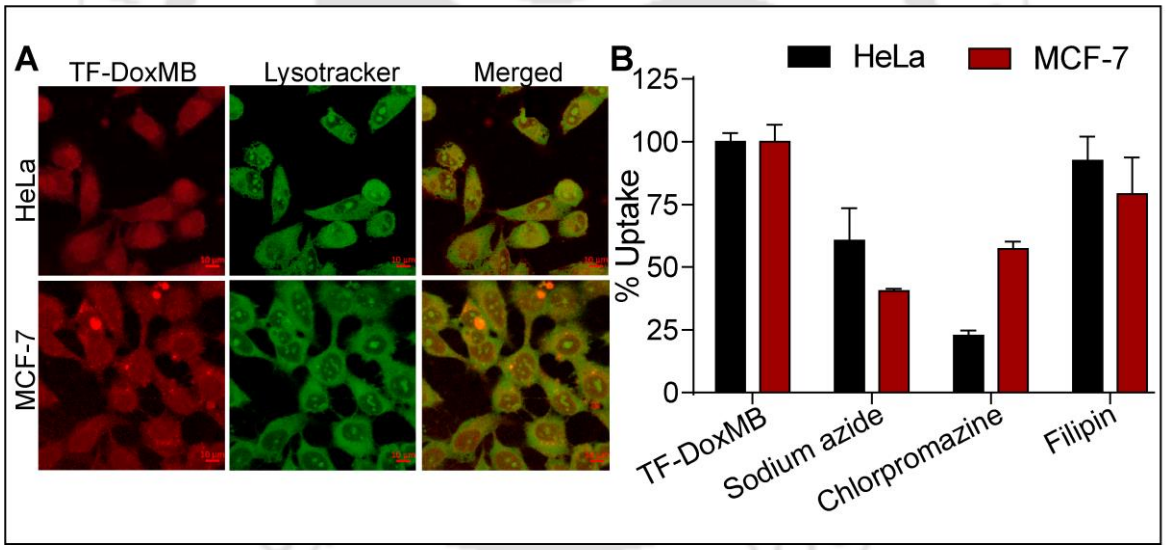

Figure 5.8 (**A**) Lysosome staining of the TF-DoxMB treated HeLa and MCF-7 cells. Scale bar: 10 µm. (**B**) % Uptake of the TF-DoxMB in the presence of endocytosis inhibitors, calculated from flow cytometric analysis.

5.3.5 Synergistic Antiproliferative effects of the nanoparticulate formulations

To study the viability of the cells after treatment, phosphatase assays were carried out.[12] Though this assay is commonly being used to study the viability of the cells, the efficiency of the assay was examined by keeping number of the cells equal. To obtain the linearity of the phosphatase assay, HeLa cells were seeded with increasing density in 96 well plate. From the assay results, shown in **Figure 5.9**, it was seen that the assay absorbance was increasing linearly with an increase in the number of cells. This confirmed that the phosphatase assay could be utilized to study cell death after the NPs treatment. Viability assays were performed to study the anti-proliferative effects of free drugs and their drug formulations in the form of nanoparticles.

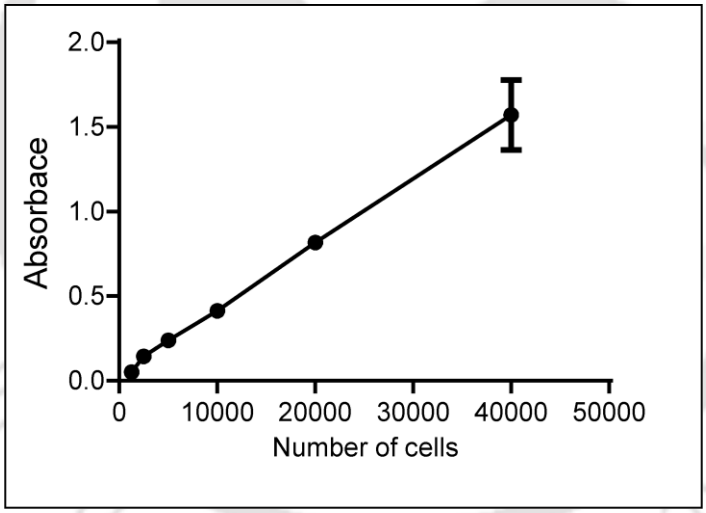

Figure 5.9 Phosphatase assay carried out on an increasing number of cells**.**

HeLa, MCF-7, and HEK293 cells were treated with increasing concentrations of the free Dox, MB, RB-DoxMB, and TF-DoxMB. In order to compare the viability assay results, Dox and MB concentrations were kept similar in free drug combinations or nanoparticulate form. For assessing the

effect of co-treatment of MB, the laser was irradiated to the cells treated with MB containing formulations.

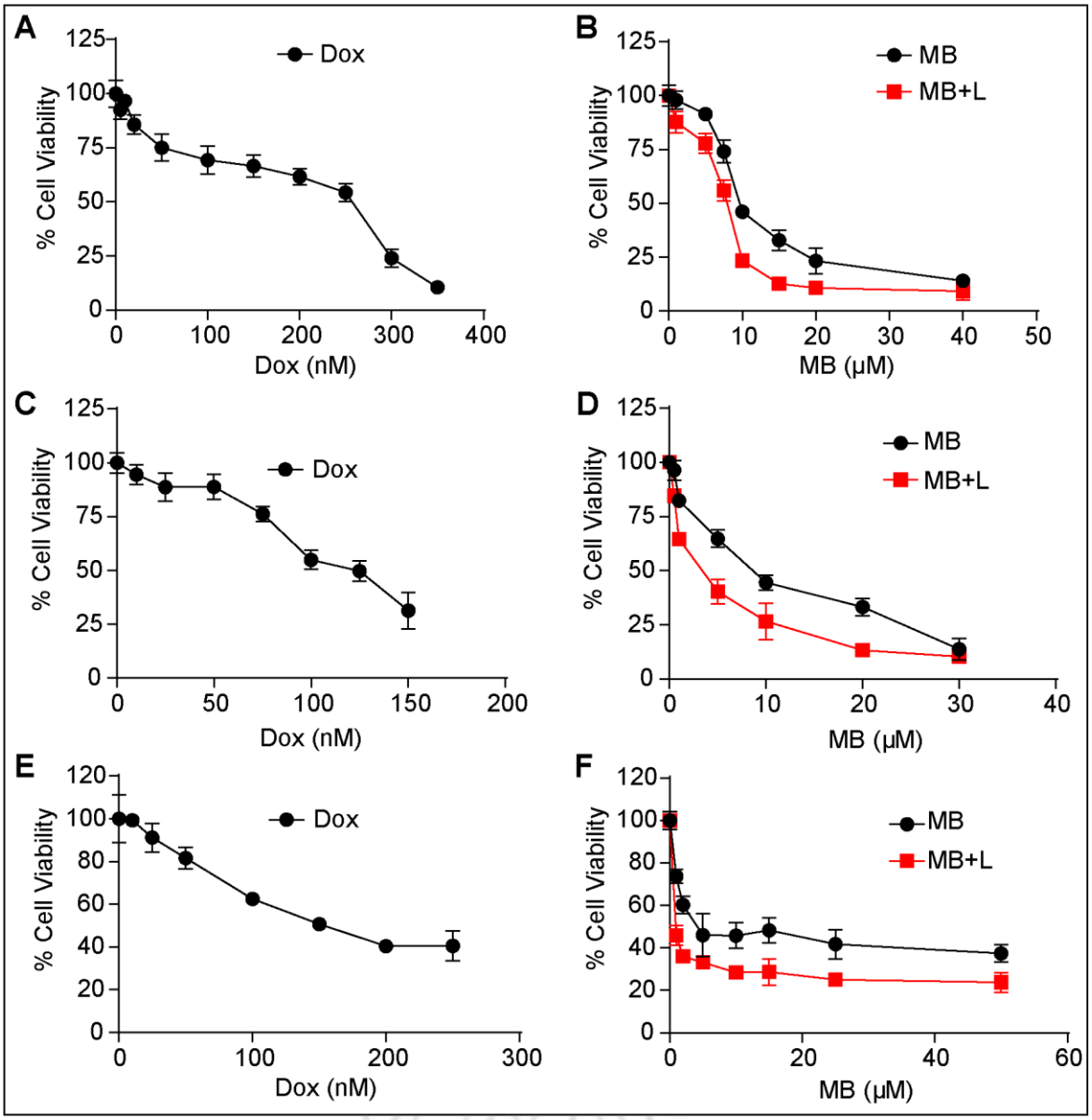

Figure 5.10 Viability assays of the Dox, MB and MB along with laser irradiation (MB+L) in HeLa (**A**, **B**), MCF-7 (**C**, **D**) and HEK293 (**E**, **F**) cells.

From viability testing on HeLa, MCF-7, and HEK293 cells for Dox and MB treatment, it was observed that the free drug molecules could inhibit the proliferation of the cells (**Figure 5.10**). Especially, Dox showed its IC_{50}

concentrations at 186±7 nM, 142±16 nM, and 158±7 nM in HeLa, MCF-7, and HEK293 cells, respectively (**Figure 5.10, Table 5.2**). The IC_{50} concentrations for Free MB were found to be 9.2±0.3 μM, 8±0.3 μM and 6.1±1.3 μM in HeLa, MCF-7 and HEK293 cells respectively; without laser irradiation (**Figure 5.10** and **Table 5.2**). Afterward, to correlate the activity of the MB along with laser, free MB treated cells were irradiated with laser (MB+L). A clear difference in the IC_{50} of the MB and MB+L treatments depicted a significant increase in cell death in MB+L treatment. The results of free Dox, MB, and MB+L treatments confirmed that the individual drug could be delivered through the nanocarriers.

In the next step, cells were treated with combinations of Dox and MB (DoxMB), and the nanoparticles (RB-DoxMB, and TF-DoxMB) for 8 h and laser was irradiated onto these cells for 2 min. Laser-irradiated treatments were denoted as DoxMB+L, RB-DoxMB+L, and TF-DoxMB+L. From the results shown in **Figure 5.11A, B and Table 5.2**, a significant difference in the viability of the laser irradiated treatments was observed. For example, IC_{50} concentrations of the free Dox in HeLa cells was 186±7 nM, it was further reduced to 172±4.8 nm, 58±1.8 nM, and 28±2 nM in laser-irradiated DoxMB+L, RB-DoxMB+L, and TF-DoxMB+L treatments. Similarly, in MCF-7 cells, IC_{50} concentrations of the Dox and MB were reduced significantly in the nanoparticulate formulations as compared to free drugs (**Table 5.2**).

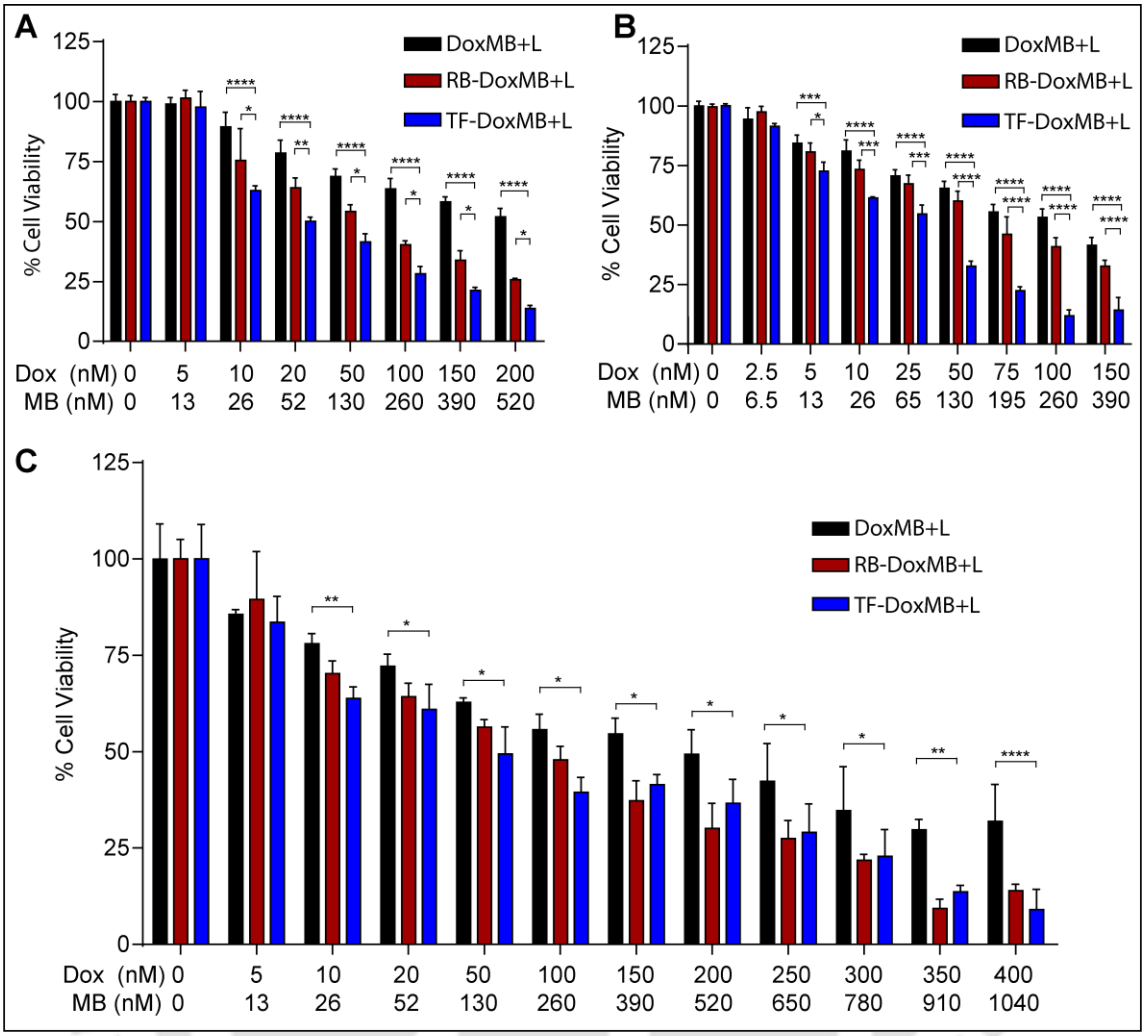

Figure 5.11 (**A**, **B, C**) Viability assays for DoxMB+L, RB-DoxMB+L and RF-DoxMB+L treatments in HeLa (**A**), MCF-7 (**B**) and HEK293 (**C**) cells.

Similar observations were made regarding IC_{50} concentrations of MB in DoxMB+L, RB-DoxMB+L, and TF-DoxMB+L treatments. These results suggested a significant higher antiproliferative response in the combination of Dox and MB along with laser in treated cells. Surprisingly, RBC membrane coating has been shown to improve the uptake and drug delivery inside the cells. From the comparison of the IC_{50} concentrations of the RB-DoxMB+L and TF-DoxMB+L, the significant improvement in the antiproliferative response was seen (**Figure 5.12)** after TF conjugation.

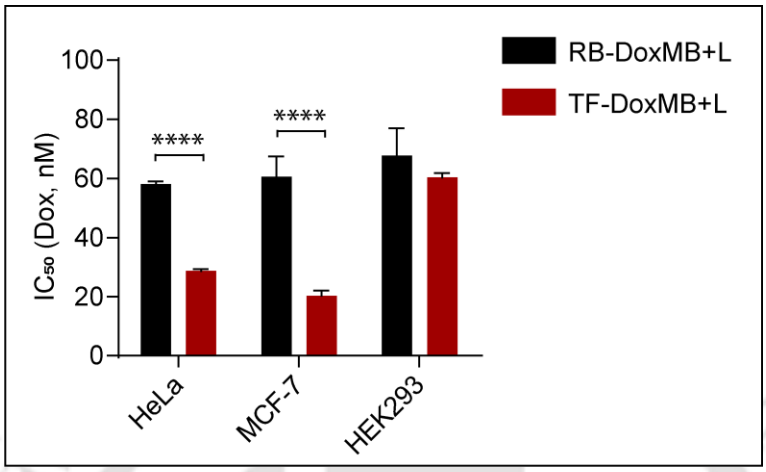

Figure 5.12 Comparison of the IC_{50} concentration of the RB-DoxMB+L and TF-DoxMB+L in HeLa, MCF-7 and HEK293 cells.

To further examine the synergistic action of the chemo- and photodynamic therapy, combination indexes (CI) were calculated for each combination treatment (**Table 5.2**). CI values for RB-DoxMB+L and TF-DoxMB+L in HeLa and MCF-7 cells were found to be less than 1, confirming the synergistic action for cell death. From the IC_{50} concentrations, CI and the uptake study, it was indeed observed that TF conjugation has significantly improved the internalization of TF-DoxMB; thereby producing significant synergistic response.

Table 5.2 IC_{50} concentrations and combination indexes calculated for DoxMB+L, RB-DoxMB+L and TF-DoxMB+L treatments.

	Free Drugs			**Nanoparticles**					
	DoxMB+L			**RB-DoxMB+L**			**TF-DoxMB+L**		
	IC_{50}		**CI**	**IC_{50}**		**CI**	**IC_{50}**		**CI**
	Dox(nM)	MB(nM)		Dox(nM)	MB(nM)		Dox(nM)	MB(nM)	
	2D Monolayer Culture								
HeLa	172±4.8	447+17	1	58±1.8	149±3	0.3	28±2	74±3	0.16
MCF-7	88.3±3	227±7	0.7	60.5±5	156±16	0.5	20.3+2	52±4.5	0.2
HEK293	147±17	376±38	1.1	68+8	174±22	0.5	60±1.5	156±4.8	0.4
	3D Multicellular Spheroids								
	Dox(μM)	MB(μM)		Dox(μM)	MB(μM)		Dox(μM)	MB(μM)	
HeLa	4.6±0.3	12±2	1.6	2±0.3	5.2±0.9	0.7	0.95±.08	2.4±0.2	0.3

Similar viability assays carried out in HEK293 cells showed a slight decrease in the IC_{50} concentrations of the Dox in DoxMB+L, RB-DoxMB+L, and TF-DoxMB+L treatments (**Table 5.2**). IC_{50} of the Dox and laser treated MB was found to be 158±7 nM and 1.7±0.2 μM. RBC membrane coated NPs (RB-DoxMB) showed decrease in the IC_{50} of the Dox and MB to 68±8 and 174±22 nM, respectively. Although the reduction in IC_{50} of the RB-DoxMB+L was seen, there was no significant difference in IC_{50} of the RB-DoxMB+L and targeted TF-DoxMB+L treatment (**Figure 5.12**). The reason behind this might be the lower expression of the transferrin receptor and the slower proliferation of the non-cancerous cells. It has also been seen that Dox treatment is associated with cardiotoxicity, major side effect of the Dox when used for therapeutic purpose.[16] The non-targeted therapies resulting in the distribution of the Dox to cardiac cells results in multiple molecular changes and affecting the normal functioning of the cells. Thus, targeting Dox to cancer cells and achieving a similar therapeutic response at a lower dose would definitely reduce cardiotoxic effects and improve the patient's health.

5.3.6 TF-DoxMB induced ROS and DNA damage mediated cell death

Doxorubicin is a potent anticancer drug which inhibits the DNA topoisomerase II.[17] It has also been reported that Dox can induce ROS generation inside the cells.[18] Likewise, another molecule MB used in this study was a photodynamic agent, which also generates ROS after laser treatment.[19] Thus, different assays were carried out to study the underlying mechanism of the action of cell death. Initially, using ABDA [9,10-anthracenediyl-bis(methylene)dimalonic acid] based assay, generation of the singlet oxygen after laser irradiation was determined.[20] For this study, solution of the ABDA and MB were irradiated with laser for up to 120 seconds, and absorbance of the ABDA was measured at 400 nm.

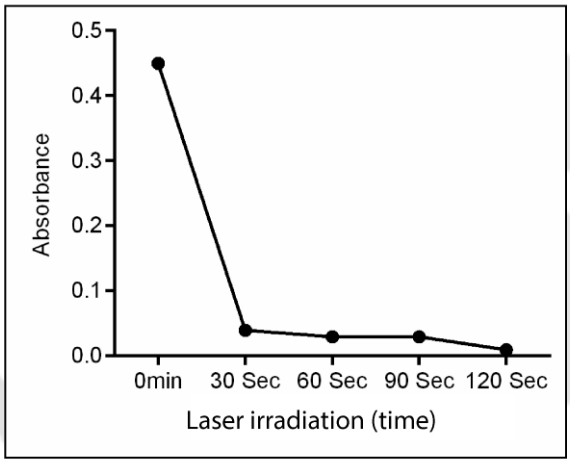

Figure 5.13 Absorbance of the ABDA at 400 nm to confirm photo-oxidation of the ABDA from singlet oxygen generated after laser irradiation on MB.

From results shown in **Figure 5.13,** it was observed that the absorbance of the ABDA decreased with an increase in the irradiation time. Since the oxidation of the ABDA due to the presence of the singlet oxygen results in a reduction in the absorbance at 400 nm, it confirmed the photodynamic action of the MB. Following this, ROS generated inside the cells were also detected by DCFDA staining. Flow cytometric assay carried out on HeLa and MCF-7 cells

(**Figure 5.14A, B**) showed free Dox, Dox+MB in PLGA NPs (PLGA-DoxMB) or RB-DoxMB+L, and TF-DoxMB+L resulted in the ROS generation. Without a doubt, the laser-irradiated (TF-DoxMB+L) cells showed maximum ROS generation.

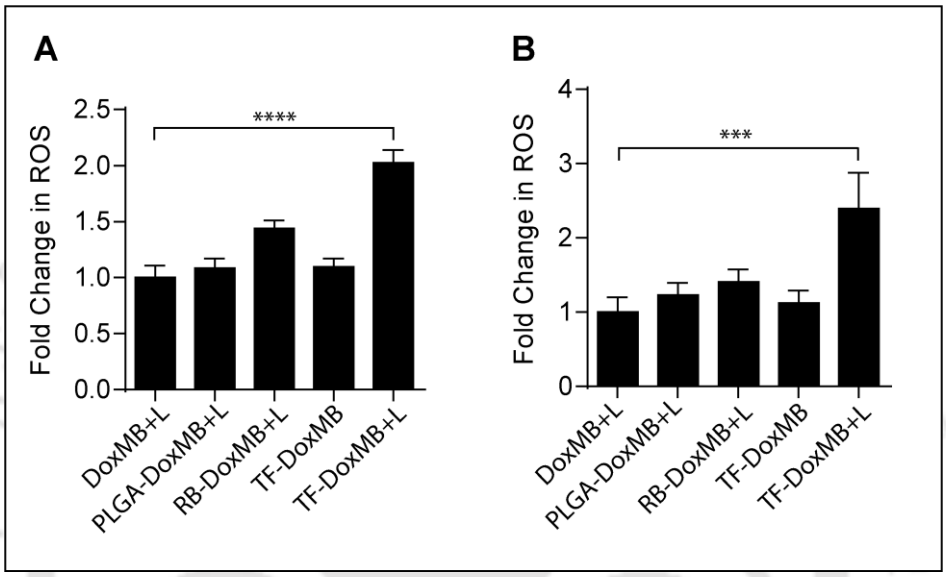

Figure 5.14 (**A**, **B**) Fold changes in ROS of the treated HeLa (**A**) and MCF-7 (**B**) cells corresponding to free Dox.

These results concluded that the TF-conjugation caused increased localization of the Dox and MB, and subsequent laser irradiation generated reactive oxygen species at higher amount. The presence of the Dox and laser irradiation of the MB resulted in the generation of ROS species; these ROS alters the molecular processes, including induction of DNA damage and mitochondrial dysfunction. Herein, cells possessing fragmented DNA after treatment with TF-DoxMB and laser irradiation were studied. TUNEL assay results in **Figure 5.15** showed that 55% and 44% of the HeLa and MCF-7 cells were positive for DNA damage. After laser treatment, induction of the apoptosis via ROS mediated DNA damage was the probable fate of the treated

cells. As mentioned earlier, use of the ROS generating molecules or ionizing radiations is a common practice in chemo and radiation therapy. The generated ROS directly or indirectly induce single or double-strand breaks in DNA. The targeted combination therapy module like TF-DoxMB to deliver chemotherapeutic, as well as the photodynamic agent, will undoubtedly help to achieve maximum therapeutic response.

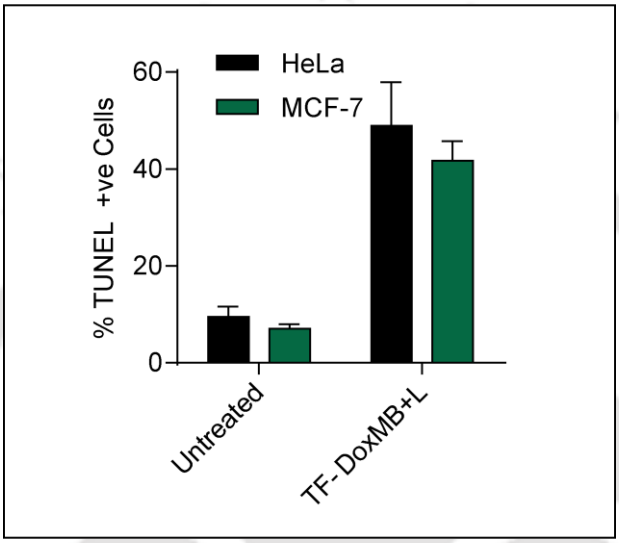

Figure 5.15 Percentage of TUNEL positive cells after treatment with TF-DoxMB+L.

5.3.7 Induction of Apoptosis by TF-DoxMB

Dox is being used for the treatment of the breast, lung cancers and Hodgkin's & non-Hodgkin's lymphoma.[17] The end result of the generated ROS and DNA damage renders apoptosis mediated cell death. Therefore, the apoptotic population of the HeLa and MCF-7 cells treated with the same concentrations of the Dox and MB in free form and nanoparticulate form were recorded. Treated and laser-irradiated cells with DoxMB+L, PL-DoxMB+L, RB-DoxMB+L, and TF-DoxMB+L treatments were stained with annexin V-FITC antibody and analyzed on a flow cytometer. Form the results obtained in

Figure 5.16A,B; it was evident that a number of the apoptotic cells were highest in TF-DoxMB+L treatment. In case of HeLa cells (**Figure 5.16A**), Free DoxMB+L treatment resulted in apoptosis induction in 17% cells, whereas PLGA-DoxMB+L showed 21% apoptotic cells. RBC membrane-coated nanoparticles (RB-DoxMB+L) also induced apoptosis in 26% of cells following the laser treatment. Along with this, TF-DoxMB treatment without laser showed a similar apoptotic population (27%) as RB-DoxMB+L, whereas TF-DoxMB+L increased it to 44% in HeLa cells. Similar results were seen in case of MCF-7 cells (**Figure 5.16B**), where DoxMB+L, PLGA- DoxMB+L and RB-DoxMB+L treatment resulted in 11%, 16% and 21% apoptotic cells, respectively. Similarly, TF-DoxMB and TF-DoxMB+L treatment resulted in 20% and 36% cell apoptosis, respectively. The evidence from this study suggested a higher number of the apoptotic cells were present in TF-DoxMB+L than with the same concentrations of the Dox or MB in free Dox or RB-DoxMB+L.

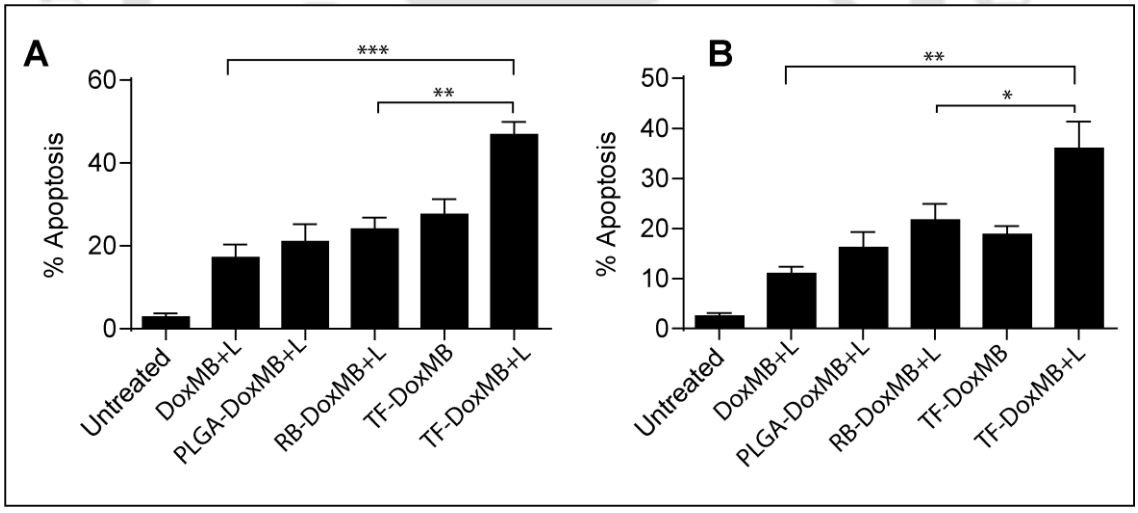

Figure 5.16 (**A**, **B**) Summary of the results of the annexin-v PI assay for apoptosis in treated HeLa (**A**) and MCF-7 (**B**) cells.

It was observed here that TF conjugation and laser irradiation significantly increased the percentage of apoptotic cells. The results obtained in this assay

supports the uptake studies. TF- conjugation has considerably increased the internalization of these NPs, resulting in higher drug accumulation in cells.

5.3.8 Enhanced Penetration of the TF-DoxMB in 3D Spheroids

Successful delivery of the Dox and MB to HeLa and MCF-7 cells ensured the reduction in proliferation and induction of apoptosis in monolayer of HeLa and MCF-7 cells. Though this therapeutic strategy worked effectively on monolayer cells, it was important to study its course of action in the 3D tumor environment.

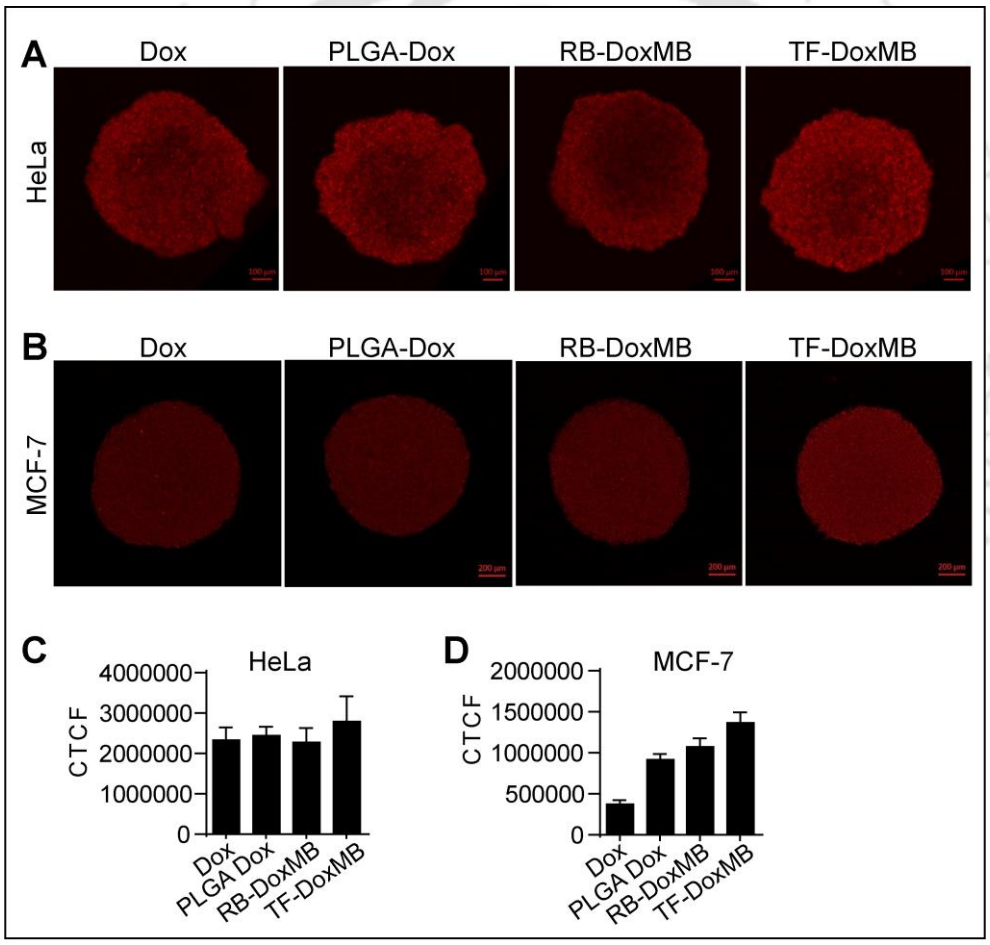

Figure 5.17 (A, **B)** Uptake of the Dox in free form, in PLGA NPs, RB-DoxMB, and TF-DoxMB NPs in HeLa (**A**) and MCF-7 (**B**) spheroids. (**C**, **D**) Corrected total cell fluorescence calculated from the fluorescence images of the HeLa (**C**) and MCF-7 (**D**) spheroids.

For further confirmation of the effectiveness of the TF-DoxMB and laser treatment (TF-DoxMB+L), spheroidal models of these cells were tested. Initially, the internalization and penetration ability of the TF-DoxMB was studied on HeLa and MCF-7 spheroids.

Spheroids treated with free Dox, PLGA-DoxMB, RB-DoxMB, and TF-DoxMB were observed under confocal microscopy. From the results seen in **Figure 5.17A-D,** it was observed that the fluorescence obtained from TF-DoxMB treated spheroids was higher as compared to other treatments. Along with the microscopic confirmation (**Figure 5.17A, B**), CTCF (Corrected Total Cell Fluorescence) were also calculated from fluorescent images of the spheroids. The CTCF shown in **Figure 5.17C, D** confirmed the highest uptake of the TF-DoxMB in both the HeLa and MCF-7 spheroids. The metabolism and the proliferation of the cells in the tumor core follow a different route than the cells at the tumor surface. Thus, the higher penetration ability of the TF-DoxMB would certainly help to localize these drugs in the tumor core; while laser treatment might selectively destroy the core cells.

5.3.9 Synergistic Cell death induction in the spheroid model

As mentioned earlier, the targeting efficiency of the RB-DoxMB in monolayer, as well as 3D spheroids, was increased after conjugation of TF (TF-DoxMB) on their surface. In addition to this, viability assays were carried out to study the effectiveness of the TF conjugated NPs. Firstly, HeLa spheroids were treated with free drugs, and the IC_{50} concentrations were determined. From the viability assay results shown in **Figure 5.18**, it was evident that Dox treatment inhibited the proliferation of the cells at IC_{50} concentration of 7.5±1.2 μM (**Table 5.2**); whereas MB treatment did not reach IC_{50} even at 30 μM. Surprisingly, only MB treated and laser-irradiated (MB+L) treatment showed a reduction in spheroidal cell viability significantly with IC_{50} concentration at 12±0.5 μM (**Figure 5.18** and **Table 5.2**). It was evident from

the viability assays that IC_{50} concentrations of the Dox and MB were significantly decreased in RB-DoxMB+L (Dox: 2±0.03 μM, MB: 5.2±0.1 μM) and TF-DoxMB+L (Dox: 0.95±0.08 μM, MB: 2.4±0.25 μM) treatments. Reduction in IC_{50} concentrations of the Dox and MB in case of TF-DoxMB+L confirmed that due to the targeting of NPs, a higher amount of the Dox and MB were delivered in those spheroidal cells, which upon laser treatment-induced cell death. Similar to the assays on monolayer cells, CI of the combination treatments were calculated (**Table 5.2**), and the synergistic response was observed for RB-DoxMB+L and TF-DoxMB+L treatment with CI of 0.7 and 0.3, respectively. In case of spheroids, due to the complex nature and 3D arrangement of the cells, IC_{50} concentrations of the free Dox were very high as compared to IC_{50} of the monolayer cells. Surprisingly, the use of TF-conjugated NPs reduced the concentrations of the Dox and MB to attain IC_{50} effect. Targeting of the RBC membrane coated NPs with TF to the tumor cells provide an efficient strategy for targeted drug delivery.

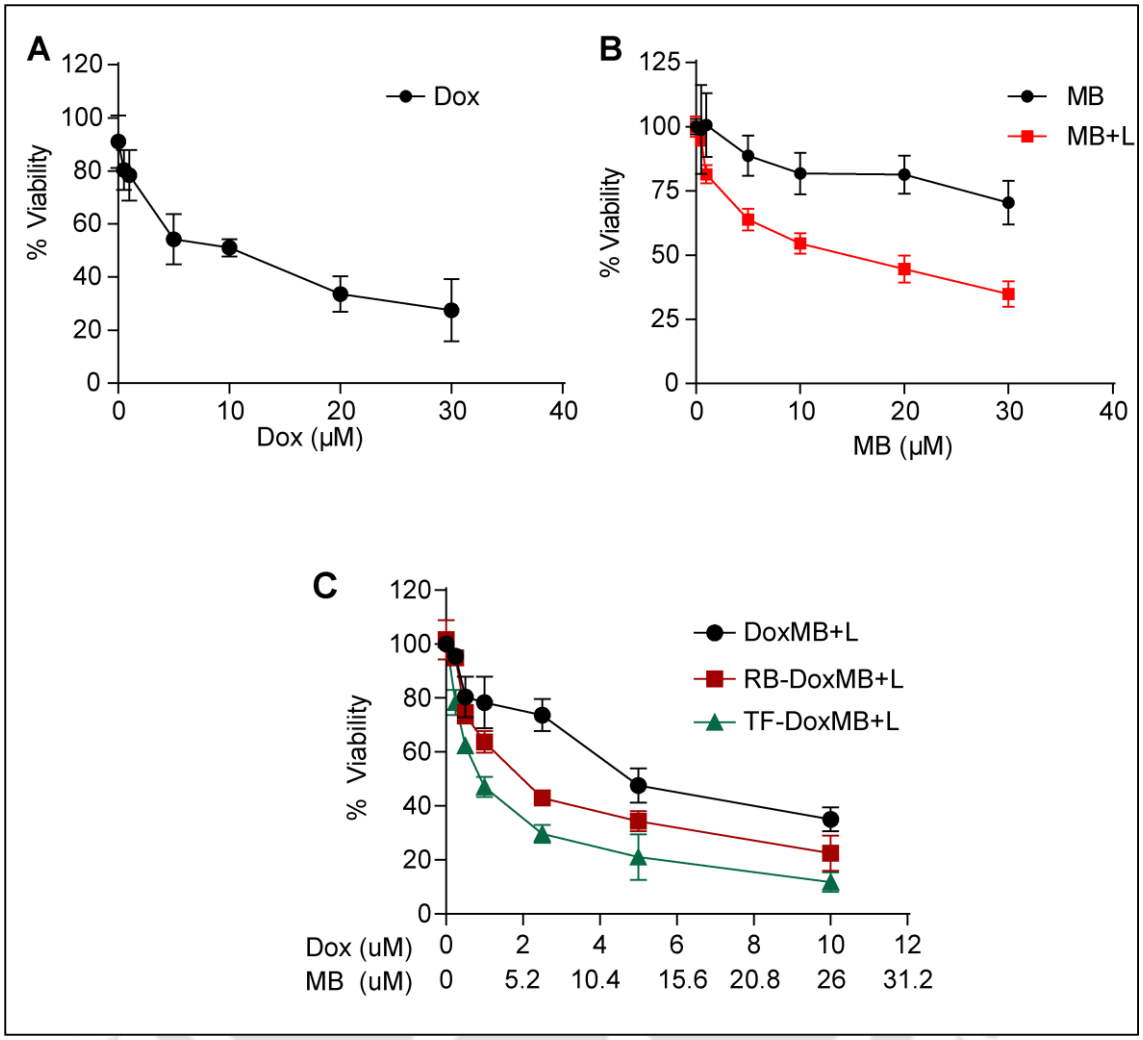

Figure 5.18 Viability assays of the Dox (**A**), MB and MB along with laser irradiation (MB+L) (**B**) in HeLa cells spheroids. (**C**) Viability assays carried out on HeLa cells spheroids after treatment with DoxMB+L, RB-DoxMB+L, and TF-DoxMB+L.

To further confirm cell death in spheroids, live-cell staining dye (Calcein-AM) was utilized. Spheroids treated with equal concentrations of free Dox and MB (DoxMB+L) or TF-DoxMB+L containing Dox (1μM) and MB (2.6μM) with laser irradiation were stained with Calcein-AM and observed under the confocal microscope.

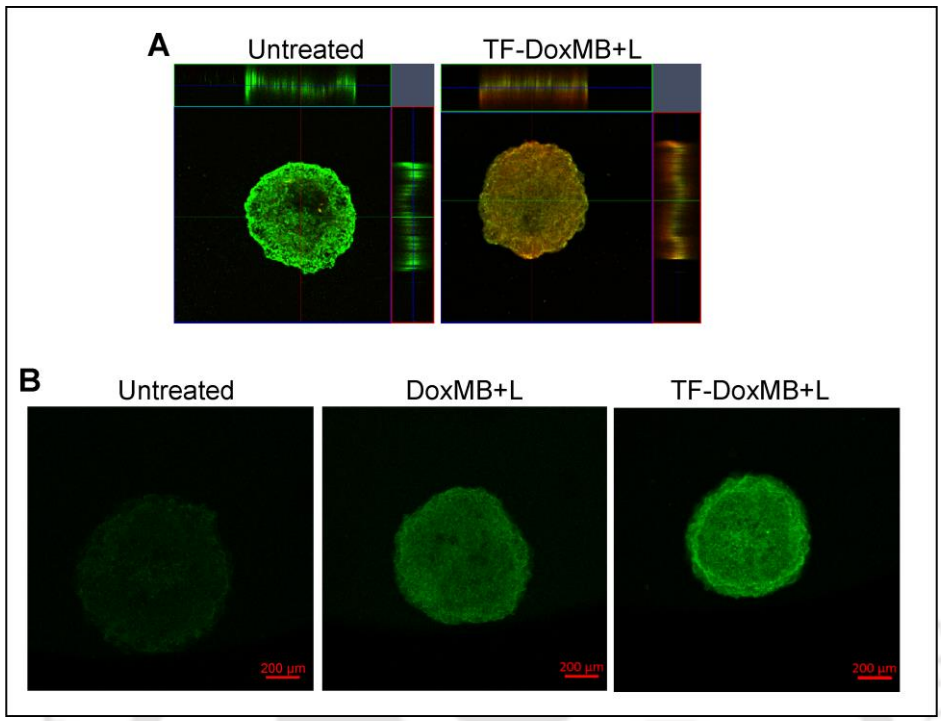

Figure 5.19 (**A**) Calcein-AM staining of the untreated and TF-DoxMB+L spheroids. (**B**) ROS detection by DCFDA staining of the treated HeLa spheroids.

From the microscopic images in **Figure 5.19A,** it was evident that untreated cells showed maximum green fluorescence due to the presence of the live cells. In the case of treated samples, decrease in green fluorescence was noticed. Orthogonal view of the TF-DoxMB+L treated spheroids showed red fluorescence from Dox and decreased green fluorescence due to the presence of dead cells. The visual confirmation of the dead cell indicated the potential use of the TF receptor-targeted NPs for drug delivery to cancer cells overexpressing TF receptors. As observed in case of monolayer cells, ROS plays an important role in inducing DNA damage mediated cell death, ROS generation in treated HeLa spheroids was also detected. For ROS detection in the spheroids, the spheroids incubated with DCFDA were treated with above-mentioned combinations for 24 h. Microscopic images in **Figure 5.19B** showed that untreated spheroids had very low fluorescence from DCF, whereas

DoxMB+L and TF-DoxMB+L treatment resulted in the acquisition of detectable green fluorescence. The highest fluorescence was observed in TF-DoxMB+L treatment. From the studies carried out on 3D spheroids, it was concluded that treated spheroids also followed the similar path of the cell death starting from generation of ROS to DNA damage leading to cell apoptosis. Another key point to remember is that a higher free Dox was needed in spheroidal cells in order to achieve IC_{50}, but the amount of the Dox in TF-DoxMB+L was comparatively very less indicating the synergistic action of the Dox and laser-irradiated MB.

5.4 Conclusions

In conclusion, novel TF-conjugated RBC membrane-coated PLGA NPs were prepared for delivery of anticancer drug molecules. TF conjugation on RBC membrane produced stable and cancer cell-targeted nano-carrier, which showed selective internalization of these NPs via TF receptor-mediated endocytosis in HeLa and MCF-7 cells. Study pursuing the endocytosis mechanism of these NPs revealed that TF-DoxMB NPs followed the clathrin-mediated endocytosis pathway. The results of uptake study and anti-proliferative action of these NPs revealed successful delivery of the Dox and MB, which synergistically improved the efficacy of cell killing upon laser irradiation. The outcome of the study revealed apoptotic cell death of the treated cells via ROS induced DNA damage. The evidence from the assays carried out on 3D spheroids of HeLa cells supported targeting and cell-killing activity of the present nano-formulation. Taken together, a biocompatible nanocarrier, achieving targeted chemotherapeutic as well as photodynamic action may help to improve the efficacy of cancer treatment.

5.5 References

(1) Tannock, I. F. Conventional Cancer Therapy: Promise Broken or Promise Delayed? *Lancet (London, England)* **1998**, *351 Suppl 2*, SII9-16. https://doi.org/10.1016/s0140-6736(98)90327-0.

(2) Peer, D.; Karp, J. M.; Hong, S.; Farokhzad, O. C.; Margalit, R.; Langer, R. Nanocarriers as an Emerging Platform for Cancer Therapy. *Nat. Nanotechnol.* **2007**, *2* (12), 751–760. https://doi.org/10.1038/nnano.2007.387.

(3) Bahrami, B.; Hojjat-Farsangi, M.; Mohammadi, H.; Anvari, E.; Ghalamfarsa, G.; Yousefi, M.; Jadidi-Niaragh, F. Nanoparticles and Targeted Drug Delivery in Cancer Therapy. *Immunol. Lett.* **2017**, *190*, 64–83. https://doi.org/10.1016/J.IMLET.2017.07.015.

(4) Gu, F. X.; Karnik, R.; Wang, A. Z.; Alexis, F.; Levy-Nissenbaum, E.; Hong, S.; Langer, R. S.; Farokhzad, O. C. Targeted Nanoparticles for Cancer Therapy. *Nano Today* **2007**, *2* (3), 14–21. https://doi.org/10.1016/S1748-0132(07)70083-X.

(5) Luk, B. T.; Fang, R. H.; Hu, C.-M. J.; Copp, J. A.; Thamphiwatana, S.; Dehaini, D.; Gao, W.; Zhang, K.; Li, S.; Zhang, L. Safe and Immunocompatible Nanocarriers Cloaked in RBC Membranes for Drug Delivery to Treat Solid Tumors. *Theranostics* **2016**, *6* (7), 1004–1011. https://doi.org/10.7150/thno.14471.

(6) Schiller, J. H.; Harrington, D.; Belani, C. P.; Langer, C.; Sandler, A.; Krook, J.; Zhu, J.; Johnson, D. H. Comparison of Four Chemotherapy Regimens for Advanced Non–Small-Cell Lung Cancer. *N. Engl. J. Med.* **2002**, *346* (2), 92–98. https://doi.org/10.1056/NEJMoa011954.

(7) Green, J. A.; Kirwan, J. J.; Tierney, J.; Vale, C. L.; Symonds, P. R.; Fresco, L. L.; Williams, C.; Collingwood, M. Concomitant Chemotherapy and Radiation Therapy for Cancer of the Uterine Cervix. *Cochrane Database Syst. Rev.* **2005**, No. 3. https://doi.org/10.1002/14651858.CD002225.pub2.

(8) Yi, X.; Dai, J.; Han, Y.; Xu, M.; Zhang, X.; Zhen, S.; Zhao, Z.; Lou, X.; Xia, F. A High Therapeutic Efficacy of Polymeric Prodrug Nano-Assembly for a

Combination of Photodynamic Therapy and Chemotherapy. *Commun. Biol.* **2018**, *1* (1), 202. https://doi.org/10.1038/s42003-018-0204-6.

(9) Chen, Y.; Gao, Y.; Li, Y.; Wang, K.; Zhu, J. Synergistic Chemo-Photodynamic Therapy Mediated by Light-Activated ROS-Degradable Nanocarriers. *J. Mater. Chem. B* **2019**, *7* (3), 460–468. https://doi.org/10.1039/C8TB03030H.

(10) Peng, C.-L.; Lai, P.-S.; Lin, F.-H.; Yueh-Hsiu Wu, S.; Shieh, M.-J. Dual Chemotherapy and Photodynamic Therapy in an HT-29 Human Colon Cancer Xenograft Model Using SN-38-Loaded Chlorin-Core Star Block Copolymer Micelles. *Biomaterials* **2009**, *30* (21), 3614–3625. https://doi.org/10.1016/J.BIOMATERIALS.2009.03.048.

(11) Hu, C.-M. J.; Zhang, L.; Aryal, S.; Cheung, C.; Fang, R. H.; Zhang, L. Erythrocyte Membrane-Camouflaged Polymeric Nanoparticles as a Biomimetic Delivery Platform. *Proc. Natl. Acad. Sci. U. S. A.* **2011**, *108* (27), 10980–10985. https://doi.org/10.1073/pnas.1106634108.

(12) Yang, T.-T.; Sinai, P.; Kain, S. R. An Acid Phosphatase Assay for Quantifying the Growth of Adherent and Nonadherent Cells. *Anal. Biochem.* **1996**, *241* (1), 103–108. https://doi.org/10.1006/ABIO.1996.0383.

(13) Rao, L.; Bu, L.-L.; Xu, J.-H.; Cai, B.; Yu, G.-T.; Yu, X.; He, Z.; Huang, Q.; Li, A.; Guo, S.-S.; et al. Red Blood Cell Membrane as a Biomimetic Nanocoating for Prolonged Circulation Time and Reduced Accelerated Blood Clearance. *Small* **2015**, *11* (46), 6225–6236. https://doi.org/10.1002/smll.201502388.

(14) McMahon, H. T.; Boucrot, E. Molecular Mechanism and Physiological Functions of Clathrin-Mediated Endocytosis. *Nat. Rev. Mol. Cell Biol.* **2011**, *12* (8), 517–533. https://doi.org/10.1038/nrm3151.

(15) Xu, S.; Olenyuk, B. Z.; Okamoto, C. T.; Hamm-Alvarez, S. F. Targeting Receptor-Mediated Endocytotic Pathways with Nanoparticles: Rationale and Advances. *Adv. Drug Deliv. Rev.* **2013**, *65* (1), 121. https://doi.org/10.1016/J.ADDR.2012.09.041.

(16) Cai, F.; Luis, M. A. F.; Lin, X.; Wang, M.; Cai, L.; Cen, C.; Biskup, E.

Anthracycline-Induced Cardiotoxicity in the Chemotherapy Treatment of Breast Cancer: Preventive Strategies and Treatment. *Mol. Clin. Oncol.* **2019**, *11* (1), 15–23. https://doi.org/10.3892/mco.2019.1854.

(17) Thorn, C. F.; Oshiro, C.; Marsh, S.; Hernandez-Boussard, T.; McLeod, H.; Klein, T. E.; Altman, R. B. Doxorubicin Pathways: Pharmacodynamics and Adverse Effects. *Pharmacogenet. Genomics* **2011**, *21* (7), 440–446. https://doi.org/10.1097/FPC.0b013e32833ffb56.

(18) Wang, S.; Konorev, E. A.; Kotamraju, S.; Joseph, J.; Kalivendi, S.; Kalyanaraman, B. Doxorubicin Induces Apoptosis in Normal and Tumor Cells via Distinctly Different Mechanisms. Intermediacy of H(2)O(2)- and P53-Dependent Pathways. *J. Biol. Chem.* **2004**, *279* (24), 25535–25543. https://doi.org/10.1074/jbc.M400944200.

(19) Tardivo, J. P.; Del Giglio, A.; de Oliveira, C. S.; Gabrielli, D. S.; Junqueira, H. C.; Tada, D. B.; Severino, D.; de Fátima Turchiello, R.; Baptista, M. S. Methylene Blue in Photodynamic Therapy: From Basic Mechanisms to Clinical Applications. *Photodiagnosis Photodyn. Ther.* **2005**, *2* (3), 175–191. https://doi.org/10.1016/S1572-1000(05)00097-9.

(20) Jiang, J.; Qian, Y.; Xu, Z.; Lv, Z.; Tao, P.; Xie, M.; Liu, S.; Huang, W.; Zhao, Q. Enhancing Singlet Oxygen Generation in Semiconducting Polymer Nanoparticles through Fluorescence Resonance Energy Transfer for Tumor Treatment. *Chem. Sci.* **2019**, *10* (19), 5085–5094. https://doi.org/10.1039/C8SC05501G.

Conclusion & Future scopes

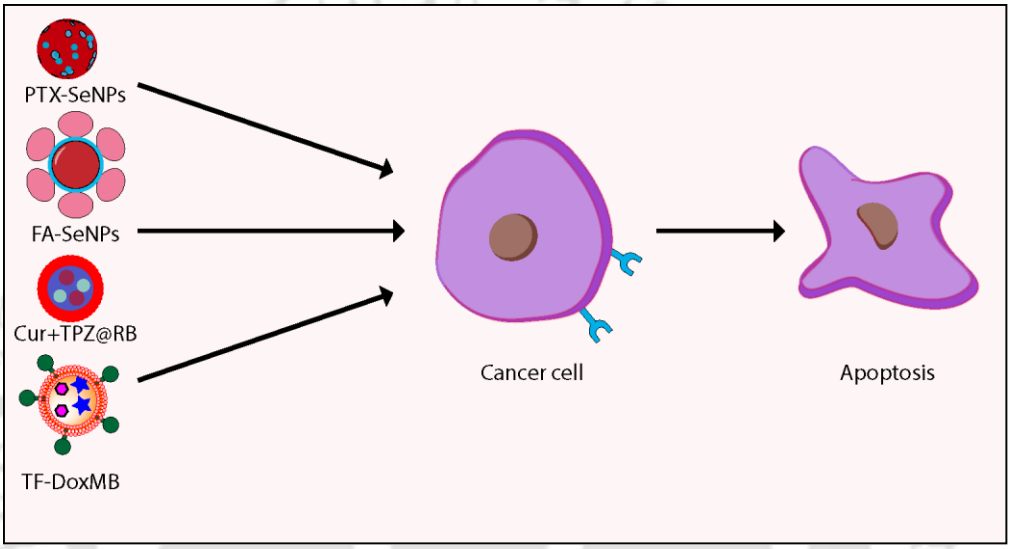

This section summarizes the important findings of the thesis work. In addition, possible future research scopes are also included.

CONCLUSIONS

Burgeoning research in the field of nanomedicine has developed several nanocarriers for drug delivery applications. Particularly, nanocarriers for delivery of chemotherapeutic drugs have gained much attention to combat incidence of cancer-related deaths. The essential characteristics of a nanocarrier for potential therapeutic use include stability, biocompatibility and targeting ability. To achieve these properties, surface modification of nanocarriers can be performed. Selenium and RBC membrane-based nanocarriers are quite important due to their stability and biocompatibility. Selenium-based compounds possess antiproliferative properties and thus, selenium nanoparticles could be utilized for drug delivery as well as targeted therapy.

Initially in **chapter 2**, selenium based nanocarrier was formulated for delivery of hydrophobic drug (paclitaxel) using F-127 polymer. Repeating units of hydrophobic and hydrophilic segments of F-127 was useful to load paclitaxel. These drug-loaded NPs showed excellent antiproliferative and cell-killing properties against cancer cells. The cancer cells proliferate uncontrollably due to genetic mutations that could alter signaling pathways. Although abnormal signaling events can be blocked with signaling inhibitors, but such inhibition is temporary and the cells start dividing once the concentration of inhibitor recedes. Another property of the cancer cell is the overexpression of the specific receptors like folic acid receptor. Thus, in the **chapter 3**, the selenium nanoparticles were decorated with folic acid to target cancer cells expressing high folic acid receptor. Such cancer cells have mutations in MAPK pathway genes. Targeted selenium nanoparticles entered into the cancer cells efficiently. In addition, concomitant blocking of MAPK signaling by small molecule inhibitor improved the therapeutic potential of the selenium nanoparticles.

In **chapter 4**, RBC membrane based nanoparticles were developed for delivery of therapeutic molecules. The PLGA nanoparticles loaded with curcumin and tirapazamine were coated with RBC membrane layer. Uptake of the nanoparticles was facilitated resulting in more accumulation of drugs after RBC membrane coating. Growth of the hypoxic 3D tumor spheroids were reduced significantly by treatment with drug loaded RBC membrane coated nanoparticles.

Though the RBC membrane coated nanoparticles were shown to deliver considerable amount of drugs to the cancer cells, but it was observed that solo RBC membrane coating could not able to distinguish between cancer cells and normal cells. In order to resolve the issue, targeting transferrin receptor was planned, because cancer cells express higher amount of transferrin receptors than normal cells. Thus, to achieve targeted delivery of drugs to the cancer cells, transferrin was conjugated on the surface of the nanoparticles (**chapter 5**). The transferrin conjugated RBC membrane coated PLGA nanoparticles exhibited efficient delivery of doxorubicin and methylene blue into cancer cells. While doxorubicin revealed profound chemotherapeutic effect, methylene blue enabled photodynamic effect upon laser irradiation leading to synergistic anti-cell proliferation. Selective delivery of the drugs to cancer cells resulted higher anticancer effect as compared to RBC membrane coated or PLGA NPs containing drugs. The combined photodynamic and chemotherapeutic effects generated ROS mediated DNA damage resulting synergistic cell apoptosis.

Future Prospects:

The potential scopes of the present findings include:

- The therapeutic ability of the Se nanoparticles could be explored by targeted delivery of combination of drugs.

- For a better understanding of pro-oxidant roles, the effect of Se nanoparticles may be explored in *in-vivo* model. The output of this study would help to design a dose of Se supplementation required for antioxidant or therapeutic applications.
- Se nanoparticles can be combined with metallic nanoclusters (Au, Ag) for luminescent based bioimaging studies.
- A comparative study of RBC membrane versus cancer cell membrane coating may be explored.
- RBC or transferrin conjugated RBC membranes could be efficiently used for drug delivery *in-vivo*.
- Molecules such as, proteins, peptides and siRNAs prone to degradation by cellular hydrolysis could be stabilized by cell membrane vesicles.

PUBLICATIONS & CONFERENCES

Publications from Thesis work:

1. **Bidkar, A. P.**, Sanpui, P., Ghosh, S. S., Enhanced Chemo and Hypoxia Activated Therapy Using RBC Membrane Coated Nanoparticles. ***ACS Applied Bio Materials,*** **2019,** DOI: 10.1021/acsabm.9b00584.

2. **Bidkar A. P**., Pallab Sanpui, and Siddhartha Sankar Ghosh, Combination Therapy with MAPK-Pathway-Specific Inhibitor and Folic-Acid Receptor targeted Selenium Nanoparticles Induces Synergistic Antiproliferative Response in BRAF Mutant Cancer Cells, *ACS Biomaterial Science & Engineering*. 2019, *5* (5), pp 2222–2234, DOI: 10.1021/acsbiomaterials.9b00112

3. **Bidkar A. P**., Sanpui, P., Ghosh, S. S. Efficient induction of apoptosis in cancer cells by paclitaxel-loaded selenium nanoparticles. ***Nanomedicine (Lond).*** **2017,** *12* (21), 2641–2651 DOI: 10.2217/nnm-2017-0189.

4. **Bidkar, A. P.**; Sanpui, P.; Ghosh, S. S., Targeted delivery of doxorubicin and methylene blue using membrane coated nanocarriers. [Manuscript under preparation],

Collaborative work:

5. Binita Nath*, **Bidkar, A. P.***, Vikash Kumar, Amaresh Dalal, Mohit Kumar Jolly, Siddhartha S. Ghosh and Gautam Biswas. Deciphering Hydrodynamic and Drug-Resistant Behaviors of Metastatic EMT Breast Cancer Cells Moving in a Constricted Microcapillary. ***Journal of Clinical Medicine.*** **2019**, 8(8), 1194; DOI: 10.3390/jcm8081194 [* equal Contribution]

6. Rupam Sinha, **Bidkar, A. P,** Ravula Rajasekhar; Siddhartha S Ghosh; Tapas K Mandal. A Facile Synthesis of Nontoxic Luminescent Carbon Dots for Detection of Chromium and Iron in Real Water Sample and Bio-imaging. ***The Canadian Journal of Chemical Engineering,*** **2019,** DOI: 10.1002/cjce.23630

7. Selvarajan, V., **Bidkar, A. P**., Shome, R.; Banerjee, A.,Chaubey, N., Ghosh, S. S., Sanpui, P. Studying in vitro phagocytosis of apoptotic cancer cells by recombinant GMCSF-treated RAW 264.7 macrophages. ***International Journal of Biological Macromolecules,*** **2017,** 102, 1138–1145 DOI: 10.1016/j.ijbiomac.2017.05.003.

8. Pandit, G, Ilyas, H, Ghosh, S; **Bidkar, A. P.**, Bhunia, An, Satpati, P; Chatterjee, S Insights into the Mechanism of Antimicrobial Activity of Seven-Residue Peptides. ***Journal of Medicinal Chemistry,*** **2018,** 61 (17), pp 7614–7629

9. Gopal Pandit, Karishma Biswas, Suvankar Ghosh, Swapna Debnath, Msc; **Anil P Bidkar**, Priyadarshi Satpati, Anirban Bhunia, Sunanda Chatterjee. Rationally Designed Antimicrobial Peptides: Insight into the Mechanism of Eleven Residue Peptides against Microbial Infections. [Manuscript under Revision].

Conferences and Workshops

1. Poster presentation in International Conference on Advanced Nanomaterials and Nanotechnology, ICANN-2017, December 18-21, 2017.

2. Participated in hands on training course on “Advanced Microscopy and Imaging Techniques”, organized by DSS Imagetech and Olympus Medical Systems Pvt Ltd. 18th-20th April 2017.

3. Attended "National Conference on Recent Advance in Cancer Biology and Therapeutics-2014", organized by Dept. of Biotechnology, IIT Guwahati. December 5th, 2014.

4. Participated in seminar on "Translational Research & Biomarker Discovery", Sponsored by DBT Program Support and SCIEX at IIT Guwahati. 4th September 2018

5. Participated as a member of organizing committee to impart training in fluorescence activated cell sorting (FACS) in the DBT program support project sponsored Hands on workshop on: Gene Expression and Function Analysis for Crop Improvement". IIT Guwahati, 16th-20th January, 2018

Copyright Clearance Center RightsLink®

Home | Account Info | Help

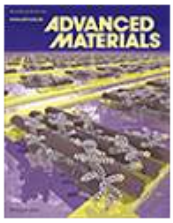

Title: Cell Membrane Coating Nanotechnology
Author: Liangfang Zhang, Weiwei Gao, Ashley V. Kroll, et al
Publication: Advanced Materials
Publisher: John Wiley and Sons
Date: Mar 27, 2018

Logged in as:
Anil Parsram Bidkar
Account #:
3001304928
LOGOUT

Order Completed

Thank you for your order.

This Agreement between Mr. Anil Bidkar ("You") and John Wiley and Sons ("John Wiley and Sons") consists of your license details and the terms and conditions provided by John Wiley and Sons and Copyright Clearance Center.

Your confirmation email will contain your order number for future reference.

printable details

License Number	4645460878979
License date	Aug 10, 2019
Licensed Content Publisher	John Wiley and Sons
Licensed Content Publication	Advanced Materials
Licensed Content Title	Cell Membrane Coating Nanotechnology
Licensed Content Author	Liangfang Zhang, Weiwei Gao, Ashley V. Kroll, et al
Licensed Content Date	Mar 27, 2018
Licensed Content Volume	30
Licensed Content Issue	23
Licensed Content Pages	34
Type of use	Dissertation/Thesis
Requestor type	University/Academic
Format	Print and electronic
Portion	Figure/table
Number of figures/tables	2
Original Wiley figure/table number(s)	Figure 1
Will you be translating?	
Title of your thesis / dissertation	Multifaceted approaches for cancer therapeutics
Expected completion date	Oct 2019
Expected size (number of pages)	100
Requestor Location	Mr. Anil Bidkar Room No- G140, Brahmaputra Hostel, Indian Institute of Technology Guwahati Guwahati, other 781039

Copyright Clearance Center

Note: Copyright.com supplies permissions but not the copyrighted content itself.

1 PAYMENT 2 REVIEW **3 CONFIRMATION**

Step 3: Order Confirmation

Thank you for your order! A confirmation for your order will be sent to your account email address. If you have questions about your order, you can call us 24 hrs/day, M-F at +1.855.239.3415 Toll Free, or write to us at info@copyright.com. This is not an invoice.

Confirmation Number: 11842007
Order Date: 08/15/2019

If you paid by credit card, your order will be finalized and your card will be charged within 24 hours. If you choose to be invoiced, you can change or cancel your order until the invoice is generated.

Payment Information

Anil Parsram Bidkar
a.bidkar@iitg.ac.in
+91 9435685175
Payment Method: n/a

Order Details

Nanoscale

Order detail ID:	71981508
Order License Id:	4650291097010
ISSN:	2040-3372
Publication Type:	e-Journal
Volume:	
Issue:	
Start page:	
Publisher:	RSC Pub
Author/Editor:	National Center for Nanoscience and Technology ; Royal Society of Chemistry (Great Britain)

Permission Status:	Granted
Permission type:	Republish or display content
Type of use:	Thesis/Dissertation
Requestor type	Author of requested content
Format	Print
Portion	image/photo
Number of images/photos requested	1
The requesting person/organization	Anil Parsram Bidkar
Title or numeric reference of the portion(s)	Figure 1
Title of the article or chapter the portion is from	Erythrocyte membrane-coated NIR-triggered biomimetic nanovectors with programmed delivery